

THE NATURE OF NEAR-EARTH ASTEROIDS
FROM THE STUDY OF THEIR THERMAL
INFRARED EMISSION

Dissertation zur Erlangung des Grades
eines Doktors der Naturwissenschaften

vorgelegt von

Dipl.-Phys. Marco Delbo

Angefertigt am Institut fuer Weltraumsensorik und Planetenerkundung des
Deutschen Zentrums fuer Luft- und Raumfahrt e.V. in Berlin, Deutschland
und im Istituto Nazionale di Astrofisica – Osservatorio Astronomico di
Torino, Italien

und eingereicht im Fachbereich
Geowissenschaften der Freien
Universität Berlin

2004

Gutachter

1. Gutachter: Prof. G. Neukum
2. Gutachter: Prof. E. Sedlmayr

A b s t r a c t

Freie Universität Berlin

THE NATURE OF NEAR-EARTH ASTEROIDS
FROM THE STUDY
OF THEIR THERMAL INFRARED EMISSION

The topic of this dissertation is the investigation of physical properties of near-Earth Asteroids (NEAs) to improve our understanding of their nature, origin and their relation to main-belt asteroid (MBAs) and comets. A major aspect of the research is the use and the improvement of models of the thermal infrared emission of asteroids (the so-called thermal models) to facilitate the determination of sizes, albedos and other physical properties of NEAs.

A major development within this study is the discussion of the results from new observing programs with the 10m - Keck 1 telescope, the NASA-Infrared Telescope Facility (IRTF) on Mauna Kea, Hawaii and the 3.6m telescope at the European Southern Observatory (ESO), La Silla, Chile. In the framework of these observing programs, thermal emission continua of thirty-two NEAs have been obtained in the medium infrared (MidIR) (5-20 μ m).

By fitting thermal models to the observational data, we have derived the sizes and the albedos of a significant sample of the near-Earth asteroid population. This work increments the number of NEAs with measured sizes and albedos by 54%. If we include objects for which the diameter and the albedo have been refined, this increment increases up to almost 70%. The uniqueness of our project was the possibility of studying smaller and fainter objects which are only accessible with the most up-to-date Mid-IR instrumentations and the largest telescopes on the ground. There were very few thermal infrared observations of asteroids in the 1-kilometer size range, and we have more than doubled the number of subkilometer-NEAs with measured size and albedos. The good quality data that we have obtained constitute the largest database of NEAs radiometric diameters and albedos.

An accurate determination of sizes for a significant sample of NEAs, besides providing crucial input for the assessment of the impact hazard these objects pose for our planet, gives important clues about their surface characteristics.

Although we confirm that the spread of NEA albedos is very large ($p_V = 0.02 - 0.55$), consistent with their being supplied from more than one source region, we have found that observed NEAs are on average brighter than MBAs. The average value of radiometrically determined albedo is 0.27, which is much higher than the mean albedo of observed MBAs (~ 0.11). In several cases the albedos are in the ranges expected for their taxonomic types, although some exceptions are evident. Overall, we find that observed S-type NEAs are on average 20% brighter than S-type MBAs, whereas observed C-type NEAs have on average albedos 57% higher than C-type MBAs. Such dichotomy between the albedo statistics of large and small asteroids implies a fundamental difference in surface properties of small asteroids with respect to the larger ones. We show, moreover, that a variation of surface properties with size exists within the NEA population itself. A trend of increasing albedo with decreasing diameter for S-type NEAs has been identified. We argue that this trend is indicative of recently exposed, relatively unweathered surfaces. Although a selection effect in favor of the discovery of the brightest asteroids would give rise to such trend, this result is also consistent with the trend to ordinary-chondrite-type reflection spectra with decreasing size observed in the NEA population. This last effect is also attributed to a lack of space weathering of relatively young surfaces.

NEAs do not only have higher albedos than larger MBAs, but they differ also in surface thermal properties. Our work confirms the hypothesis that these asteroids have higher thermal inertias than large MBAs. We have derived a best-fit estimate for the thermal inertia of the observed near-Earth asteroids of $550 \pm 100 \text{ J m}^{-2} \text{ s}^{0.5} \text{ K}^{-1}$. This value is about eleven times higher than that of the Moon and more than 30 times larger than that of the largest asteroids 1 Ceres and 2 Pallas. This result has important implications for our understanding of the nature and the origin of these bodies. For instance, the higher thermal inertia is an indication that these asteroids have surfaces covered with a regolith coarser than the lunar one and, very likely, different surface fractional rock coverage than large MBAs.

This result was obtained by studying the correlation of the observed distribution of surface color temperatures that NEAs display as a function of the phase angle in the light of a thermophysical model. The thermophysical model that we have developed in this work, takes account of the effects of rotation rate, thermal inertia and surface roughness on the thermal emission of airless bodies. In particular, we have demonstrated that the observed distribution of the color temperature with the phase angle can be used to constrain the thermal inertia (and partially the surface roughness) of the observed asteroids in the hypothesis that their spin vectors were randomly oriented.

By means of our thermophysical model, we have also obtained a quantitative assessment of the uncertainties in the NEAs albedos and diameters derived by using the Standard Thermal Model (STM) and the near-Earth asteroids thermal (NEATM) model, which both make assumption about the surface temperature distribution and the thermal inertia of NEAs. We have numerically estimated a correction function for NEAs radiometric diameters and albedos derived by means of the STM and of the NEATM, provided that spin status and thermal parameter of the asteroid are known. When such information is not available, the accuracy of NEATM results can be still estimated on the basis of the derived color temperature of the objects.

Our intriguing new results suggest that, by analyzing thermal infrared observations of NEAs of different sizes and classes by means of thermophysical modeling, it is possible to study the range of thermal properties and surface structure present in the NEA population.

Deutsche Zusammenfassung

DIE NATUR VON ERDNAHEN ASTEROIDEN ABGELEITET AUS DEM STUDIUM IHRER THERMISCHEN INFRAROT-EMISSIONEN

Das Thema dieser Dissertation ist die Untersuchung der physikalischen Eigenschaften von erdnahen Asteroiden (NEAs), um unser Verständnis ihrer Natur, ihren Ursprungs und ihre Beziehung zu Hauptgürtelasteroiden (MBAs) zu verbessern.

Ein Hauptaspekt dieser Forschungsarbeit ist der Einsatz verbesserter thermischer Modelle zur Beschreibung der Infrarot-Emissionen von Asteroiden. Ziel der Modellierung ist die Bestimmung von Größe, Albedo und anderen Eigenschaften von NEAs aus Beobachtungsdaten.

Einen Kernpunkt dieser Arbeit stellt die Diskussion der Ergebnisse von drei neuen Beobachtungsprogrammen, mit dem 10m Keck 1 Teleskop, dem NASA-Infrared Telescope F. (IRTF) auf dem Mauna Kea, Hawaii, und dem 3,6m Teleskop auf der Europäischen Südsternwarte (ESO) in La Silla, Chile, dar. Diese Beobachtungsprogramme umfassten die Messung der thermalen Emission von 32 NEAs im mittleren Infrarot (Mid-IR) von 5-20 μm .

Durch einen Fit der thermischen Modelle an die Beobachtungsdaten konnten wir Größe sowie Albedo einer beachtlichen Anzahl von erdnahen Asteroiden bestimmen. Diese Arbeit erhöht die Anzahl von NEAs mit bekannten Größen und Albedos um 54%. Nimmt man Objekte hinzu, deren Durchmesser und Albedo korrigiert wurden, so erhöht sich diese Zahl sogar auf 70%. Die Besonderheit unseres Projektes besteht in der Möglichkeit, kleinere und lichtschwächere Objekte zu studieren, die sonst nur mit neuesten Mid-IR Instrumenten und den größten erdgebundenen Teleskopen zugänglich waren. Bisher gab es nur sehr wenige Beobachtungen von Asteroiden der Größenordnung von einem Kilometer und wir konnten die Anzahl von Sub-Kilometer NEAs mit bekannter Größe und Albedo mehr als verdoppeln. Die von uns erhaltenen qualitativ guten Daten bilden die größte Datenbank von radiometrischen Durchmessern und Albedos von NEAs.

Die genaue Größenbestimmung einer großen Anzahl von NEAs ermöglicht uns, neben der Beurteilung der Auswirkungen eines möglichen Einschlages auf unserem Planeten, wichtige Rückschlüsse auf deren Oberflächeneigenschaften.

Wir konnten bestätigen, dass die Verteilung der NEA-Albedos sehr breit ist ($p_v = 0.02 - 0.55$), was im Einklang zu der Tatsache steht, dass sie aus mehr als einer Ursprungsregion gespeist werden. Allerdings erwiesen sich die beobachteten NEAs im Allgemeinen als heller als MBAs. Der durchschnittliche Wert der radiometrisch bestimmten Albedos kann mit 0.27 angegeben werden und liegt damit viel höher als die durchschnittliche Albedo von beobachteten MBAs (~ 0.11). In den meisten Fällen bewegen sich die Albedos in den aufgrund ihrer taxonomischen Art erwarteten Bereichen, obwohl einige Ausnahmen evident wurden. Im Allgemeinen fanden wir, dass beobachtete S-type NEAs im Durchschnitt 20% heller als S-type MBAs sind, wobei beobachtete C-type NEAs im Durchschnitt 57% höhere Albedos als C-type MBAs haben. Solch eine Diskrepanz in der Albedo Statistik zwischen großen und kleinen Asteroiden impliziert einen fundamentalen Unterschied in den Oberflächeneigenschaften von kleinen Asteroiden im Vergleich zu den größeren. Wir zeigen weiterhin, dass es eine Variation der Oberflächeneigenschaften mit der Größe innerhalb der NEAs selbst gibt. In diesem Zusammenhang konnte ein Trend von steigender Albedo mit sinkendem Durchmesser von S-type NEAs identifiziert werden. Wir argumentieren weiter, dass dieser Trend ein Anzeichen von erst letztlich freigelegten und dem „space-weathering“ ausgesetzten Oberflächen ist. Dieses Ergebnis ist konsistent mit dem Trend zu Reflexionsspektren von gewöhnlichen Chondriten bei kleineren NEAs, der auch auf das verringerte space weathering an jungen Oberflächen zurück geführt wird.

NEAs weisen nicht nur eine höhere Albedo als die größten MBAs auf, sie differieren auch in ihren thermalen Oberflächeneigenschaften. Unsere Arbeit bestätigt die Hypothese, dass diese Asteroiden eine größere thermische Trägheit als große MBAs haben und wir leiten im Zuge dessen einen best-fit Wert von $550 \pm 100 \text{ J m}^{-2} \text{ s}^{-0.5} \text{ K}^{-1}$ für die thermische Trägheit der beobachteten NEAs ab. Dieser Wert ist ungefähr 11-mal höher als der des Mondes und 30-mal höher als der der größten Asteroiden 1 Ceres und 2 Pallas. Dieses Resultat hat wichtige Implikationen für unser Verständnis von Natur und Ursprung dieser Objekte. Zum Beispiel weist eine höhere thermische Trägheit auf gröberes Regolith auf der Oberfläche dieser Asteroiden im Vergleich zu der des Mondes und, sehr wahrscheinlich, auf eine andere Oberflächen-Felsverteilung in Bezug auf große MBAs hin.

Dieses Resultat ergab sich aus dem Studium der Korrelation von beobachteter Verteilung der Oberflächen-Farbtemperatur von NEAs als Funktion des Phasenwinkels im Lichte eines thermophysikalischen Modells. Das in dieser Arbeit entwickelte Modell bezieht Effekte wie Rotationsrate, thermische Trägheit und Oberflächen-Rauhigkeit für die Berechnung der thermischen Emission von Körpern ohne Atmosphäre ein. Im Speziellen konnten wir demonstrieren, dass die beobachtete Verteilung der Farbtemperatur in Abhängigkeit vom Phasenwinkel als Mittel zur Bestimmung der thermischen Trägheit (und zum Teil der Oberflächen-Rauhigkeit) der beobachteten Asteroiden unter der Annahme von zufällig verteilten Spin-Vektoren benutzt werden kann.

Mit Hilfe unseres thermophysikalischen Modells konnten wir eine quantitative Bestimmung der Unsicherheiten in Albedo und Durchmesser der NEAs, abgeleitet mit dem Standard Thermal Model (STM) und dem Near Earth Asteroid Thermal Model (NEATM), die beide Annahmen über die Oberflächentemperaturverteilung und thermische Trägheit von NEAs machen, gewinnen. Weiterhin haben wir numerisch eine Korrekturfunktion für die radiometrischen Durchmesser und Albedos, die aus dem STM bzw. aus NEATM ermittelt werden, bestimmt, vorausgesetzt Spin Status und thermische Parameter des Asteroiden sind bekannt. Sind solche Informationen nicht verfügbar, kann die Genauigkeit der NEATM Ergebnisse immer noch auf Basis der abgeleiteten Farbtemperatur der Objekte abgeschätzt werden.

Unsere aufregenden neuen Ergebnisse legen nahe, dass die Analyse von thermischen Infrarot-Beobachtungen von NEAs unterschiedlicher Größe und Klasse mit Hilfe von thermophysikalischen Modellen ein Studium der in der NEA Population vorkommenden thermischen Eigenschaften und Oberflächenstrukturen möglich macht.

TABLE OF CONTENTS

Abstract	iv
Deutsche Zusammenfassung	viii
<i>Chapter 1</i>	<i>1</i>
Introduction	1
1.1 Asteroids	1
1.2 Main Belt Asteroids	2
1.3 Physical characteristics of Near Earth Asteroids and Near Earth Objects	5
1.4 The need of physical characterization of NEOs: statement of the problem	10
1.5 Scope of this work	12
<i>Chapter 2</i>	<i>13</i>
Sizes and albedos of asteroids: the radiometric method and asteroid thermal models	13
2.1 Foreword	13
2.2 Introduction	13
2.3 Asteroid surface temperatures	15
2.4 Calculation of the emitted thermal infrared flux	18
2.5 Constraints on diameter and albedo from the visible absolute magnitude	19
2.6 Radiometric diameters and albedos	19
2.7 Thermal models of asteroids	20
2.7.1 The Standard Thermal Model (STM)	20
2.7.2 The Fast Rotating Model (FRM)	22
2.7.3 The near-Earth asteroid thermal model (NEATM)	23
2.8 Uncertainties	26
2.8.1 Rotational variability effects and lightcurve correction of infrared fluxes	26
2.8.2 The actual temperature distribution differs from the modeled one	26
2.8.3 Accuracy of the H values	27
2.9 Thermophysical models	27
2.10 Summary	28
<i>Chapter 3</i>	<i>31</i>
Thermal infrared observations of near-Earth asteroids and data reduction	31
3.1 Foreword	31
3.2 Introduction	31
3.3 Thermal infrared ground based observations	33
3.4 Thermal IR photometry	36
3.5 Aperture photometry and photometric uncertainties	38

3.6	Data reduction of thermal IR data	39
3.7	Thermal infrared observations of NEAs: a method for accurate nod-set registering	42
3.8	Color correction	44
3.9	Thermal IR spectroscopy at the TIMMI2	45
3.10	Visible CCD observations at ESO: data reduction	49
3.11	The data set	50
3.11.1	Near-Earth asteroids observed at KECK	51
3.11.2	Near-Earth asteroids observed at ESO	52
3.11.3	Near-Earth asteroids observed at the NASA-IRTF	53
3.12	Summary	54

Chapter 4 57

Thermal model fits to thermal infrared data and derivation of albedos and diameters **57**

4.1	Foreword	57
4.2	Introduction	57
4.2.1	Diameters, albedos and η -values derived from observations at Keck	58
4.2.2	Diameters, albedos and η -values derived from observations at ESO	59
4.2.3	Diameters, albedos and η -values derived from observations made at the NASA-IRTF	60
4.3	Comments on individual asteroids	60
4.3.1	15817 Lucianotesi (1994 QC)	61
4.3.2	2000 EV ₇₀	62
4.3.3	2001 HW ₁₅	62
4.3.4	25143 Itokawa (formerly known as 1998 SF ₃₆)	62
4.3.5	2001 LF	65
4.3.6	5381 Sekmeth	67
4.3.7	25330 (1999 KV ₄)	69
4.3.8	2002 AV ₄	70
4.3.9	5587 (1990 SB)	71
4.3.10	19356 (1997 GH ₃)	75
4.3.11	5604 (1992 FE)	75
4.3.12	37314 (2001QP)	76
4.3.13	33342 (1998WT ₂₄)	76
4.3.14	35396 (1997 XF ₁₁)	79
4.3.15	1580 Betulia	83
4.4	Physical characterization of NEAs: summary of results	85

Chapter 5 91

Analysis of results from thermal models: the observed albedo distribution of NEAs and the correlation of η with the phase angle **91**

5.1	Foreword	91
5.2	The observed albedo distribution of NEAs	91
5.3	Phase angle dependence of the observed color temperature	95
5.3.1	NEAs with anomalous thermal properties ($\eta > 2$)	96

5.3.2	NEAs with “common” thermal properties	97
5.4	The infrared phase curve of NEAs with “common” thermal properties	98
5.5	Comparison of radiometric diameters with radar	100
5.6	On the recalibration of the STM for NEAs	105
5.7	Correlation of radiometric albedos with solar phase angle	108
5.8	Conclusions	109

Chapter 6 113

Estimate of the thermal inertia of NEAs and assessment of the accuracy of thermal models 113

6.1	Foreword	113
6.2	Introduction	113
6.3	Thermophysical model components	116
6.4	Thermal Inertia and the heat diffusion within spherical craters	117
6.5	Numerical simulations	120
6.6	Results of the simulations	124
6.6.1	Effects of thermal inertia and rotation rate on the theoretical dependence of the NEATM η -value with the phase angle	124
6.6.2	Effects of surface roughness on the theoretical dependence of the NEATM η -value with the phase angle	126
6.6.3	Combined effects of thermal inertia, rotation rate and surface roughness on the theoretical dependence of the NEATM η -value with the phase angle	127
6.7	The thermal inertia of NEAs	132
6.8	Implications for the Yarkovsky effect on kilometer and sub-kilometer size asteroids	138
6.9	Effects of surface roughness, thermal inertia and rotation rate on the accuracy of NEA radiometric diameters and albedos.	139
6.10	Conclusions	146

Chapter 7 149

Conclusion and future works 149

7.1	Conclusions	149
7.1.1	This work increases the number of NEAs with measured sizes and albedos by 54%	149
7.1.2	The observed NEAs are on average brighter than main belt asteroids	149
7.1.3	There is a trend of increasing albedo with decreasing size for observed S-type NEAs	150
7.1.4	The ambiguous taxonomic classifications of six asteroids have been clarified in the light of the new albedo values.	150
7.1.5	The apparent color temperature of the observed NEAs is phase angle dependent	150
7.1.6	The variation of the color temperature with phase angle depends on the albedo	151
7.1.7	The observed distribution of the color temperature with the phase angle can be explained in terms of thermal inertia and surface roughness	151
7.1.8	The best-fit thermal inertia of the observed NEAs is $550 \pm 100 \text{ J m}^{-2} \text{ s}^{-0.5} \text{ K}^{-1}$ or about 11 times that of the Moon	151
7.1.9	There are asteroids with anomalously low color temperature	152

7.1.10	The observed distribution of color temperature allows a calibration of thermal models for applications to NEAs	152
7.1.11	We have derived a quantitative assessment of the accuracy of thermal models and a correction function for the nominal results of the NEATM and the STM	153
7.2	Future works	153
7.2.1	Application of thermophysical models to NEAs	153
7.2.2	Study of the contribution of a selection bias in the observed trend of increasing albedo with decreasing size	154
7.2.3	Study the range of thermal and surface properties of NEAs by means of thermal infrared	154
REFERENCES		155
<i>Appendix A</i>		<i>113</i>
Observed thermal Infrared Fluxes of near-Earth asteroids		165
<i>Appendix B</i>		<i>113</i>
Colour correction factors for LWS, TIMMI2, MIRSI and MIRLIN filters		173
B.1	LWS at Keck 1 filters and color correction factors	173
B.2	TIMMI2 filters and color correction factors	176
B.3	MIRLIN filters and color correction factors	177
B.4	MIRSI filters and color correction factors	178
<i>Appendix C</i>		<i>179</i>
Thermal Infrared photometry: NOTES		179
LEBENS LAUF		181

LIST OF FIGURES

<i>Figure number</i>	<i>Page</i>
Fig. 1.1 Plot of the semi-major axis versus eccentricity for main belt asteroids. Note the presence of significant clumpings of objects already identified by Hirayama in 1819 as “families” and the Kirkwood gaps.	3
Fig. 1.2 Three-dimensional rendering of the shape model of the near Earth asteroid 433 Eros obtained by the NEAR-Schoemaker mission. This rendering has been calculated using the freely distributed computer program Wings 3-D.	6
Fig. 1.3 Histogram of the relative proportions of measured taxonomic properties for more than 300 NEOs listed in Table 1, Binzel et al. 2002.	8
Fig. 1.4 Two examples of reflectance spectra of asteroids along with their meteorites analogs. One explanation for the spectral mismatches is that space weathering processes affect the surfaces of the asteroids, altering them from their original spectral properties. Figure obtained from Clark et al., 2002.	9
Fig. 2.1 N-band a) and Q-band b) spectra of the thermal infrared emission of the near-earth asteroid 5587 (1990SB) observed on April 09, 2001 with the TIMMI2 installed at the 3.6m telescope, La Silla, ESO (Chile). This asteroid has a diameter of almost 4km.	13
Fig. 2.2 Observed thermal infrared fluxes of the NEA 5587 on the left and of the largest asteroid 1 Ceres. Note the noise affecting Q-band data which have been binned for increasing the signal to noise ratio. Continuous line is a black body fit to the infrared spectra.	14
Fig. 2.3 Dependence of the sub-solar temperature as a function of its heliocentric distance for an asteroid in instantaneous thermal equilibrium with sunlight at all points on its surface. For objects orbiting the Sun in the near-Earth space, the surface temperature is about 400K and the emitted thermal radiation peaks around 8 μm . However, the radiation of more distant asteroids shifts toward longer wavelength as their temperature decreases. The following parameters have been used to produce the plot: $A = 0.0393$ (corresponding to $p_V = 0.1$ and $G = 0.15$) emissivity = 0.9, and solar constant = 1373 W m^{-2} .	17
Fig. 2.4 Dependence of the sub-solar temperature of an asteroid as a function of the bolometric Bond albedo A . This dependence does not depend on the heliocentric distance of the body.	17
Fig. 2.5 Constraints on the albedo and effective diameter from thermal infrared observations and visible absolute magnitude. Solid line: curve defined by Eq. (2-15), dashed-line: curve defined by Eq. (2-16).	19
Fig. 2.6 As of Fig. 2.3, but T_{ss} is calculated for different value of the parameter η . Solid-line: $\eta=1.0$; dashed-line: $\eta=0.756$ as in the “refined” STM of Lebofsky and Spencer (1989); dotted-line: $\eta=0.6$, dashed- and dotted-line: $\eta=\pi$ which is the value used within the FRM.	25
Fig. 3.1 Atmospheric transmission above Mauna Kea, Hawaii. Note the narrow window at 5 μm (M band), the ozone absorption band at about 9.5 μm in the middle of the N band. The atmosphere is opaque between 13.5 and about 17 μm . Beyond 17 μm up to about 20-23 μm the Q band opens.	33
Fig. 3.2 A typical “chop-nod” observing sequence of a standard star obtained with the Thermal Infrared Multimode Instrument (TIMMI2) installed at the ESO 3.6m telescope at La Silla,	

- Chile. Although the star is very bright, its signal is completely buried in the background radiation. Only in the differential frames it becomes visible. 35
- Fig. 3.3 On the left, chopping and nodding throws at TIMMI2, MIRSI and MIRLIN for small source imaging and for spectroscopy. On the right chopping and nodding at the LWS at Keck. Note that the detector field of view is too small to contain both positive and negative beams. This figure was adapted from the TIMMI2 web site: (http://www.lis.eso.org/lasilla/Telescopes/360cat/timmi/images/quick_chop_nod.gif) 36
- Fig. 3.4 The ATV tool: on the left (a), ATV shows a mid-IR image of a standard star obtained with the TIMMI2 at the ESO 3.6 m telescope. On the right (b), the ATV aperture photometry plug-in used to analyze one of the four chop-nod channels. 40
- Fig. 3.5 Growth curves calculated for the one of the four chop-nod channels of a $11.7\mu\text{m}$ -image of the asteroid 2001 LF, observed on June 03, 2003 with TIMMI2 at the ESO 3.6 m telescope (image file name: 306030840.fits). On the left plot a background value of 0.497 counts yielded 1190 counts for the source in an aperture of 10 pixels of radius. On the right, a larger background value – i.e. 0.687 counts – subtracted over an increasing aperture radius causes the net flux of the source to decrease. Such background value yielded 844 counts for the source in an aperture of 10 pixel of radius. 41
- Fig. 3.6 On the right (a), strong smearing effect in the coadded LWS image of the asteroid 2002 CT₄₆ without registering. (b) the same dataset but registering of each nodeset before coadding was performed. The improvement in the S/N is clearly evident. Further, the registered PSF more similar to the standard stars PSFs resulting in an improved photometric accuracy. 42
- Fig. 3.7 The modulus of the cross correlation function between the instrumental PSF and frames registered with arbitrary shifts of the nod sets. Shown here is a 5×5 array of trials. The v_x and v_y values (see text) are indicated by the numbers at the bottom of each framelet. 43
- Fig. 3.8 Raw image of the N-band spectrum of the standard star HD123139 observed with the ESO 3.6m telescope and TIMMI2 46
- Fig. 3.9 The one-dimensional profile of the spectrum $S''_{profile}(x)$. It was obtained by summing up the contribution of all pixels along each row. 47
- Fig. 3.10 Raw extracted spectrum of the standard star HD123139. Note the characteristic ozone feature between pixels 110-190 48
- Fig. 3.11 N-band raw spectrum of the NEA 5587. Dotted vertical lines are drawn in correspondence to the bin extremes. The binning intervals were taken at the following detector columns (1 20), (21 40), (41 60), (61 80), (81 100), (101 120), (201 220), (221 240), (241 260), (261 290). 48
- Fig. 3.12 Histogram of the number of observations as a function of the absolute magnitude H of the target asteroids and the as a function of the solar phase angle. H values for each object are obtained from the MPC. 7 objects out of 32 were observed with different instrument and under different observing geometries. 54
- Fig. 4.1 Thermal model fits to observed infrared fluxes for 15817 Lucianotesi, 2000 EV₇₀ and 2001 HW₁₅ obtained at Keck and not included in Delbò et al. (2003) work. Continuous line: STM, dashed line: FRM; dotted line: NEATM with default η -value of 1.0 61

- Fig. 4.2 Synthetic lightcurve of the asteroid 1998 SF36 and the best fit to the observed V-band data. Measurements obtained on 9 April, 2001 have got a square symbol superimposed. The two lightcurves were composited on the 12.13 hours sidereal period basis. 63
- Fig. 4.3 Thermal models fit to the observed infrared flux for 25143 Itokawa. Continuous line: STM, dashed line: FRM; dotted line: NEATM with default η -value of 1.2 and 1.5 64
- Fig. 4.4 Thermal models fit to the 2001 LF data observed on June 03, 2003. No correction for lightcurve was applied. Continuous line: STM, dashed line: FRM; dotted lines: NEATM Note how, in this case, the fitted η -value is very close to its default value of 1.5 65
- Fig. 4.5 Observing sequence used to image 2001 LF in the Q-band at the 3.6 m telescope with TIMMI2. Q1_1 represent the first nod-set Q1_8 the eighth. The gray round patch indicates the position of the source moving on the detector array and below detection on each exposure. The black circle corresponds to the position of the object on 11.9 μ m-images where the asteroid was detected. 66
- Fig. 4.6 Thermal models fit to the 2001 LF data observed on June 02, 2003. Continuous line: STM, dashed line: FRM; dotted lines: NEATM In this case, the fitted η -value of 1.1 is lower than its default value of 1.5 66
- Fig. 4.7 The synthetic light curve (continuous line) fitted to the differential V magnitudes (squares) obtained on June 02, 2003 with WFI at 2.2m ESO/MPI telescope. Vertical lines are drawn in correspondence with the epoch of thermal infrared observations. 68
- Fig. 4.8 Thermal models fit to the 5381 Sekhmet data observed on June 02, 2003. No correction for the lightcurve has been performed in plot (a), whereas data points in plot (b) have been corrected for lightcurve. 69
- Fig. 4.9 Thermal model fits to multi-filter photometry of the NEA 1999 KV₄ obtained at the ESO 3.6m telescope. Continuous line: STM, dashed line: FRM; dotted line: NEATM with $\eta=1.0$ (the one closer to STM prediction) and with $\eta=1.2$. 70
- Fig. 4.10 Thermal model fits to multi-filter photometry of the NEA 2002 AV₄ obtained at the ESO 3.6m telescope. Continuous line: STM, dashed line: FRM; dotted line: NEATM. 71
- Fig. 4.11 Continuous line represent the synthetic lightcurve generated assuming the asteroid to be a triaxial ellipsoid with a geometric scattering law. Dashed line is the Pravec et al. lightcurve. Small squares are the DFOSC observations. Vertical lines are drawn in correspondence to the thermal infrared observations. Differential correction factors are of less than 0.2 magnitudes. 72
- Fig. 4.12 Thermal infrared photometry of the NEA 5587 obtained at ESO and thermal models fits. Continuous line: STM, dashed line: FRM; dotted line: NEATM. 72
- Fig. 4.13 The continuous sinusoidal line represents the visible lightcurve as in the case of Fig. 4.11. Vertical lines are drawn in correspondence with the epochs of the thermal spectroscopy measurements. 73
- Fig. 4.14 The binned spectrum of the NEA 5587 obtained at 05:46:41 UT on April 09, 2001 (first spectrum) and thermal models fits. Continuous line: STM, dashed line: FRM; dotted line: NEATM. 74
- Fig. 4.15 Thermal infrared photometry of the NEA 19356 obtained at ESO and thermal models fits. Continuous line: STM, dashed line: FRM; dotted line: NEATM. 75

- Fig. 4.16 Thermal model fits to N-band infrared data obtained at ESO. Continuous line represents the spectral energy distribution derived by the STM, dashed line that of the FRM and the dotted one is the NEATM. 76
- Fig. 4.17 Thermal model fits to N-band infrared data obtained at ESO. Continuous line represents the spectral energy distribution derived by the STM, dashed line that of the FRM and the dotted one is the NEATM. 77
- Fig. 4.18 Visible and thermal lightcurve of 33342 on December 2001. Filled diamonds are infrared relative magnitudes derived from $11.7\mu\text{m}$ -fluxes obtained on December 18, 2001. Empty diamonds represent $11.7\mu\text{m}$ magnitudes obtained on December 19, 2001 and empty squares those measured on December 21, 2001. Infrared magnitudes were composed on the basis of a 0.15415-days period. Continuous line is the R-band lightcurve derived from CCD observation of Pravec et al. (Pravec, personal communication, 2002). Thick dashed line is a sinusoidal fit with a period equal to half of that of the asteroid to infrared magnitudes. 78
- Fig. 4.19 Thermal model fits to multi-filter photometry of the NEA 33342 obtained at the NASA-IRTF. No correction for lightcurve was applied. Continuous line: STM, dashed line: FRM; dotted line: NEATM. Figures are drawn with the same y-axis scale. Note the clear variation of the apparent color temperature between the observing dates. 79
- Fig. 4.20 Thermal model fits to the observed flux of the asteroid 35396. Continuous line: STM, dashed line: FRM; dotted line: NEATM. 80
- Fig. 4.21 Lightcurve of the NEA 35396 at $11.7\mu\text{m}$ obtained with MIRSI@NASA-IRTF on November 05, 2002 (a) and on November 03, 2002 (b). The continuous line is a sinusoid function with period half of the rotational period of the asteroid fit to the measured relative magnitudes. The thicker dashed line is the V-band lightcurve of Pravec et al. Note the difference in amplitude and the phase shift. 82
- Fig. 4.22 Thermal models fit to the $11.7\mu\text{m}$ lightcurve-corrected data obtained with MIRSI@NASA-IRTF on November 05, 2002 (a) and on November 03, 2002 (b). Note in both data set the very high thermal flux measured at $4.9\mu\text{m}$. 83
- Fig. 4.23 The 5th-order polynomial fitted to the R-band magnitudes measured by Fernandez. 84
- Fig. 4.24 On the left thermal model fits to the observed infrared fluxes before applying lightcurve correction (see text). On the right lightcurve corrected fluxes. Continuous line: STM, dashed line: FRM; dotted line: NEATM. 84
- Fig. 4.25 The scientific relevance of this work in terms of newly derived NEA sizes and albedos. The histogram in blue shows the number of NEAs with measured size and albedo as a function of their diameter according to the Table 1 in Binzel et al. (2002) chapter on "Physical Properties of Near-Earth Objects" in Asteroids III. In red are shown new and refined diameters and albedos obtained from this work. 86
- Fig. 4.26 Increment in the number of NEAs with measured diameter and albedo as a function of their diameter. Note how this work contributes manly to the increment of our knowledge for the sub-kilometer population of NEAs. 87
- Fig. 5.1 Comparison of albedo distribution for the NEAs observed in this program (histogram a which contains 30 NEAs); all NEAs with radiometric reliable albedo (histogram b with 40 objects); SIMPS asteroids with diameter less than or equal to 10 km (c with 75 asteroids) and all SIMPS asteroids (d, with 2228 objects). In the first three histograms bins are 0.15-wide in

logarithmic albedo, whereas in the last one they are 0.05-wide in logarithmic albedo. In the case of NEAs and SMASSII-asteroids the taxonomic class is displayed.

92

Fig. 5.2 Plot of the geometric visible albedo versus diameter derived by NEATM for S-type NEAs. Taxonomic classes included are ‘S’, ‘Sq’, ‘Sr’ and ‘Sl’. The plot suggests a significant trend of increasing albedo with decreasing size. The trend may be due to a bias in favor of the discovery and characterization of high albedo objects. In the case of 433 Eros results are shown at lightcurve maximum and minimum.

93

Fig. 5.3 Best-fit beaming parameter, η , from the NEATM fits plotted against solar phase angle, α . The continuous line represents a linear fit, $\eta = (0.011 \pm 0.002)\alpha + (0.92 \pm 0.07)$ to all values of η . Filled diamonds with error-bars at $\eta > 2$ are those data points considered anomalous by Delbò et al. (2003). Filled triangles are the η -values for 5381 Sekmeth and the dashed line represent their linear fit: $\eta = (0.017 \pm 0.013)\alpha + (0.9 \pm 0.03)$. Open squares represent the η -values for 25330 (1999 KV₄). Significant deviations of η from the linear fit may be due to the effects of unusually high or low thermal inertia and/or surface roughness, and/or an irregular shape, influencing the surface temperature distribution presented to the observer. The “evening/morning” effect probably contributes to the scatter of the points (see text). The dotted curve represents the expected η values for an FRM-like asteroid, whereas the continuous one corresponds to the η -values derived by fitting NEATM to the infrared continuum of a perfectly conducting smooth sphere in thermal equilibrium with the solar radiation.

95

Fig. 5.4 Infrared phase curves for a spherical asteroid at the heliocentric distance of 1AU with a STM-like temperature distribution. However, the η -value is varied as a linear function of the phase angle α : $\eta = \beta_\eta \alpha + \eta_0$. See the text for further details.

99

Fig. 5.5: Comparison of STM diameters with radar ones as a function of the solar phase angle (a) and diameter (b) for those asteroids observed at phase angles less than or equal to 80° . For 433 Eros results are given at lightcurve maximum and at lightcurve minimum. A systematic error of -16% is evident between the two sets of data. The RMS fractional difference between the STM diameters and diameters derived from radar measurements is of 16%. No clear trend of the relative error with phase angle is evident. Error bars were calculated assuming a 15% uncertainty on STM radiometric diameters and 10% uncertainty on the radar one if such information was not available from the original source in the literature. The thick continuous line on plot (a) and (b) was obtained with a 6-elements central running box average. Plot (c) shows the histogram of the relative error distribution with superimposed the mean and the median values. Plot (d) shows how STM diameters are in good agreement with radar ones if asteroids 2100, 1580, 6489 and 33342 are removed from the sample.

101

Fig. 5.6 Comparison of FRM diameters with radar ones as a function of the solar phase angle (a) and diameter (b) for those asteroids observed at phase angles less than or equal to 80° . For 433 Eros results are given at lightcurve maximum and at lightcurve minimum. A systematic error of +35% is evident between the two sets of data. The RMS fractional difference between the FRM diameters and diameters derived from radar measurements is of about 40%. There is a clear trend of the relative diameter error with the phase angle and with the diameter. Error bars were calculated assuming a 15% uncertainty on FRM radiometric diameters and 10% uncertainty on the radar one if such information was not available from the original source in the literature. The thick continuous line on plot (a) and (b) was obtained with a 6-elements central running box average. Plot (c) shows the histogram of the relative error distribution with superimposed the mean and the median values.

103

- Fig. 5.7 Comparison of NEATM diameters with radar results as a function of the solar phase angle (a) and diameter (b) for those asteroids observed at phase angles less than or equal to 80° . For 433 Eros results are given at lightcurve maximum and at lightcurve minimum. A systematic error of +8% is evident between the two sets of data. The RMS fractional difference between the STM diameters and diameters derived from radar measurements is of about 20%. No clear trend of the relative error with phase angle and size is evident. Error bars were calculated assuming a 15% uncertainty on STM radiometric diameters and 10% uncertainty on the radar one if such information was not available from the original source in the literature. The thick continuous line on plot (a) and (b) was obtained with a 6-elements central running box average. Plot (c) shows the histogram of the relative error distribution with superimposed the mean and the median values. 104
- Fig. 5.8 Dependence of the STM-derived radiometric diameter at wavelengths of 5, 10 and 20 μm as a function of the beaming parameter η . Dashed line was obtained by fitting the STM simultaneously to 10 and 20 μm fluxes. 105
- Fig. 5.9 Infrared phase curves in terms of relative infrared magnitudes for a spherical asteroid calculated at 10 and 20 μm . Continuous line: NEATM with $\eta=0.011\alpha+0.9$ where α is the phase angle and η the beaming parameter (see text). Dashed line: STM for which $\eta=0.9$ was assumed. The 10 μm phase curve was obtained with a β_E -value of 0.015 mag/degree, whereas for the 20 μm curve β_E was set equal to 0.011 mag/degree. Those value were chosen to fit the NEATM phase curve in the range $0^\circ < \alpha < 30^\circ$. Dotted lines represent the phase curve of a NEATM-like asteroid with a fixed η -value of 0.9. 106
- Fig. 5.10 Plot of the geometric visible albedos versus solar phase angle for each radiometric observation. a) STM; b) FRM; c) NEATM. Continuous lines were calculated by taking the 5-elements-wide central moving average of the data points in each plot. 108
- Fig. 6.1 The model herewith implemented can handle spheres of with a small (a) or a large number of elementary triangular facets (b). General shapes can also be modeled as in the case of the radar model of the NEA 6489 Golevka (c). 116
- Fig. 6.2 Plot of the thermal parameter Θ as a function of the heliocentric distance. The thermal inertia, $\Gamma = 40 \text{ J m}^{-2} \text{ s}^{-1} \text{ K}^{-1}$, has a quasi-lunar like value. The bolometric bond albedo $A = 0.05$; emissivity $\epsilon = 1$ and asteroid sidereal rotation period $T_{\text{SID}} = 5$ hours. Note that for a given value of Γ and T_{SID} , NEAs have smaller values for Θ than objects more distant from the Sun. 118
- Fig. 6.3 The temperature of an equatorial tile of the spherical mesh monitored during the “warming up” phase. In this case the temperature of all the tiles of the mesh has been set equal to 0 K as starting conditions. After a few rotations the temperature stabilize within 0.5 K. 121
- Fig. 6.4 Diurnal temperature profiles for an object with sub-solar latitude equal to zero as a function of the thermal parameter Θ . 122
- Fig. 6.5 This plot allows the thermal parameter Θ to be estimated given the thermal inertia Γ and the asteroid rotational period in hours. From the bottom of the figure to the top, the lines refers to the following values of $\Gamma = [5, 25, 50, 100, 200, 400, 900, 2500, 5000] \text{ J m}^{-2} \text{ s}^{-1/2} \text{ K}^{-1}$. The typical lunar-like value for Γ is about $40\text{-}50 \text{ m}^{-2} \text{ s}^{-1/2} \text{ K}^{-1}$. 123
- Fig. 6.6 NEATM derived beaming parameter η as a function of the phase angle and thermal parameter Θ . The sun and the observer are in the equatorial plane of the synthetic asteroid. Different colors are used for different values of Θ : η -values derived for $\Theta=0.25$ are coded with black color; those obtained for $\Theta=0.50$ are coded with red; green is used for $\Theta=1.00$ with; blue for $\Theta=2.00$; pink for $\Theta=4.60$; light-blue for $\Theta=12.70$ and yellow for $\Theta=25.5$. Note

that there are two curves for each value of the thermal parameter Θ : continuous curves refer to those η -values derived by observing the morning side of the asteroid, whereas dashed-dotted curves indicate those η -values obtained observing the afternoon side. Curves obtained for $\Theta=0.025$ and 0.13 are not plotted since the derived η -values are constant with phase angle and their values between 1 and 1.05. The dotted black curve represents the expected η values for an FRM-like ($\Theta \rightarrow \infty$) asteroid.

124

Fig. 6.7 NEATM derived η parameter as a function of the phase angle and macroscopic surface roughness $\bar{\theta}$. The sun and the observer are in the equatorial plane of the synthetic asteroid. The thermal parameter Θ is equal to 0. Different colors are used for different values of $\bar{\theta}$: η -values derived for $\bar{\theta}=58^\circ$ are coded with black color; those obtained for $\bar{\theta}=36^\circ$ are coded with red; for $\bar{\theta}=20^\circ$ with green and for $\bar{\theta}=10^\circ$ with blue.

126

Fig. 6.8 Continuous line: diurnal temperature profiles for an equatorial tile of an object with sub-solar latitude equal to zero. Dashed-dotted line: diurnal temperature profiles for one of the four tiles on the floor of an equatorial crater with opening angle equals to 45° (a) and with opening angle equals to 90° (hemispherical crater).

127

Fig. 6.9 Combined effects of thermal inertia, rotation rate and surface roughness on the theoretical dependence of the NEATM η -value with the phase angle.

130

Fig. 6.10 Combined effects of thermal inertia, rotation rate and surface roughness on the theoretical dependence of the NEATM η -value with the phase angle.

131

Fig. 6.11 Verification of the hypothesis that η -values derived for asteroids observed from randomly oriented directions are limited by the “morning” curve M and the curve of zero thermal inertia N. The thermophysical model was run for three values of the sub-solar latitude B_{SS} . Crosses represent those η -values derived for asteroids with $B_{SS}=0^\circ$, asterisks for asteroids with $B_{SS}=30^\circ$ and diamonds for $B_{SS}=60^\circ$. Note how η -values collapse to the curve of zero thermal inertia as B_{SS} approaches 90° . Following our notation M is the curve with $\eta=\eta(-|\alpha|, \Theta, \bar{\theta})$, A that with $\eta=\eta(|\alpha|, \Theta, \bar{\theta})$ and N that with $\eta=\eta(|\alpha|, \Theta=0, \bar{\theta})$.

133

Fig. 6.12 Limiting curves which do not fit properly the observed η -values. See Fig. 6.13 caption for a description of the symbols.

134

Fig. 6.13 Limiting curves which DO fit the observed η -values. The values of the Θ and the $\bar{\theta}$ parameter used to draw the curves are shown on the upper left side of each plot. For each value

135

Fig. 6.14 Limiting η - α curves to fit observed η -values of 5381 Sekmeth. Those curves were calculated for $\Theta=4.4$ and $\bar{\theta}=36^\circ$

136

Fig. 6.15 Limiting η - α curves to fit observed η -values of 433 Eros. Those curves were calculated for $\Theta=1.0$ and $\bar{\theta}=20^\circ$

137

Fig. 6.16 Section of the STM relative albedo error function i.e. $(p_{V_STM}(\alpha, \Theta, \bar{\theta}) - p_{V_TM}) / p_{V_TM} \times 100$ at constant value of $\bar{\theta}$. The refined STM of Lebosfky and Spencer (1989) was used with constant $\eta=0.756$ and $\beta_E=0.01$ magnitude per degree. The function was numerically evaluated on a grid of ten degree of step size in α and at $\Theta=[0.13, 0.25, 0.40, 0.50, 1.00, 2.00, 4.60, 12.70, 25.5]$.

141

Fig. 6.17 Section of the STM relative albedo error function i.e. $(p_{V_STM}(\alpha, \Theta, \bar{\theta}) - p_{V_TM}) / p_{V_TM} \times 100$ at constant value of $\bar{\theta}$. In contrast to Fig. 6.16, here η is constant but equal to 0.95 and $\beta_E=0.015$ magnitude per degree, as described in section 5.6. The function was numerically

evaluated on a grid of ten degree of step size in α and at $\Theta=[0.13, 0.25, 0.40, 0.50, 1.00, 2.00, 4.60, 12.70, 25.5]$. 142

Fig. 6.18 Section of the NEATM relative albedo error function i.e. $(p_{V_NEATM}(\alpha, \Theta, \bar{\theta}) - p_{V_TM}) / p_{V_TM} \times 100$ at six different constant values of $\bar{\theta}$. The function was numerically evaluated on a grid of ten degree of step size in α and at $\Theta=[0.13, 0.25, 0.40, 0.50, 1.00, 2.00, 4.60, 12.70, 25.5]$ 143

Fig. 6.19 Distribution of the albedo relative error as a function of the η -value for asteroid observed at phase angle between -40 and 40 degrees (a) and at phase angle larger than 40° or smaller than -40° . 146

Fig B.1 Transmission curves for the filters installed at the LWS (Wirth & Campbell, personal communication, 2000). In the case of the M filter, the curve is the product of the transmission of the filter with that of the atmosphere and the optics of the instrument. 175

ACKNOWLEDGMENTS

When I was a kid, I often thought, probably in the late '80, about the year 2000, and about what I could have been doing at that time. However, I never thought I could have been, in the year 2000, in Berlin. For me, this was not only a scientific and working experience, but it changed deeply my life. I wish to thank everybody who has helped me to be here, today, writing this final page of this dissertation. (To be honest it is not exactly the last page: I have to fix a couple of paragraphs, before get this dissertation printed and handed in to the FU....)

Thank you, then, **Alan Harris**, because you have introduced me to this fascinating topic of planetary science, for the good advice and for the lively and professional collaboration that I hope will continue in future.

Thank you, **Mario Di Martino**. I am happy to have listened one of your advice, years ago, when we have observed together my first NEA in Torino. I am also indebted for your collaboration during the observing campaigns in Chile¹.

Thank you, **Gerhard Neukum** and **Vincenzo Zappalà** for the opportunity that you gave to me of working on this interesting topic.

Thank you, **Alberto Cellino** for your suggestions and the carefully reading of this work.

Thank you, **Rick Binzel**. This work would have not been possible without your collaboration. I wish to thank you, also for the opportunity you gave to me to come and stay in Hawaii. I have appreciated very much the trust you gave to me.

A special thank goes to **Stefano, Mirella, and Roberto Mottola**. Thank you *amici*, for your hospitality, your friendly attitude, and because you have always made me to feel *a casa* in Berlin. Thank you for the whole amount of things you have shown for me feasible to do, **Stefano**. From programming the thermophysical model, to... climbing the *quarta bassa*.

Thank you, **Martin Prescher** for the many thought provoking discussions we had together and for your help, especially in the very beginning part of this dissertation.

Thank you, **Ekkehard Kührt** because I have always been welcome in your office. For the support you gave to me and because I know that you have never doubted that I could come to this final result.

Thank you, **Davide Loreggia** for you friendly support those days when sometimes I thought to give up.

Thank you, **Erick Wenderoth** and **Michael Sterzik**, for your collaboration at the 3.6m ESO telescope with TIMMI2 in La Silla, Chile.

¹ ...especially for your effort in the data reduction....

Thank you **Bobby Bus** and **Michael Mueller**, for the very good work you have done with the NASA-IRTF.

Thank you **Randy Campbell** and **Greg Wirth**, for your support at Keck.

Finally, a special thank goes to **Anders Erikson, Ljuba Moroz, Stephanie Werner, Joern Helbert, Joerg Knollenberg**. You, guys, are very important for me. I have enjoyed very much the scientific meetings we had together drinking I don't know how many cups of coffee, but also the bit less scientific meetings we had drinking I don't know how many beers, in particular at the *Blauer Angel*.

I cannot forget to thank you, **Heike Rauer**, and I apologize for having been talking too loudly at the phone, sometimes.

I have also to say thank to you, **Fabio**, for the many times you have driven me to the Malpensa Airport, Milan, and along with my parents, **Mamma e Papà** for the support you always gave to me during some difficulties that I have certainly encountered.

Part of the data presented herein was obtained at the W.M. Keck Observatory, which is operated as a scientific partnership among the California Institute of Technology, the University of California and the National Aeronautics and Space Administration.

This work is partially based on observation obtained at the European Southern Observatory, La Silla. Project IDs 67.C-0543, 68.C-0447, 69.C-0619, 70.C-0608, 71.C-0241

The two years work at DLR, Berlin, as well as the travel expenses was supported by the Deutsche Forschungsgemeinschaft (DFG).

The INAF – OATo has supported some of the travel expenses to Berlin.

A mio padre e mia madre

Introduction

1.1 Asteroids

Asteroids are a population of “small bodies” orbiting the Sun at distances ranging from inside the orbit of the Earth to beyond Saturn’s. Other objects with orbital semi-major axes beyond the orbit of Neptune have been recently discovered. These are the so-called Kuiper Belt Objects (KBOs) which, although sharing the asteroid nomenclature, are more closely related to comets. Asteroids are thought to be remnants of the building blocks that formed the planets 4.6 G.y. ago. Therefore, they conserve the record of the primordial material and possibly the initial conditions existing in the solar nebula at the time of the planet formation process. The nature, size and orbital distribution, as well as the evolution of asteroids are crucial for the understanding of the formation and evolution of the planets and the entire solar system. The large majority of asteroids orbit the Sun between Mars and Jupiter in the so called Main Belt, but one of the most important legacies of planetary science of the last century is the discovery of a population of small bodies orbiting the Sun in the near Earth space.

Crossing the region of the inner planets is a heterogeneous population of minor bodies coming from almost everywhere in the solar system, the so-called near-Earth objects or NEOs. NEOs include also some nuclei of extinct comets. NEOs of asteroidal origin are called near-Earth asteroids (NEAs). The crater record on the inner planets, on our Moon and on the Earth demonstrates how NEAs (asteroids dominate the population of crater-forming bodies in the inner solar system) have punctuated the history of the terrestrial planets with large scale impacts and that they will continue doing so (Ivanov et al., 2002). The study of asteroids, and in particular of NEAs, is therefore ultimately related to the history and evolution of the Earth’s biosphere and, so to say, to the past and future existence of life on our planet. For instance, over the last two decades, it has been convincingly argued that the impact of a multikilometer asteroid or comet 65 m.y. ago led to a mass extinction event that eliminated the dinosaurs (e.g., Alvarez et al., 1980). In addition, asteroids offer a source of volatiles and an extraordinarily rich supply of minerals that can be potentially exploited for the exploration and colonization of the solar system in the twenty-first century.

The following paragraphs are devoted to a description of the major characteristics of asteroids relevant for this study. An extended and up-to-date overview of asteroids is given by Bottke et al. (2002a). It is of interest to compare the rapid growth of new scientific findings and discoveries in the last 10 years to what we already knew in 1989 (e.g. Binzel et al., 1989).

1.2 Main Belt Asteroids

Nowadays, more than two hundred thousand asteroids are known orbiting the Sun in the Main Belt. The biggest object, 1 Ceres, about 900km in diameter, was the first asteroid to be discovered back in 1801 by Giuseppe Piazzi. 2 Pallas and 4 Vesta are about 500 km large and 10 Hygiea, the fourth bigger asteroid, has a diameter of about 400 km. The number of asteroids rapidly grows as their size decreases. The size-frequency-distribution (SFD) of Main Belt Asteroids (MBAs) can be expressed mathematically as a power law: $N(>D) = K D^{-b}$, where b is the cumulative diameter population index. Although there is evidence for a variable index in the size distribution of asteroids, the value of b for relatively small objects (50-10km) lies between 1.95 and 3.0, according to different extrapolations. It is recognized how the size frequency distribution of MBAs is a direct consequence of the collisional evolution (Davis et al., 2002) that asteroids experienced during their history. Dohnanyi (1969) predicted that an asteroid population in collisional equilibrium should eventually evolve to a SFD with a cumulative power law slope index of -2.5 . However, it is widely believed that the largest asteroids (although where “largest” begins is a debated question) are primordial objects whose sizes have not been significantly altered by collisions. There are indications that the whole asteroidal population made of objects with diameter smaller than about 400 km is collisionally evolved. However, the slope index of the actual SFD does not follow exactly Dohnanyi’s law. This is due to the fact that effects of collisions are not independent on the size of the bodies as Dohnanyi’s hypothesis assumes.

Collisions have modified not only the size frequency distribution, but also the orbital distribution of MBAs: it is worth to point out here how a plot of asteroids orbital eccentricities as a function of the semi-major axis reveals a non uniform distribution, as shown in the picture below. The figure has been obtained by plotting the synthetic proper elements² of 71291 numbered asteroids calculated by Knezevic and Milani. The database of asteroid proper elements is available on-line from the web page of the AstDys service at: http://hamilton.dm.unipi.it/cgi-bin/astdys/astibo?proper_elements:0;main

² proper elements are quasi-integrals of motion, and thus represent the "average" characteristics of motion over very long time spans. See Z. Knezevic et al. 2002 or visit, for instance, the help page of the AstDys database, maintained on-line at <http://hamilton.dm.unipi.it/cgi-bin/astdys/astibo?help:0;menu>

One of the major features clearly visible in Fig. 1.1 is the presence of significant clumpings of objects already identified by Hirayama in 1918 as “families” (Hirayama, 1918). There are approximately 25 reliable families and over 60 statistically significant clusters identified in asteroid proper orbital elements (see Zappalà et al., 2002 and Bendjoya and Zappalà, 2002 for detailed discussions of asteroid families). Hirayama used the term “families” because he believed to be the outcome of the catastrophic disruption of a parent body and indeed, confirmation of their likely collisional origin from dedicated spectroscopic campaigns has been a major result. Detailed studies of the physical properties of these “groupings” have been carried out (see Cellino et al. 2002).

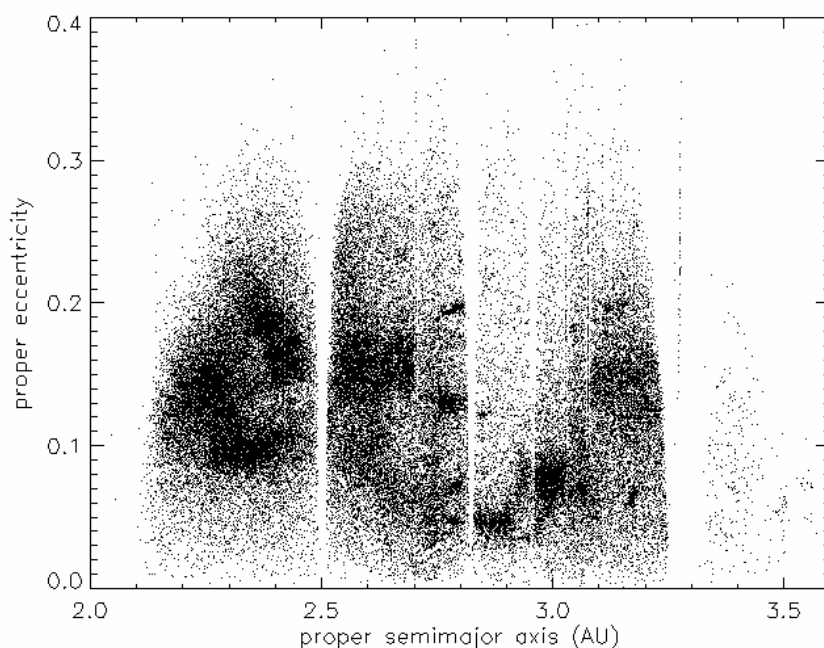


Fig. 1.1 Plot of the semi-major axis versus eccentricity for main belt asteroids. Note the presence of significant clumpings of objects already identified by Hirayama in 1918 as “families” and the Kirkwood gaps.

Asteroid shapes are also a direct consequence of their collisional evolution that these objects have experienced during their histories. They range from rather spherical to elongated concave and irregular, indicative of a fragmental origin. The easiest way to infer information about asteroid shapes is from their lightcurve, which is primarily related to the varying illuminated portion of the cross section visible to the observer as the asteroid rotates. Typical rotation periods are about 9 hours with extremes ranging from under 3 hours up to several weeks.

Moreover, a common side effect of asteroid collisions is the production of ejecta and regolith. Polarimetric observations (e.g. Dollfus et al., 1989) have suggested that large asteroids have a thick layer

of regolith covering their surfaces. However, regolith has also been observed directly on smaller objects such as 951 Gaspra and the near Earth asteroid 433 Eros. The discovery of a deep layer of regolith on objects with low escape velocities was somehow surprising. Moreover, on the asteroid 253 Mathilde, the existence of large scale craters whose boundaries are adjacent one to another and whose diameters are almost comparable with the radius of the asteroid, made necessary to review our knowledge of the bulk porosity and surface composition of these bodies.

As a matter of fact, although the orbital distribution of asteroids has been known since a long time, a clear picture of the compositional structure and distribution was obtained only at the end of the '80s. On the basis of visible spectroscopy and/or UBVRI color photometry, it was possible to identify two broad classes: neutrally colored asteroids were labeled "C" type and more reddish objects were classified as "S". The letters were chosen for spectral similarities with carbonaceous (C) and stony (S) meteorites. C types appear to be more abundant in the outer part of the belt, while S types are more prominent in the inner. By 1979 two other major classes were added: E (enstatite) and M (metallic). The Eight Colors Asteroid Survey – ECAS – (Zellner et al., 1985) gave a strong boost to the asteroid taxonomic classification and the observations collected by the Infra-Red Astronomical Satellite (IRAS) (Tedesco et al., 1992) allowed the albedo for more than 2000 asteroids to be derived and a cross correlation with taxonomy to be performed. C type asteroids were found to be predominantly dark with an albedo in general no higher than 0.10. S type objects correlate with intermediate albedos ranging from 0.10 to 0.25. Likewise do M type asteroids. Although E types show reflectance spectral or color feature very similar to M types, their albedo is higher: from 0.25 to 0.60.

Another important feature clearly visible in Fig. 1.1 is the presence of gaps (the Kirkwood gaps) in correspondence with orbital resonances with Jupiter. It has been shown that test bodies entering several powerful mean-motion resonances with Jupiter (e.g., 3:1, 4:1, 5:2) can have their eccentricities pumped up to Earth-crossing values, usually over timescales of ~ 1 million years. In some cases, orbital motion inside these resonances is chaotic enough that test bodies can be pushed directly onto Sun-grazing orbits. Similarly, the ν_6 secular resonance, lying along the inner edge of the main belt, is now seen as one of the primary sources of near-Earth objects (see Morbidelli et al, 2002a, for further details).

Dynamical calculations (see, for instance, Morbidelli et al., 2002a; Bottke et al., 2002a) show that typical orbits for NEOs are chaotic and non stable. Lifetimes for NEOs are of a few million years with these objects finally ending up with a crash into the Sun, being ejected from the solar system, or impacting one of the inner planets. Given such short lifetimes, the present NEO population cannot be

made of objects that orbits amongst the inner planets since the beginning of the solar system: NEO population must have some source of resupply.

Years of work in the field of Celestial Mechanics have shown that the near-Earth Objects come mainly from 5 sources :

1. the ν_6 resonance region at the inner border of the asteroid main belt,
2. the 3:1 resonance region in the middle of the asteroid main belt,
3. the Intermediate Mars-Crossing (IMC) population,
4. the Outer Belt (OB) population,
5. the population of dormant Jupiter Family Comets (JFC).

Moreover, non-gravitational forces like that produced by the so-called Yarkovsky effect³ (e.g. Bottke et al., 2002b and references therein) may play an important role in allowing small asteroids and asteroidal material to undergo a drift in orbital semimajor axis and eventually escape the main belt by entering a mean-motion and/or a secular resonance. The general scenario, very much simplified in the scheme which follows, for how asteroids are delivered from the main belt to the inner solar system (and Earth) is the following: an asteroid undergoes a catastrophic disruption or cratering event and ejects numerous fragments; most are not directly injected into a resonance. Fragments with diameter smaller than 20 km start drifting in semimajor axis under the Yarkovsky effect . These bodies jump over or become trapped in chaotic mean-motion or secular resonances that change their eccentricity and/or inclination. These resonances are capable of pushing them onto planet-crossing orbits. From here, they may become directly members of the NEA populations. Alternatively, objects may be trapped on Mars-crossing orbits and, eventually, a close encounter with Mars modifies their orbits such that they become NEAs.

1.3 Physical characteristics of Near Earth Asteroids and Near Earth Objects

The near-Earth object population includes asteroids, active and extinct comets and the precursor bodies for meteorites. NEOs are defined as those small bodies having perihelion distances $q \leq 1.3$ AU and aphelion distances $Q \geq 0.983$ AU. For objects which clearly do not display any coma or cometary activity or simply presuppose an asteroidal origin, the term near-Earth Asteroid (NEA) is used. Subcategories of the NEA population include the Apollos ($a \geq 1.0$ AU, $q \leq 1.0167$ AU) and Atens ($a < 1.0$ AU, $Q \geq 0.983$ AU), which are on Earth-crossing orbits, and the Amors (1.0167 AU $< q \leq 1.3$ AU), which are on nearly-Earth-crossing orbits. A population inside Earth's orbit ($Q < 0.983$ AU), the so-

³ The Yarkovsky effect is a thermal radiation force due to the reactive force of emitted thermal radiation that causes objects to undergo semimajor axis drift and spinup/spindown as a function of their spin, orbit, and material properties.

called IEOs or inner-Earth Object, is also expected to exist (see Morbidelli et al., 2002a; Michael et al., 2000)⁴. These classes are based on osculating orbital elements and it is possible for a NEA to move from a class to another one. It is not possible to compute proper orbital elements for NEAs since dynamical lifetimes for the planet crossing asteroids are short ($<10^7$ yr) compared to the age of the solar system. Gravitational interactions with planets lead to their ejection from the solar system or to planetary impacts or to they fall into the Sun. However, Milani et al. (1989) studying the orbital evolution of a sample of NEAs over a time span of 200 thousand years, proposed six dynamical classes, named after the best-known and most representative object in each class: Geographos, Toro, Alinda, Kozai, Oljato, and Eros.

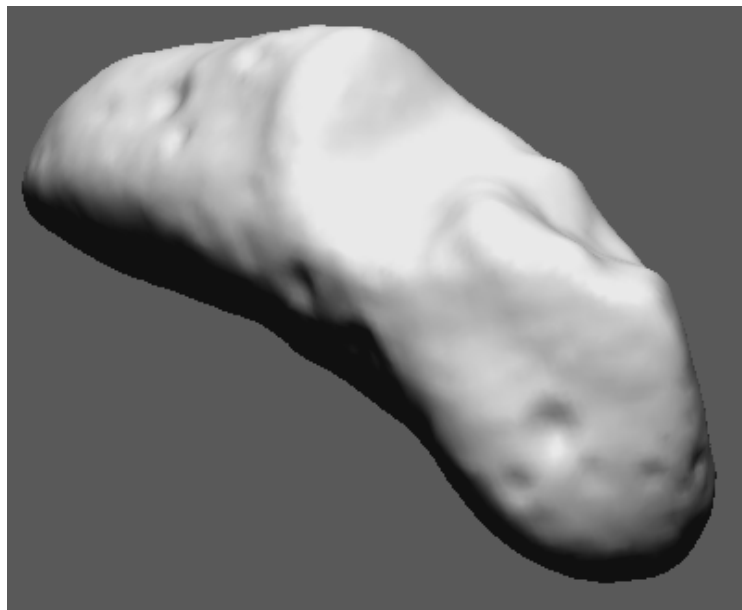


Fig. 1.2 Three-dimensional rendering of the shape model of the near Earth asteroid 433 Eros obtained by the NEAR-Schoemaker mission. This rendering has been calculated using the freely distributed computer program Wings 3-D.

NEAs are small objects: the largest known object is 1036 Ganymed, whose spherical equivalent diameter is about 39 km. For the second biggest NEA, 433 Eros, size and shape have been accurately measured by the NEAR-Schoemaker spacecraft, which orbited the asteroid for almost one year. Its elongated and concave shape measures 13 x 13 x 33 km (Thomas et al., 2002).

Several NEAs have been extensively studied by radar (Ostro et al., 2002). Radar observations showed the large variety of shapes within the NEA population. Spheroids and highly elongated shapes, contact-

⁴ We recall that $Q=0.983$ and $q=1.017$ are the values for the Earth.

binary shapes, and binary systems have been revealed down to a size of few hundreds meters (Ostro et al., 2002; Zaitsev et al., 2002). By measuring the total echo power in the two opposite circular polarization, radar is also able to estimate the roughness of the surface at centimeter scale. A large range of polarization ratios have been measured. Their values vary from nearly one, which is an indication of extreme roughness, down to almost zero, which, on the other hand, is an indication of a perfectly smooth surface. Not only radar can provide such an amount of information: it has been recently shown how information about the shape of an airless body can be successfully derived if disk integrated visible photometry is available for a large variety of illumination and viewing geometries (Kaasalainen et al., 2002). NEAs are in this respect the ideal case: they are often observed under a large range (from zero up to more than hundred degrees) of solar phase angles due to their proximity to the Earth and the power of the lightcurve inversion methods can be fully exploited. Furthermore, lightcurve inversion methods allow the direction of the asteroid rotation axis to be determined along with the shape.

Accurate shape models and pole directions for small NEOs open the door to a wide variety of theoretical investigations that are crucial to our understanding of the nature, origin, and evolution of these objects (e.g. Ostro et al., 2002; Kaasalainen et al., 2002). Moreover, the availability of three-dimensional shapes for a number of well studied NEOs is of crucial importance for the investigation of asteroid surface thermal properties and for the calibration of the models of asteroid thermal emission.

NEOs display a wide diversity not only in shapes and sizes, but their physical properties show a broader range of values comparable to what is seen across the entire main belt, consistent with their being supplied from more than one source region. This larger diversity with respect MBAs is also due to the fact that those objects are fifty times the sizes and five orders of magnitude more massive than a typical 1km NEO. Besides meteoritic and dust material, NEOs are amongst the smaller objects in the solar system that we can study. Almost all taxonomic classes of main-belt asteroids are represented among classified NEOs, including the P- and D-types most commonly found in the outer asteroid belt, among the Hilda and Trojan asteroids, or possibly among comet nuclei.

Fig. 1.3 shows that the large majority of NEAs known to-date belongs to the S type taxonomic class, which indicates the inner part of the Main Belt is the major supply region where NEOs come from. However, Binzel et al. (2002), Lupishko and Di Martino (1998), Luu and Jewitt (1989) describe how a bias factor in favor of the discovery of S type NEOs might play a major role in defining the taxonomic type distribution of this population. Given their higher albedo, in limited magnitude surveys, S type asteroids are more likely to be discovered. Moreover, the fall off of the apparent brightness of the darker C types as a function of the solar phase angle is stronger than for S types. Therefore, since NEOs

are often discovered at large phase angles the coupling of the two effects might explain the lack of dark objects within the population known so far. Benedix et al. (1992), Lupishko and Di Martino (1998), and Whiteley (2001) all find that after applying bias-correction factors to the observed NEO population, at any given size there are relatively equal proportions of C- and S-type objects within near-Earth space⁵.

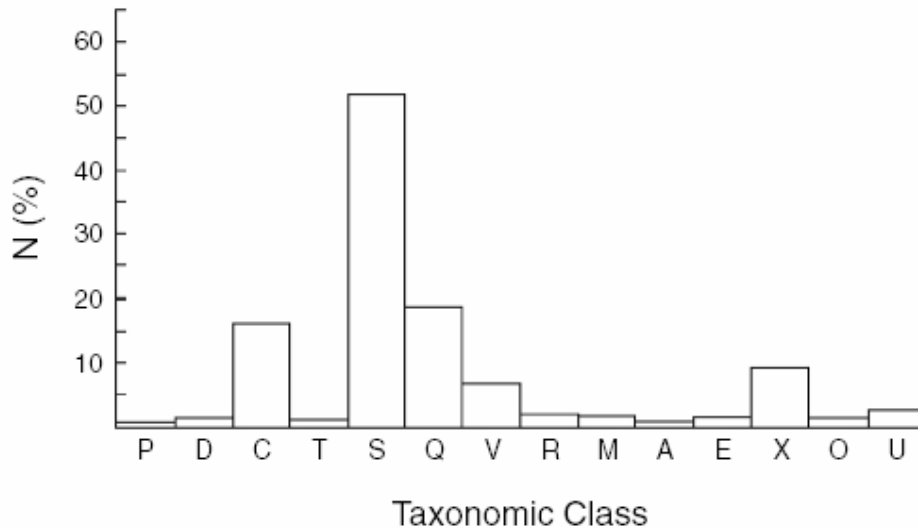


Fig. 1.3 Histogram of the relative proportions of measured taxonomic properties for more than 300 NEOs listed in Table 1, Binzel et al. 2002.

The study of NEO taxonomy and reflectance spectroscopy has always been of great interest in the search for the precursor bodies of the most common types of meteorites: the ordinary chondrites. A long debate over whether the most common (in near-Earth space) S-type asteroids are related to the most common meteorites is outlined by Clark et al. (2002) and by Binzel et al. (2002). This debate has been raised by the fact that over the last 30 years several studies have compared reflectance spectra of asteroids to measurements of meteoritic samples performed in the laboratory. Although links between some asteroidal taxonomic class and some meteoritic population have been found (e.g. V-type asteroids and EHD meteorites), statistically asteroids and meteorites show consistent offsets in spectral parameters such as the depth of some absorption bands as shown in Fig. 1.4. A space weathering effect, i.e. the aging of the asteroid surface due to its exposure to the space environment, has been invoked to explain these spectral alterations.

Chapman (1996) describes the discovery of terrains with different spectral properties on asteroids 951 Gaspra and especially 243 Ida from data obtained by the Galileo spacecraft. This is the

⁵ A bias-correction analysis of the main belt performed by Zellner (1979) suggests that C-types dominate among all main-belt asteroids by as much as 5:1.

demonstration of a "space weathering" process operating on their surfaces, which modifies the reflectance spectra of fresh material to be redder, straighter, and have shallower absorption bands. It operates in the sense that would tend to convert spectra of ordinary chondrites to have the spectral signature of S-type asteroids. These results appear to resolve the major obstacles of the long standing "S-type conundrum" about the provenance of ordinary chondrite meteorites.

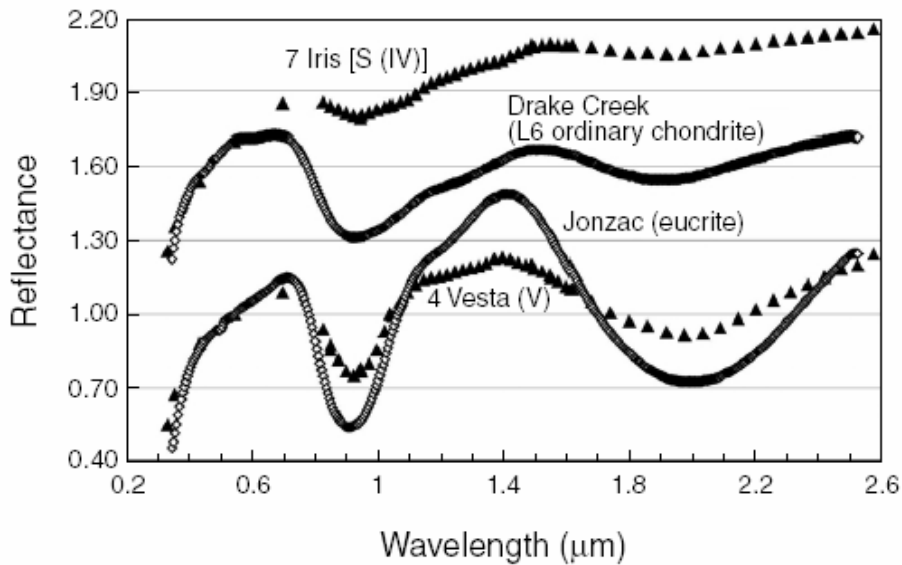


Fig. 1.4 Two examples of reflectance spectra of asteroids along with their meteorites analogs. One explanation for the spectral mismatches is that space weathering processes affect the surfaces of the asteroids, altering them from their original spectral properties. Figure obtained from Clark et al., 2002.

The physical investigation of NEAs, in this respect, opened the door to the possibility of measuring reflectance spectra of small objects not observable in the Main Belt. Within the NEA population, a continuous distribution of spectral properties ranging from the spectral signature common for S type asteroids to the spectrum of ordinary chondrites has been observed. This result is consistent with a size dependent trend indicating that smaller NEAs have younger and fresher surfaces therefore less weathered which most likely display spectral signature resembling that of the ordinary chondrites. For a detailed discussion of space weathering on asteroid surfaces see Clark et al. (2002).

Despite the above-mentioned important improvements that have been made in recent years in understanding the origin and nature of NEOs, many answers are not yet conclusive, and a number of critical problems are still open and deserve further investigations. Although much effort has been devoted in our understanding of the origins of NEOs from a dynamical point of view and in modeling

the dynamical transport mechanisms from the main asteroid belt to the region of the terrestrial planets, one of the major problems remains the currently insufficient effort devoted to physical characterization (see Cellino et al., 2002b). A short list of the most fundamental open issues in this respect includes:

1. An assessment of the real inventory and size distribution of NEOs down to small sizes, well below 1 km. An accurate size distribution is the key to integrating the total NEO population for hazard assessment and optimizing survey strategies.
2. A reliable albedo distribution of the NEO population, which can yield to a precise assessment of the contribution of comets, extinct comets and dark objects to the overall NEO inventory.
3. A real understanding of the internal structures of these objects: i.e. are they monolithic, or loose aggregates of chunks of rock held together by gravity? This issue is of crucial importance for the development of effective techniques of orbital deflection and impact mitigation.
4. A better assessment of the real distribution of different taxonomic classes in the NEO population and a clear picture of the way these taxonomic classes correlate with albedos.

1.4 The need of physical characterization of NEOs: statement of the problem

The albedo – the percentage of incoming solar light that the surface of the object reflects – is a fundamental physical parameter for an asteroid. The albedo is the missing link in determining the nature of the NEO population. The distribution of albedos and its correlation with the taxonomic types and the orbital elements of NEOs is the key to understanding their nature, their origin and to obtaining a reliable size distribution for this population of objects (i.e. knowledge of the albedo distribution allows converting the NEO absolute magnitude distribution, which is now well constrained, into a size distribution which, at present, is not). This information is crucial for developing and improving reliable and truly debiased NEO population models (Bottke et al., 2000; 2002a; Morbidelli et al., 2002b). Such models are crucial for the assessment of the impact hazard that NEOs pose to civilization on our planet. The NEO albedo distribution is also crucial to addressing asteroid-comet relationship: could a significant fraction of NEOs be the nuclei of extinct short-period comets? The likely contribution of comets to the NEO population is still an open question.

Unfortunately, upon discovery the only physical information for a NEO is its absolute visual magnitude, H . For albedos in the range 0.05-0.3 (typical of main belt asteroids), an object having an absolute magnitude equal to 18 has an uncertainty in the diameter ranging from 0.6 and 1.5 km. Clearly, this error, larger than a factor of two, makes any reliable assessment of the size distribution of the NEO

population very uncertain. Moreover, the typical accuracy of H values for a NEO is of the order of 0.5 magnitudes due to (1) the low signal to noise ratio of the measurements performed by automated discovery surveys, (2) the ambiguity introduced by light curve effects and (3) the often rough data reduction procedure which does not use filters and standard stars from photometric catalogues. Taking into account this large uncertainty on the H value the error on the diameter is thus even larger.

Even though more than 2400 NEOs have been discovered to-date, a reliable albedo is known for less than 40-50 objects only. The size distribution of the total population is therefore very uncertain and, at present, it relies on assumed average values of the albedo (usually derived by extending taxonomic schemes valid for the main belt, to the NEO population) to convert the absolute magnitude distribution into the size distribution. Werner et al. (2002) considered size-dependent values of the visual geometric albedo, namely $p_v = 0.11$ and $p_v = 0.25$, for objects with diameters above and below about 1 km. Stuart (2001) used $p_v=0.11$, while Bottke et al. (2000) assumed $p_v \approx 0.15$.

Color information obtained with visible wavelength measurements (UBVRI-photometry or spectroscopy) can be used to classify asteroids into broad compositional types (taxonomy), restricting the albedo uncertainty to within the ranges of 0.05-0.15 for C-type objects and 0.10-0.30 for S-type asteroids. Those albedo ranges which are too broad for any reliable diameter determination are based on measurements obtained for main-belt asteroids, which sizes are in general larger than 50 km of diameter. It is worth to point out here that those objects are fifty times the sizes and five orders of magnitude more massive than a typical 1km NEO.

At present, no reliable information for the albedo range of C-type and S-type NEOs exists. There is evidence that NEOs and small asteroids in general might have a different albedo distribution than larger main-belt asteroids. Studies of the albedos derived by IRAS had shown how the albedo distribution of main-belt asteroids smaller than 50 km has different properties than the one of larger bodies (i.e. the mean albedo increases with decreasing diameter and the clear separation between C-type and S-type asteroids vanishes at the smaller sizes: see Tedesco et al., 1993, for instance). It is not clear whether this is a real effect or it is due to the low signal to noise ratio of IRAS measurements for asteroids of that size. Cellino et al. (1999, 2003) are currently carrying out a campaign of polarimetric observations of small ($D < 50$ km) asteroids observed by the IRAS satellite in order to obtain independent albedo estimates of these objects. Although some indication that IRAS-derived albedos tend to be on the average slightly higher than polarimetric albedos, further data are necessary to draw definitive conclusions.

Moreover, it is not clear whether the present asteroid taxonomic scheme, which is based on the visible spectra and albedos of main-belt asteroids, may be directly applicable in the case of NEOs. For example, in the case of two NEOs with optical reflection spectra typical of C-type asteroids it was derived a radiometric albedo much higher than the value inferred from the taxonomic classification (e.g., Harris et al., 1998; Harris and Davies, 1999). There appears to be several examples of high-albedo C types asteroids in the main belt as well (Harris, 2001).

Assumed values for the albedo on the basis of taxonomy are therefore not only very uncertain, but they might be even affected by large systematic errors.

1.5 Scope of this work

This work aims to significantly increase the sample of NEOs for which size and albedo are available thereby contributing to the first physically based NEO population size distribution.

Albedos and sizes of NEOs are derived by means of the so called radiometric method. This technique makes use of measurements of the thermal infrared radiation that the object emits at mid-IR wavelengths (5–20 μm) and of its visible reflected light, combined with a suitable model of the surface thermal emission (thermal model).

Albedo measurements have been obtained for a sample of carefully selected objects of the NEO population for which reliable reflection spectra and taxonomic information are at disposal. This is to study the correlation of albedos with spectral types and possibly constrain the albedo range for the various compositional classes found within the NEO population.

Gathering data for objects which sizes and/or albedos have been measured with independent techniques (such as radar or polarimetry) is crucial to explore the limitations of the thermal models used in the analysis. A major aspect of the research is the improvement of the models of the thermal infrared emission of asteroids to facilitate the determination of sizes, albedos and other physical parameters of NEOs.

Sizes and albedos of asteroids: the radiometric method and asteroid thermal models

2.1 Foreword

Even on the largest 10m class telescopes most NEAs appear as point like sources. However, the *size* and the *albedo* of an atmosphere-less body can be derived by means of the so-called radiometric technique, which combines observations obtained in the thermal infrared region with the visible brightness of the object. In this chapter we illustrate the basis of this method which makes use of thermal models describing how the infrared radiation is emitted from the surface of the body. We introduce the Standard Thermal Model (STM), the Fast Rotating Thermal Model (FRM) and the NEATM, the near Earth asteroid thermal model and we give details of the algorithms used for their implementation. Assumptions involved in the use of thermal models cause the resulting asteroid diameters and albedos to be model dependent and affected by uncertainties which are discussed in section 2.8. Flux variability due to asteroid rotation alters the shape and the mean intensity of the measured spectral energy distribution. We introduce a method to refer measured infrared fluxes to lightcurve mean magnitude when visible lightcurve data are available for the epoch of thermal infrared measurements. The latter correction, which can be neglected for large main-belt asteroids, is proven to be of crucial importance for small and irregular bodies often observed at large phase angles, as NEAs are.

2.2 Introduction

With modern medium infrared instrumentation, equipping the largest existing telescopes, it is possible to measure the weak thermal infrared emission of NEOs, down to sizes of the order of some hundred meters.

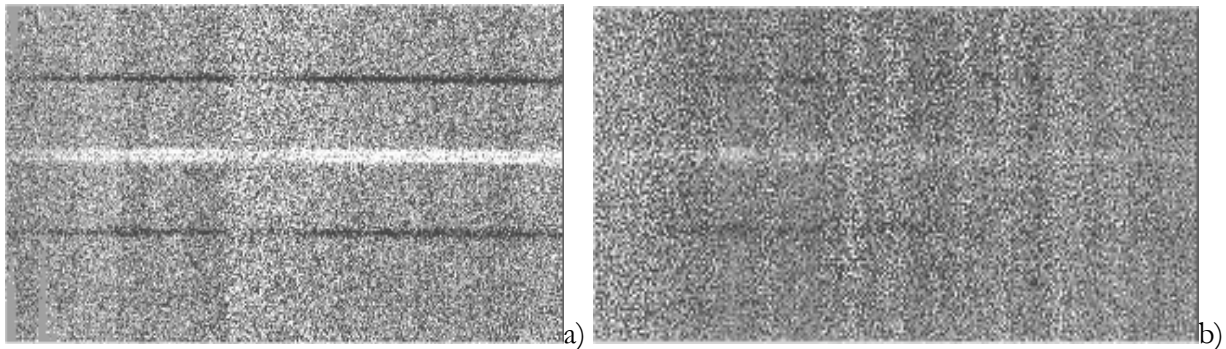


Fig. 2.1 N-band a) and Q-band b) spectra of the thermal infrared emission of the near-earth asteroid 5587 (1990SB) observed on April 09, 2001 with the TIMMI2 installed at the 3.6m telescope, La Silla, ESO (Chile). This asteroid has a diameter of almost 4km.

By comparison with calibration stars, the spectral energy distribution of which is known to high accuracy (i.e. 3%, see Cohen et al, 1999), asteroids raw data are converted to infrared fluxes. Chapter 3 of this work is mainly devoted to the methods of thermal infrared photometry that we have developed to derive asteroid infrared fluxes from observations obtained at Keck, ESO, NASA-IRTF telescopes. Fig. 2.2 shows examples for thermal infrared spectra of asteroids.

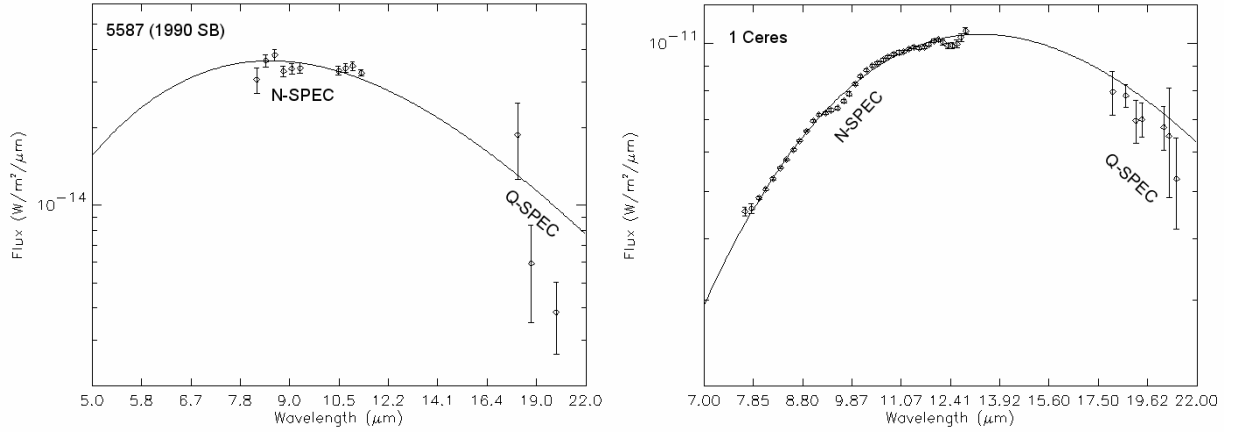


Fig. 2.2 Observed thermal infrared fluxes of the NEA 5587 on the left and of the largest asteroid 1 Ceres. Note the noise affecting Q-band data which have been binned for increasing the signal to noise ratio. Continuous line is a black body fit to the infrared spectra.

In contrast to reflected visible light, thermal infrared radiation carries direct information about the size of the asteroid: to first-order approximation, one can describe the observed thermal energy distribution (Fig. 2.2) as the emission of a black body at an effective temperature T_{eff} multiplied by the material emissivity $\varepsilon(\lambda)$ and by the solid angle the radiator subtends on the sky i.e.

$$F(\lambda) = \frac{A_p}{\Delta^2} \varepsilon(\lambda) B(\lambda, T_{eff}) \quad (2-1)$$

where $B(\lambda, T)$ is the Planck radiation function

$$B(\lambda, T) = \frac{2\pi hc^2 \lambda^{-5}}{e^{hc/\lambda KT} - 1} \quad (2-2)$$

The term A_p of Eq. (2-1) is the emitting area of the thermal radiator projected along the line-of-sight. The distance of the object from the observer, Δ , is known from the ephemerides of the asteroid. If we assume the emissivity to be constant and known at every wavelength (it is common practice to assume that asteroid surfaces have $\varepsilon(\lambda)=0.9$ for wavelengths in the range 5-20 μm), in Eq. (2-1) we have only two unknowns: A_p and T_{eff} . If the spectral energy distribution of the thermal radiator has been sampled

at several infrared wavelengths λ_i , $i=[1\dots N]$, Eq. (2-1) can be evaluated at those λ_i and we can, finally, write a system of non-linear equations: one equation for each measured spectral data point:

$$\begin{cases} F(\lambda_1) = \frac{A_p}{\Delta^2} \varepsilon(\lambda) B(\lambda_1, T_{eff}) \\ \dots \\ F(\lambda_N) = \frac{A_p}{\Delta^2} \varepsilon(\lambda) B(\lambda_N, T_{eff}) \end{cases} \quad (2-3)$$

A solution to system (2-3) can be found by a non-linear least square fit. A very effective method to be used in such cases is the *Levenberg-Marquardt* algorithm described, for instance, by Press et al. (2002), section 15.5. Such method allows the projected area and thus the effective diameter of an asteroid to be retrieved with typical accuracy of about 10%. The effective surface temperature is derived simultaneously with errors of no more than 10-20 K. At low solar phase angles, the assumption that the emitting projected area of the thermal radiator corresponds to the actual area of the object projected on the sky introduces an error of negligible contribution, given the other source of uncertainties, such as the absolute calibration of the infrared flux. We thus can obtain the unknown size of the asteroid in this very simple way. Unfortunately, for very weak targets it is not always possible to obtain measurements of the spectral energy distribution to a level of accuracy good enough to allow a stable solution to Eq. 2-1 to be found. In those cases, we have to rely on different methods which make use of models (thermal models) describing how the thermal infrared emission at the surface of asteroids originates. The first step in modeling the thermal emission of asteroids is to estimate the surface temperature distribution.

2.3 Asteroid surface temperatures

The temperature of a surface element of an asteroid is a function of the distance from the Sun, albedo, emissivity, and angle of inclination to the solar direction. A dark object absorbs more solar radiation than what brighter one does, which results in a higher equilibrium temperature. The total incoming energy incident on a surface element of area dS is:

$$dU_i = \frac{S_0}{r^2} \mu dS \quad (2-4)$$

where μ is the direction cosine of the normal to the surface with respect to the solar direction, S_0 the solar constant and r the heliocentric distance of the asteroid. Energy that is not reflected is absorbed by the asteroid surface:

$$dU_a = dU_i(1 - A) \quad (2-5)$$

where A is the bolometric Bond albedo, which is the ratio of total scattered solar energy in all directions and at all wavelengths to the incident energy. The absorbed energy and has to be balanced by thermal emission. The energy emitted by a surface dS with emissivity ϵ at a temperature T is:

$$dU_e = \sigma \epsilon T^4 dS \quad (2-6)$$

where σ is the Stefan–Boltzmann's constant. Assuming that each element of the surface is in instantaneous equilibrium with solar radiation, conservation of energy implies that $dU_a = dU_e$. The following equation for a surface element at the subsolar point ($\mu = 1$) can be written:

$$\frac{S_0(1-A)}{r^2} dS = \sigma \epsilon T_{ss}^4 dS \Rightarrow \frac{S_0(1-A)}{r^2} = \sigma \epsilon T_{ss}^4 \quad (2-7)$$

Eq (2-7) can be used to derive the value of T_{ss} , the maximum (sub-solar) temperature, as a function of heliocentric distance, r , and Bond albedo, A via the relation:

$$T_{ss} = \left[\frac{S_0(1-A)}{\sigma \epsilon r^2} \right]^{\frac{1}{4}} \quad (2-8)$$

Fig. 2.3 shows the dependence of T_{ss} as a function of the heliocentric distance and Fig. 2.4 shows the dependence of the sub-solar temperature of an asteroid as a function of the bolometric Bond albedo A . A is proportional to the geometric visible albedo p_v via the relation:

$$A \cong A_v = q \times p_v \quad (2-9)$$

where q is the phase integral which allows the parameter A to be linked directly to p_v . The geometric visual albedo p_v , which is defined as the ratio of the visual brightness of a planetary body observed at zero phase angle to that of a perfectly diffusing "Lambertian" disk of the same radius and at the same distance as the body, is a measurable and widely quoted parameter. In the standard H, G magnitude system described by *Bowell et al. (1989)*, in which H is the absolute magnitude and G is the slope parameter we have that:

$$q = 0.290 + 0.684 \times G \quad (2-10)$$

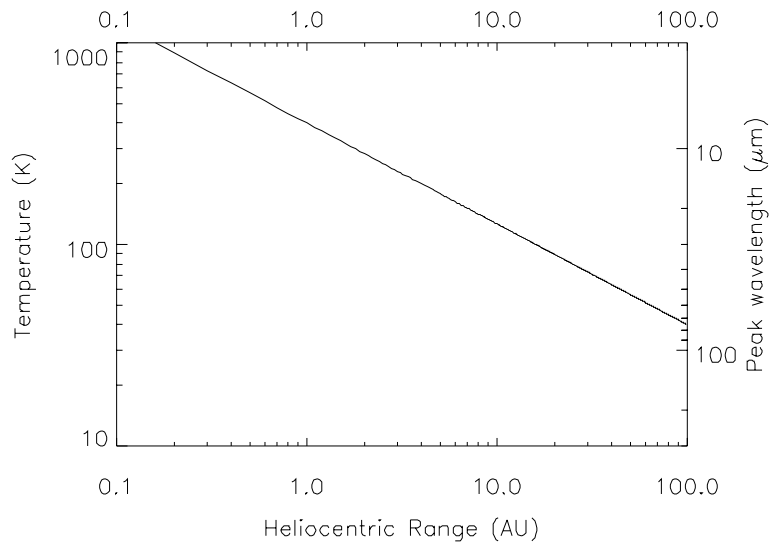


Fig. 2.3 Dependence of the sub-solar temperature as a function of its heliocentric distance for an asteroid in instantaneous thermal equilibrium with sunlight at all points on its surface. For objects orbiting the Sun in the near-Earth space, the surface temperature is about 400K and the emitted thermal radiation peaks around 8 μm . However, the radiation of more distant asteroids shifts toward longer wavelength as their temperature decreases. The following parameters have been used to produce the plot: $A = 0.0393$ (corresponding to $p_v = 0.1$ and $G = 0.15$) emissivity = 0.9, and solar constant = 1373 W m^{-2} .

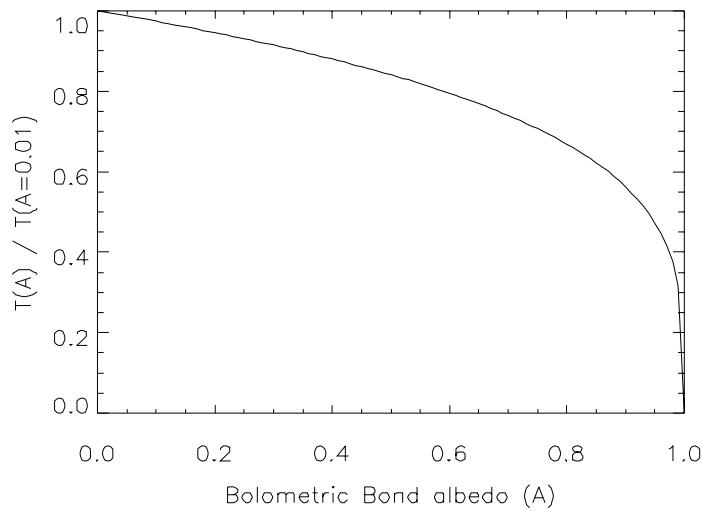


Fig. 2.4 Dependence of the sub-solar temperature of an asteroid as a function of the bolometric Bond albedo A . This dependence does not depend on the heliocentric distance of the body.

The equation of thermal equilibrium can be used not only to estimate the maximum temperature, but it determines the distribution of temperatures on the surface as well:

$$\frac{S_0(1-A)}{r^2} \mu = \sigma \varepsilon T^4(\mu) \quad (2-11)$$

and in the case of a sphere, where the direction cosine is a simple function of the solar colatitude Ω ($\mu = \cos \Omega$)

$$\frac{S_0(1-A)}{r^2} \cos \Omega = \sigma \varepsilon T^4(\Omega) \Rightarrow \begin{cases} T(\Omega) = T_{SS}(\cos \Omega)^{\frac{1}{4}} & \text{for } \Omega \leq \pi/2 \\ T(\Omega) = 0 & \text{otherwise} \end{cases} \quad (2-12)$$

Eqs. 2-8 and 2-12 are very important: they define the temperature distribution of a sphere on the assumption of instantaneous thermal equilibrium with sunlight at all points on its surface (Equilibrium Model, hereafter EM).

2.4 Calculation of the emitted thermal infrared flux

Once the temperature distribution is known (or it has been assumed), to calculate the emitted infrared flux received by an observer at a distance Δ from the asteroid is easily achieved by numerically integrating the contribution of each surface element visible to the observer, i.e.:

$$F(\lambda) = \frac{\varepsilon(\lambda)}{\Delta^2} \iint_{\Pi} B(\lambda, T) d\Omega \quad (2-13)$$

where $d\Omega$ is the projected area of the surface element, Π is the asteroid projected surface and $B(\lambda, T)$ is the Planck radiation formula. The model infrared flux scales with the projected area (i.e. with the square of the effective diameter). So, if we evaluate the integral of Eq. (2-13) on a “reference” asteroid with a emitting projected area equal to $\pi/4 \text{ km}^2$ (i.e. an asteroid with effective diameter of 1 km)

$$F_{reference}(\lambda) = \frac{\varepsilon(\lambda)}{\Delta^2} \iint_{\Pi_{reference}} B(\lambda, T) d\Omega, \quad (2-14)$$

we obtain a direct relationship between the asteroid effective diameter and the measured infrared flux:

$$D_{eff}^2 = F_{measured}(\lambda) / F_{reference}(\lambda). \quad (2-15)$$

Since $F_{reference}(\lambda)$ is a function of p_v , the ratio of Eq 2-15 is a function of the geometric visible albedo too. The trajectory of this function is shown in Fig. 2.5

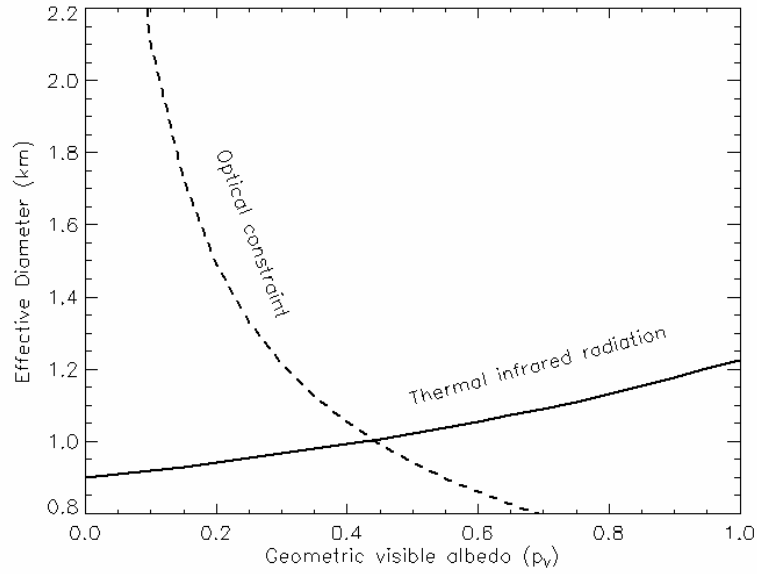


Fig. 2.5 Constraints on the albedo and effective diameter from thermal infrared observations and visible absolute magnitude. Solid line: curve defined by Eq. (2-15), dashed-line: curve defined by Eq. (2-16).

2.5 Constraints on diameter and albedo from the visible absolute magnitude

The absolute magnitude H of an asteroid, which correspond to the magnitude in the V-band measured (or extrapolated) at zero degree of phase angle, at the heliocentric and geocentric distance of 1AU is related to the geometric visible albedo, p_v , and the asteroid effective diameter D_{eff} by the relation (e.g. Fowler and Chillemi, 1986):

$$D_{\text{eff}} = \frac{1329}{\sqrt{p_v}} 10^{-\frac{H}{5}} \quad (2-16)$$

Given the H value, this equation defines the second curve shown in Fig. 2.5 by plotting the diameter as a function of the albedo. The intersection of the two curves gives the best estimate for the diameter and the albedo of the asteroid.

2.6 Radiometric diameters and albedos

The method described above defines the basis for the radiometric determination of asteroid sizes and albedos. The principle of this technique has been outlined by Morrison (1973). Furthermore, it is of interest to see Lebofsky and Spencer (1989) and Tedesco (1992). Delbo & Harris (2002) and Harris and Lagerros (2002) provided recent review of the principle on which this technique is based.

2.7 Thermal models of asteroids

As already described, several assumptions have to be made to determine the bolometric albedo from the visual albedo and a model is required to describe the temperature distribution on the surface of the asteroid and the way infrared radiation is emitted from a body of given size and bolometric albedo.

In section 2.5 we have discussed a method to derive diameters and albedos of atmosphere-less bodies of the Solar System, which assumes a non-rotating spherical shape in thermal equilibrium with solar radiation. Furthermore, the method works at zero degrees of solar phase angle only. However, real asteroids are not spherical, neither they are observed at $\alpha=0^\circ$. Moreover, in the case of objects with known size, it was observed that the assumption of thermal equilibrium leads to a zero-phase-angle model infrared flux which is too small compared to observations. Resulting asteroids diameters derived on the assumption of thermal equilibrium are thus larger than what they actually are. Modifications to the simple equilibrium model were therefore introduced to account for asteroid rotation, to compensate for the angular distribution of the thermal emission, to adjust the surface temperature to match the observed color temperature etc.

In the next sessions, we introduce the three different asteroid thermal models that will be fitted to the measured infrared fluxes to calculate diameters and albedos.

2.7.1 *The Standard Thermal Model (STM)*

The vast majority of asteroid diameters and albedos, including those in the IRAS minor planet survey (Tedesco, 1992), and those in the new release of the Supplemental IRAS Minor Planet Survey – SIMPS – (Tedesco et al., 2002) have been derived using the Standard Thermal Model (STM). The basis of the STM is the assumption of a spherical shape and instantaneous equilibrium between insolation and thermal emission at each point on the surface. It was designed to work at zero degree of solar phase angle. The angular dependence of the temperature distribution is described by Eq. 2-11. The temperature falls to zero at the terminator and there is no thermal emission from the night side. However, the “refined” STM of Lebofsky et al. (1986) and Lebofsky and Spencer (1989) includes a modification to the sub-solar temperature T_{SS} via the so-called beaming parameter η . The η parameter was introduced to match the occultation diameter of large main belt asteroids and it was included to account for the enhancement in the thermal radiation observed at small phase angles. This tendency of the radiation to be “beamed” towards the Sun is similar to the opposition effect (see Belskaya and Shevchenko, 2000) in the visible light. In the refined STM of Lebofsky and Spencer its value is set to 0.756 to match the occultation diameter of 1 Ceres and 2 Pallas. One more point has to be addressed:

observations are almost never carried out at zero degree of solar phase angle. Matson (1971) and Lebosfky and Spencer (1986) observed that asteroids had infrared phase curves which could be approximated by a linear function up to phase angles of about 30°. They derived a mean phase coefficient β_E of 0.01 magnitudes/degree. The STM should give accurate results for an asteroid that has thermal properties similar to those of large main-belt asteroids and is observed at a small phase angle. STM was designed to work with asteroid infrared magnitudes measured at a single wavelength. In those cases where infrared data were available at different wavelengths radiometric resulting diameters and albedos were given for each wavelength. It is common practice, for example, to speak of 10- μm or 20- μm diameters of asteroids. However, if photometric data are available at more than one wavelength the STM can be applied to all data points simultaneously searching for a least-square solution by minimizing the χ^2 of the residuals observed fluxes – predicted model fluxes. In this work, the STM is implemented by means of the following algorithm:

1. Guess the geometric visible albedo p_V .
2. Given the H value, calculate D from Eq. 2-16
3. From Eq. 2-8, obtain A and calculate T_{SS} using Eq (2-17) with $\eta=0.756$

$$T_{SS} = \left[\frac{S_0 (1-A)}{r^2 \eta \epsilon \sigma} \right]^{1/4} \quad (2-17)$$

4. Calculate the temperature distribution on the surface of the sphere

$$T(\Omega) = T_{SS} \cos^{1/4} \Omega \quad (2-18)$$

where Ω is the angular distance from the sub-solar point (i.e. the colatitude in a reference frame with the pole pointing towards the Sun).

5. Calculate the model flux

$$F(\lambda_i) = \frac{\epsilon D^2}{2\Delta^2} \int_0^{\pi/2} B(\lambda_i, T(\Omega)) \cos \Omega \sin \Omega d\Omega \quad (2-19)$$

6. Scale the observed flux to zero degree of phase angle, α

$$f(\lambda_i) = f_{observed}(\lambda_i) \times 10^{-(0.01|\alpha|)/2.5} \quad (2-20)$$

7. Calculate the χ^2

$$\chi^2 = \sum_{i=1}^N \left(\frac{(F(\lambda_i) - f(\lambda_i))^2}{\sigma_i^2} \right) \quad (2-21)$$

8. Change the value of the p_V parameter and reiterate the algorithm (going back to point 2) until the minimum value of the χ^2 is reached.

The value of the p_V at χ^2 minimum is the least-square best estimate for the albedo of the asteroid. The diameter D is simultaneously set to its best (least-square) estimate by Eq (2-16).

2.7.2 *The Fast Rotating Model (FRM)*

Problems arise in the application of the STM to NEAs, which are relatively small and often irregularly shaped, may lack the dusty insulating regolith (which reduces the surface thermal inertia) characteristic of larger bodies, and are often observed at large solar phase angles. For these reasons the assumptions inherent in the STM are not generally valid in the case of NEAs. In general, the STM appears to underestimate the diameters and over estimate the albedos of NEAs (Harris and Lagerros, 2002). Lebofsky et al. (1978) proposed an alternative fast-rotating/high-thermal-inertia thermal model that gives results for some NEAs that are in better agreement with diameters and albedos estimated by other means (e.g., from radar observations or spectral class). The Fast Rotating Model (FRM), also called the iso-latitude thermal model, is an alternative model appropriate for use with objects which rotate rapidly or have high surface thermal inertias in which half the thermal emission originates from the night side. The FRM assumes a perfect sphere with its spin axis perpendicular to the plane containing the asteroid, the observer and the Sun, and a temperature distribution depending only on latitude.

Consider an elementary surface strip around the equator of the spherical asteroid. The conservation of energy requires that the solar energy absorbed by the strip on the day side is reemitted as thermal radiation around its entire circumference:

$$\frac{S_0(1-A)}{r^2} 2R^2 d\theta = \varepsilon\sigma T^4 (2\pi R^2 d\theta) \quad (2-22)$$

where R is the radius of the asteroid and $d\theta$ the width of the strip. Eq (2-22) yields the following expression for the sub-solar maximum temperature:

$$T_{SS} = \left[\frac{S_0(1-A)}{r^2 \pi \varepsilon \sigma} \right]^{1/4} \quad (2-23)$$

which is the analogue of Eq (2-16) with η replaced by π . Finally the temperature on the surface of the asteroid is a function of the latitude θ only, i.e.:

$$T(\theta) = T_{SS} \cos^{\frac{1}{4}} \theta \quad (2-24)$$

We have adopted the following algorithm to implement the FRM in this work:

- 1) Guess the geometric visible albedo p_v .
- 2) Given the H value, calculate D from Eq. (2-16)
- 3) From Eq. 2-8 obtain A and calculate T_{ss} using Eq (2-23).
- 4) Calculate the temperature distribution on the sphere using Eq (2-24)
- 5) Calculate the model flux

$$F(\lambda_i) = \frac{\epsilon D^2}{\pi \Delta^2} \int_0^{\pi/2} B(\lambda_i, T(\theta)) \cos^2 \theta d\theta \quad (2-25)$$

- 6) where θ is the latitude in a astro-centric reference frame with the pole orthogonal to the plane containing the Earth and the Sun.
- 7) Calculate the χ^2

$$\chi^2 = \sum_{i=1}^N \left(\frac{(F(\lambda_i) - f(\lambda_i))^2}{\sigma_i^2} \right) \quad (2-26)$$

- 8) Change the value of the p_v parameter and reiterate the algorithm (jumping back to point 2) until the minimum value of the χ^2 is reached.

The value of the p_v at χ^2 minimum is the least-square best estimate for the albedo. Note that the FRM does not require any correction to the thermal flux for the phase angle.

2.7.3 *The near-Earth asteroid thermal model (NEATM)*

In general, neither the STM nor the FRM provide good fits to the measured spectral energy distributions of NEAs. Harris (1998) showed that it was possible to obtain a good fit to multi-wavelength thermal infrared data of NEAs with a modification to the STM. The NEATM (see Harris, 1998 for further details) assumes the asteroid to have a spherical shape and its surface temperature distribution to be described by Eq (2-18). However, in this model, Eq (2-17), which defines the sub-solar temperature, is used with the difference that the value of η is not set equal to 0.756 as it is in the case of the STM. Within the NEATM, η is a free parameter, which is iteratively adjusted to provide the best fit to the observed thermal infrared fluxes. The effect of changing η is that of changing the object's sub-solar temperature T_{ss} and, as a consequence, the whole surface temperature distribution is scaled by a factor $\eta^{-1/4}$. Moreover, with respect to the STM, the NEATM differs in the way the phase angle is taken into account. Instead of scaling the infrared flux by a factor of 0.01 magnitudes per degree, the phase angle is taken into account by calculating numerically the actual thermal flux an observer would detect from the illuminated portion of a smooth sphere visible to him at a given solar phase angle,

assuming no emission originates on the night side: see Eq (2-28). This treatment assumes a Lambertian emission model and has been applied and discussed by previous authors (e.g., Cruikshank and Jones 1977, Brown 1985). of the STM. The empirical phase coefficient (of 0.01 mag/deg) used with the STM has been derived and tested for solar phase angles no greater than 30°. NEAs, however, are often observed at much higher phase angles (up to 90°) and they surface characteristics (macroscopic roughness, thermal inertia) may differ significantly from those of large main belt asteroids on which the STM was calibrated.

It is important to emphasize that the NEATM requires good wavelength sampling of the thermal continuum (i.e., four or five filter measurements over the range 5 to 20 μm) for a stable fit of the η -parameter to be achieved. If only one or two filter measurements closely spaced in wavelength are available, the derivation of η via spectral fitting is not possible. In such cases a default value of η can be used. Harris (1998) has proposed the value of 1.2 by the comparison of albedos and diameters of objects for which independent information on these parameters is available. Delbò et al. (2003) have first studied the dependence of η values derived by the use of NEATM with the phase angle, α . They suggested that $\eta=1$ for $\alpha<45^\circ$ and $\eta=1.5$ for $\alpha>45^\circ$ provide a best fit to the observed distribution of η values.

The algorithm which implements the NEATM in this work can be described as follows:

1. Guess the geometric visible albedo pV.
2. Given the H value, calculate D from Eq. 2-15
3. From Eq. (2-8) obtain A. Provide an initial guess for the η -value (e.g. $\eta=1$) and calculate TSS using Eq (2-18) and the surface temperature distribution using Eq (2-27)

$$T(\theta, \varphi) = T_{SS} \cos^{1/4} \theta \cos^{1/4} \varphi \quad (2-27)$$

for θ in the range $[-\pi/2, \pi/2]$.

4. Calculate the model flux by integrating the Planck's function over the illuminated portion of a smooth sphere visible to the observer

$$F(\lambda_i) = \frac{\varepsilon D^2}{\Delta^2} \int_0^{\pi/2} \int_{-\pi/2}^{\pi/2} B(\lambda_i, T(\theta, \varphi)) \cos^2 \varphi \cos(\theta - \alpha) d\theta d\varphi \quad (2-28)$$

where ξ is the angular distance from the sub-solar point (i.e. the colatitude in a reference frame where the pole points toward the Sun).

5. Calculate χ^2

$$\chi^2 = \sum_{i=1}^N \left(\frac{(F(\lambda_i) - f(\lambda_i))^2}{\sigma_i^2} \right) \quad (2-29)$$

6. Change the value of pV and of the η parameter and reiterate the algorithm (going back to point 2) until the minimum value of the χ^2 is reached.

In this work, we have implemented the *Levenberg-Marquardt Method*. (Press et al. 2002) to find the minimum of the χ^2 function of Eq. 2-29.

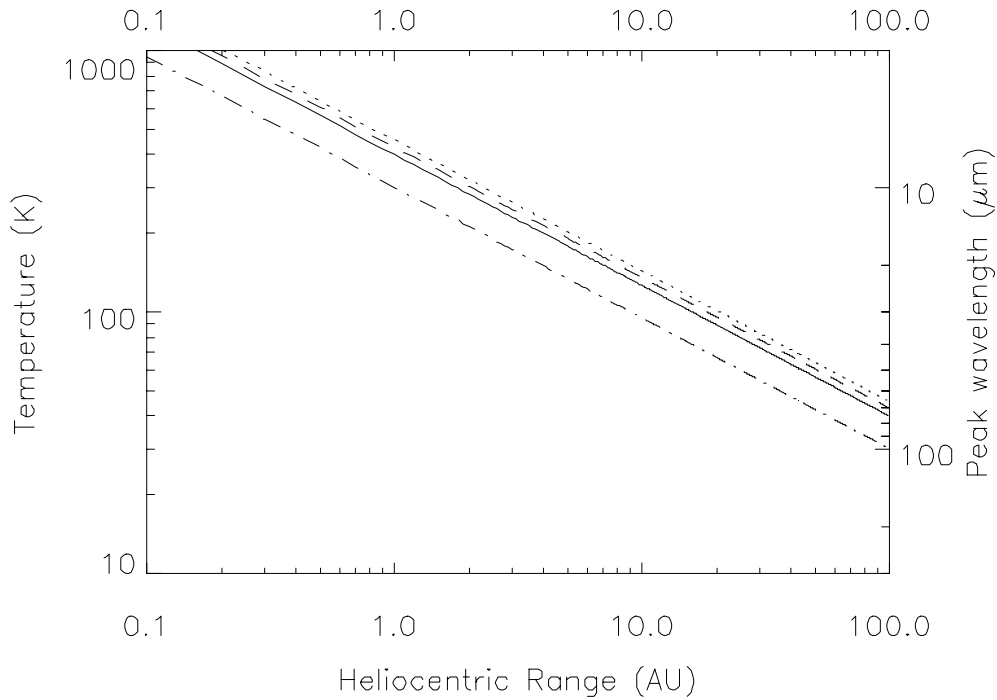


Fig. 2.6 As of Fig. 2.3, but T_{SS} is calculated for different value of the parameter η . Solid-line: $\eta=1.0$; dashed-line: $\eta=0.756$ as in the “refined” STM of Lebofsky and Spencer (1989); dotted-line: $\eta=0.6$, dashed- and dotted-line: $\eta=\pi$ which is the value used within the FRM.

It is of interest to point out that the value of T_{SS} in the thermal models we have here described is never equal to the equilibrium value, that Eq (2-8) would give, unless η is derived (in the case of the NEATM) or assumed (as in the case of the STM) equal to one. Fig. 2.6, which is the analogue of Fig. 2.3 for $\eta \neq 1$, shows the dependence of T_{SS} as a function of the heliocentric distance for different values of η and different thermal models.

2.8 Uncertainties

2.8.1 *Rotational variability effects and lightcurve correction of infrared fluxes*

The thermal infrared flux that an observer receives from an asteroid varies as the object rotates. If fluxes at different wavelengths are measured at different times, as in the case of spectro-photometry obtained with narrow band infrared filters, severe alterations of the shape and of the absolute level of the measured spectral energy distribution may result⁶. Thermal model fits may in those cases give erroneous results. Thermal infrared fluxes can be corrected for rotational variability if visible lightcurve data are available for the time of the thermal observations. Correction of the flux values to the mean lightcurve magnitude is performed on the assumption that the thermal infrared and the visible band lightcurve are identical. Clearly difference in the lightcurve (i.e. in the amplitude, phase and structures) cannot be ruled out and such differences may contribute to the scatter of the data point with respect to the thermal infrared continuum. In those cases in which no lightcurve data are available the uncertainties in the results are inevitably larger and very difficult to be estimated.

2.8.2 *The actual temperature distribution differs from the modeled one*

Due to their non-zero thermal inertia, real asteroid surfaces are not in instantaneous thermal equilibrium with insolation. Moreover, temperature distributions differing significantly from the Lambertian temperature distribution cannot be ruled out. Several factors influence the actual temperature distribution on the surface of a real body. It is very well known, for instance, that the sub-solar brightness temperature of the Moon seen at zero phase angle is higher than the temperature predicted by the equilibrium with solar radiation (e.g. Sinton, 1962). Furthermore, the temperatures along the equator at full moon vary as $\cos^{1/6}\Omega$ and not as $\cos^{1/4}\Omega$ expected from a Lambertian surface. Statistical studies showed that the falloff in brightness temperature towards the Moon's limb can be represented by a relation linear in $\cos\Omega$ ($T(\Omega)=324.2 +72.6 \cos\Omega$: Shorthill, 1972). The departures of the brightness temperature on the lunar surface can be explained by the effects of surface roughness.

Most asteroids are covered by a very porous soil, similar to the lunar regolith (Housen et al., 1979; McKay et al., 1989). Heat conduction in the regolith is extremely low, because of the high porosity. However, conduction within the porous material plays an important role in determining the surface temperature distribution especially for fast rotating asteroids. Consider a surface element of a body with

⁶ On the basis of the experience, rule-of-thumb, practical times required to obtain a measurement in one filter, taking into account overheads, are between 10 and 40 minutes. Considering that typical rotational periods for NEAs are of the order of some hours, it is clear that light curve effects have to be taken into account.

a high thermal inertia: this element behaves like a capacitor or sink for the solar energy, and thus its temperature is not only a function of albedo and heliocentric distance but depends also on its previous thermal history. With the Sun in the equatorial plane, the higher the thermal inertia is the smoother the temperature distribution with respect to longitude is. For a very high thermal inertia and rotation rate the surface element has no time to cool down on the night side: its temperature remains constant through day and night (i.e., it is independent of longitude). The effect of thermal inertia is coupled to rotation rate. A slow rotating asteroid with high thermal inertia displays a similar temperature distribution of one rotating very rapidly but with a lower thermal inertia. It is interesting to anticipate here a result described in Chapter 6. There, we will show calculated diurnal temperature profiles for an asteroid in the near Earth space for different value of the thermal inertia. For relatively low values of this parameter small variation in the range 10-20 K are expected at the sub-solar point, although the night-time temperature can rise up to 200 K. Systematic errors on the resulting diameter and albedo are likely to occur if observations are carried out at large solar phase angle and the thermal emission from the night side is ignored.

2.8.3 Accuracy of the H values

The accuracy of albedo values derived via thermal models depends strongly on the accuracy of the adopted absolute magnitude, H . In those cases in which reliable H -values are not available from other sources, we have resorted to estimates based on the values given by the JPL Horizons (ssd.jpl.nasa.gov/horizons.html), MPC (cfa-www.harvard.edu/iau/MPEph/MPEph.html), and NeoDys (newton.dm.unipi.it/neodys) web sites. It should be noted that the uncertainty in these estimates is often large, e.g., ≥ 0.5 mag. In the event that more reliable H -values become available in the future, the derived albedo and diameter values given in Chapter 3 can be updated using the convenient expressions given by Harris and Harris (1997).

2.9 Thermophysical models

It is clear that the STM and its derivatives are based on assumptions which make simplifications to the physical processes active at the surface of asteroids. Simple models have obvious limitation when a detailed investigation of the physical processes is required from high-quality observational data. The main goal of the work on thermophysical models of asteroids has been to introduce a more detailed description of the physics which governs thermal effect acting on asteroid surfaces, as compared to simple thermal models. Several authors have worked on this topic. For example, Brown (1985) introduced ellipsoids to describe the shapes of asteroids. Spencer (1990) introduced heat conduction in

combination with surface roughness. Lagerros (1996, 1997, 1998, and references therein) collected, combined, and extended these and other approaches into a single working model.

Clearly, thermophysical models are to be preferred over the simple models for accurate results. However, in the case of NEAs, parameters which are required by more complex models, such as shape, thermal inertia, pole orientation, and surface roughness, are normally not known. So, while complex models, such as those described by Lagerros, are important for furthering our understanding of the asteroid thermal processes, their use has severe limitations to derive sizes and albedos of NEAs for which a limited number of radiometric data are available.

2.10 Summary

Observations in the thermal infrared enable albedos and diameters to be derived and give some insight into the thermal properties of an object.

Thermal infrared radiation carries direct information on the size of the object. However, with limited sampling of the spectral energy distribution and with the typical measurement accuracy achieved in the medium infrared from the ground, an unconstrained solution to the problem of Eq 2-3 is unstable. Thermal models are thus required to derive diameters and albedos from radiometric measurements.

The STM was shown to provide reliable diameters and albedos for most large main belt asteroids. However, its use in the case of NEAs gives albedos that are generally too high compared to the results expected from their taxonomic classification.

The failure of the STM to derive reliable albedos for NEAs is very likely due to the different thermal properties of these objects when compared to large MBAs. With their small force of gravity and their very irregular surfaces, NEAs cannot retain a thick layer of insulating regolith and should have more exposed rock than what main belt asteroids have. This results in larger thermal inertias and consequently the hypothesis of instantaneous thermal equilibrium with sunlight at all points on their surface to break down.

The FRM was introduced to derive diameters and albedos of objects which rotate rapidly and/or have high thermal inertia. STM and FRM usually give very different results and choice of which model to use for a particular NEA, in the absence of additional information, is often quite arbitrary.

Harris (1998) have shown that neither the STM nor the FRM provide good fits to the measured spectral energy distribution of the thermal emission of NEAs. However, the fit is considerably improved if the NEATM (a modified STM) is used with a beaming parameter $\eta \geq 1$. The larger beaming

parameters, compared with the value of 0.756 used in the IRAS STM for main-belt asteroids, are consistent with the results of previous authors suggesting that NEAs have larger surface thermal inertias in general than main-belt asteroids.

Moreover, the use of the NEATM allows a first-order correction for the effects of rotation, surface roughness and thermal inertia by fitting the beaming parameter η to the multi-wavelength data to match the observed color temperature.

Application of all three thermal models gives some idea of the modeling uncertainties involved in the measurement of NEA diameters and albedos.

Thermal infrared observations of near-Earth asteroids and data reduction^{7,8}

3.1 Foreword

A major development within this study is the discussion of the results from observing programs with the 10m - Keck 1 telescope on Mauna Kea, Hawaii (Delbo et al. 2003) and with the ESO 3.6 m telescope on La Silla, Chile. Further observations have been collected with the 3.0 m NASA-Infrared Telescope Facility (IRTF) in Hawaii. In this chapter we describe the instruments, the observations and the data reduction techniques used to obtain the thermal infrared fluxes - listed in appendix A - of the target asteroids.

3.2 Introduction

An extended dataset of new thermal infrared observations of NEOs have been obtained in the years 2000-2003 within the framework of this Ph.D. project. A major development within this study is the discussion of the results obtained from observations carried out at the Keck-1 telescope, Mauna Kea Hawaii⁹ on 7 nights between March 2000 and February 2002. At the Keck-1, the Long Wavelength Spectrograph (LWS) was used in imaging mode. This is a liquid helium cooled instrument for almost diffraction limited imaging and spectroscopy in the 5-20 μm regions. Details of the instrument are given by Jones and Puetter (1993) and can be found on the Keck Observatory web site (<http://www2.keck.hawaii.edu/realpublic/inst/>). Narrow-band filters centered on 4.8, 8.0, 8.9, 10.7, 11.7, 12.5, 17.6, 17.9 and 20.0 μm were selected for observations with this instrument. Results of the Keck observing campaigns are discussed by Delbò et al. (2003).

Several additional observations have been collected using the ESO 3.6m telescope at the European Southern Observatory in La Silla, Chile¹⁰ on 10 nights between April 2001 and June 2003. The Thermal Infrared Multi-Mode Instrument (TIMMI2) was used at the ESO 3.6m telescope (see Reimann et al.,

⁷ Part of this chapter is devoted to the description of the observations and the data reduction of our program with the Keck 1 telescope. Most of the radiometric diameters and albedos derived from this project have been already published by Delbo et al. (2003). Note that Table 3-1 contains three more NEAs, with respect to the equivalent table of Delbò et al. See section 3.11 for further details.

⁸ Partially based on observation obtained at the European Southern Observatory, La Silla. Project IDs 67.C-0543, 68.C-0447, 69.C-0619, 70.C-0608, 71.C-0241

⁹ Observations were carried out by M. Delbò, R. P. Binzel, (P.I.) and A. W. Harris.

¹⁰ M. Delbò (P.I.) was the observer at the 3.6m telescope.

2000 and/or visit the ESO web page <http://www.lis.eso.org/lasilla/sciops/timmi/>). The largest majority of observations were carried out in imaging mode as well. However, the NEA 5587, observed in April 2001, was bright enough to allow TIMMI2 to be used in spectroscopic mode and reliable measurements in the 7-13 μm range to be obtained.

At ESO, to derive accurate H magnitudes of the observed asteroids and to measure their visible lightcurves simultaneously to the thermal observations, V band CCD data were obtained simultaneously with the thermal infrared observations using the Danish Faint Object Spectrograph and Camera (DFOSC) installed at the 1.5m Danish telescope at La Silla observatory¹¹. DFOSC, a focal reducer type spectrograph/camera, was operated in imaging mode. Details of the instrument and the telescope can be found on the ESO web page: <http://www.lis.eso.org/lasilla/Telescopes/2p2T/D1p5M/>. During the last two runs, in November 2002 and in June 2003, the 1.5 m Danish telescope was no longer offered to the ESO community. We resorted to the use of the Wide Field Imager (WFI) installed at the 2.2m ESO/MPI telescope (<http://www.lis.eso.org/lasilla/sciops/wfi/>).

The NASA-Infrared Telescope Facility (IRTF)¹² has also been used with the aim of performing detailed studies of selected targets. We include in this work data obtained for the NEAs 33342 (1998 WT₂₄), 1580 Betulia, 5381 Sekmeth, 6849 Golevka and for the potentially hazardous asteroid (PHA) 35396 (1997 XF₁₁). At the NASA-IRTF the Mid-Infrared Large-Well Imager (MIRLIN) array (Ressler et al., 1994) was used to carry out the largest majority of the observation. Details of this instrument are available on the web at (<http://cougar.jpl.nasa.gov/mirlin.html>). The NEA 35386 (1997 XF₁₁) was studied using the Mid-Infrared Spectrometer and Imager (MIRSI) which is a collaborative visiting instrument at the NASA-IRTF (visit the web page <http://cfa-www.harvard.edu/mirsi/> and/or see Deutsch, 2003 for further details of this instrument).

In what follows, we describe the techniques that were adopted to carry out the observations, describing the ways of obtaining reliable absolute calibrated mid-IR fluxes from the ground. We discuss the data reduction process with details of the methods adopted, in particular for what concern the estimation of photometric uncertainties.

Color correction factors have to be taken into account into multi-filter photometry if the spectral energy distribution of the unknown source is very different with respect to that of the standard stars used as calibrators. These factors were calculated for the IR filters that we have used at each instrument.

¹¹ Visible band observations were carried by M. Di Martino and, on April 2001 run, T. Vannini's collaboration was very much appreciated.

¹² S.J. Bus carried out the observation. M. Delbò, A.W. Harris (P.I.), and M. Mueller carried out the data reduction and analysis.

Reduction, wavelength and absolute flux calibration are discussed for spectroscopy at TIMMI2. In section 3.10, V-band CCD observations obtained at ESO are discussed along with the data reduction process, absolute magnitude calibration and methods to derive lightcurves of fast moving objects and their H values. A final section is devoted to show observational circumstances and relevant physical characteristics for the target asteroids of the data sets on which this work is based.

3.3 Thermal infrared ground based observations

Due to atmospheric absorption, infrared observations from the ground are limited to a number of windows in the range 5 - 20 μm as shown in Fig. 3.1.

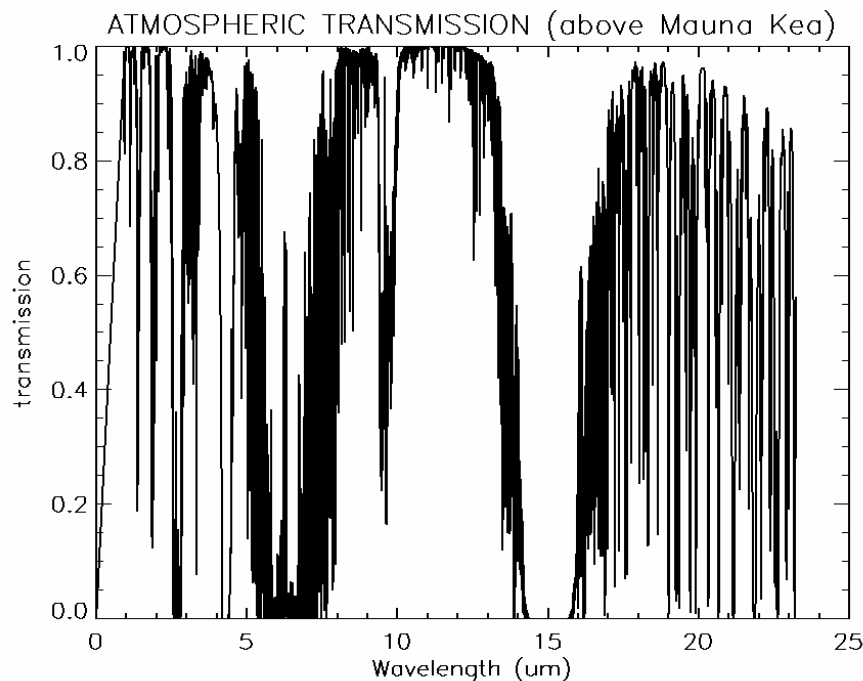


Fig. 3.1 Atmospheric transmission above Mauna Kea, Hawaii. Note the narrow window at $5\mu\text{m}$ (M band), the ozone absorption band at about $9.5\mu\text{m}$ in the middle of the N band. The atmosphere is opaque between 13.5 and about $17\mu\text{m}$. Beyond $17\mu\text{m}$ up to about $20\text{-}23\mu\text{m}$ the Q band opens.

Moreover, ground-based observations in this region are much different than the one in the optical or near infrared because of the very large thermal background flux that peaks near $10\mu\text{m}$. Even on infrared-optimized telescopes, the background is large compared to the flux from the brightest astronomical sources. Therefore, "chopping" and "nodding" techniques are needed to subtract the background to high precision. The accuracy to which the flux of an astronomical source can be obtained is basically limited by the background noise and by the " $1/f$ " noise due to variations in the background

caused by temperature drifts and thin clouds. $1/f$ sky noise is suppressed with a technique called "chopping," in which the telescope's secondary mirror is oscillated in a square-wave pattern at a frequency of several Hz. The detector alternately views two fields or "beams" on the sky: A and B beams. Computing $(A - B)$ cancels most, but not all, of the sky emission. Warm optics generates a background pattern that does not cancel out in the A-B difference. Therefore the telescope is nodded 2 – 4 times a minute to move the source from the A to the B position. By computing $A-B - (A'-B')$ the background is properly removed.

In Fig. 3.2 the field is "chopped" with 10" amplitude northwards and nodding is performed by moving the telescope 10" westwards.

Some observations, as in the case of those obtained with the LWS at Keck, are performed by chopping the field 10" North and nodding the telescope in the opposite direction. This way of observing is sometimes called "beam-switching". If the field of view of the instrument is smaller than the chopping throw, as in the case of the LWS, only one channel is imaged on the detector at a time and half of the signal is lost when beam-switching is performed. Beam-switching is also the default observing mode for spectroscopy with the TIMMI2 at ESO. Fig. 3.3 obtained from the TIMMI2 web site (http://www.la.eso.org/lasilla/Telescopes/360cat/timmi/images/quick_chop_nod.gif) gives a graphical representation of the two chopping-nodding observing modes described above.

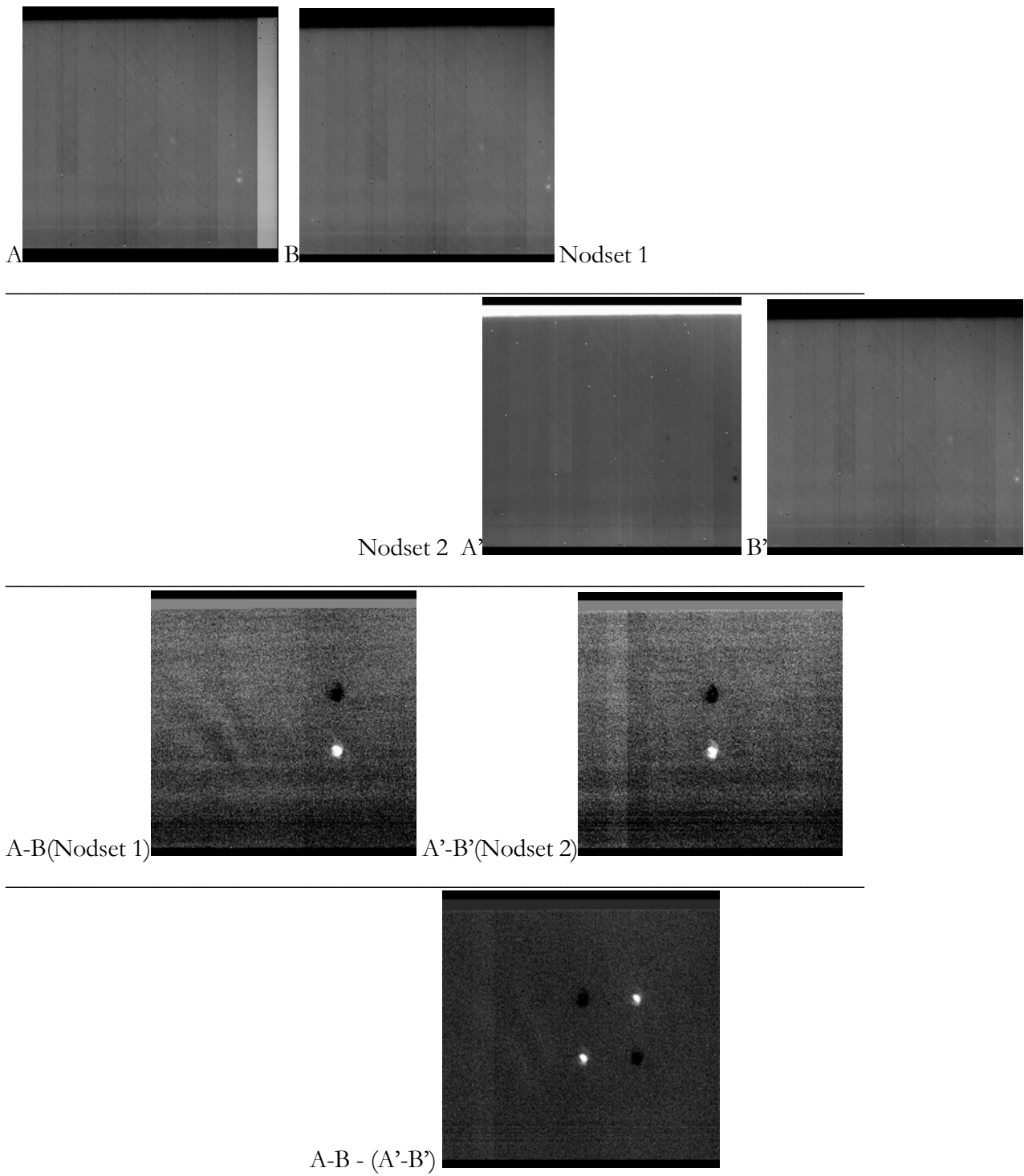


Fig. 3.2 A typical “chop-nod” observing sequence of a standard star obtained with the Thermal Infrared Multimode Instrument (TIMMI2) installed at the ESO 3.6m telescope at La Silla, Chile. Although the star is very bright, its signal is completely buried in the background radiation. Only in the differential frames it becomes visible.

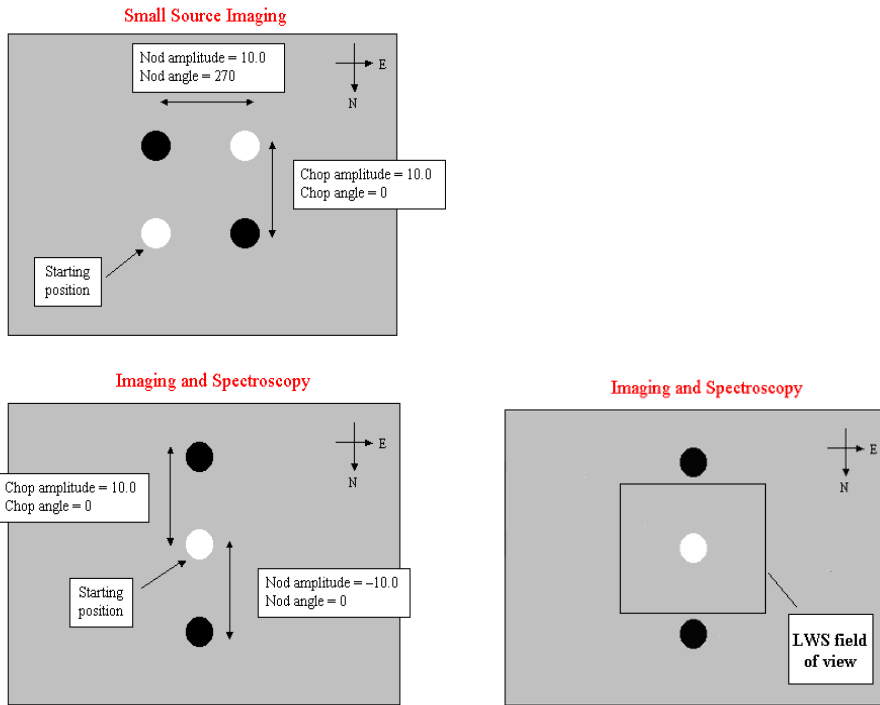


Fig. 3.3 On the left, chopping and nodding throws at TIMMI2, MIRSI and MIRLIN for small source imaging and for spectroscopy. On the right chopping and nodding at the LWS at Keck. Note that the detector field of view is too small to contain both positive and negative beams. This figure was adapted from the TIMMI2 web site: (http://www.la.eso.org/lasilla/Telescopes/360cat/timmi/images/quick_chop_nod.gif)

3.4 Thermal IR photometry

The flux (monochromatic flux density) of an astronomical source, in the medium infrared, is measured in terms of $W/m^2/\mu m$. An equivalent unit is the Jansky (Jy). 1 Jy correspond to $10^{-26} W/m^2/Hz$. Eq (3-1) allows converting fluxes from the unit of $W/m^2/\mu m$ to Janskys.

$$F_{Jy}(\lambda) = F_{W/m^2/\mu m}(\lambda) \times \lambda^2 \times 0.33357 \times 10^{12} \quad (3-1)$$

Infrared magnitudes are also used. A conversion table of magnitudes to Janskys and fluxes in terms of $W/m^2/\mu m$ for a number of wavelengths can be found at the UKIRT web site: (<http://www.jach.hawaii.edu/JACpublic/UKIRT/astronomy/conver.html>).

To obtain the absolute flux of an astronomical source like the asteroids observed in this program, bright infrared standard stars are used to calculate the instrument sensitivity i.e. the photometric zero

points for each filter (i.e. how many raw counts correspond to 1 Jy in the given integration time). Given the flux of the standard at the filter effective wavelength $F_{\text{standard}}(\lambda)$ and the instrument response raw counts in the unit time $S''_{\text{standard}}(\lambda)$, the instrument sensitivity g is the ratio F/S'' in units of Janskys/(counts/second)¹³.

Eq (3-2) is used to derive the unknown magnitude of a source at a given wavelength when its signal, S'' , in term of raw counts in the unit time, has been measured. Zp is the instrumental zero point magnitude, χ the extinction coefficient and a the airmass.

$$M = -2.5 \log(S'') + Zp + \chi a \quad (3-2)$$

If M is known (for example $M=0$ for α Lyrae) and S'' was measured at different airmasses, it is possible to solve for Zp and χ by a linear least square method. The equivalent of Eq (3-2) in terms of infrared flux is:

$$F = S'' \times 10^{Zp/-2.5} \times 10^{\chi a/-2.5} \quad (3-3)$$

The second term on the right-hand side of Eq. (3-3) is the instrument (instrument + telescope + atmosphere) sensitivity. If observations of the source and the calibration standard(s) are carried out at nearly the same airmass the extinction term can be neglected and the equation reduces to:

$$F = S'' \times g \quad (3-4)$$

where $g = 10^{-Zp/2.5}$.

The accuracy of the final flux depends on the signal-to-noise ratio of the photometric measurement and the accuracy of our estimate of the instrument sensitivity. On the basis of Eq (3-4), we can write that:

$$\left(\frac{\sigma_F}{F} \right)^2 = \left(\frac{\sigma_{S''}}{S''} \right)^2 + \left(\frac{\sigma_g}{g} \right)^2 \quad (3-5)$$

The first term on the right-hand side of the Eq (3-5) is the inverse square of the signal-to-noise ratio of the photometric measurement. Paragraph 3.5 describes the way S'' and its error can be estimated. Although an error on the value of g might arise from the finite signal-to-noise ratio of the measurements of the standard stars and the finite accuracy to which we know their absolute calibrated

¹³ Double-primed letters are used to indicate quantities in terms of counts or ADUs. Primed letters indicate number of electrons while simple letters number of photons. Unprimed letters may be used for fluxes as well: i.e number of photons/s or Jy or W/m²/μm or magnitudes.

fluxes, larger fluctuations of g are caused by sky variations in emissivity and absorption during the night¹⁴. An estimate for σ_g might be derived from those fluctuations, if several measurements of the calibration standard(s) are available. For this reason, rather than observing standards at different airmasses and derive the extinction coefficient, it is common practice to choose a calibration star to be close in the sky to the target and observe both the object and the standard at similar airmass and close in time as much as possible.

At the Keck we have selected calibration standards taken from the database of Cohen et al. (1999). Absolutely calibrated infrared spectra for each star can be obtained directly from the web via the electronic version of the paper (see table 4) which can be found at <http://www.journals.uchicago.edu/AJ/journal/issues/v117n4/980440/980440.html>

At ESO, standards were selected directly from the TIMMI2 calibration measurements web page, (<http://www.lis.eso.org/lasilla/Telescopes/360cat/timmi/html/stand.html>). Absolute photometry of those stars for wavelength corresponding to TIMMI2 filters is given. Values for HD29291, HD124897 and HD187642 are taken from spectral energy distribution models by P. Hammersely. All other values are taken from models by Cohen et al. (1999). One-sigma flux error bars are 3%.

3.5 Aperture photometry and photometric uncertainties

According to the notation introduced above, let's call $C''(x,y)$ the number of counts associated with a pixel at row x and column y . If a signal $S''(x,y)$ is imaged on the detector we can write that $C''(x,y) = S''(x,y) + B''(x,y)$ where $B''(x,y)$ represents the background contribution. Aperture photometry resembles the technique used with mono-channel detectors where an aperture (a diaphragm) was used to sample the signal from the source + background and then the telescope was offsetted to a nearby patch of blank sky to sample the background. With area-array detectors a synthetic aperture is used instead and the signal is extracted by means of the following equation:

$$S'' = C''_{aperture} - A_{aperture} \times \tilde{B}'' \quad (3-6)$$

where $C''_{aperture} = \iint_{aperture} C''(x,y) dx dy$, $A_{aperture}$ is the number (often fractional) of pixels contained within the aperture and \tilde{B}'' is some estimation of the background value. One of the standard methods for background estimation is to take an annulus surrounding the source, look at the pixel values within this

¹⁴ Observations of standard stars yield usually high S/N (>50-100) photometric measurements.

region and use some algorithm to determine the value to be assigned to the background. The final result of the procedure is the signal of the source in number of counts in the unit time.

The signal-to-noise ratio determines the uncertainty to which we know the signal S'' . It may be estimated experimentally using the following equation, hereafter written in unit counts:

$$\frac{S''}{N''} = \frac{S''}{\sqrt{S''/G + A_{\text{aperture}} \sigma_{B''}^2}} \quad (3-7)$$

where $\sigma_{B''}$ is the standard deviation of the distribution of the pixel counts of the background: i.e. within the sky annulus. $\sigma_{B''}$ is a measure of the uncertainty to which we know the value of each pixel of the background. The denominator of Eq (3-7) involves some further considerations: The first source of error is due to the Poissionian nature of the photon detection process and the second source is introduced by the background subtraction. These two error contributions are mutually independent and they have do be quadratically summed. The uncertainty associated with the signal S'' is: $\sigma_{S''}^2 = S''/G$. This equation deserves some more comments. The number of electrons S' is G times the number of counts S'' . (i.e. $S' = G \times S''$). The uncertainty on the number of recoreded electrons is given by the Poisson statistic: $\sigma_{S'} = \sqrt{S'}$. From the error propagation formula it follows that:

$$\sigma_{S''} = \frac{\partial S''}{\partial S'} = \frac{1}{G} \sigma_{S'} = \frac{\sqrt{GS''}}{G} = \sqrt{\frac{S''}{G}}. \quad (3-8)$$

Medium infrared observations from the ground are always carried out in background-limited regime, i.e. the background is orders of magnitude larger than the signal itself, and the N'' term can be estimated by the RMS value of the background in the sky annulus surrounding the source. In the signal-to-noise ratio Eq (3-7) the term due to the discrete photon detection statistic is negligible and that equation can be simplified to

$$\frac{S''}{N''} \approx \frac{S''}{\sigma_{B''} \times \sqrt{A_{\text{aperture}}}}. \quad (3-9)$$

3.6 Data reduction of thermal IR data

The data reduction has been performed using a modified version of the ATV package written in IDL by Aaron Barth (<http://www.astro.caltech.edu/~barth/atv/>) (Fig. 3.4). IDL, the Interactive Data Language, is developed by Research Systems Inc. (<http://www.rsinc.com/>).

The aperture photometry technique was adopted and applied to the final coadded frames to derive the source signals. No flat fielding was performed. Gain variations on the detector array were accounted for by imaging all sources on the same position (the center) of the array as far as possible. In the case of TIMMI2, MIRSI and MIRLIN images, where all four “chopped-nodded” channels were imaged on the detector, aperture photometry was applied to each channel separately. The resulting final signal was constructed by taking the sum of the raw counts of the four channels. However, in the case of faint objects, coadding the four channels and applying aperture photometry on the resulting source with higher S/N was found to provide more accurate results. This technique could not be exploited in the case of LWS/Keck observations, since only two superimposed channels were imaged on the array. To select the most appropriate photometric aperture the radial profile of the point spread function and the photometric growth-curve (the flux of the source as a function of the aperture radius) was studied for each source. Photometric growth-curves are extensively discussed by Howell (1989).

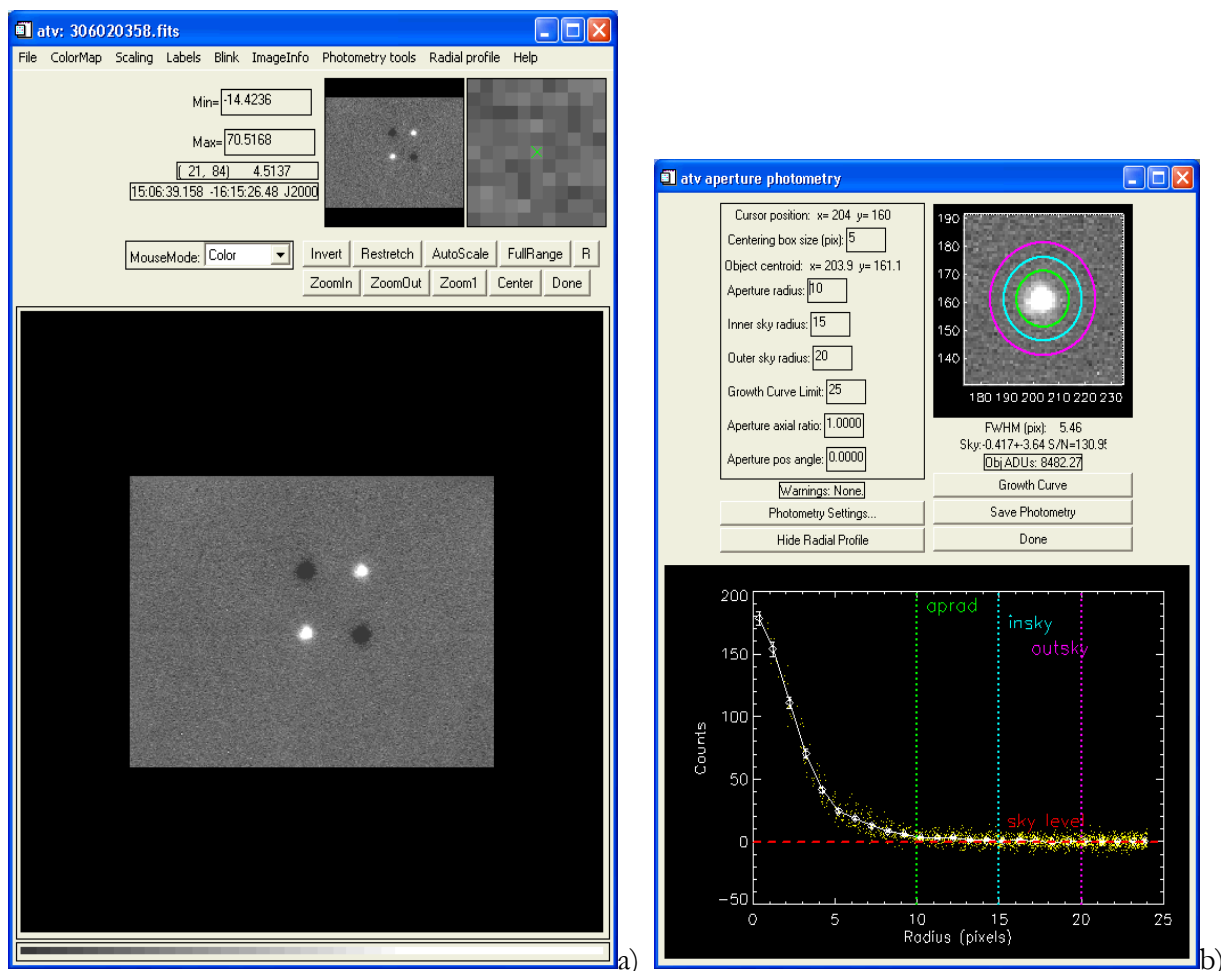


Fig. 3.4 The ATV tool: on the left (a), ATV shows a mid-IR image of a standard star obtained with the TIMMI2 at the ESO 3.6 m telescope. On the right (b), the ATV aperture photometry plug-in used to analyze one of the four chop-nod channels.

Not unexpectedly, background subtraction was found to be critical in the case of low S/N sources. The standard method for background estimation has been to take an annulus around the source, look at the pixel values within this area and use some algorithm to determine the value to be assigned to the background. This value is then multiplied by the area in pixel of the photometric aperture and subtracted from the total counts within the source area to yield a measure of the collected flux. This procedure assumes that the value for the background within the annulus is representative of its value beneath the source as well. In several thermal IR coadded observations when faint sources are imaged, however, structure in the background can be as large as the signal itself leading to a possible wrong estimate of the source flux. The study of the growth curve can yield to a much accurate estimation of the background in these cases: if the background value is correct, the flux of the source is not expected to increase by integrating within larger radii. In fact, when the photometric aperture becomes larger than the source PSF no signal is expected to be included any more and a plot of the growth curve shows a flat plateau beyond a certain aperture radius. However, this is not the case if one does the background subtraction incorrectly. For instance, if a value larger than the actual background is subtracted over increasingly larger areas, the net flux of the source decreases (see Fig. 3.5).

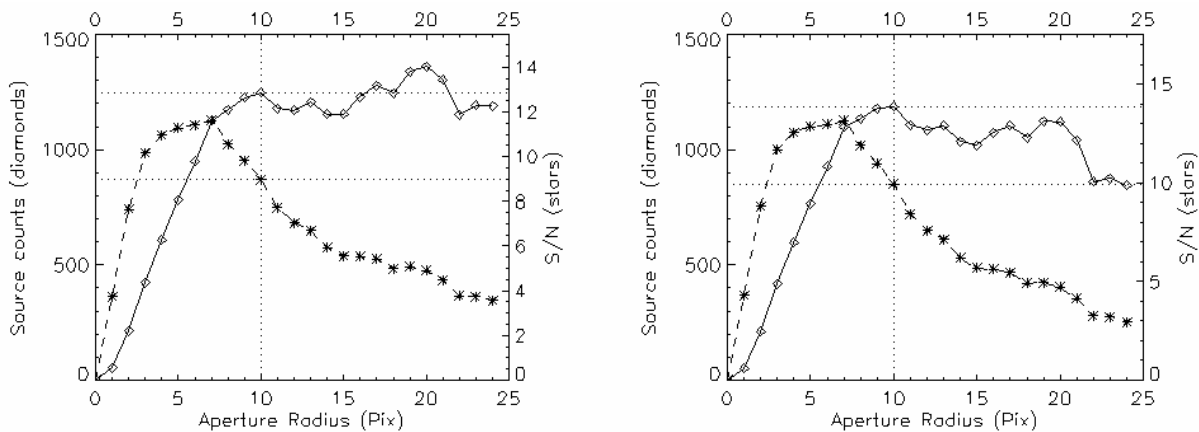


Fig. 3.5 Growth curves calculated for the one of the four chop-nod channels of a $11.7\mu\text{m}$ -image of the asteroid 2001 LF, observed on June 03, 2003 with TIMMI2 at the ESO 3.6 m telescope (image file name: 306030840.fits). On the left plot a background value of 0.497 counts yielded 1190 counts for the source in an aperture of 10 pixels of radius. On the right, a larger background value – i.e. 0.687 counts – subtracted over an increasing aperture radius causes the net flux of the source to decrease. Such background value yielded 844 counts for the source in an aperture of 10 pixel of radius.

For each source, we have selected the optimum background value by accurate adjusting the background level to make the growth curve flat at large aperture radii.

To derive the final monochromatic flux density of the target asteroids the following formula has been used:

$$F_{target}(\lambda) = F_{standard}(\lambda) \times \frac{T_{standard}}{T_{target}} \times \frac{S''_{target}}{S''_{standard}} \quad (3-10)$$

where $F_{target}(\lambda)$ is the unknown flux of the target, $F_{standard}(\lambda)$ is the absolute flux of the standard star within the filter band centered at λ , S'' 's are the background subtracted signal, in counts, measured within the photometric aperture. Eq (3-10) can be written in terms of the instrument sensitivity.

$$F_{target}(\lambda) = \frac{S''_{target}}{T_{target}} \times g(\lambda) \quad (3-11)$$

where $g(\lambda)$ is the instrument sensitivity in Jy/(counts/second).

3.7 Thermal infrared observations of NEAs: a method for accurate nod-set registering

The telescopes were tracked at the differential rate predicted from the ephemerides of each target. Nevertheless, some of the final co-added images suffered a smearing effect due to track errors or the non perfect repositioning of the telescope after each nod was performed.

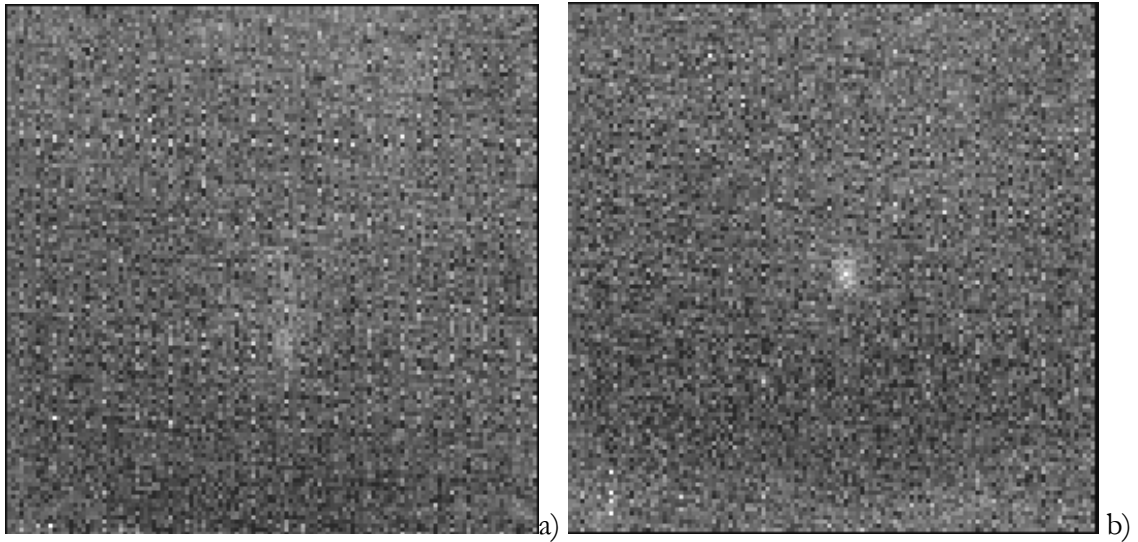


Fig. 3.6 On the right (a), strong smearing effect in the coadded LWS image of the asteroid 2002 CT₄₆ without registering. (b) the same dataset but registering of each nodeset before coadding was performed. The improvement in the S/N is clearly evident. Further, the registered PSF more similar to the standard stars PSFs resulting in an improved photometric accuracy.

Nod sets were shifted and registered before co-adding where necessary to avoid compromising photometric accuracy. Fig. 3.6 a) shows the coadded LWS image of the asteroid 2002 CT₄₆ observed on Feb. 21, 2003 without registering. Fig. 3.6 b) shows the same dataset after appropriate registering of each nod-set. The improvement in the S/N is clearly evident. Moreover, the shape of PSF of the resulting co-added registered image is more similar to the PSFs of the calibration standard stars, yielding to higher photometric accuracy of the derived final flux.

As in the case of Fig. 3.6 a), several asteroids were already visible in the original un-coadded frames. However, for the faintest ones, as in the case of 15817 Lucianotesi, 2000 EV₇₀ and 2001 HW₁₅ observed at Keck, the smearing effect was so strong to apparently compromise detection.

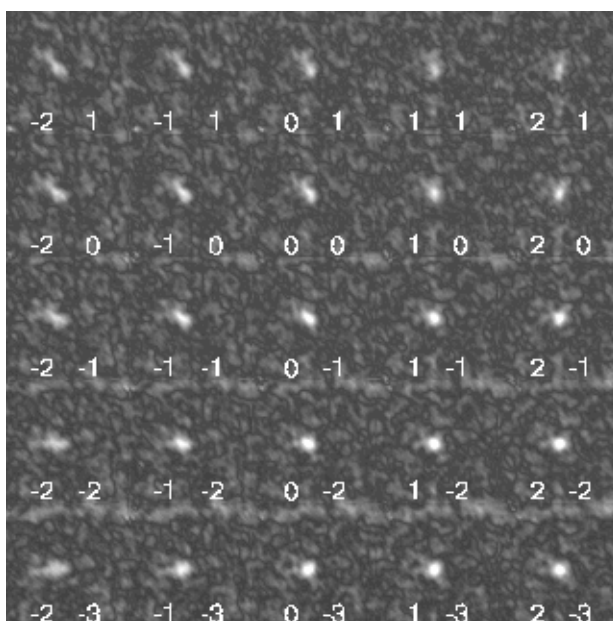


Fig. 3.7 The modulus of the cross correlation function between the instrumental PSF and frames registered with arbitrary shifts of the nod sets. Shown here is a 5×5 array of trials. The v_x and v_y values (see text) are indicated by the numbers at the bottom of each framelet.

A method for optimum registering of the nod sets was used in those cases. We have assumed that the largest contribution to the smearing effect was due to the non accurate tracking of the telescopes. In this hypothesis, the motion of the source from two successive nod-sets can be described by a vector (v_x, v_y) , where v_x , and v_y are the velocities of the source along the rows and the columns of the detector array. Under this assumption, the introduction of a shift to the i^{th} nod set of a quantity $-(v_x, v_y) \times (t_i - t_0)$, where t_i is the epoch at which the i^{th} nod-set was acquired, before coadding, allows the source to be properly registered. However, since the source is not visible on the unregistered frame, v_x and v_y are not known *a priori*. We have, therefore, registered nod sets with all possible combinations of velocities and

identified the optimal one with a cross-correlation of the registered image with the instrumental PSF obtained from the observation of a standard star. The best estimate for v_x and v_y is that set producing the registered frame with the highest value of the modulus of the cross correlation.

Fig. 3.7 shows a 5×5 array of the modulus of the cross correlation function between registered frames of the asteroid 2000 EV₇₀ and the instrumental PSF, derived from the observation of the standard star μ -UMa at 11.7 μm with LSW at Keck1. It is clearly visible that by registering nod sets with $v_x=1$ and $v_y=-2$ (the fourth framelet from the left and from the top) and it is possible to obtain the final frame with the highest cross correlation.

3.8 Color correction

If $T(\lambda)$ is the filter transmission function, the filter central wavelength may be defined by the following equation:

$$\lambda_c = \frac{\int_{-\infty}^{+\infty} T(\lambda) \lambda d\lambda}{\int_{-\infty}^{+\infty} T(\lambda) d\lambda} \quad (3-12)$$

The in-band flux of an astronomical source whose spectral energy distribution (SED) is described by the function $F(\lambda)$ is given by the following equation:

$$F(\lambda_c) = \frac{\int_{-\infty}^{+\infty} T(\lambda) F(\lambda) d\lambda}{\int_{-\infty}^{+\infty} T(\lambda) d\lambda} \quad (3-13)$$

Let us suppose an observation yielded $S''_{s \text{ tan dard}}$ counts and $S''_{t \text{ arg et}}$ counts in the unit time. We can write that:

$$\int_{-\infty}^{+\infty} T(\lambda) F_{s \text{ tan dard}}(\lambda) d\lambda \frac{S''_{t \text{ arg et}}}{S''_{s \text{ tan dard}}} = \int_{-\infty}^{+\infty} T(\lambda) F_{t \text{ arg et}}(\lambda) d\lambda \quad (3-14)$$

where $F_{s \text{ tan dard}}(\lambda)$ and $F_{t \text{ arg et}}(\lambda)$ are the SED of the standard star and the unknown SED of the target asteroid respectively.

Assuming $F_{t \text{ arg et}}(\lambda) = F_{t \text{ arg et}}(\lambda_c)$ to be constant within the filter bandwidth, Eq (3-14) may be simplified to

$$F_{target}(\lambda_c) = \frac{S''_{target}}{S''_{standard}} \times \int_{-\infty}^{+\infty} T(\lambda) F_{standard}(\lambda) d\lambda \bigg/ \int_{-\infty}^{+\infty} T(\lambda) d\lambda \quad (3-15)$$

where the second factor on the right-hand side of Eq (3-15) is the in-band flux of the standard star. However, the SED of the asteroid is not constant within the filter bandwidth and the use of Eq (3-15) yields to an error which has to be taken into account.

Without a loss of generality, we can assume the SED of the target to be described by a black-body at a given temperature multiplied by a scaling factor: i.e. $F_{target}(\lambda) = \Omega B(\lambda, T)$. The true value of the flux is therefore $\Omega B(\lambda_c, T)$ which can be written in terms of $F_{target}(\lambda_c)$ multiplied by a factor called color correction i.e.

$$\Omega B(\lambda_c, T) = F_{target}(\lambda_c) \times C_c \quad (3-16)$$

By equating the two in-band fluxes:

$$F_{target}(\lambda_c) \int_{-\infty}^{+\infty} T(\lambda) d\lambda = \Omega \int_{-\infty}^{+\infty} T(\lambda) B(\lambda, T) d\lambda \quad (3-17)$$

we can solve for Ω . Once Ω is inserted back into Eq (3-16), a solution for C_c can be found. This solution does not depend on $F_{target}(\lambda_c)$ and is a function of the black-body temperature and the filter transmission curve only:

$$C_c = B(\lambda_c, T) \int_{-\infty}^{+\infty} T(\lambda) d\lambda \bigg/ \int_{-\infty}^{+\infty} T(\lambda) B(\lambda, T) d\lambda \quad (3-18)$$

Given the transmission profiles of the filters we have used at the LWS, TIMMI2, MIRLIN and MIRSI, Eq (3-18) can be used to calculate color correction factor for each filter as a function of the color temperature of the observed asteroids. Such color corrections are given in Appendix B.

3.9 Thermal IR spectroscopy at the TIMMI2

An N-band spectrum of the NEA 5587 was obtained at the ESO 3.6m telescope with the TIMMI2 on April 9, 2001. Since the target asteroid was bright enough, the differential tracking of the telescope was turned off and the autoguider was used to accurately track the proper motion of the small body keeping the source within the 3-arcsec-wide slit of the spectrograph. The low resolution grism was used to disperse the 7-13 μm spectrum on the detector array (see Fig. 3.8).

The standard star HD123139 was observed at within 0.2 airmasses of the NEA 5587. The beam-switching observing mode was used (see Fig. 3.3). The field was chopped with a 10'' amplitude along the spectrograph slit. Nodding was performed by moving the telescope the opposite direction resulting in final co-added images where two positive spectra were superimposed approximately at the central row of the detector array and two negative spectra above and below the central channel (see Fig. 3.8). The data reduction has been carried out using IDL.

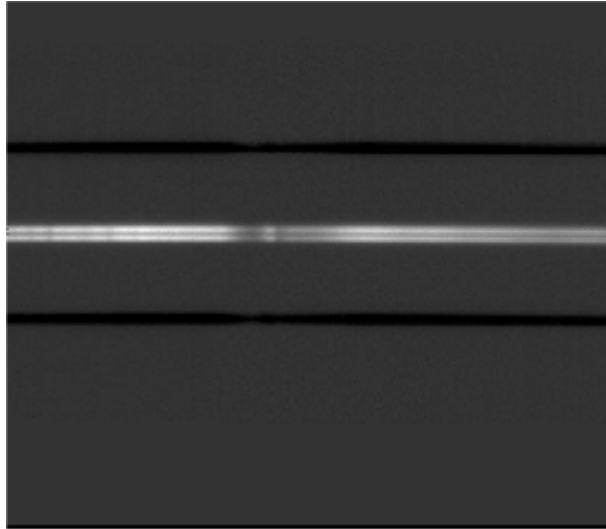


Fig. 3.8 Raw image of the N-band spectrum of the standard star HD123139 observed with the ESO 3.6m telescope and TIMMI2

The two negative spectra and the positive one were extracted separately and finally co-added. For each column, extraction of the raw spectra was accomplished by summing up the pixel values within a linear aperture 6 pixel wide centered on the signal and dividing the sum by the number of pixel of the aperture. The background value, to be subtracted on column basis, was defined as the median value of the pixels contained in two windows above and below the spectrum. Amplitudes and positions of the signal and background windows were defined by looking the one-dimensional spectral profile obtained by summing up the pixel values along each row of the infrared frames (see Fig. 3.9) i.e.

$$S''_{profile}(y) = \sum_x C''(x, y). \quad (3-19)$$

The signal-to-noise ratio of the raw spectra was derived assuming the background limited regime i.e. by using Eq (3-9).

Wavelength calibration in the N-band was performed by matching the atmospheric ozone absorption feature at about 9.5 μm on the spectrum of the bright standard HD123139. The calibration

function was found to be well represented by a linear expression i.e. $\lambda = 0.0114x + 8.0709$ where λ is the wavelength in μm and x the column coordinate on the detector array.

The absolute calibrated medium infrared spectrum of the target asteroid was obtained by taking the ratio of the raw spectrum of the target divided by the raw spectrum of the standard star multiplied by the spectral energy distribution (SED) of the latter. Of course resampling of the SED template of the standard star on those wavelengths corresponding to the detector columns was necessary.

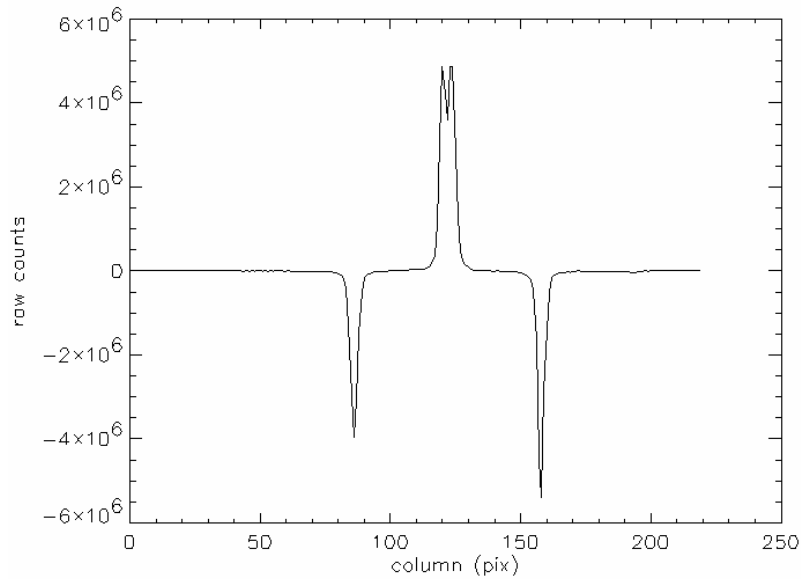


Fig. 3.9 The one-dimensional profile of the spectrum $S''_{profile}(x)$. It was obtained by summing up the contribution of all pixels along each row.

However, the low original S/N of the spectrum of the NEA 5587 would have produced poor quality results, if the raw spectra were not binned before the absolute calibration performed. A binning mask was therefore constructed and spectral regions of low signal to noise ratio (e.g. the ozone absorption feature at $9.5 \mu\text{m}$) cutted off. The signal at each bin was computed by taking the mean of the raw values of the spectrum within each bin weighted by their signal-to-noise ratio. The wavelength of the center of the bin was used as the reference wavelength for the final data set. The final derived fluxes of the NEA 5587 and their uncertainties are listed in appendix A.

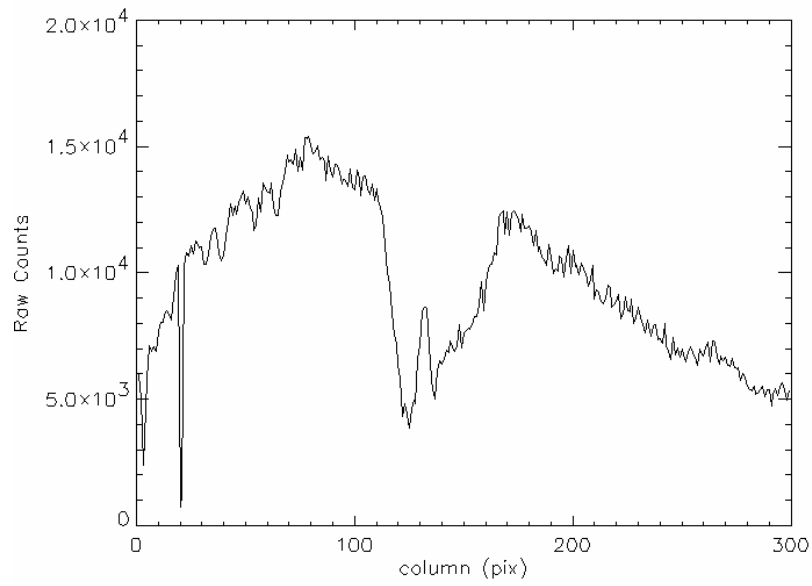


Fig. 3.10 Raw extracted spectrum of the standard star HD123139. Note the characteristic ozone feature between pixels 110-190

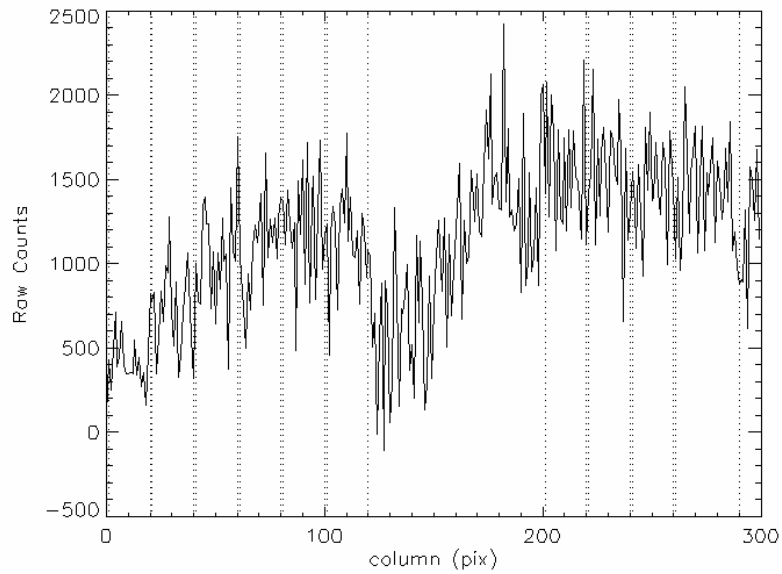


Fig. 3.11 N-band raw spectrum of the NEA 5587. Dotted vertical lines are drawn in correspondence to the bin extremes. The binning intervals were taken at the following detector columns (1 20), (21 40), (41 60), (61 80), (81 100), (101 120), (201 220), (221 240), (241 260), (261 290).

3.10 Visible CCD observations at ESO: data reduction

Visible CCD observations in the Johnson V filter, obtained with the DFOSC at the Danish 1.5 m telescope and with the WFI at the ESO/MPI 2.2 m telescope, were calibrated using the standard CCD data reduction scheme.

The digital to analog (D/A) converter of the CCD, introduces an offset to avoid negative digital numbers. In order to quantify and remove this offset from single CCD exposures a number of bias frames were obtained during the night. If the bias level was found to be constant or nearly constant during the night, an average bias frame (the so-called master bias) was calculated taking the median value of the biases for each pixel.

CCDs are affected by a pixel to pixel variation of the sensitivity. To obtain a map of the sensitivity, flat-field images are obtained for each set up used during the observation. A flat-field frame is obtained by imaging a homogeneously illuminated surface such as a screen in the dome or the sky at dusk or at dawn. A master flat is calculated by taking the median value for each pixel from a series of normalized flat fields.

Each raw CCD exposure $R(x,y)$ was calibrated using Eq. 3-21

$$I(x, y) = \frac{R(x, y) - B(x, y)}{F(x, y) - B(x, y)} \times K \quad (3-20)$$

where $I(x,y)$ is the final image, $B(x,y)$ is the master bias, $F(x,y)$ the master flat and K is a multiplicative factor equal to the mean level of the master flat.

Using the ATV package, aperture photometry was performed on each CCD image to derive raw counts for the target asteroids and a number of reference stars. The basic formula to calculate the differential magnitude between object i and j is then $\Delta m_{ij} = -2.5 \log_{10}(f_i / f_j)$, where the f values are the number of raw counts measured for each source.

Usually, when doing differential CCD photometry, it is common to consider the field covered by the CCD to be small compared to the variations in extinction over the sky. The airmass is thus the same for the asteroid of interest and the reference stars contained within the same CCD image. In the case of fast-moving objects such as NEOs close to the Earth it is not, in general, possible to use the same reference stars throughout the whole night. Formally we get a set of short lightcurves, one for each reference star. The intuitive way to connect the set into a long lightcurve might be to calculate the differential magnitude between the reference stars in those frames where they overlap. The short curves

would then have to be shifted up or down in order to compensate for the magnitude differences among the reference stars.

We have used the method of Erikson et al. (2000) to properly connect the short light curves. This procedure is to first fit the stars into a magnitude system by a least-square method and then use this system to derive the full lightcurve of the asteroids.

By plotting the instrumental magnitudes of the comparison stars as function of the airmass, we have derived the atmospheric extinction coefficients. Observation of standard stars (Landolt's fields) throughout the night yielded absolute calibration of the magnitude scale and the derivation of $V(r, \Delta, \alpha)$ apparent magnitude of the target asteroids at the heliocentric distance r , geocentric distance Δ and phase angle α . Given $V(r, \Delta, \alpha)$ at lightcurve mean for each asteroid, the absolute magnitudes $H \equiv V(r=1, \Delta=1, \alpha=0^\circ)$, i.e. the magnitude that an asteroid would have at 1AU from the Sun and the Earth and at zero degree of phase angle, were calculated using the standard method described by Bowell et al. (1989), appendix A.

3.11 The data set

Table 3-1, lists relevant observational circumstances and physical data for the target asteroids observed at Keck. Note that Table 3-1 contains three more NEAs, with respect to the equivalent table of Delbò et al. (2003). These three objects, 15817 Lucianotesi, 2000 EV₇₀ and 2001 HW₁₅, were extremely faint. Telescope tracking inaccuracy smeared their weak signal on the final co-added image compromising detection. Only the use of a new method, described in Appendix B, allowed blind registering of the nod-sets and yields their detection in the thermal infrared images obtained at LWS.

Table 3-2 shows equivalent information for the asteroids observed at ESO and Table 3-3 for the observations carried out at the NASA-IRTF. The resulting fluxes are listed in appendix A.

The quoted uncertainties in the flux measurements refer to the statistical uncertainties in the synthetic aperture photometry procedure only. Errors in the absolute calibration and fluctuations in atmospheric conditions during the observations increase the scatter in the flux data.

3.11.1 Near-Earth asteroids observed at KECK

Object	H (mag)	Date	α°	R (AU)	Δ (AU)	Lightcurve		Notes
						Per. (h)	amp. (mag)	
1627 Ivar	12.87±0.1	00-03-16	5	2.057	1.073	4.795	0.35	a
1866 Sisyphus	13.00	00-03-17	16	2.903	2.194	2.400	0.11	b
2100 Ra-Shalom	16.11±0.1	00-08-21	39	1.175	0.222	19.79	0.40	a, f
4034 1986 PA	18.2	01-05-11	40	1.219	0.299	-	-	
4055 Magellan	14.90±0.1	00-03-16	13	2.058	1.122	7.475	0.46	a
4660 Nereus	18.7	02-02-21	60	1.033	0.093	15.1	0.6	
5587 1990 SB	14.1±0.5	01-05-10	42	1.213	0.301	5.052	1.1	a
5604 1992 FE	17.72±0.1	01-05-11	36	1.301	0.392	-	-	c
5751 Zao	14.93±0.07	01-05-12	49	1.250	1.180	21.7	0.12	d
14402 1991 DB	18.85±0.1	00-03-16	36	1.076	0.103	2.266	~0.1	a
15817 Lucianotesi	18.6	00-03-17	14	1.275	0.291	11.0	0.8	
16834 1997 WU ₂₂	15.9±0.5	00-08-21	59	1.142	0.331	9.348	0.4	a, f
19356 1997 GH ₃	17.0	01-05-11	5	1.421	0.413	6.714	0.74	
25330 1999 KV ₄	16.3	01-05-10	54	1.201	0.425	-	~0.1	
1999 FK ₂₁	18.0	02-02-21	35	1.142	0.195	-	-	
1999 NC ₄₃	16.1±0.5	00-03-17	59	1.130	0.366	34.5/122.3?	1.1	a
2000 BG ₁₉	17.8	00-03-17	17	1.396	0.429	-	-	
2000 EV ₇₀	20.3	00-03-17	14	1.119	0.128			
2000 PG ₃	15.74	00-08-21	2	2.118	1.108	-	≤ 0.2	f
2001 FY	18.8	01-05-12	22	1.269	0.285	-	-	
2001 HW ₁₅	20.2	01-05-12	11	1.152	0.145	-	-	
2002 BM ₂₆	20.1	02-02-21	60	1.024	0.074	~ 2.7	-	e
2002 CT ₄₆	20.8	02-02-21	23	1.107	0.129	-	-	

Table 3-1 Observational circumstances and relevant data for the Keck targets. Where no other source is given, H-values are from the web services given in section 2.8.3.

- a. Lightcurve data and mean H derived from photometry made during the apparition of the Keck thermal observations by Pravec and colleagues. In the cases of (5587), (16834), and 1999 NC43 only rough H-values could be estimated due to the high phase angle of the observations.
- b. Lightcurve data from A.W. Harris. (cfa-www.harvard.edu/iau/lists/LightcurveDat.html).
- c. H-value and lightcurve data from from observations carried out at ESO, La Silla (see section 4.3.11)
- d. Lightcurve data and mean H taken from Pravec et al. (1997). The H-value should also be valid for the 2001 apparition to an accuracy of ~ 0.1 mag as the asteroid showed little aspect-related variation in earlier apparitions.
- e. Rotational period of ~ 2.7 h from Nolan et al. (2002).
- f. Observations were carried out under poor observing conditions

3.11.2 Near-Earth asteroids observed at ESO

Object	H (mag)	Date yymmdd	α°	R (AU)	Δ (AU)	Lightcurve		Notes
						Per. (h)	amp. (mag)	
5381 Sekmeth	16.5	03-06-02	44	1.176	0.247	0.35	~0.35	g
2001 LF	17.4	03-06-02	45	1.173	0.244			h
		03-06-03	45	1.173	0.244			
2002 AV ₄	15.8	03-06-01	70	1.071	0.266			
37314 (2001 QP)	14.6	01-12-04	38	1.416	0.568			
12008		01-04-09	36	1.033	1.639			
33342(1998 WT ₂₄)	18.54±0.1	01-12-04	60	1.015	0.062	3.72336	~0.2	i
5587 1990 SB	14.1±0.5	01-04-08	20	1.412	0.448	5.052	1.1	k
		01-04-09	19	1.405	0.439			j, k
5604 1992 FE	17.72±0.1	01-05-11	36	1.301	0.392	-	-	c
25143 Itokawa	19.48	01-04-08	108	0.983	0.054			l
		01-04-09	110	0.981	0.056			
35396 (1997 XF ₁₁)	17.1±0.1	02-11-28	30	1.218	0.279	3.25	~0.7	
2002 QE ₁₅	16.3	02-11-28	50	1.132	0.261			
19356 1997 GH ₃	17.0	01-04-08	32	1.209	0.256	6.714	0.74	k
		01-04-09	31	1.215	0.259			
25330 (1999 KV ₄)	16.3	03-06-02	16	1.497	0.513	4.919	0.15	k

Table 3-2 Observational circumstances and relevant data for the targets observed at ESO. Where no other source is given, H-values are from the web services given in section 2.8.3.

- g. Lightcurve data from ESO but H-values are from the web services give in section 2.8.3
- h. H-value from Dandy et al. (2003)
- i. H-value, derived assuming $G=0.40$ (E type), and lightcurve data from from observations carried out at ESO, La Silla (see section 04.3.13)
- j. Data obtained from thermal infrared spectroscopy in the N and Q band.
- k. Lightcurve data and mean H derived from photometry made during the apparition of the ESO thermal observations by Pravec and colleagues.
- l. H value from Abe et al., 2002.

3.11.3 Near-Earth asteroids observed at the NASA-IRTF

Object	H (mag)	Date yymmdd	α°	R (AU)	Δ (AU)	Lightcurve		Notes
						Per. (h)	amp. (mag)	
33342(1998 WT ₂₄)	18.54±0.1 E	01-12-18	67	0.990	0.016			m
		01-12-19	79	0.987	0.020			m
		01-12-21	93	0.982	0.028			m
1580 Betulia	14.0	02-06-02	53	1.143	0.246			
25330 (1997 KV ₄)	16.3	03-05-14	03	1.396	0.386	-	~0.1	
5381 Sekmeth	16.5	03-05-12	42	1.114	0.146	0.35	~0.35	n
		03-05-13	38	1.117	0.140			n
		03-05-14	33	1.121	0.135			n
		03-05-15	29	1.124	0.132			n
		03-05-16	24	1.128	0.129			n,o
6489 Golevka	19.07±0.03	03-05-15	43	1.081	0.099			p
35396 (1997 XF ₁₁)	17.1±0.1 E	02-11-03	63	1.022	0.070	3.25	~1.0	q
	17.1±0.1 E	02-11-05	53	1.038	0.080	3.25	~1.0	q

Table 3-3 Observational circumstances and relevant data for the targets observed at the NASA-IRTF. Where no other source is given, H-values are from the web services given in section 2.8.3. Observations of the NEA 35396 (1997 XF₁₁) were carried out with MIRSII. All other objects have been observed using MIRLIN

- m. H-value, derived assuming $G=0.40$ (E type), and lightcurve data from from observations carried out at ESO, La Silla (see section 04.3.13)
- n. Lightcurve data from ESO but H-values are from the web services give in section 2.8.3
- o. Presence of cirrus was noted
- p. H value from Mottola et al. (1997)
- q. H-value and lightcurve data from from observations carried out at ESO, La Silla (see section 4.3.14)

3.12 Summary

Thermal infrared observations (5-20 μm) were collected primarily using the LWS installed at the Keck 1 telescope, Mauna Kea, Hawaii. A related project, started in April 2001, was awarded 10 nights at the ESO, La Silla (Chile). The TIMMI2 at the 3.6 m telescope was used to perform thermal infrared observations while the 1.5 m Danish and the 2.2 m ESO/MPI telescopes were used to obtain simultaneous V magnitudes. The NASA-IRTF has also been used with the aim of performing detailed study of selected targets.

Overall, 32 asteroids were observed. For 7 of them observations were collected under different geometries and with different instruments. Fig. 3.12 shows histograms of the number of observations as a function of the absolute magnitude, H, of the target asteroids and the as a function of the solar phase angle. From these plots it is evident that our program gathered radiometric observations mainly of the sub-kilometer population of Earth crossing asteroids. Furthermore, the large range of solar phase angles spanned by our observation allows detailed study of the thermal properties of the targets and a refinement of the thermal models to be performed.

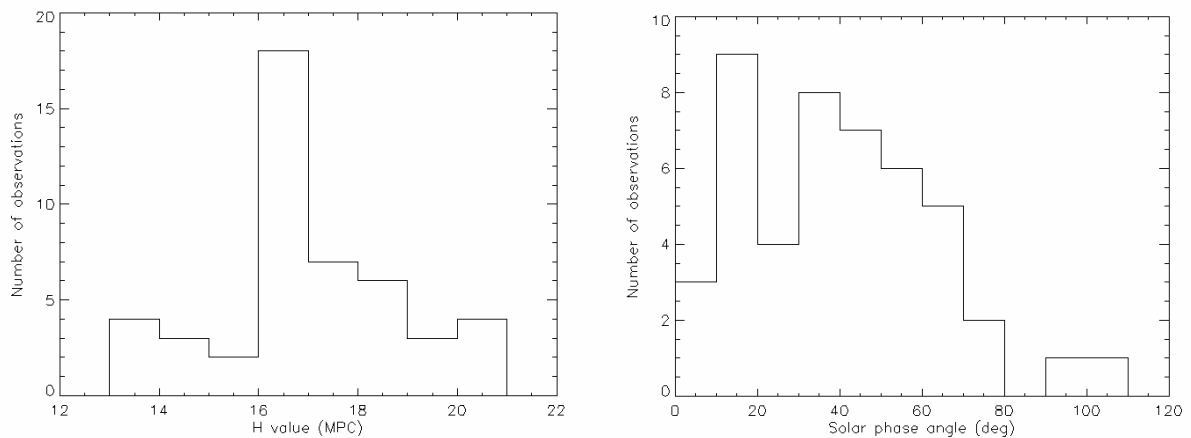


Fig. 3.12 Histogram of the number of observations as a function of the absolute magnitude H of the target asteroids and the as a function of the solar phase angle. H values for each object are obtained from the MPC. 7 objects out of 32 were observed with different instrument and under different observing geometries.

Thermal infrared ground based observations are limited to the M ($\sim 5 \mu\text{m}$), the N (between ~ 8 and $13 \mu\text{m}$) and the Q (\sim between 17.5 and $22 \mu\text{m}$). On the basis of the experience gained during this work typical measurements accuracy are of the order of 10-15% in the M and Q band and about 5% in the N

band. For 17 targets, which were found to be very weak, observations were obtained with N-band filters only.

To subtract the strong contribution of the background, observations were carried out using the chopping-nodding technique.

Differential tracking was used to minimize the effect of the large proper motion of the target asteroids. Nevertheless, in some cases registering nod-sets before coadding was necessary to avoid smearing effects.

A new method, discussed in Appendix B, have been used to search for and identify in apparently void LWS images three more asteroids observed at Keck.

Aperture photometry was performed to calculate the signal of the infrared sources. Cohen et al. (1999) standard stars were used for absolute flux calibration and they were imaged within 0.1 – 0.2 airmasses of the targets asteroids.

Color corrections were evaluated and found to be only a few percent for the filters used to carry out our multi-wavelengths observations. Color corrections were thus not applied to correct the final monochromatic flux densities derived and listed in Appendix A.

Thermal model fits to thermal infrared data and derivation of albedos and diameters

4.1 Foreword

In order to derive sizes and albedos of the NEAs, the STM, the FRM and the NEATM were fitted to the measured infrared fluxes. Thermal-model fitting and results of the observations carried out at Keck are discussed by Delbó et al. (2003). However, three more NEAs for which apparently we had no detection, could have been detected in LWS frames by accurate registration of the nod-sets. In this chapter, we comment mainly on the derivation of diameters and albedos from the thermal infrared observations obtained at the ESO and at the NASA-IRTF. A summary of radiometric results is presented at the end of this chapter.

4.2 Introduction

In order to derive sizes (in terms of effective diameter, i.e. the diameter of the sphere of equivalent projected area) and geometric albedos p_v , the STM the FRM and the NEATM were fitted to the measured infrared fluxes. For more detailed discussions of the three thermal models see Chapter 2 of this work. An assessment of the modeling error is usually very difficult. Application of the three thermal models gives idea of the modeling uncertainties involved. However, on the basis of the analysis of the radiometrically derived diameters and albedo from this set of observations and with the help of the thermophysical model developed in Chapter 6, we have estimated, in section 6.9, the modeling uncertainties inherent in the use of the STM and the NEATM.

In a number of cases in which the data are of poor quality, or observations were made over a small wavelength range, the NEATM fits and the resulting η -values are not well constrained. In these cases default values of η were used. Harris (1998) has shown that a value of 1.2 produces NEA diameters in good agreement with radar results and albedos consistent with the values inferred from NEAs taxonomic classification. However, one of the results of this study, Chapter 5, is the identification of a trend of the dependence of the NEATM best-fit parameter η with the phase angle. The best linear fit to the observed distribution of NEAs η -values is: $\eta=(0.011\pm 0.002)\alpha+(0.90\pm 0.07)$, where α is the phase angle. This linear dependence can be used as the best estimate for the default η -value. However, given the accuracy of the fit, diameters and albedos in significant agreement are obtained if default η -values of 1.0 for $\alpha < 45^\circ$ and of 1.5 for $\alpha \geq 45^\circ$ where α indicates, as usual, the phase angle.

4.2.1 Diameters, albedos and η -values derived from observations at Keck

Object	D_{eff} (km)				p_v			Tax Class	Notes
	STM	NEATM	η	FRM	STM	NEATM	FRM		
1627 Ivar	7.94	9.12	(1.0)	15.9	0.20	0.15	0.050	S	Lc corrected
1866 Sisyphus	7.47	8.48	(1.0)	16.3	0.20	0.15	0.042	S	Lc amp. small
2100 Ra-Shalom	1.60	2.79	2.32	2.60	0.25	0.083	0.095	Xc	Lc corrected
4034 1986 PA	0.40	0.42	(1.0)	0.57	0.58	0.52	0.29	O	
4055 Magellan	2.20	2.49	(1.0)	4.36	0.39	0.31	0.10	V	
4660 Nereus	0.26	0.33	(1.5)	0.33	0.86	0.55	0.54	Xe→E	
5587 1990 SB	3.56	3.57	0.84	5.14	0.51	0.50	0.24	Sq	Lc corrected
5604 1992 FE	0.52	0.55	(1.0)	0.77	0.69	0.61	0.32	V	
5751 Zao	1.80	2.30	(1.5)	2.53	0.58	0.36	0.29	X→E	Lc amp. small
14402 1991 DB	0.56	0.60	1.04	0.81	0.17	0.14	0.08	C	Lc amp. small
15817 Lucianotesi	0.30	0.32	(1.0)	0.47	0.73	0.64	0.29	X→E	
16834 1997 WU ₂₂	1.51	2.00	(1.5)	2.06	0.53	0.30	0.29	S	
19356 1997 GH ₃	0.83	0.91	0.98	1.45	0.41	0.34	0.13	S	
25330 1999 KV ₄	2.34	3.21	1.50	3.41	0.098	0.052	0.046	B	Lc amp. small
1999 FK ₂₁	0.58	0.59	0.91	0.85	0.33	0.32	0.15	S	
1999 NC ₄₃	1.22	2.22	2.86	1.62	0.47	0.14	0.27	Q	Lc corrected
2000 BG ₁₉	1.88	1.77	0.74	3.25	0.038	0.043	0.013	X→P	
2000 PG ₃	3.90	4.60	(1.0)	8.59	0.059	0.042	0.012	D	Lc amp. small
2000 EV ₇₀	0.14	0.15	(1.0)	0.22	0.68	0.60	0.29	Q	
2001 FY	0.30	0.32	(1.0)	0.48	0.59	0.52	0.23	S	
2001 HW ₁₅	0.16	0.18	(1.0)	0.27	0.54	0.43	0.20	?	
2002 BM ₂₆	0.41	0.84	3.10	0.57	0.094	0.023	0.050	X→P	
2002 CT ₄₆	0.15	0.16	(1.0)	0.24	0.36	0.32	0.15	Sr	

Table 4-1 Diameters and albedos from thermal model fits to infrared observations obtained at Keck. NEATM's diameters and albedos are given in boldface. On the basis of results of this work, Chapter 5 and Chapter 6, we take those values as our best estimate for NEAs diameters and albedos. The estimated overall uncertainties in the NEATM values of diameter and albedo are 10 and 20%, respectively for observations carried out at phase angles smaller than 40° . At larger phase angles such error increase for increasing η -values. For $1 < \eta < 1.5$ NEATM albedo uncertainty is about 40%. For phase angles larger than 40° and η -values larger than 1.5 NEATM albedos are likely to be underestimated by about 35% and they uncertainties of about 40% (see Chapter 6). D_{eff} is the diameter of a sphere presenting the same projected area to the observer. Values of η in brackets are phase-angle dependent default values chosen on the basis of the results of this study. Taxonomic classes are from Bus and Binzel (2002), Binzel et al. (2002) and the results of Binzel et al. (2004), with the exceptions of (4055) Magellan (Cruikshank et al., 1991).

For convenience diameters, albedos and η -values derived from observations obtained at Keck are reported here in Table 4-1. Note that Table 4-1 contains derived physical parameters for three more objects, 15817 Lucianotesi, 2000 EV₇₀ and 2001 HW₁₅, which were not included in Delbò et al., (2003) work. Their detection in LWS co-added frames was made possible by an accurate method of registering nod-sets – described in section 3.7 – developed in this work. Table 4-2 lists novel results obtained from ESO observations, whereas Table 4-3 shows diameters, albedos and η -values obtained from the radiometric observations carried out at the NASA-IRTF.

4.2.2 Diameters, albedos and η -values derived from observations at ESO

Object	D _{eff} (km)				p _v			Tax Class	Notes
	STM	NEATM	η	FRM	STM	NEATM	FRM		
5381 Sekhmet	1.05	1.3	(1.5)	1.5	0.4	0.25	0.2	S	
		1.5	1.9			0.22			
5587(1990 SB) ¹⁵	3.4	4.0	1.1	6.7	0.35	0.25	0.09	Sq	LC corr
	3.5	3.74	(1.0)	5.78	0.34	0.29	0.12		N-Spec
									LC corr
5604(1992 FE)	0.7	0.7	(1.0)	1.1	0.3	0.3	0.12	V	N-Filters
12008	3.55	3.76	(1.0)	5.35	0.81	0.72	0.36	-	p _v error~40%
19356(1997GH ₃)	0.95	1.0	(1.0)	1.4	0.3	0.29	0.14	S	Large scatter
25143 Itokawa	0.20	0.37	(1.5)	0.22	0.61	0.19	0.54	S	ESO08apr01
		0.33	1.2			0.23			
33342(1998 WT ₂₄)	0.28	0.37	(1.5)	0.38	0.84	0.50	0.48	E	Dec 04, 2001
35396(1997 XF ₁₁)	0.75	0.80	(1.0)	1.16	0.45	0.40	0.19	Xk→E	H: this work
		0.89	1.3			0.32			LC corr.
25330 (1999 KV ₄)	2.26	2.5	(1.0)	4.16	0.1	0.09	0.03	B	LC ampl. small
		2.7	1.2			0.08			
2001 LF (3Jun03)	1.5	2.0	1.4	2.5	0.08	0.05	0.03	C	N + Q Jun,3
		2.1	(1.5)			0.04			
2001 LF (2Jun03)	1.7	1.9	(1.5)	2.2	0.1	0.06	0.04	C	N band only
		1.67	1.1			0.07			
2001QP	3.7	4.0	(1.0)	6.0	0.22	0.19	0.08	-	
2002 AV ₄	1.1	1.5	(1.5)	1.4	0.73	0.38	0.43	-	
		1.54	1.57			0.37			
2002 QE ₁₅	1.15	1.49	(1.5)	1.63	0.40	0.24	0.20	-	

Table 4-2 Diameters and Albedos from Thermal Model Fits of ESO targets. See Table 4-1 caption for further details. Taxonomic classes are from Bus and Binzel (2002), Binzel et al. (2002) and the results of Binzel et al. (2004) with the exception of 2001 LF which is from Dandy et al., 2003; 1998 WT24 which is from Kiselev et al., (2002) and 5381 Sekmeth which is from Nolan et al., (2003)

¹⁵ Mean of the two N-band spectra.

It is worth to stress again that our data set contains asteroids which have been observed with different instruments and under different observing geometries.

Comments on the derivation of albedo and diameters for each individual object are given in section 4.3. Extensive comments on the target observed at Keck are given in Delbò et al., (2003).

4.2.3 Diameters, albedos and η -values derived from observations made at the NASA-IRTF

Object	D_{eff} (km)				p_v			Tax Class	Notes
	STM	NEATM	η	FRM	STM	NEATM	FRM		
1580 Betulia	3.54	4.35	1.27	5.06	0.17	0.11	0.08	C	
6489 Golevka	0.30	0.33	(1.0)	0.47	0.46	0.39	0.18	Q	
5381 Sekmeth	-	1.3	1.5	-	-	0.25	-	S	$\alpha=25$
5381 Sekmeth	1.0	1.4	1.7	1.62	0.42	0.24	0.17	S	$\alpha=29$
5381 Sekmeth	-	1.2	1.3	-	-	0.3	-	S	$\alpha=33$
5381 Sekmeth	1.0	1.4	1.8	1.55	0.45	0.24	0.18	S	$\alpha=38$
5381 Sekmeth	-	1.4	1.9	-	-	0.22	-	S	$\alpha=42$
25330 1999 KV ₄		2.55	1.06			0.084		B	
35396 (1997 XF ₁₁)	0.81	0.91	1.2	1.07	0.39	0.31	0.22	Xk→E	05nov02 H from ESO
	0.83	1.18	1.8	1.05	0.37	0.18	0.23	Xk→E	03nov02 H from ESO
33342(1998 WT ₂₄)	0.32	0.34	0.9	0.40	0.68	0.59	0.43	E	18dec01 no LCC
	0.32	0.44	1.5	0.38	0.66	0.35	0.48	E	19dec01 no LCC
	0.31	0.50	1.85	0.36	0.70	0.27	0.53	E	21dec01 no LCC

Table 4-3 Diameters and Albedos from Thermal Model Fits of IRTF targets. See Table 4-1 caption for further details. Taxonomic classes are from Bus and Binzel (2002), Binzel et al. (2002) and the results of Binzel et al. (2004) with the exception of 2001 LF which is from Dandy et al., 2003; 1998 WT₂₄ which is from Kiselev et al., (2002) and 5381 Sekmeth which is from Nolan et al., (2003)

4.3 Comments on individual asteroids

The results listed in Table 4-1, Table 4-2 and Table 4-3 should be analyzed by taking into account the following notes on individual objects. We note that for several objects, the measured albedo is a decisive parameter for determining a unique taxonomic class. In the taxonomic system of Tholen (1984) and Bus (1999), objects having neutral spectra within the X-complex typically display three categories of albedos. The “X” designation for an object is resolved into the classes E, M, or P based on its having a high, moderate, or low albedo, respectively. For the objects originally tabulated by Bus and Binzel (2002) or Binzel et al. (in preparation) as belonging to the X-complex, we indicate our resolution of the spectral degeneracy from X to (→) E, M, or P.

4.3.1 15817 Lucianotesi (1994 QC)

No lightcurve data are available for the time of the Keck observations. The scatter of the flux values does not allow η to be adequately constrained; therefore the results given in Table 4-1 for the NEATM were obtained assuming a default value for η of 1.0 (see Fig. 4.1).

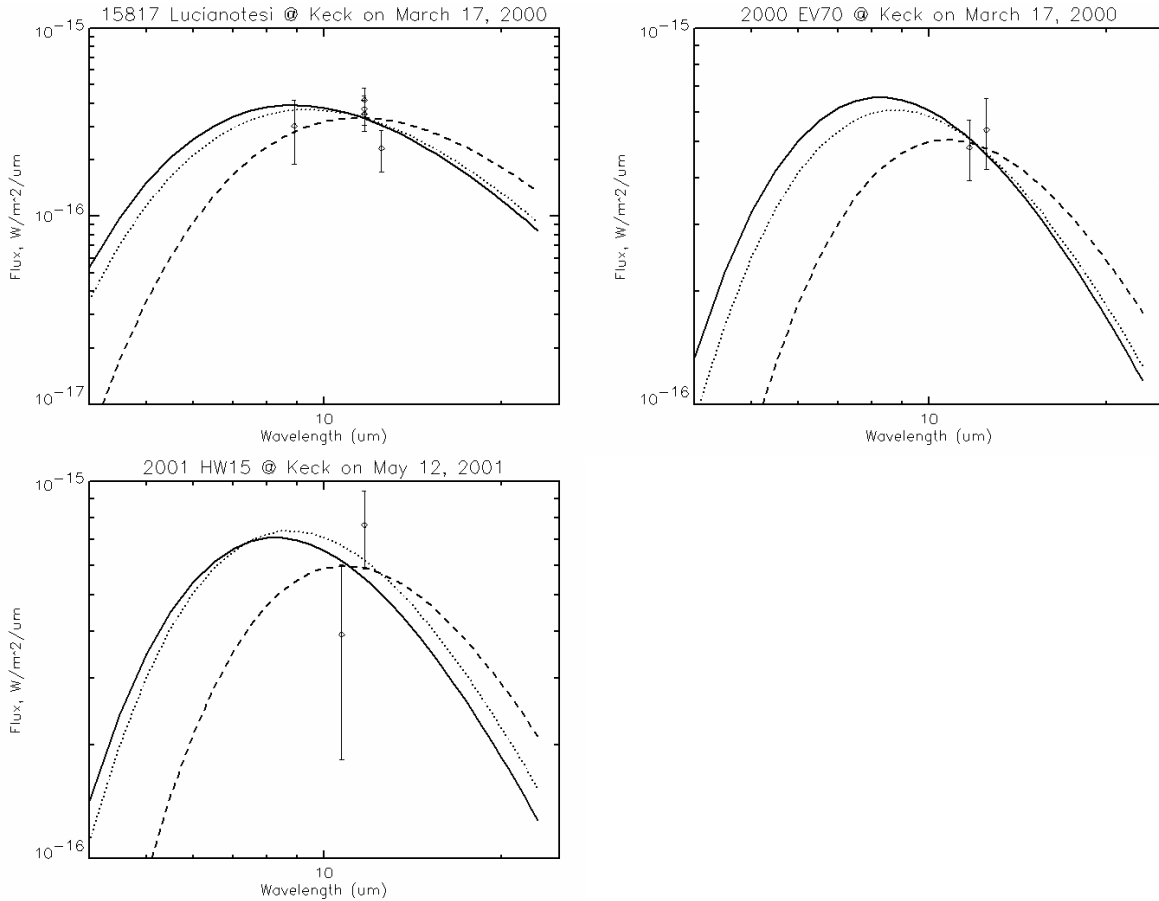


Fig. 4.1 Thermal model fits to observed infrared fluxes for 15817 Lucianotesi, 2000 EV₇₀ and 2001 HW₁₅ obtained at Keck and not included in Delbò et al. (2003) work. Continuous line: STM, dashed line: FRM; dotted line: NEATM with default η -value of 1.0

The results indicate a very high albedo (though its uncertainty from photometry is of ~ 0.1), which is consistent with refining the taxonomic type from X- to E-type. The identification of E type asteroids is important for our understating of dynamical transport mechanisms from the source region to the near-Earth space. E-type are, for instance, abundant amongst Hungaria asteroids.

4.3.2 2000 EV₇₀

Thermal infrared data, obtained in two filters only, do not allow η to be constrained adequately (see Fig. 4.1). I have resorted to the default value for η of 1.0 for the NEATM. The derived albedo is very high and it makes 2000 EV₇₀ the smallest object for which radiometric diameter has been measured. Note that the albedo uncertainty is very large, 0.13, given the low signal to noise ratio of the thermal infrared photometry. Moreover, no lightcurve data are available for the time of the Keck observations which makes the uncertainty of the radiometric results even larger.

4.3.3 2001 HW₁₅

The source was extremely weak in the 11.7 and in the 10.7 μm filters. The latter measurement is affected by a large uncertainty: about 50%. The resulting error on the albedo is therefore of the order of 0.2 (see Fig. 4.1). No lightcurve data are available and no estimation for the lightcurve amplitude, rotational period and taxonomic class are at present at disposal.

4.3.4 25143 Itokawa (formerly known as 1998 SF₃₆)

25143, recently named **Itokawa**, is the target of the successfully launched Japanese sample-return mission Hayabusa (Muses-C), which will rendezvous with this target in June 2005. V band CCD data were obtained simultaneously to the thermal infrared observations using the DFOSC installed at the 1.5m Danish telescope. Observations were carried out on April 8, 2001 between 09:27 UT and 10:14 UT and on April 9, 2001 between 09:17 and 10:14 UT. However, these two time intervals were long enough only to cover a small fraction of the asteroid lightcurve period. Nevertheless, using a simplified tri-axial ellipsoid model¹⁶ with the rotational period, pole and shape solution of Kaasalinen et al. (2003), I have generated a synthetic lightcurve which was fitted to the data. The best fit (see Fig. 4.2) was obtained with an absolute rotational phase $\varphi_0 = -32.5^\circ$ at JD=2452007.5.

On the basis of the synthetic lightcurve, note that thermal infrared observations were carried out near lightcurve maximum. Differential correction factors for each infrared observation were calculated, but the largest of these was found to be of 0.11 magnitudes i.e. less than 10% in flux. The synthetic lightcurve, based on the simple variation of the illuminated area projected along the observer direction, shows amplitude of 1.77 magnitudes. The aspect angle at the time of lightcurve maximum was 71.5° and

¹⁶ See A. Pospieszalska-Surdej & Surdej (1985) for details.

the sub-Earth longitude $\psi=320^\circ$. The aspect angle with respect to the Sun was 95.5° , the object was therefore almost equator on if seen from the Sun. The asteroid rotational phase with respect to the Sun ψ_{Sun} was equal to 24° at the time of lightcurve maximum which occurred at 10.3 UT on April 09, 2001. The H magnitude to be used as input parameter for the thermal model has to be corrected to take into account the geometry at the time of the thermal observation. Abe et al. (2002), derived $H = 19.9 \pm 0.10$ calculating the mean magnitude at 90 degrees of aspect angle.

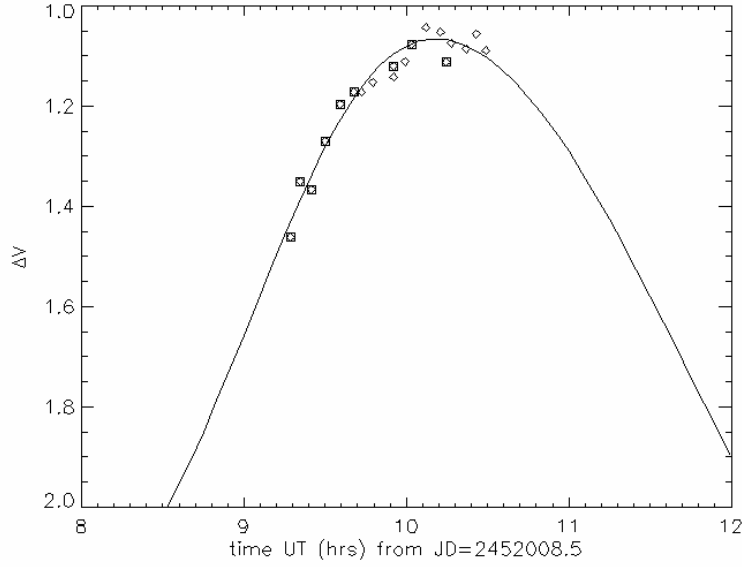


Fig. 4.2 Synthetic lightcurve of the asteroid 1998 SF36 and the best fit to the observed V-band data. Measurements obtained on 9 April, 2001 have got a square symbol superimposed. The two lightcurves were composited on the 12.13 hours sidereal period basis.

The illuminated portion of a triaxial ellipsoid can be easily obtained using the following expression adapted from A. Pospieszalska-Surdej & Surdej (1985):

$$S = \pi abc \sqrt{\sin^2 A_{Sun} \left(\frac{\sin^2 \psi_{Sun}}{a^2} + \frac{\cos^2 \psi_{Sun}}{b^2} \right) + \frac{\cos^2 A_{Sun}}{c^2}} \quad (4-1)$$

and the mean magnitude at $A_{Sun} = 90^\circ$ by taking -2.5 times the logarithm of $\langle S \rangle$ i.e.

$$\langle S \rangle = \frac{1}{\pi} \int_0^\pi S(\psi_{Sun}, A = 90^\circ) d\psi_{Sun} = \pi abc \sqrt{\sin^2 A_{Sun} \left(\frac{1}{2a^2} + \frac{1}{2b^2} \right) + \frac{\cos^2 A_{Sun}}{c^2}} \quad (4-2)$$

The correction to the H value is simply equal to $-2.5\log(S/\langle S \rangle)$. Inserting the numerical values into Eq. (4-2) and Eq. (4-1) I have derived the actual absolute magnitude H_{actual} at the time of thermal IR observations to be $H=19.7$.

The STM the FRM and the NEATM were fitted to the thermal IR data (see Fig. 4.3). The derived effective diameters and geometric albedos are reported in Table 4-2. Note the agreement of the NEATM's results with the published diameter and albedo by Sekiguchi et al. (2003). The NEATM best fit were obtained with $\eta = 1.2 \pm 1.0$, which is reasonably below the value suggested by Delbo et al. (2003) to be displayed by NEAs at such large phase angle. However, the fitted η value is not very well constrained: fluxes were obtained for a limited number of wavelengths in the N band (the object was not bright enough for fluxes in the 5 and 20 μm ranges to be obtained) and their errors of about 10%. The large error on the fitted η and therefore on our estimate of the actual color temperature makes the size and albedo determination not very reliable: $\sigma_D \approx 35\%$ and $\sigma_{p_v} \approx 50\%$. A more stable solution ($\sigma_D \approx 3\%$ and $\sigma_{p_v} \approx 5\%$.) can be found by fixing the η value to 1.5 on the basis of the Delbo et al. (2003) results.

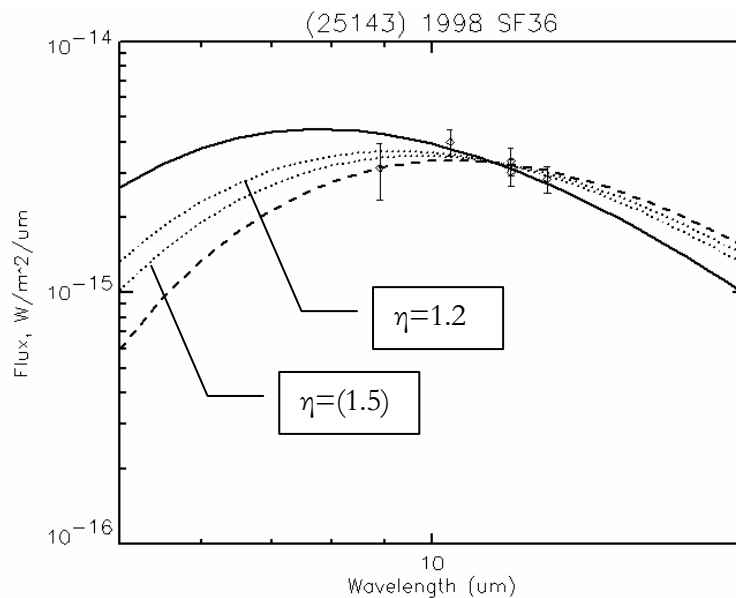


Fig. 4.3 Thermal models fit to the observed infrared flux for 25143 Itokawa. Continuous line: STM, dashed line: FRM; dotted line: NEATM with default η -value of 1.2 and 1.5

Thermal IR data obtained on April 09, 2001 are of poorer quality and have not been included in this analysis so far.

4.3.5 2001 LF

N and Q band data were obtained on June 03, 2004 at the 3.6 m telescope at ESO. P. Pravec and colleagues (Pravec, personal communication) got lightcurve data for this object from late June/early July 2003 from the Ondrejov observatory and the observatory of the University of Western Ontario. Although the solution is uncertain, 2001 LF appears to have a rotational period of about 10 hours with a lightcurve amplitude within 0.2 magnitudes. The object is classified as a C-type by Dandy et al (2003). The H value used as input parameter for thermal models has been obtained from Dandy's et al. work. The G value was assumed to be equal to 0.15 given the taxonomic type of this asteroid as suggested by Bowell et al. (1989). Given the not dramatically large lightcurve amplitude, no lightcurve correction was applied to the thermal infrared flux. Fig. 4.4 shows STM, FRM and NEATM fits to data points. NEATM gives a stable solution (i.e. $\sigma_D \approx 4\%$, $\sigma_{p_v} \approx 5\%$, $\sigma_\eta = 7\%$). The derived η -value of 1.4 ± 0.1 is in good agreement with the value expected on the basis of Delbo et al. (2003) results. The NEATM derived albedo of 0.05 is consistent with the C-type classification for this asteroid.

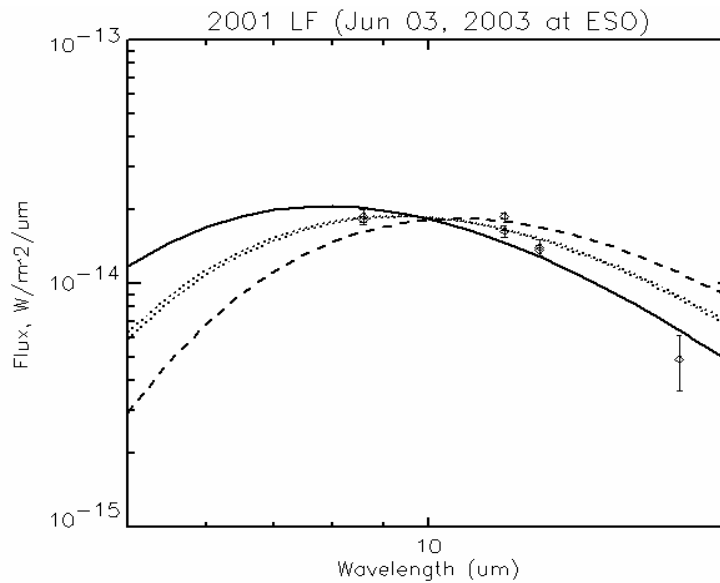


Fig. 4.4 Thermal models fit to the 2001 LF data observed on June 03, 2003. No correction for lightcurve was applied. Continuous line: STM, dashed line: FRM; dotted lines: NEATM. Note how, in this case, the fitted η -value is very close to its default value of 1.5

Apparently, the flux measured at $17.8 \mu\text{m}$ (Q1 filter) is lower than what expected from thermal models fits (see Fig. 4.4). The presence of thin cirrus, noted at down, might have affected the reliability of the absolute photometry especially in the Q band. Furthermore, the method used to obtain the Q-band measurement was subject to possible loss of flux. A slowly drift of the asteroid in the TIMMI2

field of view due small tracking errors of the telescope was noted while images in the N-band filters were acquired. The integration in the Q1 filter was almost one hour long and divided into 8 nodsets. Shifting each nod-set before co-adding was thus necessary to avoid smearing effects and compromise the detection of the object. Unfortunately, the source was not visible on each nod-set. To properly register the nod-sets and, the exposures in the Q1-filter were bracketed by two 11.9 μ m-images, where the asteroid was clearly visible (see Fig. 4.5).

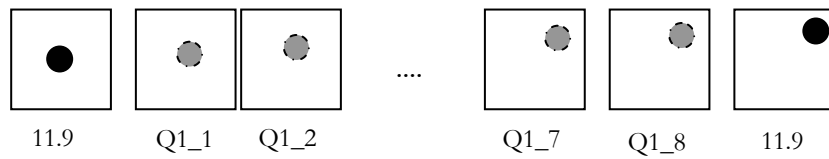


Fig. 4.5 Observing sequence used to image 2001 LF in the Q-band at the 3.6 m telescope with TIMMI2. Q1_1 represent the first nod-set Q1_8 the eighth. The gray round patch indicates the position of the source moving on the detector array and below detection on each exposure. The black circle corresponds to the position of the object on 11.9 μ m-images where the asteroid was detected.

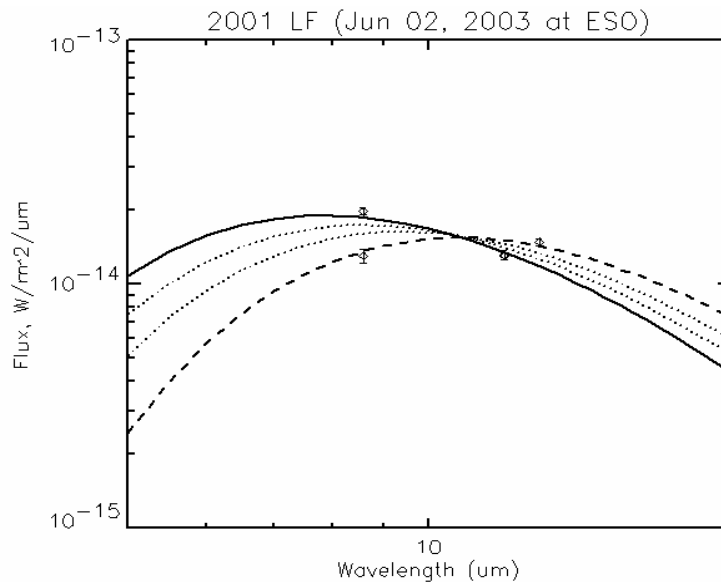


Fig. 4.6 Thermal models fit to the 2001 LF data observed on June 02, 2003. Continuous line: STM, dashed line: FRM; dotted lines: NEATM In this case, the fitted η -value of 1.1 is lower than its default value of 1.5

On the basis of the position of the asteroid on the two 11.9 μm -exposures, its drift motion as a function of time was calculated and the differential shifts for each nod-set calculated. Finally, Q1-nod-sets were co-added taking into account of the appropriate shifts.

Data of 2001 LF, although of lower quality, were obtained on June 02, 2003 as well. A large variation in the flux at 8.6 μm is visible, though at 11.9 μm such variation in the flux is not visible. Even though just N band flux were measured, the NEATM η value is well constrained to 1.1 ± 0.1 . The resulting diameter of 1.67 km is a lower than the value obtained by using the default $\eta=1.5$, but given the uncertainties, the agreement is good.

4.3.6 5381 Sekmeth

This asteroid was found to be a binary system in radar images (Nolan et al., 2003) with a rotation period of the primary of about 3 hours (P. Pravec, 2003) and the orbit of the secondary not well constrained, but probably of the order of a day. V band CCD data, along with thermal infrared observations, were obtained on June 02, 2003. Unfortunately, the non photometric quality of the night did not allow an absolute calibration of the V magnitude of the asteroid to be performed. However, the differential photometry indicates a lightcurve amplitude of about 0.35 mag. A fit of a synthetic lightcurve to the uneven and sparse data sample are in favor of a rotational period longer than 3 hours: we have obtained a good visually solution with a sidereal rotational period of about 3.6 hours (see Fig. 4.7). Correction factors for each thermal infrared observation have been calculated on the basis of the synthetic lightcurve, which assumes the variation in brightness of the asteroid to be proportional to the illuminated projected area seen by the observer. As discussed by Delbò et al. (2003) the assumption of the thermal lightcurve to have the same amplitude and phase of the one observed in reflected light might cause errors in the final diameters and albedos difficult to be estimated. Nevertheless, results of the thermal modeling using both the lightcurve-corrected and uncorrected data are in good agreement and they indicate the color temperature of the asteroid to be lower than the STM prediction: although only N band data have been obtained, the STM fit to the thermal continuum is poor (see Fig. 4.8 (a) and (b)).

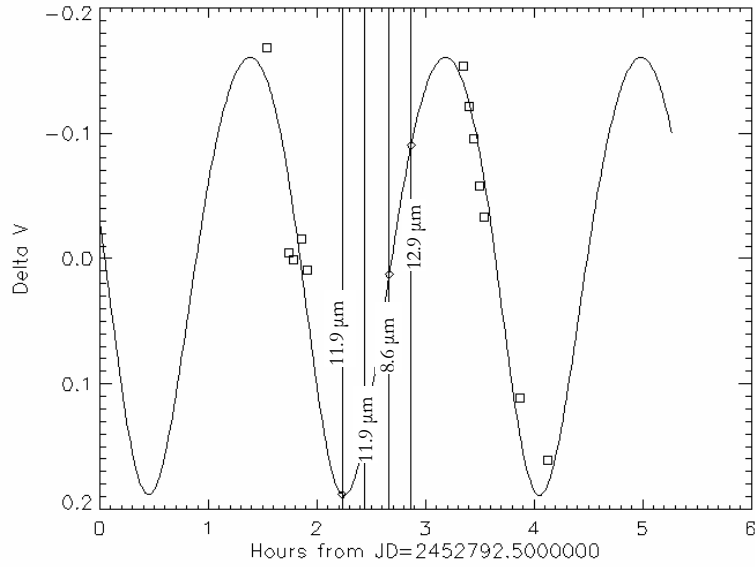


Fig. 4.7 The synthetic light curve (continuous line) fitted to the differential V magnitudes (squares) obtained on June 02, 2003 with WFI at 2.2m ESO/MPI telescope. Vertical lines are drawn in correspondence with the epoch of thermal infrared observations.

Given the uncertainties of the fluxes and the non photometric quality of the night (deduced from the analysis of the visible CCD frames) η is not well constrained. I have therefore carried out a study of the NEATM derived diameter and albedo as a function of the input value for η . Results for both lightcurve corrected and lightcurve uncorrected data are shown in Fig. 4.8

Lightcurve corrected		Raw (no lightcurve correction)		η
D(km)	Pv	D (km)	Pv	
1.03	0.42	1	0.44	0.756
1.15	0.34	1.12	0.35	1
1.27	0.28	1.24	0.29	1.25
1.51	0.2	1.47	0.21	1.8
		1.65±0.43	0.16±0.09	2.3±1.2
1.51±0.37	0.22±0.10			1.9±0.9
1.08	0.38	1.06	0.4	0.756 (STM)
1.55	0.18	1.51	0.19	- (FRM)

Table 4-4 Derived diameters and albedos by means of the NEATM as a function of the η -value. If η is derived by fitting the observed spectral energy distribution, error estimates are reported.

Judging from the fit to the thermal infrared continuum, the best solution appears to indicate an effective diameter between 1.3 and 1.5 km and an albedo between 0.28 and 0.22 for 5381 Sekmeth. The

color temperature of the object seems to be lower than that suggested by Delbò et al (2003) for the behavior of common NEAs: i.e. $\eta=1.25$ produces a poorer fit to the thermal infrared continuum. 5381 Sekhmet, like some other binaries, has rather high η . Interestingly, results from IRTF observations (Mueller et al, 2003) indicate $D=1.38$ and $P_v=0.24$ in perfect agreement with this the ESO data set. Such results are included in this work.

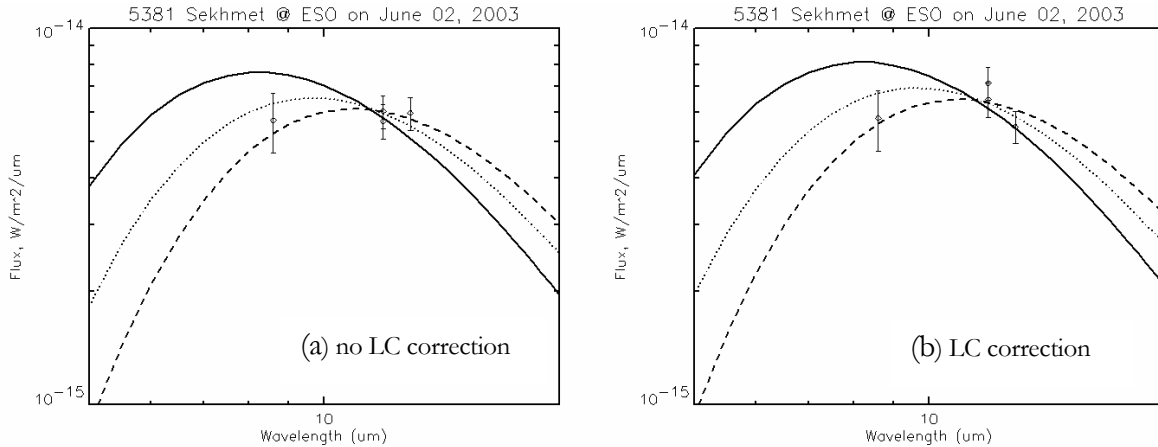


Fig. 4.8 Thermal models fit to the 5381 Sekhmet data observed on June 02, 2003. No correction for the lightcurve has been performed in plot (a), whereas data points in plot (b) have been corrected for lightcurve.

However, the radar effective diameter $D_{radar} = 2\sqrt{R_{Max}^2 + R_{Min}^2}$ calculated on the basis of the size of the primary, $R_{Max} = 0.5km$, and that of the companion, $R_{Min} = 0.15km$, is close to 1km (Nolan et al., 2003). Given the H-value of 16.5, the resulting albedo of 0.40 is higher than what expected from the S-type classification of this object. In this respect, our radiometric albedo is consistent with the stony composition inferred from spectroscopic observation carried out at Kitt Peak (Nolan et al., 2003).

4.3.7 25330 (1999 KV₄)

V band CCD data obtained with WFI at the 2.2m ESO/MPI telescope suggests a lightcurve amplitude of about 0.1 magnitudes, in agreement with Delbò et al. (2003) and with the summary of “pre-published” periods of NEAs of Pravec et al. (<http://sunkl.asu.cas.cz/~ppravec/newres.htm>). Given that small lightcurve amplitude (about 10% in flux), no correction were applied to the thermal infrared fluxes. The NEATM yields the best fit to the data points as shown in Fig. 4.9. The derived albedo of 0.08 ± 0.02 is higher than the value obtained from the observations carried out at Keck (i.e.

0.052), thought still compatible with the B taxonomic classification of this object. STM and FRM produce poorer fits, as visible in Fig. 4.9. NEATM predictions, obtained both by fitting η (which resulted equal to 1.2 ± 0.3) and fixing its value to 1.0 (according to Delbo et al., 2003 for observations made at phase angle less than 45°) are shown in Fig. 4.9 with dotted lines. Derived diameter and albedo are listed in Table 4-2.

NEATM fit to MIRLIN observations carried out at the NASA-IRTF at the very small phase angle of 3° yields a diameter of 2.5 km and an albedo of 0.08 in perfect agreement with the ESO data set (see Mueller et al., 2003).

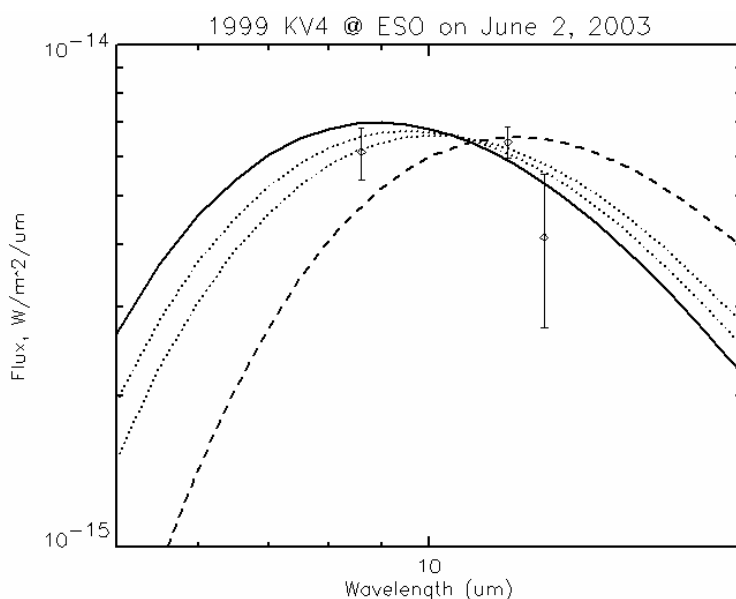


Fig. 4.9 Thermal model fits to multi-filter photometry of the NEA 1999 KV₄ obtained at the ESO 3.6m telescope. Continuous line: STM, dashed line: FRM; dotted line: NEATM with $\eta=1.0$ (the one closer to STM prediction) and with $\eta=1.2$.

4.3.8 2002 AV₄

This asteroid has been classified with an Apollo-type orbit. A preliminary solution to the V-band CCD data indicates a lightcurve amplitude of about 0.3 magnitudes and most likely a rotational period of 2.9 hours. Neither the FRM nor the STM are able to provide a good fit to the thermal infrared continuum. NEATM best fits with $\eta=1.57 \pm 0.25$ (Fig. 4.10). Resulting diameter and albedo are listed in Table 4-2.

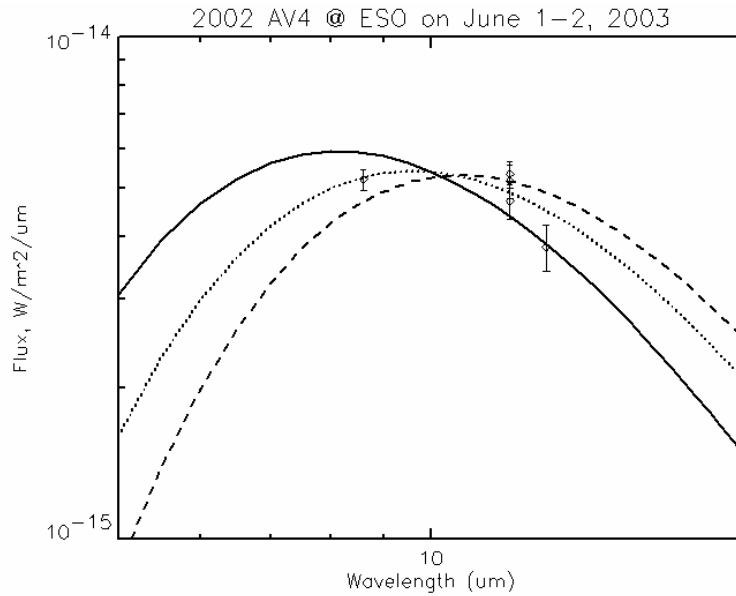


Fig. 4.10 Thermal model fits to multi-filter photometry of the NEA 2002 AV₄ obtained at the ESO 3.6m telescope. Continuous line: STM, dashed line: FRM; dotted line: NEATM.

4.3.9 5587 (1990 SB)

Lightcurve data are derived from photometry obtained during the April 2001 apparition by Pravec and colleagues (Pravec personal communication, 2000). Visible CCD observations obtained with the DFOSC at 1.5m Danish telescope covering a bit more than one hour were also obtained. The Pravec et al. and the ESO lightcurve superimpose nicely (both data set are not absolute calibrated: this superposition was achieved by arbitrarily sliding the lightcurves vertically). The synthetic lightcurve has been generated assuming the asteroid to have a tri-axial ellipsoidal shape and geometric scattering to be valid. The fit of the synthetic lightcurve to the observed ones has been obtained by varying the ratio of the semisaxis a/b parameter and the absolute rotational phase of the asteroid. The differential correction factors to the thermal infrared fluxes were calculated with respect to the mean magnitude of the visible lightcurve. Fig. 4.11 shows the three lightcurves.

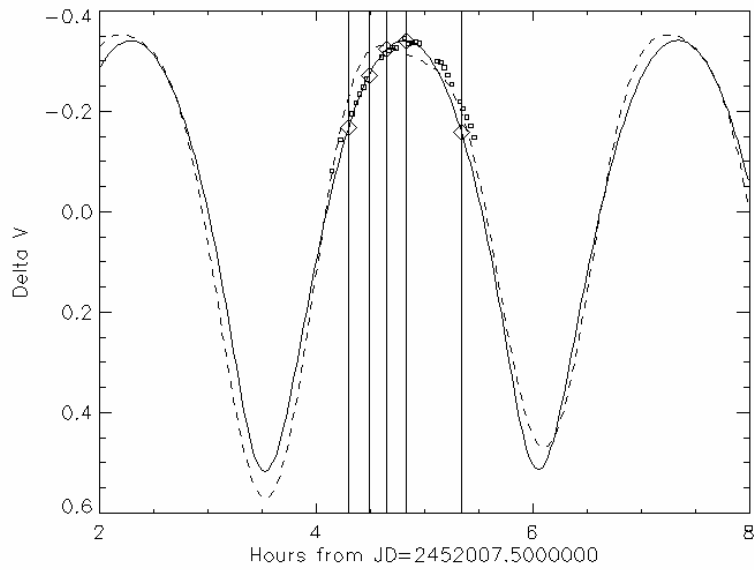


Fig. 4.11 Continuous line represent the synthetic lightcurve generated assuming the asteroid to be a triaxial ellipsoid with a geometric scattering law. Dashed line is the Pravec et al. lightcurve. Small squares are the DFOSC observations. Vertical lines are drawn in correspondence to the thermal infrared observations. Differential correction factors are of less than 0.2 magnitudes.

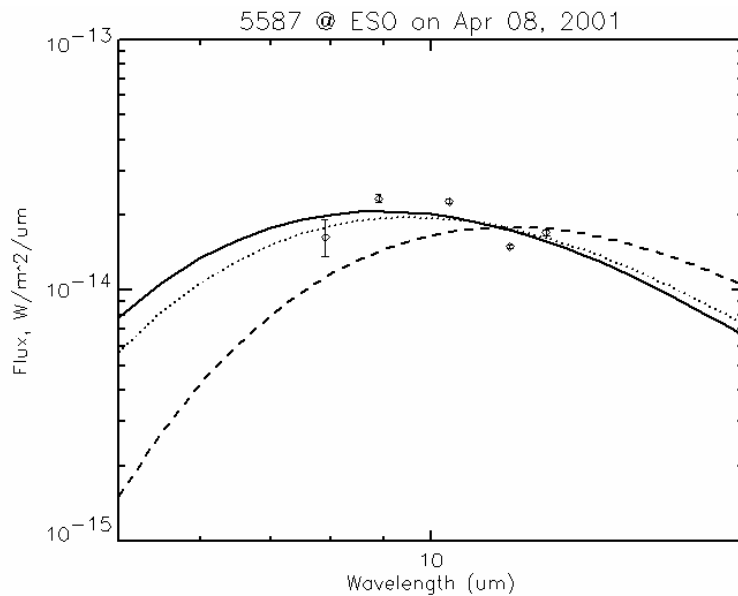


Fig. 4.12 Thermal infrared photometry of the NEA 5587 obtained at ESO and thermal models fits. Continuous line: STM, dashed line: FRM; dotted line: NEATM.

Photometric observations at 7.9, 8.9, 10.4, 11.9 and 12.9 μm were carried out on April 08, 2001. The diameters and albedos derived by fitting thermal models to the lightcurve corrected infrared fluxes are

reported in Table 4-2. Note the good agreement of NEATM solution with the Delbo et al., (2003) results. These photometric data indicate a relatively high color temperature for the surface of this NEA. The STM produce a good fit as well and its results are in agreement with the NEATM ones, given the uncertainties.

Furthermore, given the infrared brightness of this target, N- and Q-band spectra were successfully obtained on the following night. The correction for the lightcurve does not modify the shape of the thermal infrared continuum, since fluxes at different wavelengths were all measured simultaneously. However, the H value must be varied according to the (mean) projected area the asteroid showed to the Sun during the time of the spectroscopic observations. The reference epoch for the spectroscopic observation was taken at that time when half of the integration was completed.

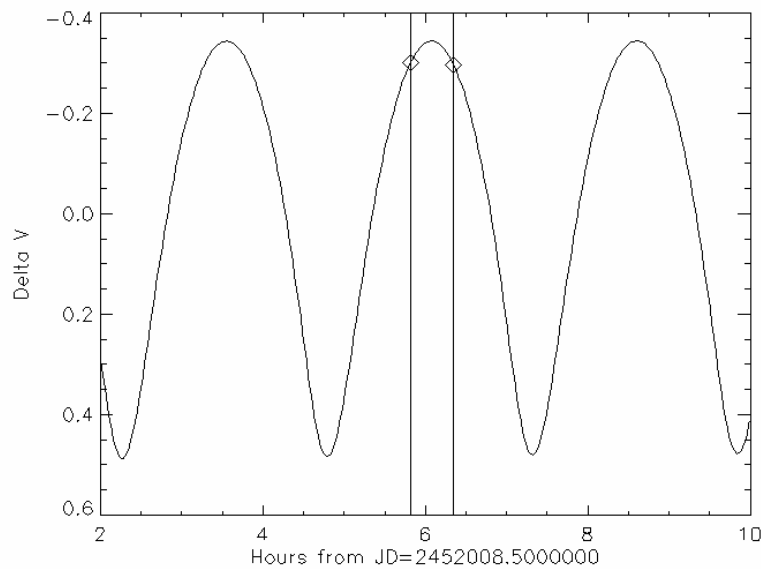


Fig. 4.13 The continuous sinusoidal line represents the visible lightcurve as in the case of Fig. 4.11. Vertical lines are drawn in correspondence with the epochs of the thermal spectroscopy measurements.

The NEATM derived a diameter of 4.1 ± 0.3 km and an albedo of 0.25 ± 0.03 from the first spectrum. The determination of the color temperature was reliable $\eta = 1.0 \pm 0.1$ and in agreement with Delbo et al., (2003) predictions. The STM fits with a lower diameter equals to 3.8 km and a higher albedo of 0.28. The FRM, which does not provide a reliable fit to the thermal continuum, gives a diameter of almost 7 km and a very low albedo of 0.08 inconsistent with the S class taxonomic classification of this object. If lightcurve correction is not taken into account, NEATM fits with a diameter 12% higher and an albedo

32% lower. η is conserved, since the lightcurve correction do not alter the shape of the thermal continuum but it does shift only its overall level.

NEATM fits the second spectrum with a diameter of $4.0 \pm 0.3 \text{ km}$, an albedo of 0.25 ± 0.03 and $\eta = 1.0 \pm 0.1$. The STM and the FRM give results within 3-5% of those obtained by fitting the first spectrum. Given the uncertainties, the radiometric results derived from the two spectroscopic observations and from the filter photometry are in good agreement.

The diameter derived from ESO observations is about 10% larger than the value derived from radiometry made at Keck. The resulting albedo is thus smaller of about 20%.

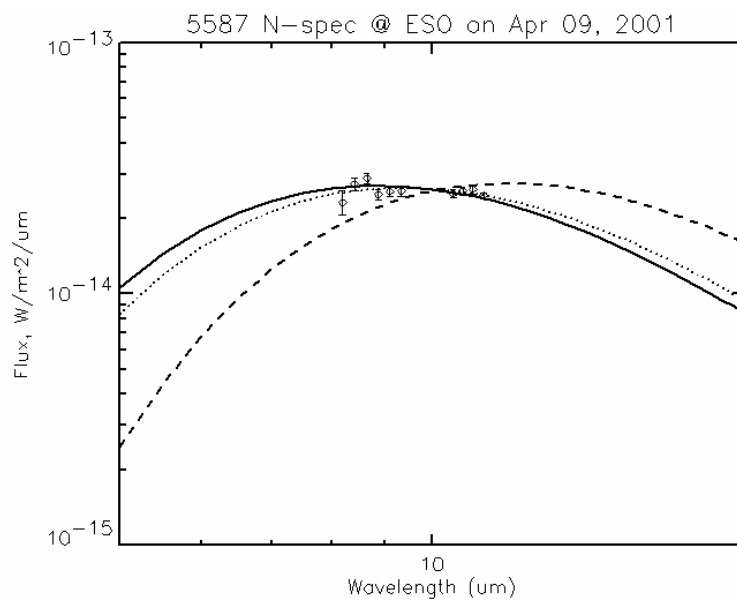


Fig. 4.14 The binned spectrum of the NEA 5587 obtained at 05:46:41 UT on April 09, 2001 (first spectrum) and thermal models fits. Continuous line: STM, dashed line: FRM; dotted line: NEATM.

It is worth pointing out how in the case of Keck observations a severe lightcurve effect had altered the measured spectral energy distribution of the flux, resulting in large scatter of the data points with respect to thermal model continua. Lightcurve correction had proved to reduce dramatically that scatter. However, this might have introduced errors on the derived η -value, diameter and albedo which explain the discrepancy between the Keck and the ESO results.

4.3.10 19356 (1997 GH₃)

This object was observed on April 09, 2001. Thermal infrared data are affected by large uncertainties and the scatter of the data points is large. Unfortunately CCD photometry obtained with the DFOSC at the Danish 1.5m telescope, although of good quality, does not allow the lightcurve amplitude and period to be estimated. Thermal model fits have to rely, therefore, on the uncorrected data. Fits are clearly not as good as in the case where appropriate lightcurve correction could have been performed. Resulting diameter and albedo are listed in Table 4-2.

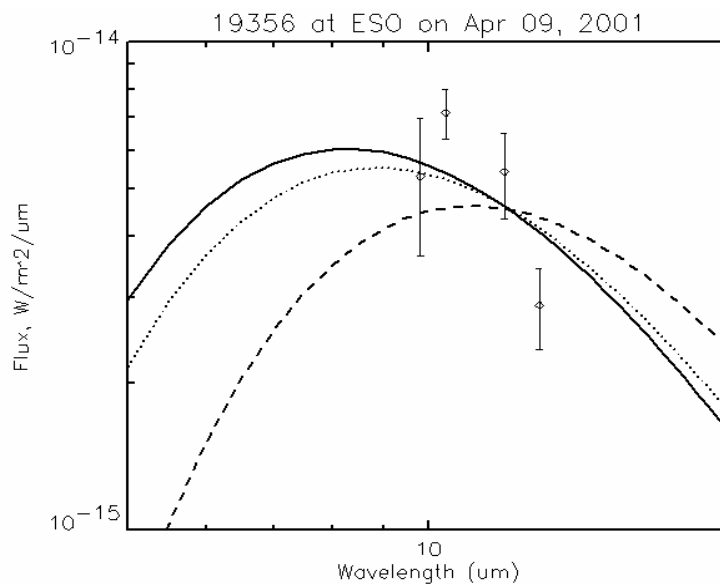


Fig. 4.15 Thermal infrared photometry of the NEA 19356 obtained at ESO and thermal models fits. Continuous line: STM, dashed line: FRM; dotted line: NEATM.

The case of NEA 19356 as well as that of 5587 shows the crucial importance of lightcurve correcting thermal infrared data obtained at different times and the need of simultaneous optical observations.

4.3.11 5604 (1992 FE)

This Aten type NEA was observed at ESO for three nights between April 07 and April 09, 2001. The lightcurve amplitude at that epoch was about 0.2 magnitudes. Absolute calibration of the CCD data was performed. The H magnitude calculated at lightcurve mean is 17.7 ± 0.1 , about 1.3 magnitudes fainter than the value given by the Minor Planet Center. This was the weakest source observed within this program (see Appendix A for flux values). Detection was achieved only in the 11.9 μm filter on April 08. However, this result is somewhat questionable since further efforts to image the asteroid in other filters during the same night and again at 11.9 μm on the following nights did not succeed.

Thermal models results are therefore based on this single wavelength measurement. The NEATM derived albedo is lower than the value derived from observations made at Keck on May 2001 (see Delbò et al, 2003) where clear detection was achieved.

4.3.12 37314 (2001QP)

This object was observed on December 02 and December 04, 2001. The V-band lightcurve at the time of the thermal infrared observations indicates a variation within ~ 0.1 magnitudes. Since two photometric standards were present in the field of view, absolute calibration was possible. The V magnitude at the time of the thermal infrared observation was found to be equal to 15.6. The H value was calculated using the formulae of Bowell et al (1989) and found to be equal to 14.4 assuming a G value of 0.25, as suggested by Bowell for moderate albedo objects A, B, M, Q or S-types. Derived radiometric albedos and diameter are reported in Table 4-2.

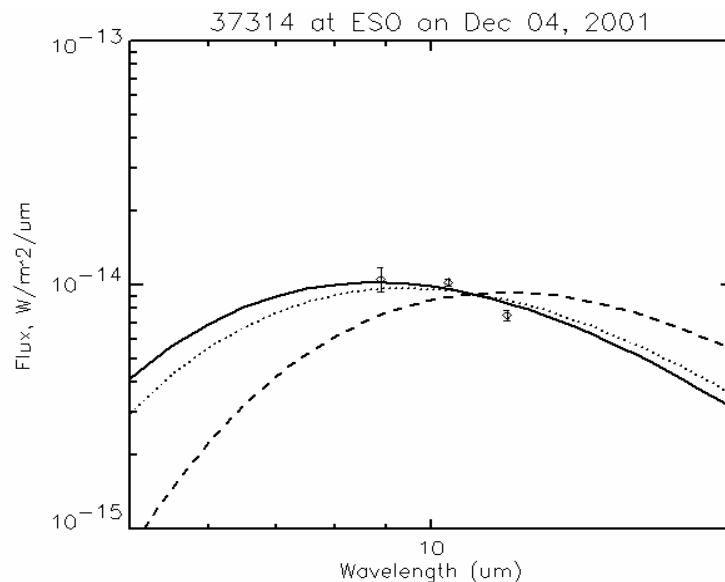


Fig. 4.16 Thermal model fits to N-band infrared data obtained at ESO. Continuous line represents the spectral energy distribution derived by the STM, dashed line that of the FRM and the dotted one is the NEATM.

4.3.13 33342 (1998WT₂₄)

CCD observations of this target were carried out from ESO on December 02 and 04, 2001. The lightcurve amplitude was found to be slightly less than 0.2 magnitudes and the absolute calibrated V magnitude at lightcurve mean of 14.63 and 14.23 respectively. The uncertainty of the absolute

calibration is of the order of 0.1 magnitudes. On the basis of the method described by *Bowell et al. (1989)*, I have calculated an H value for 33342 of 18.54 ± 0.1 assuming $G=0.4$ as expected for this E-type asteroid (*Kiselev et al, 2002*). The reliability of the H value derived is somewhat questionable given the large phase angle ($\sim 60^\circ$) at the time of the observations. Thermal infrared data were obtained at 8.9, 10.4 and 11.9 μm and the derived monochromatic flux densities are listed in Appendix A.

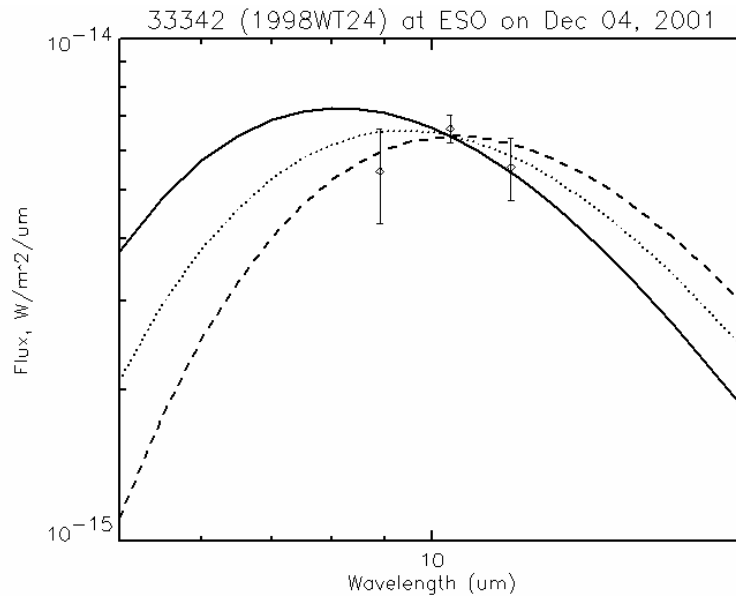


Fig. 4.17 Thermal model fits to N-band infrared data obtained at ESO. Continuous line represents the spectral energy distribution derived by the STM, dashed line that of the FRM and the dotted one is the NEATM.

Resulting radiometric diameter and albedo, from thermal models fit shown in Fig. 4.17, are reported in Table 4-2. NEATM with η fixed to the value of 1.5 gives results which are closer to the radar diameter of *Zaitsev et al. (2002)* and the polarimetric albedo derived by *Kiselev et al. (2002)*. Fig. 4.17 shows how a smaller η -value, closer to the one assumed by the STM, provide a poor fit to the measured fluxes, indicating that the STM solution is not in agreement with the observations.

Further radiometric observations of this target were obtained with the NASA-IRTF on December 18, 19 and 21, 2001. Fig. 4.18 shows the thermal infrared lightcurve obtained by composing all the 11.7 μm -magnitudes of the three nights. A rotational period of 0.15415 days (*Pravec, personal communication*) was used. Note that the 11.7 μm -magnitudes appear to indicate an amplitude of the thermal infrared lightcurve smaller than the optical one. In fact, a sinusoid with period equal to half of the rotation period of the asteroid best fits with an amplitude of 0.18 ± 0.04 magnitudes. However, it is worth to remember that the observing geometry of the target had changed strongly between the three

observing dates at IRTF. This might explain the scatter of the composite thermal lightcurve and might have introduced errors difficult to be estimated. Fig. 4.19 shows thermal model fits to the measured infrared fluxes, which are listed in Appendix A. Lightcurve correcting the observed infrared fluxes in all cases of Fig. 4.19 produces changes of their values no larger than 10%. The shape and the absolute level of the spectral energy distribution resulting from multi-filter photometry are thus not altered significantly. I therefore have applied the thermal models to the uncorrected data increasing their error-bars to about 10% level, where necessary, to account for lightcurve effects.

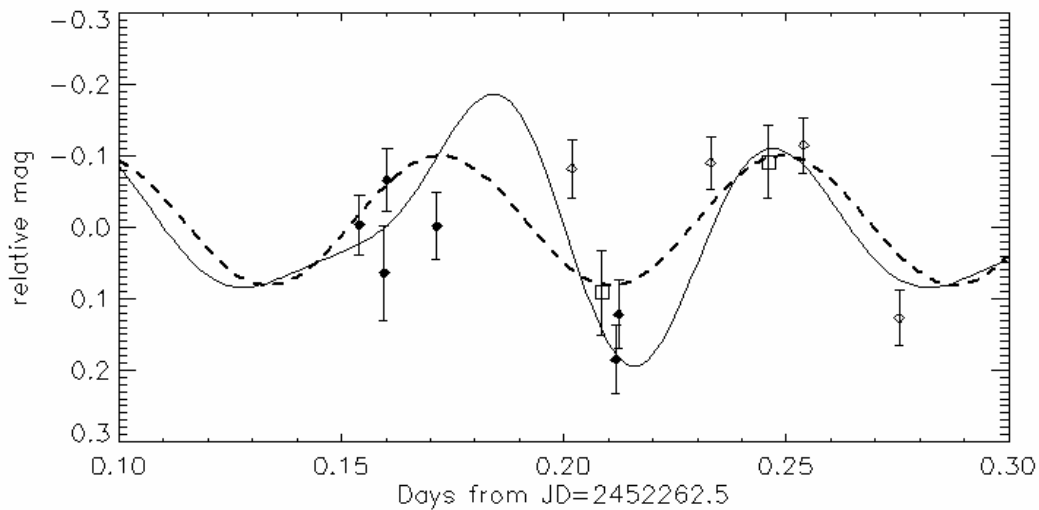


Fig. 4.18 Visible and thermal lightcurve of 33342 on December 2001. Filled diamonds are infrared relative magnitudes derived from $11.7\mu\text{m}$ -fluxes obtained on December 18, 2001. Empty diamonds represent $11.7\mu\text{m}$ magnitudes obtained on December 19, 2001 and empty squares those measured on December 21, 2001. Infrared magnitudes were composed on the basis of a 0.15415-days period. Continuous line is the R-band lightcurve derived from CCD observation of Pravec et al. (Pravec, personal communication, 2002). Thick dashed line is a sinusoidal fit with a period equal to half of that of the asteroid to infrared magnitudes.

Resulting diameters and albedos, along with the NEATM fitted η -value are listed in Table 4-3. The spread of the results is very large: the uncertainty on the albedo is almost by a factor of two. The increase of the η -value with the phase angle appears to be real and not the cause of inadequate lightcurve correction or errors in the absolute calibration of the infrared flux. In contrast with the case of 5381 Sekmeth, here, large variations of the η -value correspond to large variations in the resulting diameters and albedos. However, it is worth to point out that observations of the asteroid 33342 were carried out at a different phase angle range with respect to that of the NEA 5381 Sekmeth. The STM fits with a higher albedo, though its value is more stable than the one derived with the NEATM. The FRM appears to give a solution with better agreement with the taxonomic classification for this asteroid,

but it clear that further modeling efforts are in the need to obtain a more realistic explanation for what is going on in this case.

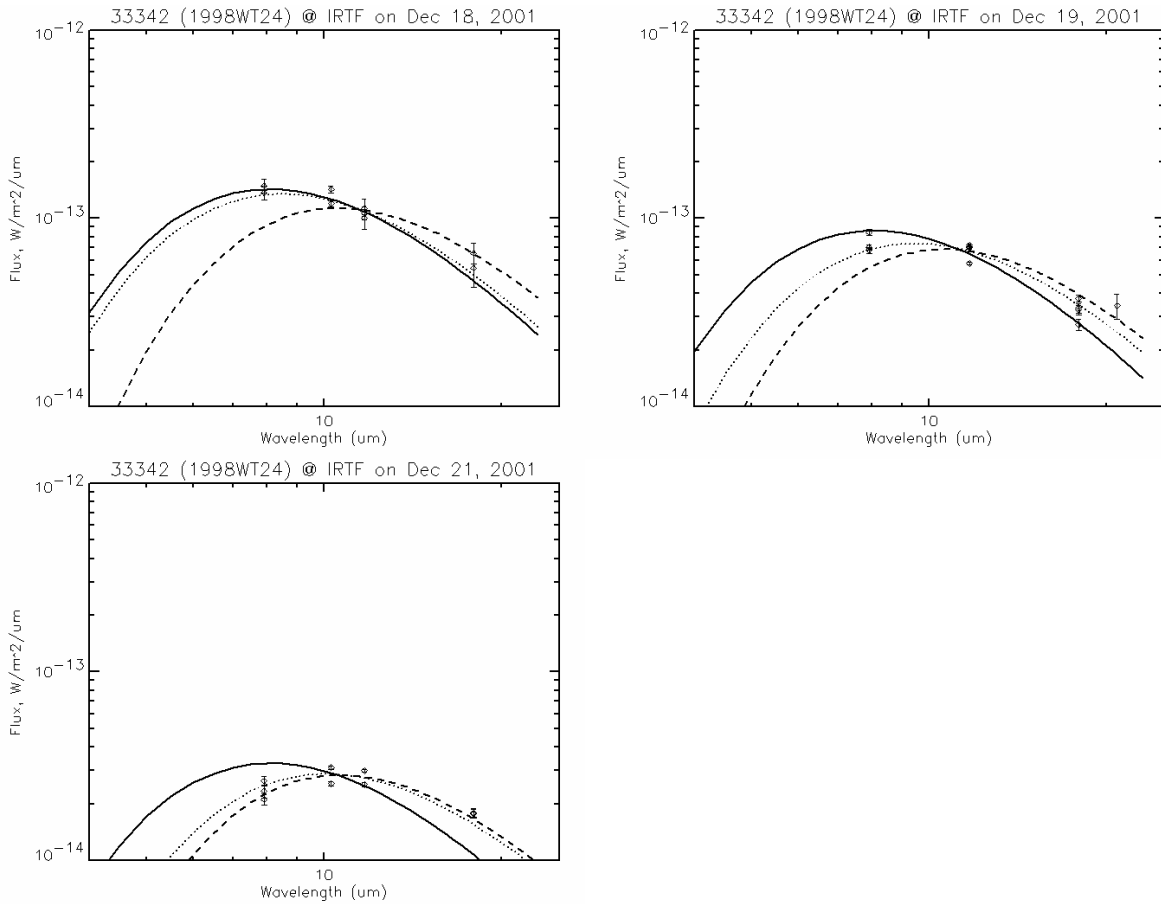


Fig. 4.19 Thermal model fits to multi-filter photometry of the NEA 33342 obtained at the NASA-IRTF. No correction for lightcurve was applied. Continuous line: STM, dashed line: FRM; dotted line: NEATM. Figures are drawn with the same y-axis scale. Note the clear variation of the apparent color temperature between the observing dates.

4.3.14 35396 (1997 XF₁₁)

This object is a potentially hazardous asteroid (PHA). It was one of the first asteroids which in early 1998 was predicted to have a small probability of impacting the Earth in 2028. The asteroid was quickly proven safe with more observations and better orbit analysis. It was observed at ESO on November 28, 2002. V band CCD data obtained using the WFI installed at the ESO/MPI 2.2m telescope indicate a lightcurve amplitude not smaller than 0.7 magnitudes. Absolute calibration of the photometry was made observing Landolt's standards at nearly the same airmass of the object and yielded $V=15.6\pm 0.1$ at mean lightcurve. Assuming $G=0.4$ as indicated by Bowell et al. (1989) for high albedo objects the resulting H

value was found to be equal to 17.1 ± 0.1 . Taking into account the provisional rotational period solution of 3.25730 ± 0.0003 hours (Pravec, 2002)¹⁷ A synthetic lightcurve was fitted to the observational data and the correction factors for the thermal infrared fluxes were derived. In order to account for the rotational variability, thermal infrared fluxes were lightcurve corrected. They are shown in Fig. 4.20 along with thermal models fit continua. Unfortunately, the η value cannot be constrained with sufficient accuracy. The assumption of $\eta=1.0$ (phase angle $< 45^\circ$) yields a geometric albedo of 0.4.

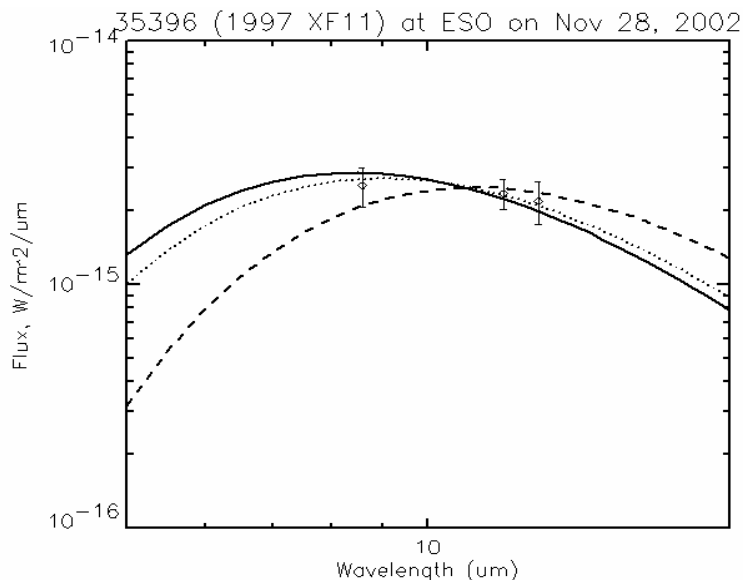


Fig. 4.20 Thermal model fits to the observed flux of the asteroid 35396. Continuous line: STM, dashed line: FRM; dotted line: NEATM.

Further thermal infrared measurements of this object were obtained on November 05 and November 03, 2002 using the MIRS I at the NASA Infrared Telescope Facility (IRTF) on Mauna Kea, Hawaii. Weather conditions were good and the sky transparency of photometric quality (Bus, personal communication). Because of the rapid rotation of the asteroid, several measurements were obtained at $11.7 \mu\text{m}$ to define the thermal lightcurve. Additional measurements defining the spectrum from 4.9 to $18.7 \mu\text{m}$ were interspersed so that the spectral behavior could be determined by interpolation at any point on the lightcurve. The derived monochromatic flux densities at each wavelength and epoch are listed, as usual, in appendix A. The standard star β PEG was used for the reduction of the aperture photometry and observed before and after the target asteroid within about 0.2 airmasses.

¹⁷ MPML Date: Mon Nov 25, 2002 4:42 pm Subject: Re: (35396) 1997 XF11 Lightcurve Observations

In order to construct the thermal infrared lightcurve, the $11.7\mu\text{m}$ fluxes and their uncertainties were converted to magnitudes¹⁸. The epoch of measurements were adjusted for light travel time. As described by Harris and Davies (1999), a sinusoidal curve with period equal to half of the sidereal rotational period of 35396 was fitted to the derived relative magnitudes. This curve is shown in Fig. 4.21 with the thin continuous line. The maximum to minimum amplitude of the best fit sinusoid is 0.6 ± 0.07 and 0.5 ± 0.02 magnitudes for the November 05 and November 03 infrared data respectively. Although no simultaneous optical observations were available, Pravec and colleagues obtained a composite V band lightcurve on the basis of observations taken between November 01 and 29. The Pravec et al. lightcurve is superimposed on the thermal one and it is shown in Fig. 4.21 with a dashed thick line. The amplitude of the $11.7\mu\text{m}$ lightcurve is almost a factor of two smaller than the V band one (The best sinusoidal lightcurve fit yielded an amplitude of 0.92 ± 0.005 magnitudes). Moreover, a phase shift of about 8.5 minutes (i.e. 16°) between the thermal and the visible lightcurve can be measured by comparing the time at which lightcurve minima and maxima occur.

Thermal models fit to the lightcurve corrected fluxes are shown in Fig. 4.22. Note, in both data sets, the very high thermal flux measured at $4.9\mu\text{m}$. No explanation for the anomalous results has been found so far. The contribution of the reflected light contributes to the total at $4.9\mu\text{m}$ flux. However, such contribution cannot account for the measured high flux.

Taking the mean of the ESO and IRTF results weighted with their uncertainties, the final geometric visible albedo of 35396 is 0.20 ± 0.02 with a diameter of 1.06 ± 0.04 . Given the error on the H value estimation of about 10%, the final uncertainties on diameter and albedo result a bit larger.

¹⁸ $m = -2.5 \log(F)$; $\sigma m = |2.5/F / \ln 10 \sigma F|$

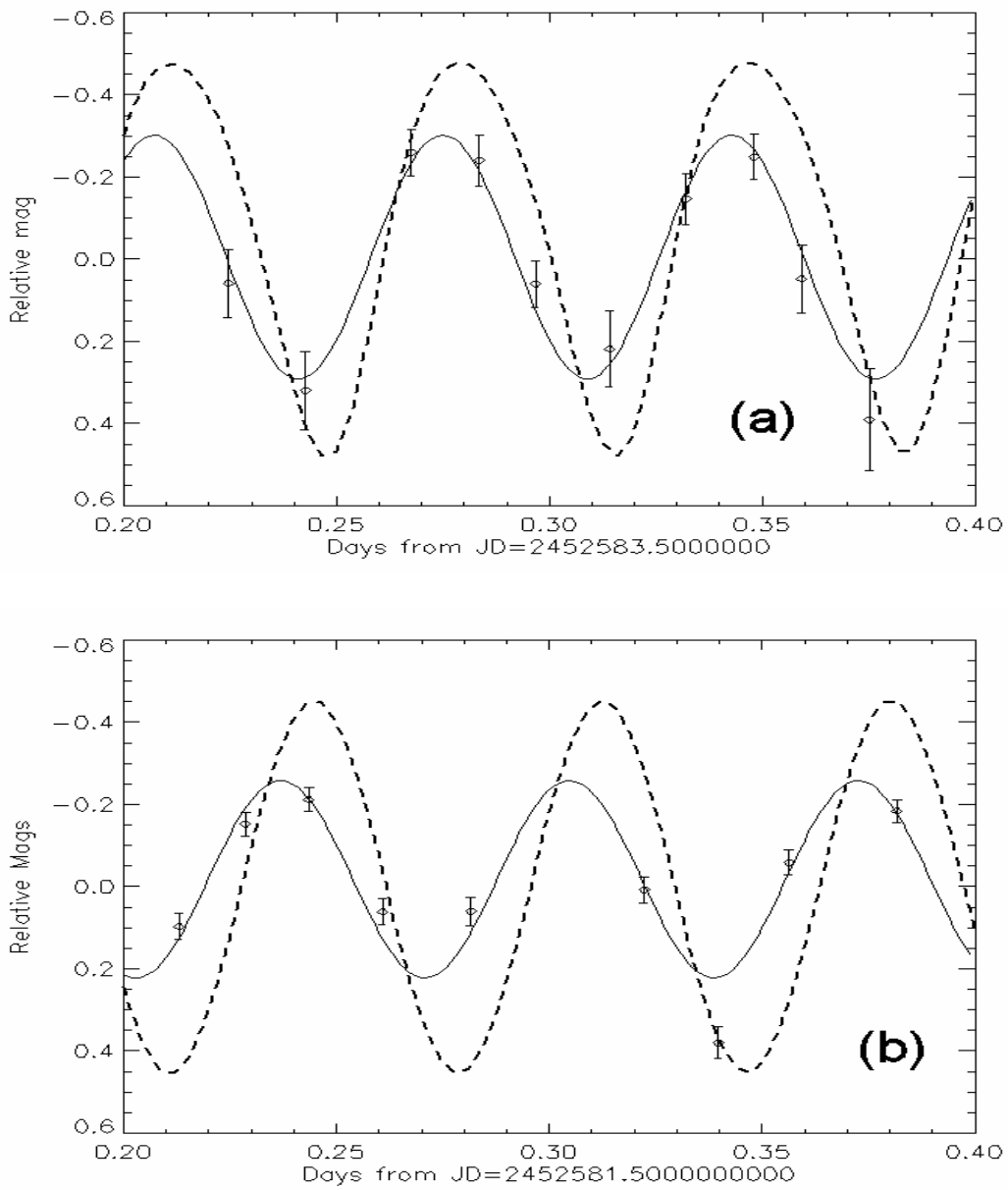


Fig. 4.21 Lightcurve of the NEA 35396 at 11.7 μ m obtained with MIRSI@NASA-IRTF on November 05, 2002 (a) and on November 03, 2002 (b). The continuous line is a sinusoid function with period half of the rotational period of the asteroid fit to the measured relative magnitudes. The thicker dashed line is the V-band lightcurve of Pravec et al. Note the difference in amplitude and the phase shift.

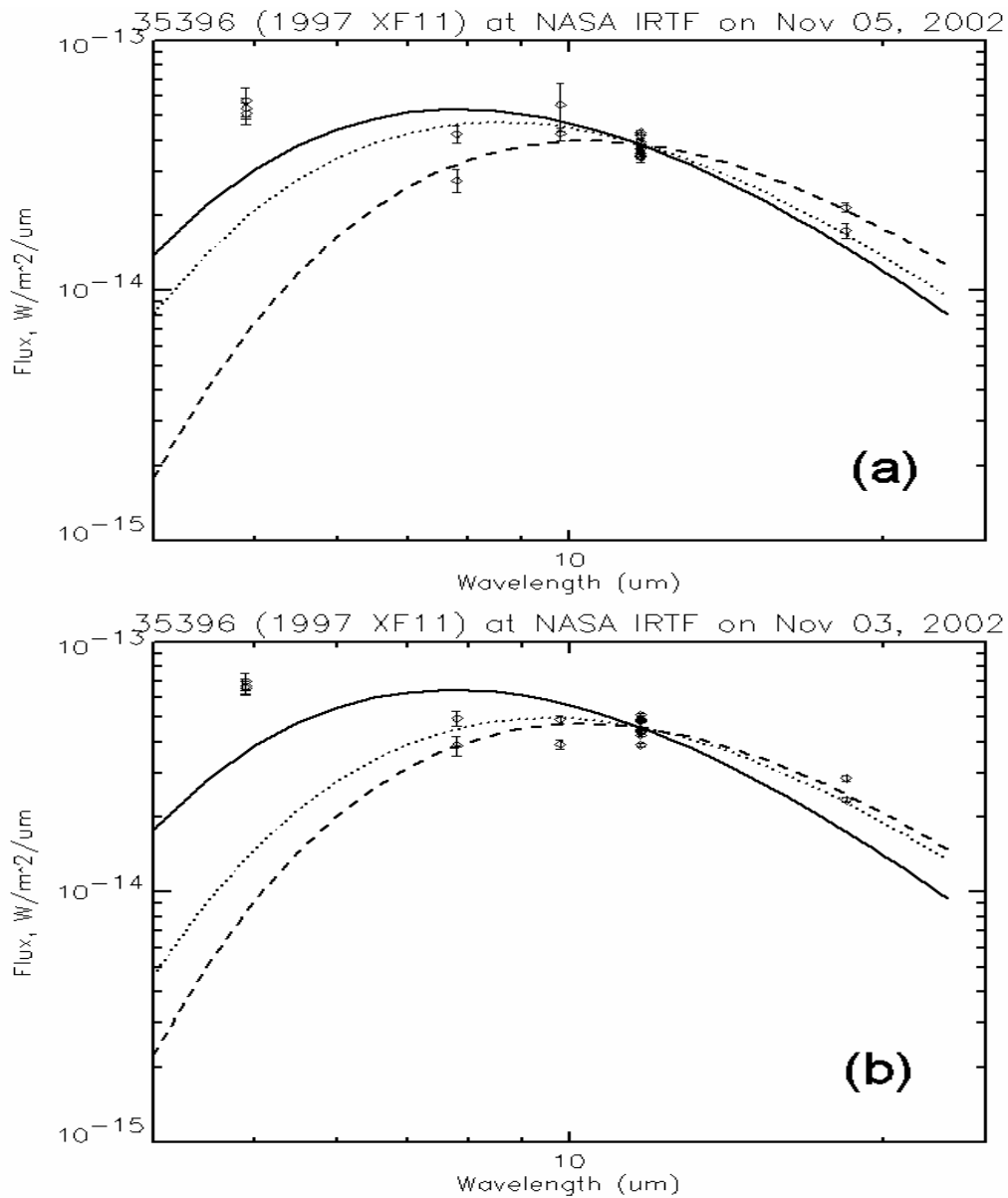


Fig. 4.22 Thermal models fit to the $11.7\mu\text{m}$ lightcurve-corrected data obtained with MIRS@NASA-IRTF on November 05, 2002 (a) and on November 03, 2002 (b). Note in both data set the very high thermal flux measured at $4.9\mu\text{m}$.

4.3.15 1580 Betulia

Harris (personal communication) analyzed the thermal infrared fluxes obtained at the IRTF on June 02, 2002 and attempted to lightcurve correct them on the basis of the R-band CCD magnitude measured by Yan Fernandez at the 2.2 m University of Hawaii Telescope (Fernandez, personal communication). A 5th-order polynomial was fitted to the R-band magnitudes and used that to

normalize the infrared fluxes to the lightcurve mean. Unfortunately, the R-band lightcurve spans only 2.25 hours of the 6.1-hours-rotational period of this asteroid. The lightcurve mean was estimated by taking the H-value (14.8) from Wisniewski et al. (1997) and calculating the corresponding V magnitude for the geometry of our observations on the basis of the H, G magnitude system. The resulting V-magnitude is 14.12. Assuming $V-R = 0.35$ for C-type, we get $R = 13.77$ for the lightcurve mean.

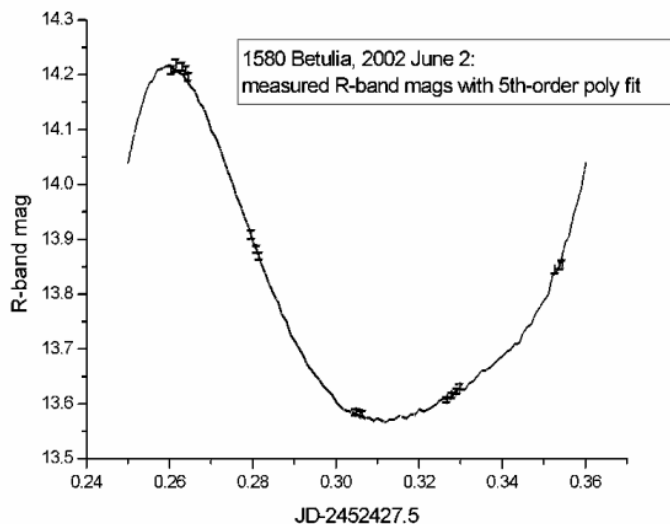


Fig. 4.23 The 5th-order polynomial fitted to the R-band magnitudes measured by Fernandez.

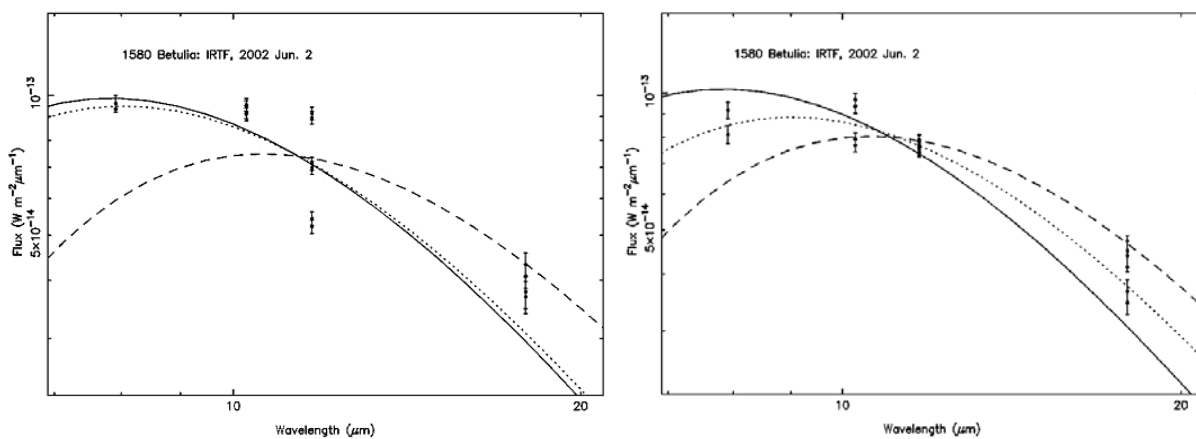


Fig. 4.24 On the left thermal model fits to the observed infrared fluxes before applying lightcurve correction (see text). On the right lightcurve corrected fluxes. Continuous line: STM, dashed line: FRM; dotted line: NEATM.

Harris used the polynomial fit to lightcurve correct thermal infrared fluxes, excluding those taken at times outside the time span of the R-band magnitudes. (5 flux values excluded out of a total of 21). Thermal models were fitted to the data points, first without lightcurve correction (Fig. 4.24 left) and then after lightcurve correction (Fig. 4.24 right). Resulting diameters and albedos are listed in Table 4-5.

STM		NEATM			FRM	
D (km)	pV	D (km)	pV	η	D (km)	pV
No lightcurve correction						
3.48	0.18	3.38	0.19	0.78	4.89	0.09
With lightcurve correction						
3.54	0.17	4.35	0.11	1.27	5.06	0.08

Table 4-5 Comparison of radiometric derived diameters and albedos on the basis of the three thermal models used in this work. Note the importance of lightcurve correcting the observed thermal infrared fluxes. (see the text for further details)

Pettengill et al. (1979) give a diameter for Betulia of 5.8 ± 0.4 km. However, given the pole solution of Kaasalainen et al. (2004) $\lambda_0 = 136^\circ$ and $\beta_0 = 22^\circ$ the resulting aspect angle at the time of radar observations was about 88° . The true diameter (i.e. $5.8 \times \cos(\xi)$, where ξ is the aspect angle) is therefore very near the radar result. Assuming the dimensional ratios of Kaasalainen et al. (2004), ($a/b=1.1$ and $b/c=1.4$) the radar shape of 1580 Betulia is consistent with a tri-axial ellipsoid with semi-axes of $2.9 \times 2.6 \times 1.9$ km. The maximum projected area along the line-of-sight was about 15.8 km^2 at the time of radar observations. On the other hand, at the time of the IRTF observations the aspect angle was about 129° and the projected area between 14 and 12.7 km^2 which imply an effective diameter between 4.2 and 4.0 km. Given the uncertainties introduced by lightcurve correcting the observed thermal infrared fluxes and taking into account that the real shape of this asteroid differs significantly from that of a tri-axial ellipsoid (see Kaasalainen et al. 2004), the agreement of radar and NEATM results is good.

The derived albedo is about 0.1. This is consistent with Betulia being a C-type asteroid, but somewhat higher than previous estimates.

4.4 Physical characterization of NEAs: summary of results

We have obtained radiometric diameters and albedos for 32 NEAs. 7 of them were observed under different observing geometries. For 7 objects in our data base the diameter and the albedo had already

been published. However, our new observations have led to a refinement of those values by means of multi-wavelength thermal infrared observations, as in the problematic case of 1580 Betulia.

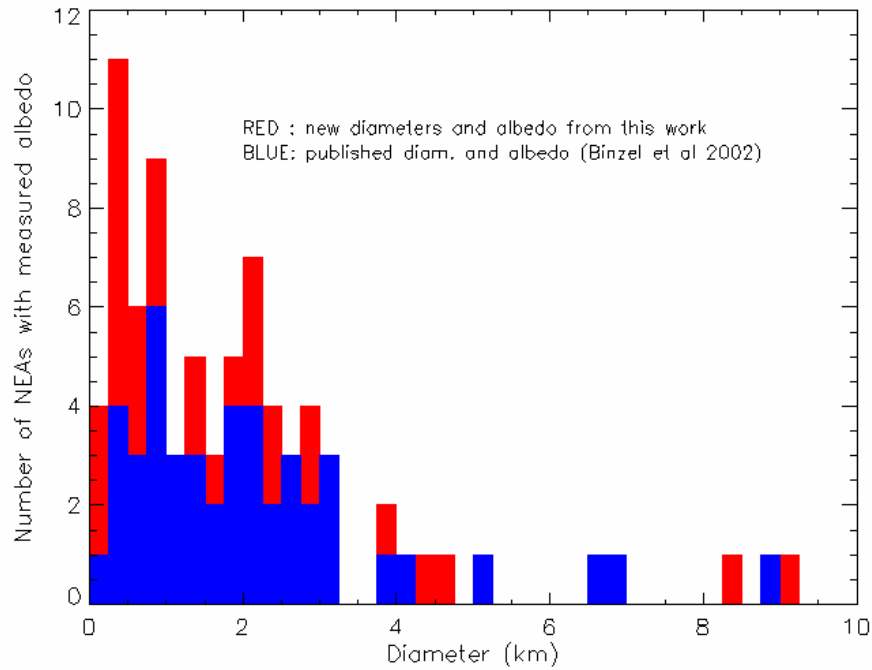


Fig. 4.25 The scientific relevance of this work in terms of newly derived NEA sizes and albedos. The histogram in blue shows the number of NEAs with measured size and albedo as a function of their diameter according to the Table 1 in Binzel et al. (2002) chapter on "Physical Properties of Near-Earth Objects" in Asteroids III. In red are shown new and refined diameters and albedos obtained from this work.

Fig. 4.25 shows the scientific relevance of this work in terms of newly derived NEA sizes and albedos in comparison to what was known before. The histogram in blue color represents the number of NEAs with measured albedo and diameter (as a function of their size) that Binzel et al. (2002) have included in their review paper on the book Asteroids III. In red are shown new and refined diameters and albedos obtained from this work. This work increments the number of NEAs with measured sizes and albedos by 54%. However, if the objects for which we have refined the diameter and the albedo are included, this increment increases to almost 70%.

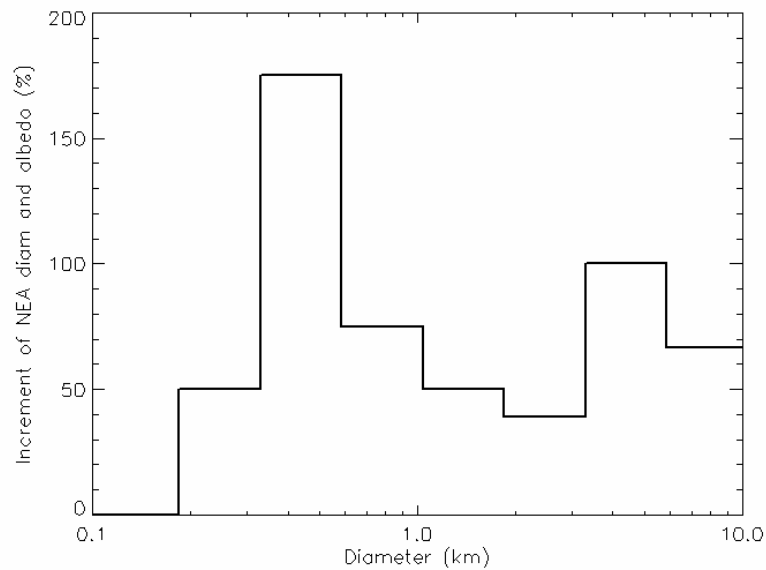


Fig. 4.26 Increment in the number of NEAs with measured diameter and albedo as a function of their diameter. Note how this work contributes mainly to the increment of our knowledge for the sub-kilometer population of NEAs.

Fig. 4.26 shows that this work mainly contributed to the physical characterization of object smaller than 1 kilometer. In particular this was possible thanks to the unrivalled sensitivity of the Keck telescope which enabled smaller and fainter objects to be observed, thereby removing the bias inherent in surveys carried out with smaller telescopes that are limited to the largest and brightest objects. The fact that great importance was given to obtain physical information for the sub-kilometer part of the NEA population is important to explore a number of issues of crucial relevance for planetary sciences: are peculiar surface characteristics associated with small asteroids, e.g. lack of space weathering due to the relatively young surfaces of small objects? What are the limitations of asteroid thermal models and what their accuracy for the study of such small objects?

Table 4-6 lists physical parameters for the NEAs studied in this work. Further asteroids with published STM, FRM and NEATM derived sizes and albedos have been included in the list. Taxonomic classes are indicated, where available. Some of the objects were observed under different observing conditions and at different apparitions. Since the solar phase angle is one the most relevant parameter for modeling the thermal emission of asteroids, Table 4-6 reports its value for each observation. Size estimates derived from radar are available for some of the NEAs for which we have obtained radiometric observations. The radar observations put strong constraints on the size and shape of this object thereby providing "ground-truth" data for checking the reliability of the thermal models used.

num	name	α	NEATM				STM		FRM		Radar		Tax
			D	η	pv	$\sigma\eta$	D	pv	D	pv	D	pv	
433	Eros (lc max)	10	23.6	1.05	0.20	0.21	20.5	0.27	36.2	0.09	20.06	0.28	S
433	Eros (lc max)	31	23.6	1.07	0.21	0.22	21	0.26	36.6	0.09	20.06	0.28	S
433	Eros (lc min)	10	14.3	1.15	0.22	0.23	11.8	0.32	21	0.1	14.1	0.22	S
1566	Icarus	97	1.27	(1.2)	0.33	-	0.88	0.7	1.05	0.49	1-4	0.09	S
1580	Betulia	12	3.9	(1.2)	0.17	-	3.3	0.24	5.7	0.28	6	0.06	C
1580	Betulia	53	4.35	1.27	0.11	0.3	3.54	0.17	5.06	0.08	6	0.06	C
1620	Geographos	34	2.5	(1.2)	0.26	-	2.2	0.33	3.4	0.14	2.56	0.07	S
1627	Ivar	5	9.12	(1.0)	0.15	-	7.94	0.2	15.9	0.05	8.5±3	0.17	S
1627	Ivar	53	10.2	(1.2)	0.12	-	8.5	0.17	12.6	0.08	8.5±3	0.17	S
1862	Apollo	35	1.4	1.15	0.26	0.23	1.2	0.35	1.9	0.15	1.2	0.38	Q
1685	Toro	18	4.1	(1.2)	0.29	-	3.3	0.44	6.5	0.12	3.3	0.43	S
1866	Sisyphus	16	8.48	(1)	0.15	-	7.47	0.2	16.3	0.042	-	-	S
1866	Sisyphus	35	8.9	1.14	0.14	0.2	7.5	0.2	13.1	0.07	-	-	S
1915	Quetzalcoatl	29	0.4	(1.2)	0.31	-	0.34	0.42	0.55	0.16	-	-	S
1980	Tezcatlipoca(lcM)	63	6.7	1.54	0.14	0.308	4.5	0.31	6.80	0.14	-	-	SI
1980	Tezcatlipoca(lcM)	63	6.6	1.64	0.15	0.328	4.5	0.31	6.80	0.14	-	-	SI
2100	Ra-Shalom	39	2.79	2.32	0.083	0.4	1.6	0.25	2.60	0.095	2.4	0.11	Xc
2100	Ra-Shalom	41	2.5	1.8	0.13	0.36	1.7	0.26	2.60	0.11	2.4	0.11	Xc
2062	Aten	50	0.91	(1.2)	0.28	-	0.77	0.39	1.10	0.18	-	-	S
3200	Phaethon	48	5.1	1.6	0.11	0.32	3.6	0.22	5.50	0.09	-	-	B,F
3554	Amun	16	2.1	1.2	0.17	0.24	1.8	0.23	2.90	0.09	-	-	M
3671	Dionysus	58	1.5	3.1	0.16	0.62	0.86	0.52	1.10	0.31	-	-	Cb
4034	(1986 PA)	40	0.42	(1.0)	0.52	-	0.4	0.58	0.57	0.29	-	-	O
4055	Magellan	13	2.49	(1.0)	0.31	-	2.2	0.39	4.36	0.1	-	-	V
4660	Nereus	60	0.33	(1.5)	0.55	-	0.26	0.86	0.33	0.54	-	-	E
5381	Sekmeth	25	1.3	1.5	0.25	0.2	-	-	-	-	1.05	0.4	S
5381	Sekmeth	29	1.4	1.7	0.24	0.2	1	0.42	1.62	0.17	1.05	0.4	S
5381	Sekmeth	33	1.2	1.3	0.3	0.1	-	-	-	-	1.05	0.4	S
5381	Sekmeth	38	1.4	1.8	0.24	0.2	1	0.45	1.55	0.18	1.05	0.4	S
5381	Sekmeth	42	1.4	1.9	0.22	0.3	-	-	-	-	1.05	0.4	S
5381	Sekmeth	44	1.5	1.9	0.22	0.8	1	0.4	1.50	0.2	1.05	0.4	S
5604	(1992 FE)	18	0.7	(1.0)	0.3	-	0.7	0.3	1.10	0.12	-	-	V
5604	(1992 FE)	36	0.55	(1.0)	0.61	-	0.52	0.69	0.77	0.32	-	-	V
5587	(1990 SB)	19	4	1.1	0.25	0.1	3.4	0.35	6.70	0.09	-	-	Sq
5587	(1990 SB)	42	3.57	0.84	0.32	0.2	3.56	0.51	5.14	0.24	-	-	Sq
5751	Zao	49	2.3	(1.5)	0.36	-	1.8	0.58	2.53	0.29	-	-	E
6178	(1986 DA)	31	2.1	(1.0)	0.17	-	2	0.19	3.05	0.08	-	-	M
6489	Golevka	43	0.33	(1.0)	0.39	-	0.3	0.46	0.47	0.18	0.53	0.15	S
9856	(1991 EE)	36	1	1.15	0.3	0.23	0.85	0.42	1.40	0.16	-	-	S
14402	(1991 DB)	36	0.6	1.04	0.14	0.1	0.56	0.17	0.81	0.08	-	-	C
15817	Lucianotesi	14	0.32	(1.0)	0.64	-	0.3	0.73	0.47	0.29	-	-	E
16834	(1997 WU22)	59	2	(1.5)	0.3	-	1.51	0.53	2.06	0.29	-	-	S
19356	(1997 GH3)	5	0.91	0.98	0.34	0.1	0.83	0.41	1.45	0.13	-	-	S
19356	(1997 GH3)	31	1	(1.0)	0.29	-	0.95	0.3	1.40	0.14	-	-	S
25143	Itokawa	28	0.23	(1.0)	0.38	-	0.22	0.41	0.32	0.19	-	-	S
25143	Itokawa	108	0.37	(1.5)	0.19	-	0.2	0.61	0.22	0.54	-	-	S

25330	(1999 KV4)	3	2.55	1.06	0.084	0.17	-	-	-	-	-	-	B
25330	(1999 KV4)	16	2.7	1.3	0.08	0.3	1.26	0.1	4.16	0.03	-	-	B
25330	(1999 KV4)	54	3.21	1.5	0.052	0.2	2.34	0.098	3.41	0.046	-	-	B
33342	(1998 WT24)	60	0.37	(1.5)	0.5	-	0.28	0.84	0.38	0.48	0.41	0.4	E
33342	(1998 WT24)	67	0.34	0.9	0.59	0.1	0.32	0.68	0.40	0.43	0.41	0.4	E
33342	(1998 WT24)	79	0.44	1.5	0.35	0.16	0.32	0.66	0.38	0.48	0.41	0.4	E
33342	(1998 WT24)	93	0.5	1.85	0.27	0.13	0.31	0.77	0.36	0.53	0.41	0.4	E
35396	(1997 XF11)	30	0.89	1.3	0.32	0.8	0.75	0.45	1.16	0.19	-	-	E
35396	(1997 XF11)	53	0.91	1.2	0.31	0.1	0.81	0.39	1.07	0.22	-	-	E
35396	(1997 XF11)	63	1.18	1.8	0.18	0.2	0.83	0.37	1.05	0.23	-	-	E
1999FK21		35	0.59	0.91	0.32	0.4	0.58	0.33	0.85	0.15	-	-	S
1999NC43		59	2.22	2.86	0.14	0.5	1.22	0.47	1.62	0.27	-	-	Q
2000BG19		17	1.77	0.74	0.043	0.2	1.88	0.038	3.25	0.013	-	-	P
2000EV70		14	0.15	(1.0)	0.6	-	0.14	0.68	0.22	0.29	-	-	Q
2000PG3		2	4.6	(1.0)	0.042	-	3.9	0.059	8.59	0.012	-	-	D
2001HW15		11	0.18	(1.0)	0.43	-	0.16	0.54	0.27	0.2	-	-	-
2001FY		22	0.32	(1.0)	0.52	-	0.3	0.59	0.48	0.23	-	-	S
2001LF		45	2	1.4	0.05	0.1	1.5	0.08	2.50	0.03	-	-	C
2002AV4		70	1.5	1.6	0.37	0.25	1.1	0.73	1.40	0.43	-	-	-
2002BM26		60	0.84	3.1	0.023	0.4	0.41	0.094	0.57	0.05	-	-	P
2002CT46		23	0.16	(1.0)	0.32	-	0.15	0.36	0.24	0.15	-	-	Sr
2002QE15		50	1.49	(1.5)	0.24	-	1.15	0.4	1.63	0.2	-	-	S

Table 4-6 Radiometric diameter and albedos, compared with the one derived from radar observations.

If not otherwise stated, radiometric diameters and albedos are from this work. Other original data sources: (433), (1980), (3671): see Harris and Davies, (1999); (1862), (3200), (3554): see Harris, (1998); (2100), (9856): Harris et al., (1998). For (3671) we have taken the NEATM solution requiring $\eta = 3.1$ (see Harris and Davies, 1999). The FRM also provides a reasonable fit to the data for (3671), but it gives a much higher albedo of 0.30–0.35, which is seriously inconsistent with the taxonomic type of Bus and Binzel (2002). (25143) Sekiguci et al., (2002).

Taxonomic classes are from Bus and Binzel (2002) and from Binzel et al. (2002) with the exceptions of (4055) Magellan (Cruikshank et al., 1991) and (4660) Nereus (Binzel et al., 2004).

For 433 Eros results, given for lightcurve maximum and minimum, are from Harris and Lagerros (2002). The albedo from *NEAR Shoemaker* is 0.25 ± 0.06 (Veverka et al., 2000). Lightcurve effects have been taken into account where corresponding optical photometry is available; in all other cases included.

Radar diameter sources: (1566), (1580), (1627), (1862), (2100), (6178), (6489): Harris and Lagerros, (2002); (1620) Equivalent spherical diameter from shape model, Hudson and Ostro (1999); (5381): Nolan et al. (2003); (33342): Zaitsev et al. (2002). However, Di Martino et al. (2004) give indication of a larger diameter ~ 0.6 km. (1685) Ostro et al., (1983).

Other radar diameters at: http://echo.jpl.nasa.gov/~lance/asteroid_radar_properties/nea.radaralbedo.html

Analysis of results from thermal models: the observed albedo distribution of NEAs and the correlation of η with the phase angle

5.1 Foreword

This chapter is devoted to the analysis of results obtained from thermal model fits to the measured infrared fluxes of the NEAs observed in this study. Additional published radiometric diameters and albedos have been included to our data set. The albedo distribution of the observed NEAs is derived and correlation of albedos with taxonomic classes discussed.

Our data indicate a correlation of the NEATM best-fit parameter η with the phase angle. A linear dependence of the η -value versus the phase angle α , i.e. $\eta = (0.011 \pm 0.002)\alpha + (0.92 \pm 0.07)$ appear to describe the apparent color temperature of NEAs with common thermal properties. Some objects, however, with very low color temperature have been identified.

Furthermore, there is evidence that the slope of this linear function depends on the albedo of the objects, with the darker object of the C-complex having a steeper slope than the asteroids of the S-complex with higher albedo. This linear function can be used to estimate the default η -value in those cases where η cannot be constrained by a proper fit of the measured thermal infrared spectral energy distribution. This refinement to the default η value for the NEATM, produces infrared phase curves which are in agreement with observations of main belt asteroids and the NEA 433 Eros in the range $0^\circ < \alpha < 30^\circ$.

Our data set allows the thermal phase function of asteroids to be studied up to 80° of phase angle for the first time.

Comparison of STM-derived radiometric diameters with diameters estimated from radar allows a possible calibration of the STM for use with NEAs. I show that the use of the refined NEATM or the radar calibrated STM is equivalent to analyze radiometric observations up to $45^\circ - 50^\circ$ of phase angle.

5.2 The observed albedo distribution of NEAs

The mean albedo of the 32 objects observed in this program is 0.27 and it does not change when the mean albedo is calculated for all (46) asteroids with reliable radiometry listed in Table 4-6. This value is much higher than the mean albedo of all main-belt asteroids listed in the Supplemental IRAS Minor Planet Survey, SIMPS, database (Tedesco et al., 2002) which is around 0.1.

Tedesco et al. (2002) noted a different albedo distribution (see plot mean albedo vs. diameter), between the newly identified IRAS asteroids of the SIMPS and the original IMPS objects. The authors claim that this marked difference is due to a discovery bias in favor of objects being brighter in a magnitude limited discovery-survey. This might be our case as well. Luu and Jewitt (1989) describe how

a bias factor in favor of the discovery of S-type NEAs is important in defining the taxonomic type distribution of this population (see section 1.3 and Fig. 1.3 of this work and Binzel et al., 2002, for further details). Given their higher albedo, in limited magnitude surveys, S-type asteroids are more likely to be discovered. Moreover, the fall off of the apparent brightness of the darker C-types as a function of the solar phase angle is stronger than for S-types.

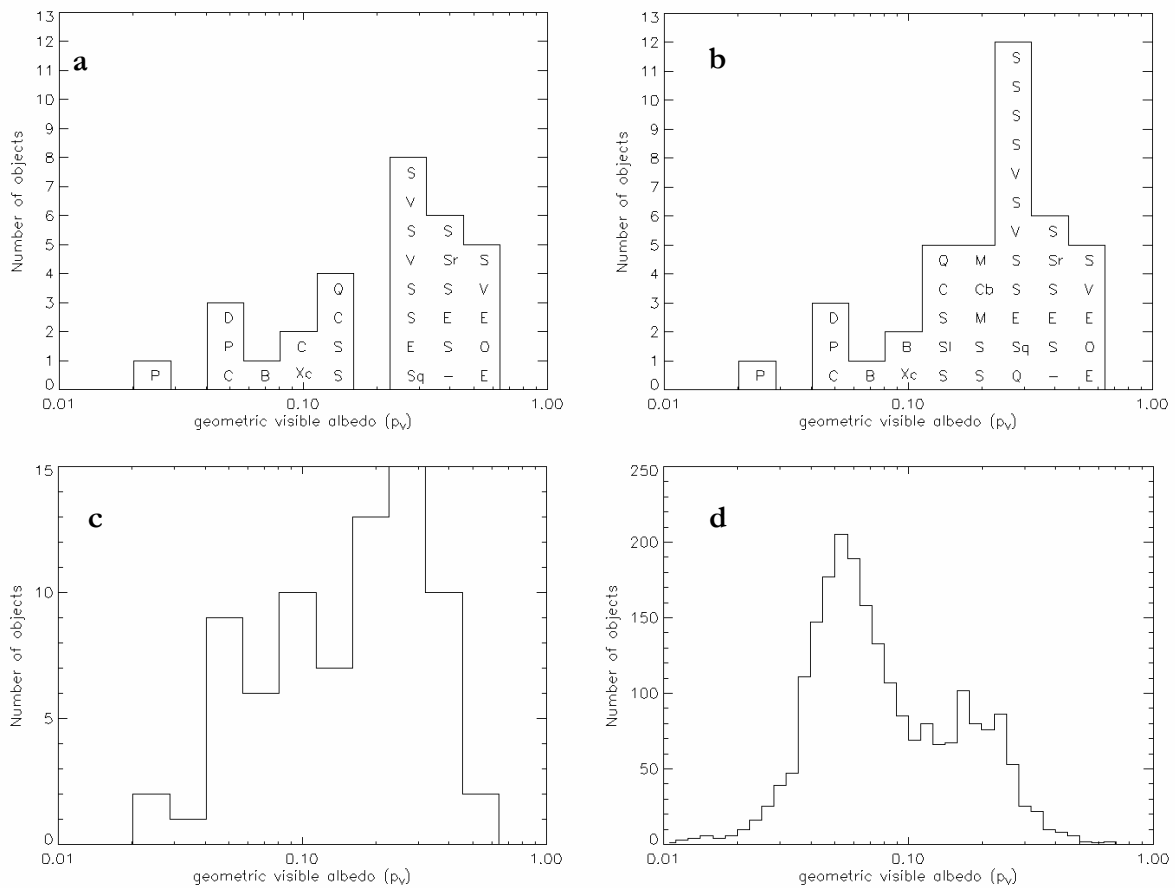


Fig. 5.1 Comparison of albedo distribution for the NEAs observed in this program (histogram **a** which contains 30 NEAs); all NEAs with radiometric reliable albedo (histogram **b** with 40 objects); SIMPS asteroids with diameter less than or equal to 10 km (**c** with 75 asteroids) and all SIMPS asteroids (**d**, with 2228 objects). In the first three histograms bins are 0.15-wide in logarithmic albedo, whereas in the last one they are 0.05-wide in logarithmic albedo. In the case of NEAs and SMASSII-asteroids the taxonomic class is displayed.

Therefore, since NEAs are often discovered at large phase angles, the coupling of the two effects might explain the lack of dark objects within the population known so far.

Fig. 5.1 shows the albedo distribution of the NEAs observed in this program (plot a) and of all NEAs for which reliable radiometric albedo is available (plot b) compared to that of all SIMPS asteroids

(plot d). We can notice in the NEA population the lack of dark asteroids with $p_V < 0.10$ which are the majority in the main belt population. 87% of the NEAs have albedo greater than or equal to 0.1. In the SIMPS database those asteroids with $p_V \geq 0.1$ are only 34%. The maximum of the NEA albedo distribution peaks in the bin roughly between p_V 0.2 and 0.3, whereas in the case of main belt asteroids the maximum lies at about $p_V = 0.06$. Moreover, the distribution of the albedos for only the S-type asteroids is different in the NEA population than in the main belt: MBAs are on average darker.

However, by comparing the SIMPS database with results obtained in this work, we are looking at asteroids which are on average dramatically different in size. Constraining the analysis to SIMPS asteroids with diameter smaller than or equal to 10 km (Fig. 5.1, plot e), about 70% of the objects are found to have p_V larger than 0.1 and the apparent albedo distribution plot is more similar to that derived for the NEA population (the maximum of the these two distributions, for example, falls in the same albedo-bin).

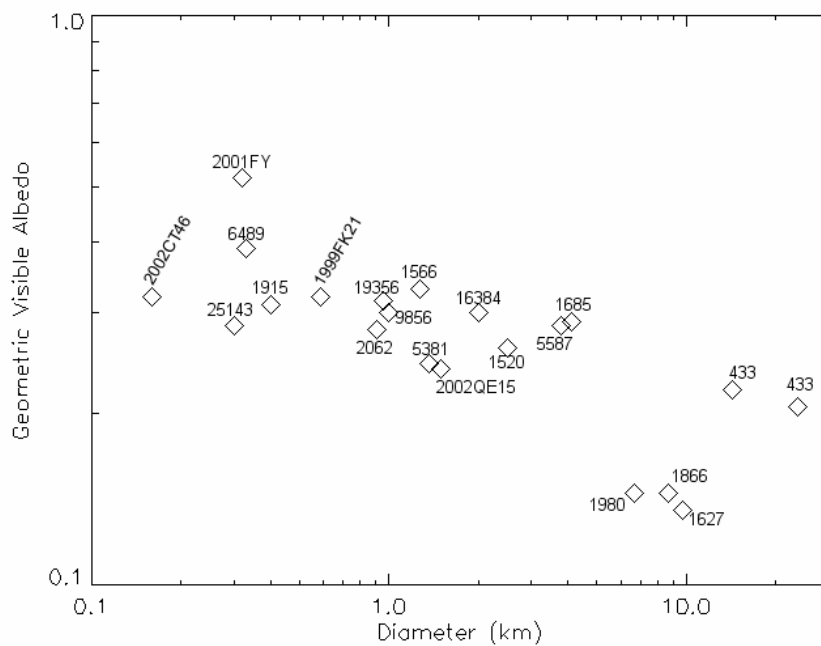


Fig. 5.2 Plot of the geometric visible albedo versus diameter derived by NEATM for S-type NEAs. Taxonomic classes included are ‘S’, ‘Sq’, ‘Sr’ and ‘Sp’. The plot suggests a significant trend of increasing albedo with decreasing size. The trend may be due to a bias in favor of the discovery and characterization of high albedo objects. In the case of 433 Eros results are shown at lightcurve maximum and minimum.

The apparent size dependence of the albedo in the IRAS data has been discussed by a number of workers and attributed to the lack of dusty regolith on small asteroids (see Tedesco, 1993). A rocky

surface should have a larger thermal inertia than that of a surface with a dusty regolith, thus causing the STM with its fixed value of 0.756 for the model parameter η to give erroneously high albedos.

We are aware that STM (with the fixed η -value of 0.756) produces radiometric albedos higher than the true value, if thermal inertia and rotation rate plays an important role in modifying the surface temperature distribution of small asteroids. Clearly, this effect is particularly important for NEAs which are observed at high phase angle (see Chapter 6). By using the NEATM, which adjust the η -value, we take into better account the modification to the surface temperature caused by the thermal inertia and rotation rate of NEAs. As we demonstrate in Chapter 6, NEATM albedos and diameters are more reliable than the ones derived by the STM. Nevertheless, objects with high albedo are the majority in our data base.

Moreover, albedos of the observed NEAs are not only on “average” higher than that of MBAs, but correlation of the albedo with size exists within the NEA population itself.

In Fig. 5.2 the albedos of 21 S-type NEAs are plotted against effective diameters. Our data suggest a trend of increasing albedo with decreasing size in agreement with Delbò et al. (2003) results. If this trend is real, it may be indicative of lack of space weathering on the recently exposed, relatively young surfaces of small objects.

However, a selection effect in favor of the discovery of brighter NEAs in a magnitude limited survey may explain such trend. A simulation of the NEA discovery process and the possible selection effect involved in the choice of the objects to be observed in the thermal infrared is an important future work that can clarify this issue.

5.3 Phase angle dependence of the observed color temperature

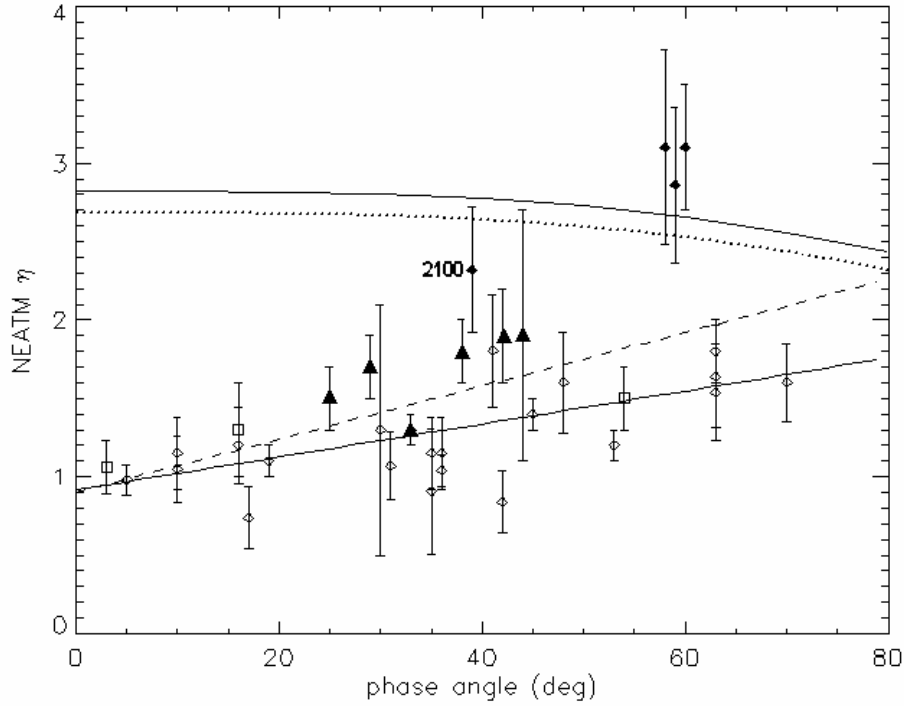


Fig. 5.3 Best-fit beaming parameter, η , from the NEATM fits plotted against solar phase angle, α . The continuous line represents a linear fit, $\eta = (0.011 \pm 0.002)\alpha + (0.92 \pm 0.07)$ to all values of η . Filled diamonds with error-bars at $\eta > 2$ are those data points considered anomalous by Delbò et al. (2003). Filled triangles are the η -values for 5381 Sekmeth and the dashed line represent their linear fit: $\eta = (0.017 \pm 0.013)\alpha + (0.9 \pm 0.03)$. Open squares represent the η -values for 25330 (1999 KV₄). Significant deviations of η from the linear fit may be due to the effects of unusually high or low thermal inertia and/or surface roughness, and/or an irregular shape, influencing the surface temperature distribution presented to the observer. The “evening/morning” effect probably contributes to the scatter of the points (see text). The dotted curve represents the expected η values for an FRM-like asteroid, whereas the continuous one corresponds to the η -values derived by fitting NEATM to the infrared continuum of a perfectly conducting smooth sphere in thermal equilibrium with the solar radiation.

Fig. 5.3 shows a plot of the η -value derived by the NEATM versus phase angle based on the results of this study and previously published results given in Table 4-6. The η -value represents the fourth power of the ratio between (1) the color temperature that an observer would derive for a smooth non-rotating sphere with each point of its surface in equilibrium with insolation and thermal emission, and (2) the actual color temperature derived from observations with both objects observed at the same phase angle: i.e.:

$$\eta = \left(\frac{T_{EQ}}{T_C} \right)^4 \quad (5-1)$$

It is clear that in the case of the observed NEAs the derived η is usually significantly larger than the value $\eta=0.756$ used in the STM of Lebofsky et al. (1989) and derived on the basis of observations of 1 Ceres and 2 Pallas. The larger η -values, compared with the value of 0.756 used in the IRAS STM for main-belt asteroids, are consistent with the results of previous authors suggesting that NEAs have larger surface thermal inertias in general than main-belt asteroids.

Moreover, the plot suggests a significant trend of increasing η -value with increasing solar phase angle and a bimodal η distribution at phase angles larger than $\sim 30^\circ$. While the majority of objects display relatively high color temperatures (low η) even at solar phase angles as large as $60-70^\circ$, a number of cases with η -values significantly larger have been found, indicating unusually low color temperatures for their surfaces.

5.3.1 NEAs with anomalous thermal properties ($\eta > 2$)

In those cases with $\eta > 2$ (shown in Fig. 5.3 with filled black diamonds and already identified by Delbò et al, 2003 as “anomalous”), the FRM best fits to the observed thermal continua are reasonably good, suggesting that the temperature distributions around the surfaces of these objects may be relatively smooth, with significant emission arising on the night side, due to high thermal inertia and/or high rotation rates. However, it is remarkable to note that two of the three objects with the highest η -values, namely 3671 Dionysus¹⁹ and 2002 BM₂₆, are fast rotators with periods around 2.7 hours. On the other hand, the other two high- η objects, namely 2100 Ra-Shalom and 1999 NC₄₃, are slow rotators (with periods of 19.8 h and at least 34 h, respectively). If their temperature distributions are well described by the FRM, Ra-Shalom and 1999 NC₄₃ must have exceptionally high surface thermal inertias comparable to, or exceeding, that of solid rock ($2500 \text{ J/m}^2 \text{ s}^{0.5} / \text{K}^1$, Jakosky, 1986).

The presence of objects with η larger than 2, with very different rotational period and the evidence for a bimodal distribution of η -values at moderate and large phase angles, suggest that the interpretation of the large η -values in terms of rotation rate and thermal inertia is an oversimplification.

Moreover, Fig. 5.3 suggests that in general the FRM does not describe properly the thermal characteristics of the asteroids in our database. The dotted line intersecting the η -axis at the value of 2.6

¹⁹ The FRM solution for 3671 from Harris and Davies (1999) requires $p_v > 0.3$, which is inconsistent with the taxonomic class Cb from Bus and Binzel (2002).

and decreasing towards larger phase angles represents the η -value expected for an FRM-like asteroid. The fact that the η -values derived from our observations are in the majority significantly below the dotted line is an indication that the FRM implies a color temperature which is too low with respect to that derived for the asteroids in our database. On the other hand, it is remarkable that the color temperature derived for 3671 Dionysus, 2002 BM₂₆ and 1999 NC₄₃ are significantly lower than the one implied by the FRM. In the case of 1999 NC₄₃, which has a high amplitude lightcurve indicative of a very irregular shape, the explanation for the high η -value may lie in shape or shadowing effects that lead to less thermal emission being received from the observed parts of the surface than predicted by the spherical geometry on which the simple thermal models are based (see Delbó and Harris, 2002). The importance of such effects increases with phase angle.

It is remarkable that even a perfectly conducting smooth sphere (PCSS), in thermal equilibrium with the solar radiation, would display a color temperature warmer (lower η -value) than the ones derived for 3671 Dionysus, 2002 BM₂₆ and 1999 NC₄₃. In fact the η -value that the NEATM would derive by fitting the thermal infrared continuum of a PCSS follows the continuous line drawn in Fig. 5.3 intersecting the η axis at the value of 2.82.

5.3.2 NEAs with “common” thermal properties

It is clear that the majority of objects display relatively high color temperatures (low η) even at solar phase angles as large as 60-70°. Delbò et al. (2003) noted that a linear function can describe the dependence of the η -values with phase angle for NEAs with “common” thermal properties. They have fitted a straight line to the points with $\eta < 2$ separating out the four points with $\eta > 2$ and derived a dependence of the η -value as a function of the phase angle α such that $\eta = 0.01\alpha + 0.81$. Here, I have included in the analysis new results from the ESO and the NASA-IRTF observation campaigns. Excluding objects with “anomalous” color temperature ($\eta > 2$) I have obtained the best linear fit of $\eta = (0.009 \pm 0.002)\alpha + (0.89 \pm 0.07)$. Given the uncertainties, the fit is in good agreement with the one by Delbò et al. and the η -value at zero degree of phase angle is slightly larger than the one obtained by Delbò et al. and significantly higher than that adopted by Lebofsky et al (1986) for use in the STM. Including also those points with $\eta > 2$ the slope of the linear fit and its value at $\alpha = 0^\circ$ become slightly larger: i.e. $\eta = (0.011 \pm 0.002)\alpha + (0.92 \pm 0.07)$, though, given the error bars of the data points, both results are still in good agreement.

If we express the phase angle dependency of the η -value with the linear relation $\eta = \beta_\eta \alpha + \eta_0$, our data-set suggests the evidence for the β_η and the η_0 parameters to be a function of the object albedo. For

the brightest objects i.e. those with $p_V > 0.25$ the best linear fit is obtained with $\beta_\eta = 0.006 \pm 0.002$ and $\eta_0 = 1.0 \pm 0.1$. A significant different value for the β_η parameter i.e. $\beta_\eta = 0.016 \pm 0.003$, but with η_0 only slightly smaller ($\eta_0 = 0.8 \pm 0.1$) can be derived for those objects with $p_V < 0.25$. If we consider only dark objects ($p_V \leq 0.1$) the slope of the linear fit keeps at the constant value $\beta_\eta = 0.016 \pm 0.006$, while the value of η_0 decrease to 0.6 ± 0.2 . This latter result might be somewhat questionable given the low number of data points (four) included in the linear fit.

The above results indicate that the linear relation $\eta = (0.011 \pm 0.002)\alpha + (0.92 \pm 0.07)$, can give the best default value for η as a function of the phase angle to use with NEATM when data at only one or two thermal wavelengths are available and spectral fitting is not possible. Clearly such a relation allows the NEATM to be used to make more accurate prediction of the expected infrared flux from an asteroid, provided it has “common” thermal properties.

5.4 The infrared phase curve of NEAs with “common” thermal properties

It is known from observations that asteroids show infrared phase curves which are approximately linear in the range $0-30^\circ$ with slopes of about 0.01 mag/degree Morrison, 1976; Matson, 1971; Lebofsky and Spencer, 1989). Moreover, Murdock, 1974 noted that in the case of Mercury, the curves of measured effective brightness temperature as a function of phase angle are steeper than those of a smooth sphere.

In this section it is shown that the infrared phase curves of NEAs with “common” thermal properties – i.e. those with an η -value following the linear function derived in the section 5.3.2 – are steeper, than those of a Lambertian emission model and in better agreement with observations. Fig. 5.4 shows infrared phase curves (the magnitude scale is set equal to zero at $\alpha = 0^\circ$) calculated at $\lambda = 11.7 \mu\text{m}$ for a spherical asteroid at the heliocentric distance of 1AU. The temperature distribution on the surface of the object is described by the formula of thermal equilibrium with solar radiation at each point: i.e.

$$T_{ss} = \left(\frac{1}{r^2} \frac{S_\oplus (1-A)}{\sigma \epsilon \eta} \right)^{1/4} \quad (5-2)$$

$$\begin{cases} T(\theta) = T_{ss} [\cos(\theta)]^{1/4} & \text{for } \theta < \pi/2 \\ T(\theta) = 0 & \text{for } \theta \geq \pi/2 \end{cases}$$

where θ is the sub-solar colatitude. The total radiated flux $F(\lambda)$ is obtained, as usual, by integrating numerically the actual thermal flux an observer would detect from the illuminated portion of the sphere

visible to him at the given solar phase angle (for further details see Delbo & Harris, 2002 Eqs. 19-21). However, the η -value is assumed here to be a linear function of the solar phase angle α with the law

$$\eta = \beta_{\eta} \times \alpha + \eta_0 \quad (5-3)$$

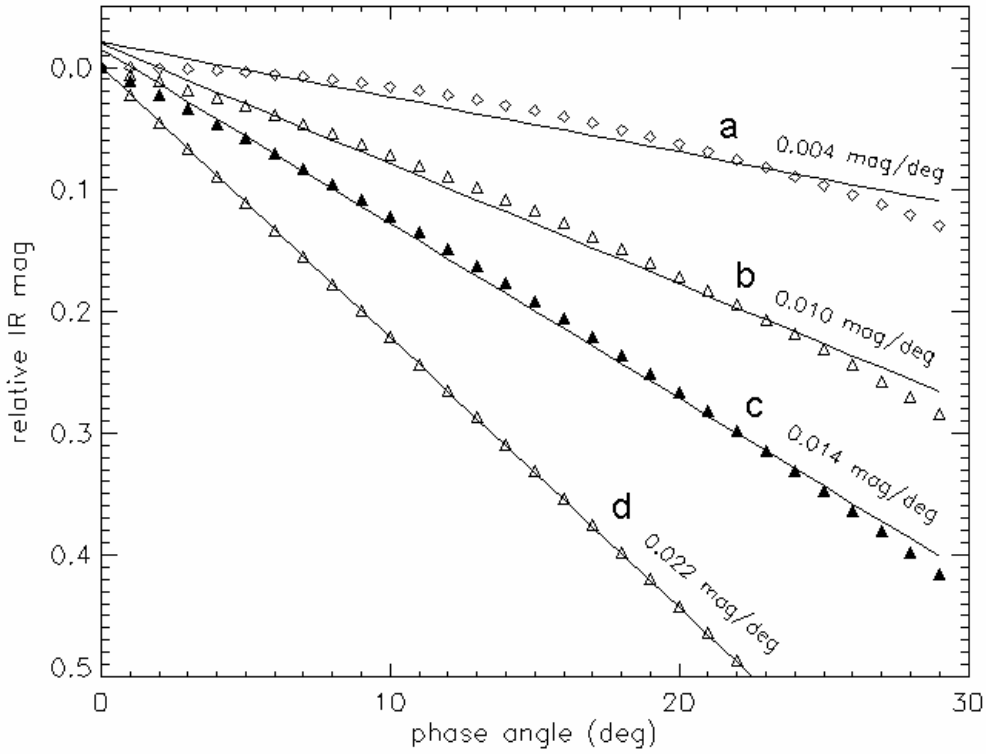


Fig. 5.4 Infrared phase curves for a spherical asteroid at the heliocentric distance of 1AU with a STM-like temperature distribution. However, the η -value is varied as a linear function of the phase angle α : $\eta = \beta_{\eta} \alpha + \eta_0$. See the text for further details.

The topmost curve, the one labeled with “a”, in Fig. 5.4 was calculated for $\beta_{\eta}=0$ and $\eta_0=1$ (i.e. $\eta=1$ and constant for every α). This curve is not sensitive to changes of η_0 . Objects at different heliocentric distance would thus display the same phase curve. Curve “b” was calculated for $\beta_{\eta}=0.006$ and $\eta_0=1.0$, curve “c” for $\beta_{\eta}=0.011$ and $\eta_0=0.92$, curve “d” for $\beta_{\eta}=0.016$ and $\eta_0=0.6$. The straight line passing through the points is the best linear fit in the range $\alpha=0^{\circ}$ - 30° to the model curves. The slope of this linear fit is the equivalent of the thermal phase coefficient, β_E , that Lebofsky and Spencer (1989) and Matson (1971) have derived for main-belt asteroids. A phase angle dependence of the η -value, as the one obtained in this work, yields a steeper phase function than the one obtained by assuming Lambertian emission at the surface of the asteroid. Table 5-1 shows the value of β_E at $11.7 \mu\text{m}$ for different values of β_{η} and η_0 for an asteroid at 1 AU from the Sun.

β_r	η_0	β_E (mag/deg)	Note
0	1.0	0.004	Lambert
0.006	1.0	0.010	$p_V > 0.25$
0.011	0.92	0.014	mean value
0.016	0.60	0.022	$p_V < 0.1$

Table 5-1 The infrared phase coefficient, β_E , obtained as a linear fit to the phase curves produced by using the NEATM

Matson (1971) observed that main-belt asteroids had solar phase coefficient β_E in the thermal infrared that ranged from about 0.005 to 0.017 mag/deg. A mean value of 0.01 mag/deg has been used in the STM to correct measured thermal fluxes to the zero phase assumed by this model (Lebofsky and Spencer, 1989). Morrison (1976) analyzed infrared observations of 433 Eros obtained at $\alpha < 40^\circ$ before and after opposition and obtained an infrared phase slope of about 0.008 mag/deg. This value is in good agreement with the lunar-type model for 4 Vesta computed by Matson (1972).

The linear relation of the η -value may be used as the default value for η when it is not possible to derive it via a fit of the thermal infrared continuum. Such relation determines a dependence of the infrared flux with phase angle which mimics, in the range $0^\circ < \alpha < 30^\circ$ the measured phase curves of main belt asteroids and of 433 Eros. The mean value for slope of the infrared phase curve is 0.011 mag/deg in the case of those NEAs analyzed in this work.

5.5 Comparison of radiometric diameters with radar

Uncertainties in thermal modeling usually exceed the formal errors resulting from the scatter of the flux measurements. Comparison of diameters derived by means of other techniques such as radar offers the opportunity to test the thermal models we have adopted and estimate the overall errors involved in their use. In this section the relative error between radiometric diameters ($D_{\text{radiometry}}$) and radar diameters (D_{radar})- i.e. $(D_{\text{radiometry}} - D_{\text{radar}}) / D_{\text{radar}}$, has been calculated for those asteroid for which size estimates are available from radar observations. Original source for each radar diameter is given in Table 4-6. The error bars of Fig. 5.5, Fig. 5.6 and Fig. 5.7 were calculated assuming a 15% uncertainty on radiometric diameters and the formal error of radar sizes, $\sigma_{D_{\text{radar}}}$. A 15% uncertainty on radar diameters was also assumed in those cases where the diameter error is not available from the original source. The formal error of the quantity “relative diameter error” is given by Eq. 5-4.

$$\sigma_{relative_diameter_error} = \sqrt{\left(\frac{0.15 * D_{radiometry}}{D_{radar}}\right)^2 + \left(\frac{\sigma_{D_{radar}} D_{radiometry}}{D_{radar}^2}\right)^2}, \quad (5-4)$$

For those asteroids with radiometric observations available at different geometries, the relative diameter error was calculated for each observation. For example, three data points are drawn for the asteroid 433 Eros. In that case radiometric measurements were obtained at lightcurve maximum and at lightcurve minimum and at two different phase angles, namely 10° and 31° .

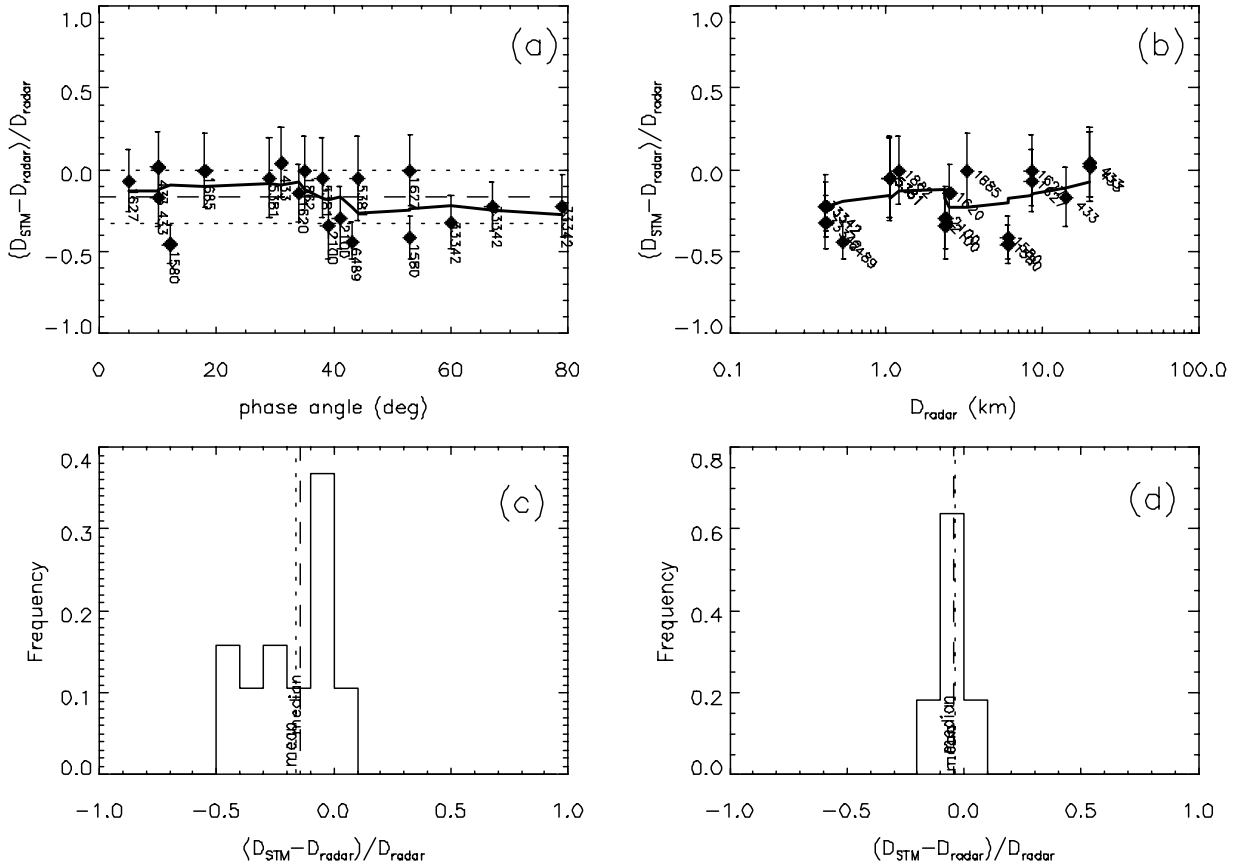


Fig. 5.5: Comparison of STM diameters with radar ones as a function of the solar phase angle (a) and diameter (b) for those asteroids observed at phase angles less than or equal to 80° . For 433 Eros results are given at lightcurve maximum and at lightcurve minimum. A systematic error of -16% is evident between the two sets of data. The RMS fractional difference between the STM diameters and diameters derived from radar measurements is of 16%. No clear trend of the relative error with phase angle is evident. Error bars were calculated assuming a 15% uncertainty on STM radiometric diameters and 10% uncertainty on the radar one if such information was not available from the original source in the literature. The thick continuous line on plot (a) and (b) was obtained with a 6-element central running box average. Plot (c) shows the histogram of the relative error distribution with superimposed the mean and the median values. Plot (d) shows how STM diameters are in good agreement with radar ones if asteroids 2100, 1580, 6489 and 33342 are removed from the sample.

The radiometric diameter of 6489 Golevka is a new value derived by applying the thermal models to infrared observations obtained at the NASA-IRTF during the June 2003 apparition. Although the new observations have been obtained at a phase angle of 43° , a value much smaller than the extreme case of 90° at the time of Mottola et al. (1997) UKIRT observation, the radiometric diameter is still almost 40% smaller (in the case of the NEATM and the STM) than the value derived by the radar.

In Fig. 5.5 the relative diameter errors of the STM are plotted against phase angle and size. STM-derived diameters are on average significantly smaller than radar diameters: a systematic error with a mean difference of about 16% and an RMS fractional difference of 16% is evident between the two sets of data. This latter value is in good agreement with the typical STM diameter uncertainty of 15% that we have assumed as the result of thermal modeling. No clear trend of the error with the phase angle is visible, although from the plot (b) of Fig. 5.5, it looks like that the STM gives more accurate diameters in the case of large NEAs. It is worth to point out that the NEAs 2100 Ra-Shalom, 1580 Betulia, 6489 Golevka and 33342 (1998 WT₂₄) carry the largest contribution to the deviation from the mean and the median value of the distribution from zero and appear to have STM radiometric diameter significantly smaller than the radar ones. In fact, the mean difference between STM derived diameters and radar one reduces to -5% with RMS equal to 6% if those asteroids are excluded. This might be an indication that the STM fails to reproduce the thermal properties of those asteroids. In fact, large η -values have been derived in those cases, which is an indication of low color temperature. The STM fits to the thermal continua measured for those asteroids is poor. It is possible that shadowing or shape effects may invalidate the application of simple thermal models in such cases (see Delbó and Harris, 2002), and it is clear that an alternative explanation to that of having large thermal inertia has to be considered for those objects (see section 5.3.1).

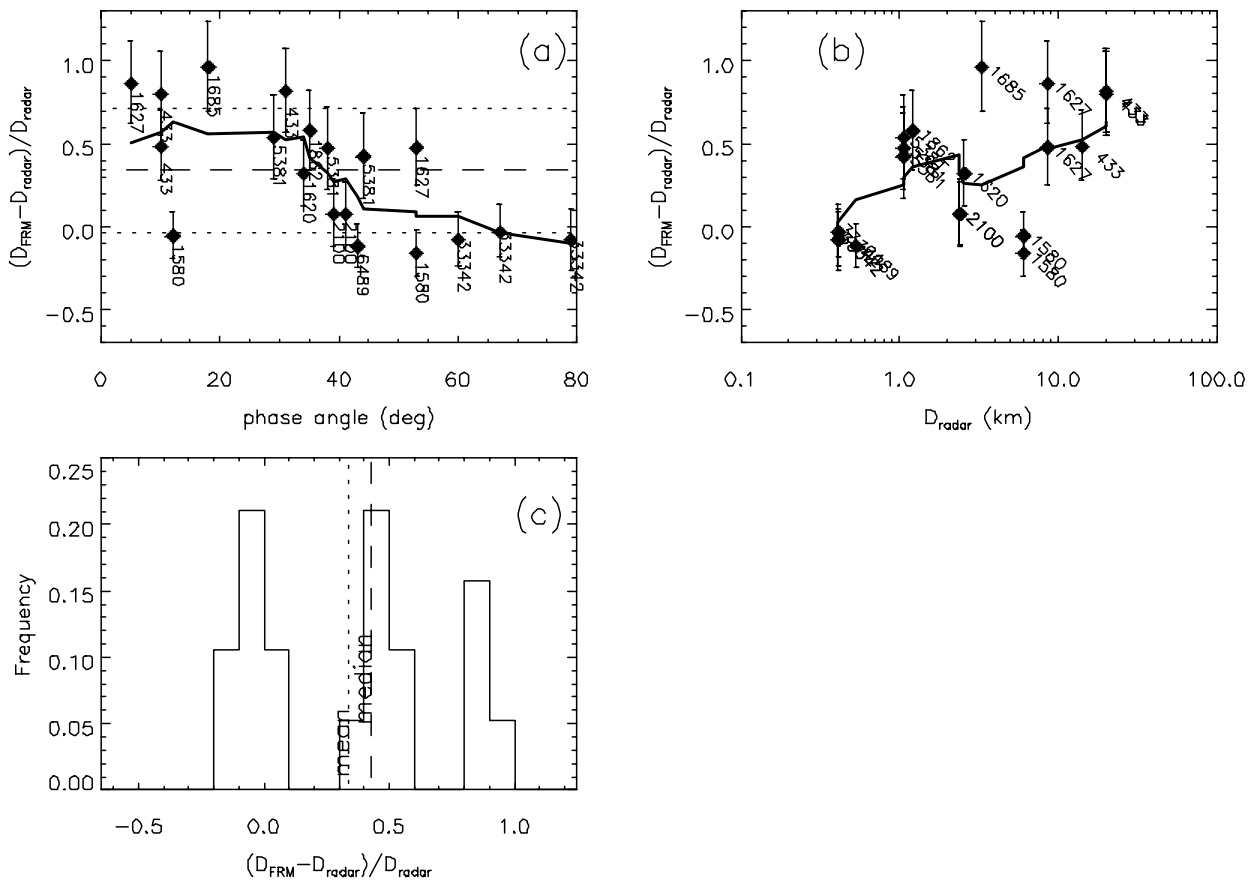


Fig. 5.6 Comparison of FRM diameters with radar ones as a function of the solar phase angle (a) and diameter (b) for those asteroids observed at phase angles less than or equal to 80° . For 433 Eros results are given at lightcurve maximum and at lightcurve minimum. A systematic error of +35% is evident between the two sets of data. The RMS fractional difference between the FRM diameters and diameters derived from radar measurements is of about 40%. There is a clear trend of the relative diameter error with the phase angle and with the diameter. Error bars were calculated assuming a 15% uncertainty on FRM radiometric diameters and 10% uncertainty on the radar one if such information was not available from the original source in the literature. The thick continuous line on plot (a) and (b) was obtained with a 6-elements central running box average. Plot (c) shows the histogram of the relative error distribution with superimposed the mean and the median values.

A large discrepancy between radar and FRM-derived diameters is clearly visible in Fig. 5.6. A correlation of the diameter errors with the phase angle is evident even excluding asteroids 2100, 1580, 6489 and 33342 for which the FRM produces results consistent with radar ones. It is remarkable that the FRM fails to reproduce radar diameter for those asteroids which were observed at low or moderate phase angle.

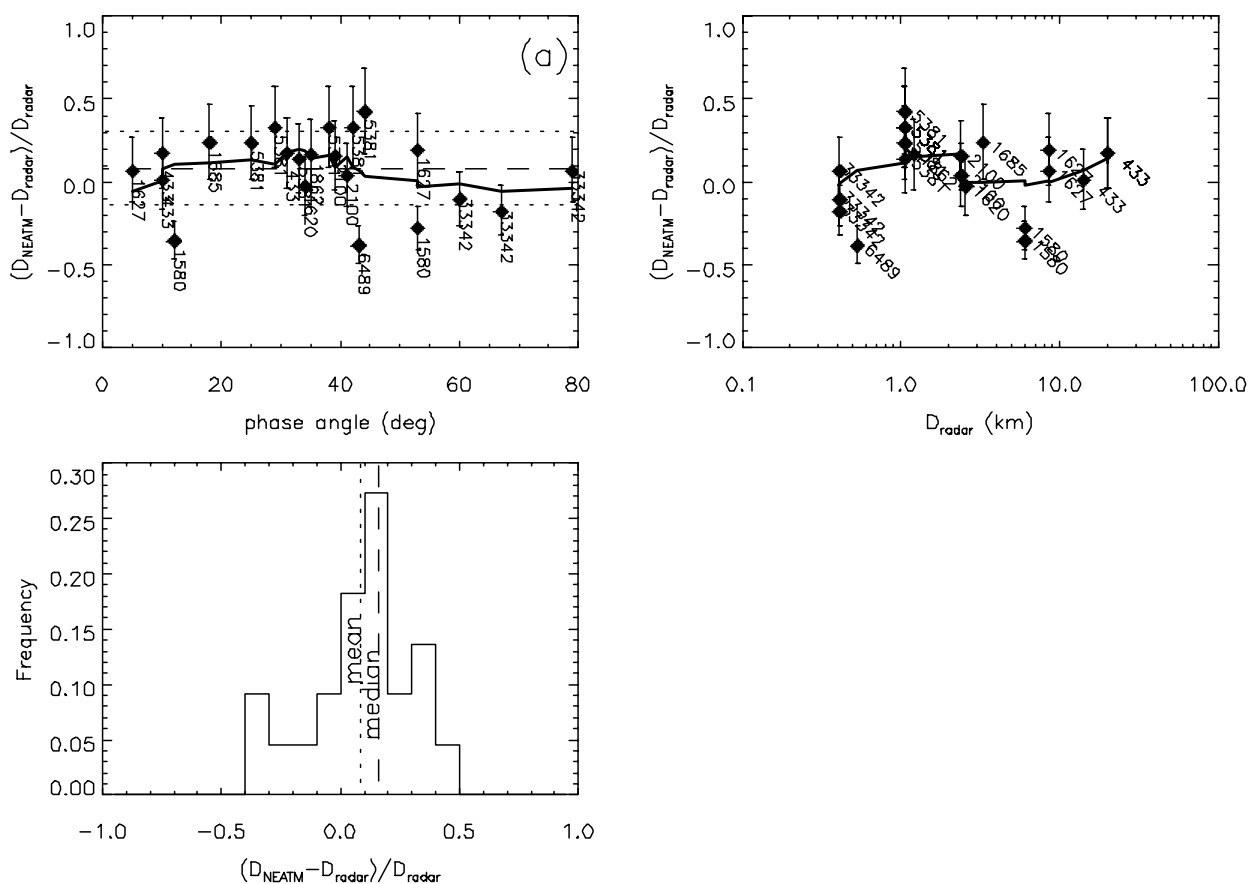


Fig. 5.7 Comparison of NEATM diameters with radar results as a function of the solar phase angle (a) and diameter (b) for those asteroids observed at phase angles less than or equal to 80° . For 433 Eros results are given at lightcurve maximum and at lightcurve minimum. A systematic error of +8% is evident between the two sets of data. The RMS fractional difference between the STM diameters and diameters derived from radar measurements is of about 20%. No clear trend of the relative error with phase angle and size is evident. Error bars were calculated assuming a 15% uncertainty on STM radiometric diameters and 10% uncertainty on the radar one if such information was not available from the original source in the literature. The thick continuous line on plot (a) and (b) was obtained with a 6-elements central running box average. Plot (c) shows the histogram of the relative error distribution with superimposed the mean and the median values.

In Fig. 5.7 NEATM relative errors with respect to radar diameters are plotted as a function of the phase angle and the diameter. The mean relative error is of +8% between the two sets of data. The RMS fractional difference between the NEATM diameters and diameters derived from radar measurements is of 20%. A gaussian function of the form $A \times \exp(-(x-x_0)^2 / (2\sigma)^2)$ best fits to the relative error distribution with a σ parameter equal to 0.17 and a mean value $x_0=0.08$. The NEATM mean relative error of 0.08 ± 0.04 (the error of the mean is σ / \sqrt{N}) is therefore significant and indicates a systematic error between radar and NEATM diameters.

5.6 On the recalibration of the STM for NEAs

Comparison of STM-derived radiometric diameters with diameters estimated from radar observations offers the opportunity to calibrate the STM for use with NEAs. Despite its simplicity STM has proved to produce diameters in good agreement with those derived from occultation measurements in the case of large main-belt asteroids (see Harris and Lagerros, 2002). However, STM results depend on the assumed η -value. In the STM of Lebofsky et al (1986) η is set equal to 0.756. This value was derived by constraining the thermal model to match the occultation diameters of 1 Ceres and 2 Pallas and their thermal infrared fluxes measured at 10 μm . η takes account of effects that alter the apparent day side temperature distribution compared to that of a perfectly smooth, non-rotating sphere, such as the enhanced sunward thermal emission due to surface roughness and the fact that in reality all asteroids rotate and thus radiate some of their thermal emission on the night side. In practice η can be considered as a normalization or calibration factor. However, there is no reason to assume that an η -value of 0.756 makes the STM to produce reliable results for all small bodies in our solar system. For example, Morrison (1973) and Morrison and Chapman (1976) determined a beaming factor of about 0.86 from stellar and lunar occultation of the Jovian satellites and of Iapetus. Spencer et al (1989) determined a disk integrated η -value of 0.72 for the Moon.

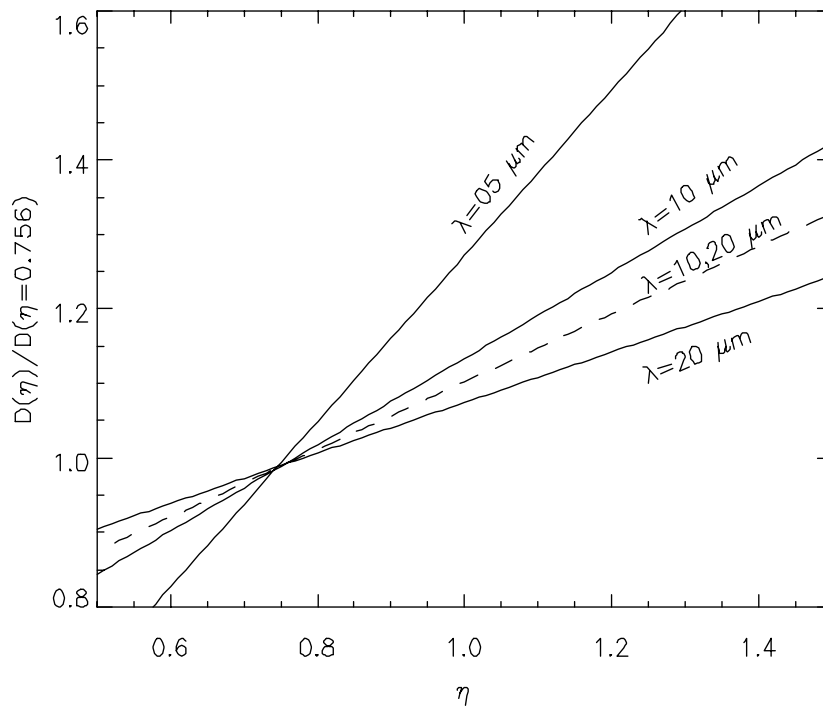


Fig. 5.8 Dependence of the STM-derived radiometric diameter at wavelengths of 5, 10 and 20 μm as a function of the beaming parameter η . Dashed line was obtained by fitting the STM simultaneously to 10 and 20 μm fluxes.

To produce the results of Fig. 5.5 the standard η -value of 0.756 was adopted. However, doing so the STM underestimates radar diameters by a factor between 5 and 15% depending on whether the asteroids 2100 Ra-Shalom, 1580 Betulia, 6489 Golevka and 33342 (1998 WT₂₄) are excluded.

By assuming a larger η -value STM-derived diameters become larger (and geometric albedo consequently smaller). I have studied the dependence of the radiometric diameter as a function of the model input parameter η when the STM is used to fit thermal infrared fluxes obtained at one wavelength. Fig. 5.8 shows this functional dependence: the STM-derived diameter divided by the diameter obtained by setting η equal to 0.756 is plotted against the input η value. This calculation was carried out at the wavelengths of 5, 10 and 20 μm . These results are shown with continuous lines. Dashed line was obtained by fitting the STM simultaneously to multi-wavelength fluxes obtained at 10 and 20 μm .

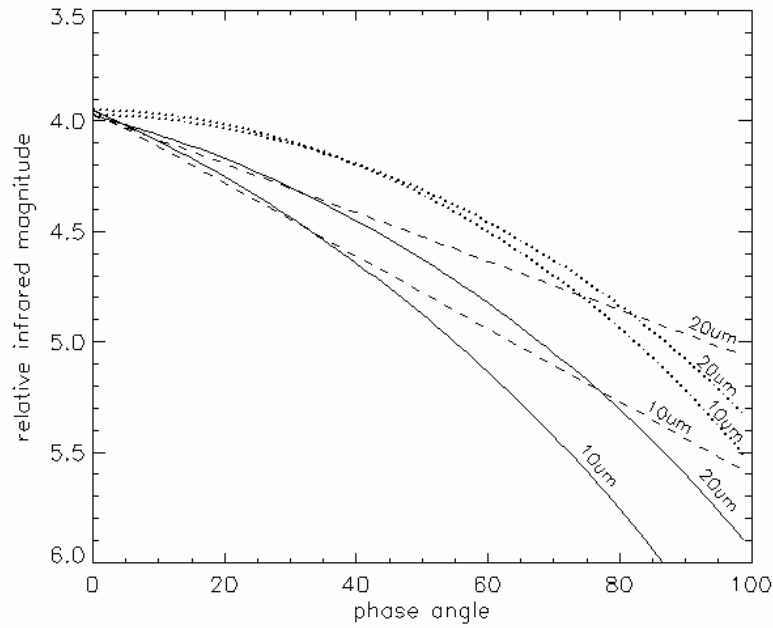


Fig. 5.9 Infrared phase curves in terms of relative infrared magnitudes for a spherical asteroid calculated at 10 and 20 μm . Continuous line: NEATM with $\eta=0.011\alpha+0.9$ where α is the phase angle and η the beaming parameter (see text). Dashed line: STM for which $\eta=0.9$ was assumed. The 10 μm phase curve was obtained with a β_E -value of 0.015 mag/degree, whereas for the 20 μm curve β_E was set equal to 0.011 mag/degree. Those value were chosen to fit the NEATM phase curve in the range $0^\circ < \alpha < 30^\circ$. Dotted lines represent the phase curve of a NEATM-like asteroid with a fixed η -value of 0.9.

From Fig. 5.8 it is evident that setting η to a value between 0.85 and 0.95 yields a resulting diameter between 5 and 15% larger on average than the value the STM derives with $\eta=0.756$.

Furthermore, Fig. 5.8 shows how this calibration is a function of the wavelength at which the thermal model is used. Radiometric diameters obtained at $20\mu\text{m}$ are less sensitive to change in the η parameter (the slope of the diameter variation with η being shallower than the slope at $10\mu\text{m}$). It is worth to remark here that an η value between 0.85 and 0.95 is close to the η_0 parameter derived in section 5.1 where the phase function of the NEATM has been studied at a wavelength of $11.7\ \mu\text{m}$. Since both the STM and the NEATM assume the same temperature distribution on the spherical asteroid, it is clear that η_0 represent the STM η value. They should have therefore the same numerical value. In Fig. 5.9 infrared phase curves were calculated at 10 and $20\ \mu\text{m}$ using NEATM but forcing the η -value to change with the phase angle α according to the relation $\eta=0.011\times\alpha+0.9$. As discussed in section 5.4 those phase curves can be very well approximated in the range $0<\alpha<30$ degrees by a linear relation the slope of which is the β_E parameter. The best fit value for β_E in the range $0<\alpha<30$ degrees was found to be 0.015 mag/deg at $10\ \mu\text{m}$ and of 0.011 mag/deg at $20\ \mu\text{m}$. Instead of using the standard infrared phase coefficient of 0.01 mag/deg of the STM, I have adopted the previously determined values to calculate the 10 and $20\ \mu\text{m}$ infrared magnitude which have been plotted in Fig. 5.9 with dashed lines. The STM η was set to 0.9 for this calculation.

The resulting NEATM and STM phase curves are in very good agreement up to a phase angle of about 50 degrees where the error is within 0.1 magnitudes (i.e. $\sim 10\%$ in term of flux). At $\sim 70^\circ$ the difference between NEATM and STM phase curves approach 0.25 mag ($\sim 25\%$ in flux) at $10\ \mu\text{m}$ and about the same value at $20\ \mu\text{m}$. If thermal infrared data do not the η -value to be properly fit, in section 5.2 a default relation $\eta=0.011\times\alpha+0.9$ has been proposed. However, the use of the STM with $\eta=0.9$ and $\beta_E=0.013$ mag/deg gives results within measurement errors.

5.7 Correlation of radiometric albedos with solar phase angle

Harris (1998) showed that, in the majority of cases, neither the STM nor the FRM provide a good fit to the observed thermal infrared continuum of NEAs. In those cases, he demonstrated that a better fit to the observed spectral distribution of the energy could be achieved by using the NEATM.

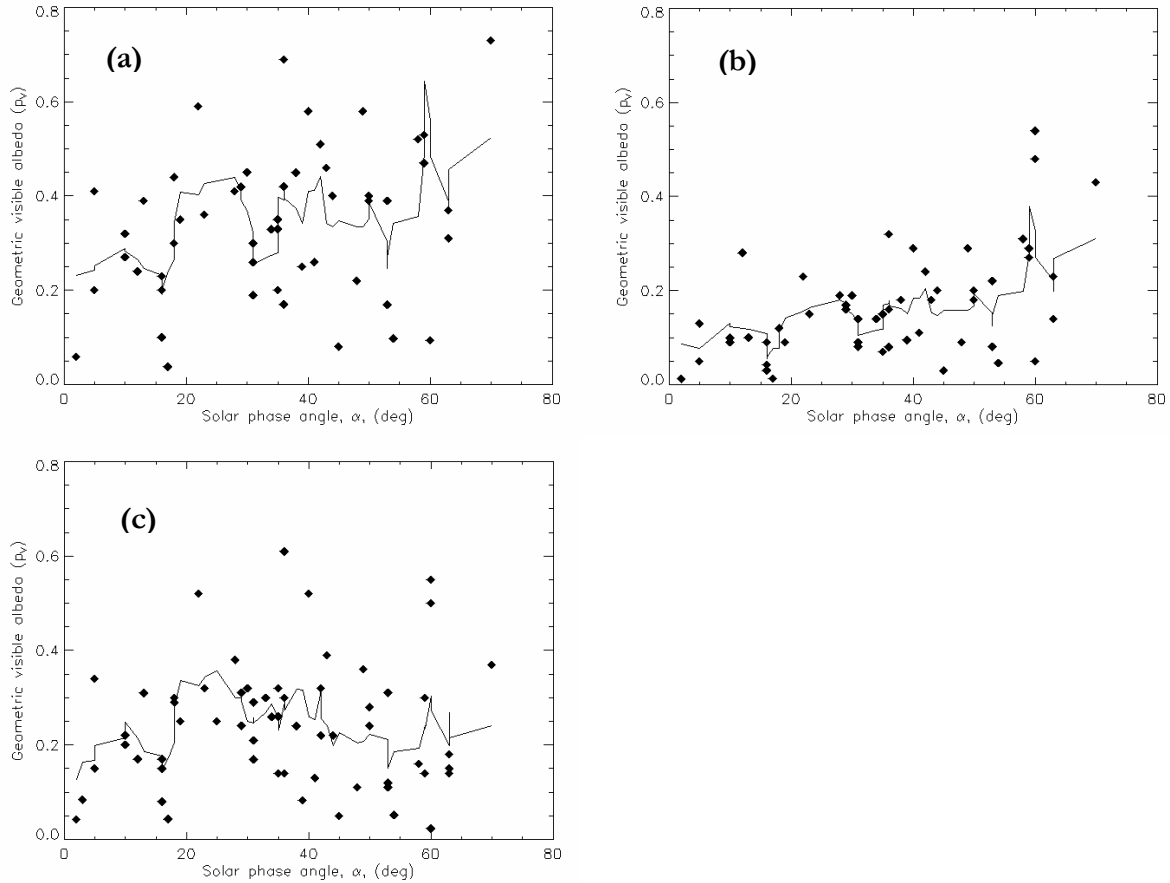


Fig. 5.10 Plot of the geometric visible albedos versus solar phase angle for each radiometric observation. a) STM; b) FRM; c) NEATM. Continuous lines were calculated by taking the 5-elements-wide central moving average of the data points in each plot.

In Fig. 5.10 plots a) and b) clearly show a second problem that affects the application of both the STM and the FRM to the study of NEAs. In that figure I have plotted the thermal model-derived albedo as a function of the solar phase angle at which each observation has been obtained. In both cases a trend of increasing albedo with increasing phase angle is visible. If the thermal model phase function does not properly account for the actual variation of the infrared flux with the phase angle, resulting diameters and albedos are correlated with this angle. Higher albedos derived at higher phase angle result from an underestimation of the infrared phase curve. It is clear that is the case of the FRM, for which no flux correction for the phase angle applies (flat model phase curve). In the case of the STM, it

appears the 0.01 mag/deg correction to be not large enough to account for the actual drop of infrared flux that NEAs display. Roughly speaking, plot a) of Fig. 5.10 shows that there is almost a factor of 2 increment in the average albedo in about 70° of phase angle. Since within the thermal model, diameter and albedo are constrained by the H value, the variation of the infrared flux is almost inverse proportional to variation of the albedo. A factor of 2 in terms of flux corresponds to 0.75 magnitudes, and in the hypothesis that the observed trend of Fig. 5.10 is linear, an extra term of ~0.01 mag/deg should be added to the standard β_E -value to make the STM able to account for the actual infrared phase function of NEAs.

The distribution of albedos derived by means of the NEATM appears to have no correlation with the phase angle, indicating that the procedure used to model observations at non-zero phase angle does not introduce systematic errors in the final results. I remind here what that procedure is about: In the NEATM the solar phase angle is taken account of by calculating numerically the actual thermal flux an observer would detect from the illuminated portion of a smooth sphere visible to him at a given solar phase angle, assuming that the night side does not irradiate. Further, the model temperature is modified, by changing η , to force consistency with the observed apparent color temperature of the asteroid. In those cases where the infrared data are not good enough for η to be constrained properly, η is assumed to be equal to 1 for phase angles less than 45° and equal to 1.5 beyond that value. However, one of the crucial issues concerning the reliability of the NEATM is to assess the error incurred by ignoring thermal emission from the night side. Ignoring the night side flux causes the resulting diameter to be overestimated and the albedo consequently underestimated. If such an error had played a major role, one would expect to see a trend of decreasing albedos with increasing phase angle. Results of this work indicate that this is not the case up to $\alpha \sim 60^\circ$.

5.8 Conclusions

The beaming parameter, η , is phase-angle dependent and, on average, significantly higher than the value 0.756 adopted by Lebofsky et al. (1986) in their version of the STM. The best linear fit to the derived η values is:

$$\eta = (0.011 \pm 0.002)\alpha + (0.9 \pm 0.07) \quad (5-5)$$

where α is the phase angle. A refinement of the NEATM is proposed by using the linear relation (5-2) when it is not possible to derive η via a fit of the thermal infrared continuum. However, $\eta \sim 0.9$ appears to be valid at phase angles approaching zero, where the uncertainties associated with use of the STM are

at a minimum. This suggests that the assumption of the STM of low thermal inertia may be valid in most cases.

The phase angle function of the η value appears to be dependent on the asteroid albedo. Darker objects have steeper β_η slopes and lower η_0 values. So, high albedo objects have a less-pronounced beaming effect i.e. η_0 values closer to unity and less dependence of η on phase angle. We argue that the less-pronounced beaming effect might be due to their relatively lower equilibrium temperatures. This fact explains why, even at high phase angles, η could remain low (e.g. the case of the NEA 5587). An alternative explanation is that darker objects have more pristine and rougher surfaces leading to a stronger beaming effect than objects with higher albedos.

The fact that our sample contains no object observed at a low phase angle for which η is large (> 1.2) suggests that NEAs with high thermal inertia (i.e. regolith-free surfaces) are uncommon. One of the objects among the NEAs observed to date that may have a high thermal inertia is 2100 Ra-Shalom ($\eta = 2.3$, $\alpha = 39^\circ$). On the other hand, the very large values of η obtained for three objects observed at high phase angles ($\sim 60^\circ$) may be due to unusual surface structure giving rise to a strong sunward beaming effect and/or shape effects causing shadowing, rather than high thermal inertia.

In section 5.4 the thermal infrared phase curve of a refined-NEATM-like asteroid is calculated. It is worth that this infrared phase curve is linear in the range 0° - 30° with a slope ~ 0.015 mag/deg as supported by observations of main belt asteroids.

Radiometric diameters have been compared with those obtained from radar observations. On average NEATM appears to overestimate diameters of about 10% with a RMS fractional difference of 20% from radar derived NEA sizes. A large discrepancy of FRM-derived diameters with radar ones have been shown. A strong correlation of the diameter error with phase angle, α , is evident with this error being larger for α approaching zero. The fact that the FRM fails at low phase angles supports the conclusion that high-thermal inertia surfaces are uncommon amongst NEAs.

Comparison of STM-derived diameters with diameters estimated from radar measurements allows the STM to be calibrated for use with NEAs. The STM with the standard η -value equal to 0.756 of Lebofsky et al (1986) underestimate radar diameters by about 10%. I have shown how a larger η value of ~ 0.9 allows the STM to derive asteroid diameters in better agreement with radar results. It is worth pointing out how the value of 0.9 matches very well the value of η_0 derived in section 5.2 by means of an independent method.

The apparent albedo distribution of NEAs has been derived and compared to that of main belt asteroids. The mean albedo of the 46 objects listed in Table 4-6 is 0.27, which is much higher than the mean albedo of observed main-belt asteroids (~ 0.11). Further, results of this study are consistent with a trend of increasing albedo with decreasing size for S-type asteroids in the size range covered by our study (0.1 – 25 km). While we note that this apparent correlation may be real and reflect the lack of space weathering of small, young collision fragments, a selection effect in favor of the discovery and the follow-up of brighter asteroids cannot be ruled out. However, any detailed analysis of these selection effects is beyond the scope of this present work.

Finally, the statistics of albedos was calculated for the taxonomic classes represented in our sample of NEAs (see Table 5-2). Comparing the NEA albedo statistics with that derived by Bus (1999) for main belt asteroids, it appears that NEAs have higher albedos than MBAs. However, while S-type NEAs are on average 20% brighter than S-type MBAs, this difference is very striking for C-type objects: NEA C-types have on average albedos 57% higher than C-type MBAs.

Spectral type	pv min	pv max	pv mean	StDev (pv)	No. in sample	H mag for D=1km
S,Sq,Sr,Sl,Sk	0.14	0.52	0.27	0.08	20	17.0
S	0.14	0.52	0.28	0.09	17	17.0
C,B,F,Cb,Xc	0.05	0.16	0.11	0.04	7	18.0
Q	0.14	0.60	0.35	0.20	4	16.8
V	0.31	0.45	0.38	0.10	2	16.7
E	0.27	0.64	0.45	0.15	5	16.5
M	0.17	0.17	0.17	0.00	2	17.5
P	0.02	0.04	0.03	0.01	2	19.3

Table 5-2 Albedos statistics calculated for the taxonomic classes represented in our sample of NEAs

Our statistics allows an estimation of the albedo (and of the size, given the H value) to be obtained for those NEAs with known taxonomic type. Of course, this is not the case for E, M and P asteroids which are not distinguishable on the basis of spectroscopic observations.

Estimate of the thermal inertia of NEAs and assessment of the accuracy of thermal models

6.1 Foreword

To study the effects of surface roughness, thermal inertia and rotation rate on the thermal infrared emission of asteroids, a thermophysical model is developed throughout this chapter. We show that the thermal properties of the large majority of the NEAs in our database can be described by means of that model. Assuming that our objects have been observed with random orientation of their spin vector with respect to the illumination and the observing geometry, we derive a best-fit value of their thermal inertia of $550 \pm 18\% \text{ J m}^{-2} \text{ s}^{-0.5} \text{ K}^{-1}$ or some 10 times that of the lunar soil. We show that this result has consequences of extreme importance on our understanding of the Yarkovsky effect on sub-kilometer size bodies.

6.2 Introduction

In Chapter 5 it has been shown that the value of the NEATM best-fit model parameter, η , is phase angle dependent and that there are marked differences between different NEAs in the value of η when observed at phase angle larger than 30-40 degrees. Beyond that phase angle, the distribution of the η -values appears to be bimodal with the large majority of objects showing η -values no larger than two. The NEATM η -value is inversely related to the observed color temperature, T_c , such that higher values of η imply lower values of T_c (see Eq. 5-1 and section 5.2).

In the NEATM, the beaming parameter η takes account of effects that alter the temperature distribution on the surface of the asteroid visible to the observer compared to that of a perfectly smooth non-rotating sphere. It has been assumed that this alteration is largely due to surface roughness and to the fact that all asteroids rotate and radiate part of the thermal infrared emission from the night-side. Surface roughness and of rotation have competing effects on determining the final value of η . Macroscopic roughness tends to enhance the thermal infrared emission towards the Sun, causing the asteroid to appear with a color temperature hotter than that of a smooth sphere. The resulting η -value will thus be smaller than unity, when the object is observed at low phase angle. Rotation combines with the finite thermal inertia of the surface. Since asteroids spin, part of their thermal infrared radiation will be emitted from the night side. Conservation of energy implies that less radiation will be thus available for emission on the sunward direction. The color temperature of the day-side hemisphere will appear

consequently lower than the one of a non-rotating object and the η -value will be larger than unity. So, increasing roughness decrease η and increasing rotation or thermal inertia increase η .

It is clear that these considerations are valid when the asteroid is observed at low phase angles. Spencer et al. (1989) and Spencer (1990) have modeled the effects of thermal inertia, rotation rate and surface roughness on the thermal emission of main belt asteroids. They have derived η -values as a function of these parameters and of the sub-solar latitude. However, their studies were tailored to that class of asteroids and their calculation carried out at zero degree of phase angle only. The thermal effect of rotation depends not only on the object's thermal inertia, rotation rate and pole orientation, but also on its temperature. Since NEAs are closer to the Sun than what main belt asteroids are, their surfaces are hotter and differences are expected to show up in η -values derived for NEAs with respect to those obtained for MBAs for a given pole orientation, rotation rate and thermal inertia. Moreover, the possible effects on η of observing objects at large phase angle have to be studied. Results of observations discussed in this work, Chapter 5, indicate clearly that η varies with phase angle.

In Chapter 5 we have seen how the large majority of NEAs have η -values scattered around a straight line of equation $\eta=(0.011\pm 0.002)\alpha+(0.92\pm 0.07)$, where α is the solar phase angle. Delbo et al. (2003) noted that $\eta \approx 0.8$ appears to be valid at phase angles approaching zero, where the uncertainties associated with use of the STM, which assumes asteroids as non-rotating and a fixed η -value of 0.756, are at a minimum. The fact that $\eta \rightarrow 0.756$ for $\alpha \rightarrow 0^\circ$ suggests that the assumption of the STM of low thermal inertia (expected for an asteroid covered in dusty collisional debris) may be valid for “common” NEAs. Furthermore, the fact that no object was observed at a low phase angle for which η is large (> 1.2) suggests that NEAs with high thermal inertia (indicative of a rocky surface or coarse regolith) are relatively uncommon²⁰.

However, the present work revises up the η_0 value, namely the value of η at $\alpha=0^\circ$, to about 0.9 by including further observations to the linear fit of Fig. 5.3. Moreover, new IRTF observations obtained for the NEA 5381 Sekmeth have revealed η -values that appear to fill the gap between the color temperatures shown by NEAs with common thermal properties and the “anomalous” low color temperature displayed by 2100 Ra-Shalom. Is the conclusion that the large majority of NEAs have low thermal inertia still valid in the light of these new results?

²⁰ A low value of thermal inertia is compatible with a surface covered with an insulating layer of regolith as in the case of the Moon. The lunar soil has a thermal inertia between 40 and 50 J m⁻² s^{-0.5} K⁻¹. Large main belt asteroids have thermal inertia even lower: about 30% that of the moon.

The fact that NEAs appear not to have high thermal inertia is, actually, quite contrary to expectations and it is remarkable that this seems to apply even for relatively small objects in the few-100-m size range: how can such small objects retain with their low gravities insulating regoliths of collisional debris? Furthermore, the presence of three “anomalous” asteroids, including the only two binary asteroids in the Keck data set, displaying color temperatures apparently exceptionally low ($\eta \approx 3$) when observed at large phase angles ($>50^\circ$) shows the large diversity of surface structure present in the NEA population. An explanation of this behavior in terms of high thermal inertia requires values exceeding that of bare rock, which is clearly unrealistic. Alternatively, the surfaces in these cases may be unusually rough and irregular leading to enhanced thermal emission in the sunward direction (“beaming”) and consequently less (and cooler) emission observed at high phase angles.

Information on the thermal inertia and surface structure of NEAs may be obtained from the variation in effective color temperature, with solar phase angle. However, a clear picture of this dependence is at present not available. More complex thermophysical modeling is in the need for describing the variation the color temperature as a function of the illumination and viewing geometry in terms of physical quantities such as thermal inertia and macroscopic surface roughness. Unfortunately, effects of thermal inertia combine with those of rotation rate, of spin vector orientation and of macroscopic surface roughness to yield the final observed color temperature and is not clear if separating out the contribution of each component is possible on the basis of the observations we have gathered so far. However, results that may come up from applying thermophysical models to observations of NEAs have several important consequences to gain insight into the surface properties of this population of minor bodies.

An estimation of the thermal inertia of NEAs allows to quantifying systematic errors in diameters and albedos inherent in the use of simple thermal models which make assumptions about the surface temperature distributions and/or neglect the thermal infrared flux arising from the non-illuminated fraction of the body. Moreover, knowing asteroids thermal properties is directly relevant to studies of the Yarkovsky effect, namely the drift in the orbital motion of small asteroids due to the reactive force of emitted thermal radiation. Dynamicists invoke this effect to explain the delivery of km-sized asteroids from the main belt into near-Earth orbits. It is also crucial for the assessment of the impact risk from potentially hazardous NEAs, such as 1950 DA. However, the magnitude of the effect depends critically on assumed thermal properties of asteroid surfaces, and is significantly reduced in the case of bodies having low thermal inertia (Bottke et al., 2002).

In this chapter a thermophysical model, which includes the effects of thermal inertia, rotation and surface roughness, is developed and used to study the dependence of the η -value with the solar phase angle, α . Furthermore, this model will allow us to produce thermal infrared emission spectra of synthetic asteroids with different surface properties and under different illumination and observing geometries. By fitting thermal models to these spectra we will study the reliability of the derived radiometric diameters and albedos and the likely presence of systematic errors.

6.3 Thermophysical model components

The thermophysical model implemented in this study is a variant of that developed by Spencer et al. (1989) and Spencer (1990). In our thermophysical model the synthetic asteroid is made of a mesh of triangular facets²¹. Several shapes of different complexity can be handled as shown in Fig. 6.1. For each facet the one-dimensional heat diffusion differential equation is solved numerically. This differential equation depends on the so-called thermal parameter Θ which is a product of the surface thermal inertia and the asteroid rotation rate (see Spencer et al., 1989).

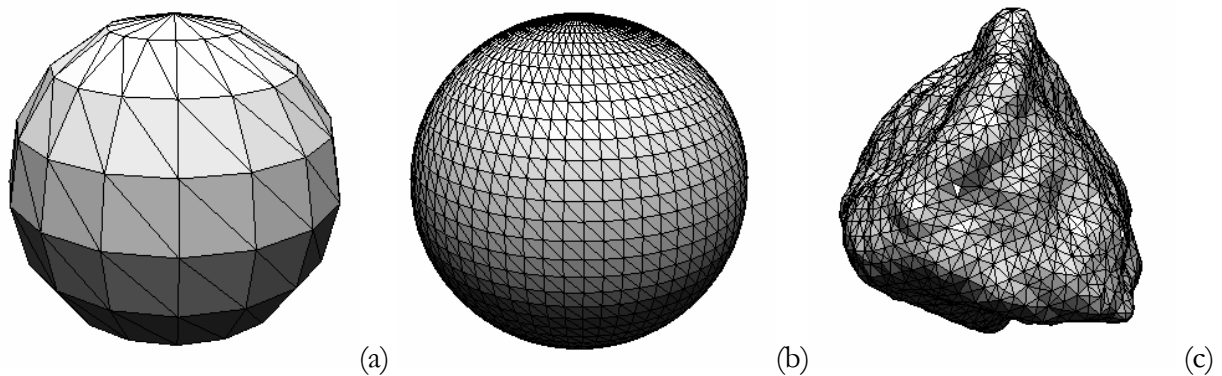


Fig. 6.1 The model herewith implemented can handle spheres of with a small (a) or a large number of elementary triangular facets (b). General shapes can also be modeled as in the case of the radar model of the NEA 6489 Golevka (c).

To simulate surface roughness, an energy balance equation is solved for temperature within spherical section craters. One crater is generated for each tile of the mesh. Surface roughness can be adjusted by changing the opening angle of the craters, the density of the crater distribution, or a combination of the two. However, Emery et al. (1998) has shown that if surface roughness is measured in terms of the mean surface slope, $\bar{\theta}$, according to the parameterization introduced by Hapke (1984), emission spectra

²¹ Part of the code that implements the thermophysical model has been developed in collaboration with Stefano Mottola.

are function of the $\bar{\theta}$ parameter only and not of the crater opening angle and crater surface density. We recall here that

$$\tan \bar{\theta} = \frac{2}{\pi} \int_0^{\pi/2} a(\theta) \tan \theta d\theta \quad (6-1)$$

where θ is the angle of a given facet from horizontal, and $a(\theta)$ is the distribution of surface slopes.

The thermophysical model includes

1. heating by direct sunlight, including the effect of shadowing;
2. subsurface diurnal heat flow normal to the local surface;
3. heating by sunlight multiply scattered within the crater;
4. self-heating by reabsorption of thermal radiation from other parts of the crater;

The model calculates disk-integrated thermal infrared flux summing up the flux from the crater of each tile of the mesh, f_i^{crat} , weighted with the crater density ρ_{crat} and the thermal flux arising from the flat part of the tile f_i^{tile} multiplied by $(1 - \rho_{crat})$:

$$F(\lambda) = \sum_{i=1}^{N_i} (\rho_{crat} f_i^{crat}(\lambda) + (1 - \rho_{crat}) f_i^{tile}(\lambda)) \mu_i \quad (6-2)$$

where μ_i is the cosine of the direction to the observer with respect to the normal of the i -th tile of the asteroid mesh. Not all elements in all craters will be illuminated by direct sunlight, nor will they all be visible from the observer. The flux originating from each crater is calculated taking into account the visibility of crater elements. The procedure we have used to test if a crater element is in shadow, which is exactly analogous to the procedure to test for visibility, is similar to that developed by Emery et al. (1998).

6.4 Thermal Inertia and the heat diffusion within spherical craters

The assumption of instantaneous thermal equilibrium with sunlight at all points on the surface of an asteroid (Equilibrium Model, hereafter EM) result in a temperature distribution which depends on the solar incident angle only μ_s and fall to zero beyond the terminator (see Eqs (2-8) and (2-12)).

However, if heat conduction is important the surface can respond not instantaneously to variation of the insolation energy. The temperature is not only a function of the albedo and the heliocentric distance but depends also on the previous thermal history of the surface and part of the energy is radiated from

the dark side of the body. Solutions of the one-dimensional heat flow equation depend on the thermal inertia parameter,

$$\Gamma = \sqrt{\rho\kappa c}, \quad (6-3)$$

which combines the material surface density ρ , the material conductivity κ and the specific heat capacity c .

However, the effect of thermal inertia is coupled to rotation rate. An asteroid rotating slowly with high thermal inertia displays a similar temperature distribution of one rotating very rapidly but with a lower thermal inertia. The degree to which the surface of an asteroid can respond to changes in insolation can be characterized by a single parameter. This is the so-called thermal parameter Θ , which combines rotation rate, thermal inertia and surface temperature and consequently depends on the heliocentric distance of the body. The thermal parameter is given by Eq. (6-4).

$$\Theta = \frac{\Gamma\sqrt{\omega}}{\varepsilon\sigma T^3}, \quad (6-4)$$

where ε is the emissivity, ω is equal to 2π divided by sidereal rotational period of the asteroid T_{SID} , and σ is the Stefan-Boltzman constant. T is the temperature of the asteroid surface.

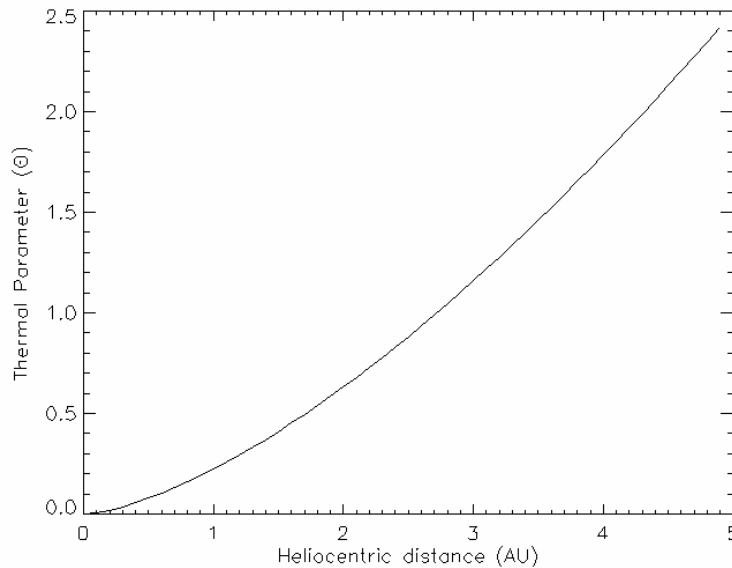


Fig. 6.2 Plot of the thermal parameter Θ as a function of the heliocentric distance. The thermal inertia, $\Gamma = 40 \text{ J m}^{-2} \text{ s}^{-1} \text{ K}^{-1}$, has a quasi-lunar like value. The bolometric bond albedo $A = 0.05$; emissivity $\varepsilon = 1$ and asteroid sidereal rotation period $T_{\text{SID}} = 5$ hours. Note that for a given value of Γ and T_{SID} , NEAs have smaller values for Θ than objects more distant from the Sun.

In the literature, it is often said that an asteroid is a “slow-” or “fast-rotator” if $\Theta=0$ or $\Theta \rightarrow \infty$ respectively. For a lunar-like thermal inertia, the typical value of Θ for a main-belt asteroid falls in the range 0.1, 2.0. The temperature of the object plays a strong role: cooler objects with constant rotation rate and thermal inertia radiate less of their heat on the day hemisphere and more on the night hemisphere. Fig. 6.2 shows the dependence of the thermal parameter, Θ , as a function of the heliocentric distance. It is interesting to note that for a given value of Γ and T_{SID} , the thermal parameter Θ assumes smaller values the closer an object is to the Sun: the temperature distribution of a NEA is more similar to the EM temperature distribution than the temperature distribution of an object further away from the Sun, in the main belt or in the Jupiter-Trojan region.

The model solves the one-dimensional heat diffusion differential equation for each tile of the mesh:

$$\frac{\partial T(X,t)}{\partial t} = \omega \frac{\partial^2 T(X,t)}{\partial X^2} \quad (6-5)$$

with the following boundary condition at the surface:

$$\sqrt{\omega} \Gamma \left(\frac{\partial T(X,t)}{\partial X} \right)_{X=0} = \omega \sigma T^4(0,t) - (1-A) \frac{S_0}{r^2} \mu_s(t) \quad (6-6)$$

where $S_0 = 1.374 \times 10^6 \text{ erg cm}^{-2} \text{ s}^{-1}$ is the solar energy flux at 1 AU from the sun, r is the solar distance in AU, μ_s is the cosine of the solar zenith angle of mesh tile, A is the bolometric Bond albedo, σ is the Stefan–Boltzmann constant, ϵ is the emissivity. See Spencer et al. (1989) for further details.

Within craters, for each crater element Eq. (6-5) holds true and describes correctly the vertical heat flow, however, the boundary condition equation has to include heating by sunlight multiply scattered within the crater and self-heating by reabsorption of thermal radiation from other parts of the crater. In symbols:

$$\begin{aligned} \sqrt{\omega} \Gamma \left(\frac{\partial T_i(X_i,t)}{\partial X_i} \right)_{X_i=0} &= \omega \sigma T_i^4(0,t) - (1-A)(1-S_i) \frac{S_0}{r_i^2} \mu_i(t) + \\ &- \epsilon \sigma \sum_{j \neq i} f_{ij} T_j^4(0,t) \cos(\beta_{ij}) - E_{\text{ref}}(0,t) \end{aligned} \quad (6-7)$$

where μ_i is the cosine of the solar zenith angle of crater element i and E_{ref} is the energy contributed from reflected solar radiation. Further, f_{ij} is the fraction of element j 's sky subtended by element i , and β_{ij} is the angle between element i 's normal and the line connecting elements i and j . S is a shadowing term which is equal to 1 if the element is in shadow and equal to zero if the element is illuminated by direct sunlight.

The second term on the right hand side of Eq. (6-7) represents heating by direct sunlight, the third term represents heating by thermal radiation emitted by other sections of the crater wall, and the first term represents thermal radiation emitted by element i . This equation is iteratively solved for each crater element to find the equilibrium temperature of each of the elements within the crater (see Emery et al., 1998).

Because heat conduction parallel to the surface is ignored, our thermophysical model results are independent of the scale of the craters, provided they are larger than the diurnal skin depth l_s which is given by:

$$l_s = \sqrt{\frac{k}{\rho c \omega}} \quad (6-8)$$

Spencer (1990) noted that in the case of main belt asteroids the value of l_s is of the order of some centimeters-millimeters assuming reasonable values for the density, heat capacity and heat conduction of the asteroid surface material. The heat diffusion process is highly localized on a diurnal timescale, implying that the application of simple one-dimensional vertical heat conduction models should be valid.

6.5 Numerical simulations

The purpose of this study is to model the effect of macroscopic surface roughness, thermal inertia and rotation rate for an object in near-Earth space as a function of the illumination and observing geometry. In particular we aim at studying the dependence of the η -value derived by the NEATM (i.e. the color temperature) as a function of the phase angle. The reliability of the NEATM derived radiometric albedos and diameter as a function of the thermal parameter Θ and the macroscopic roughness $\bar{\theta}$ will be also derived.

To this end, synthetic thermal infrared spectra have been generated at different solar phase angles using a spherical shape mesh made of 184 elementary triangular facets. Each spectrum, which depends on Θ , $\bar{\theta}$ and the phase angle, α , has been treated a single observation and NEATM has been used to fit the flux data and derive the diameter, the albedo and the η -value of the synthetic asteroid.

In this simulation, the Sun and the observer were in the equatorial plane of the asteroid which is placed at 1.0 AU of distance from both the observer and the Sun. Physical parameters of the synthetic asteroid are: Sidereal rotational period $T_{SID}=6$ hours; diameter $D=2$ km; bolometric Bond albedo

$A=0.05$; geometric visible albedo, $p_v=0.128$; resulting absolute magnitude $H=16.334$. The model does not include the effects of scattered thermal radiation and therefore assumes the emissivity equals to 1.

Each simulation starts with all the tiles of the mesh and all craters elements at a constant temperature. The solution to the heat diffusion problem is found numerically. The subsurface is divided into 32 slabs of thickness $0.25 \times l_s$. The deepest subsurface element is therefore 8 times beneath the sink depth. The model calculates the heat flow from each slab to the next in successive increment of time δt using the discrete equivalent of Eq. (6-5):

$$T(X, t + \delta t) = T(X, t) + \left(\frac{2\pi\delta t}{(\delta X)^2 T_{SID}} \right) (T(X + \delta X, t) - 2T(X, t) + T(X - \delta X, t)) \quad (6-9)$$

We choose the fewest number of time steps that gave a stable numerical solution. This value is of the order of 300 time steps per rotation for value of $\Theta > 1$, but it can become as large as 1500 for $\Theta < 0.1$. The asteroid is then let to spin for a number of rotations until the diurnal temperature stabilize and forgot the initial conditions.

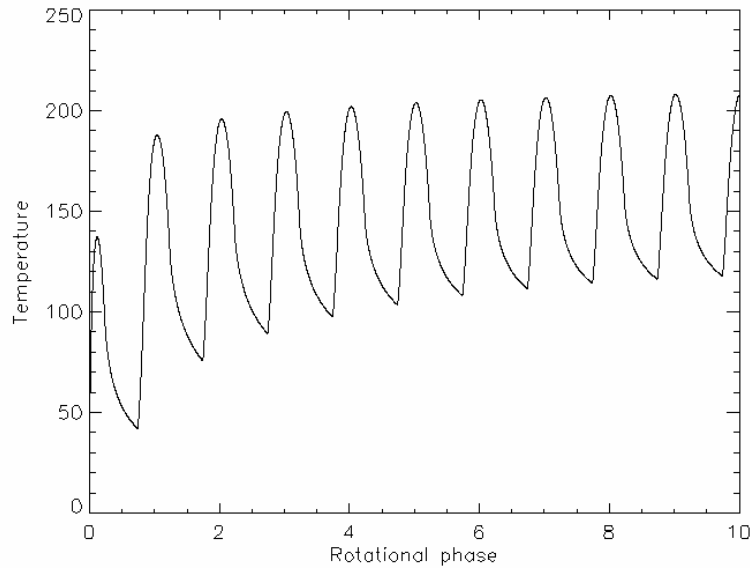


Fig. 6.3 The temperature of an equatorial tile of the spherical mesh monitored during the “warming up” phase. In this case the temperature of all the tiles of the mesh has been set equal to 0 K as starting conditions. After a few rotations the temperature stabilize within 0.5 K.

The temperature profile as a function of time, i.e. the asteroid rotational phase, has been monitored on an equatorial facet and on one of the four element on the floor of an equatorial crater during the warm

up phase, which can take up to 10-50 (depending on the value of Θ) full rotations until the temperature profile stabilizes (see Fig. 6.3).

Once the warming up process has been completed, a final rotation of the object allows the final solution to the surface temperature distribution to be derived. Fig. 6.4 shows the diurnal temperature profiles for an object with sub-solar latitude equal to zero as a function of the thermal parameter Θ .

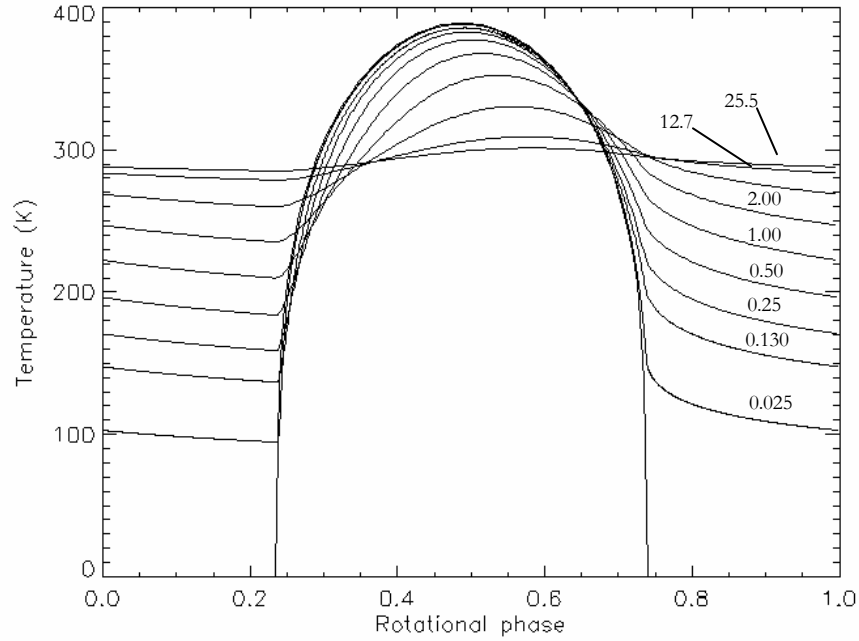


Fig. 6.4 Diurnal temperature profiles for an object with sub-solar latitude equal to zero as a function of the thermal parameter Θ .

Although these simulation has been carried out for a given rotational period of 6 hours by changing the thermal inertia, the results of the experiment, actually, depends on the thermal parameter Θ . Fig. 6.5 allows the thermal parameter Θ to be estimated for different rotational periods and different thermal inertias for an asteroid in near earth space.

A discrete set of wavelengths at 5.0, 8.0, 10.3, 12.5 and 20 μm has been adopted to sample the infrared spectra in the range 5 – 20 μm . Those wavelengths roughly correspond to the central wavelengths of narrow band filters used to carry out the ground-based observations discussed in the Chapter 3 of this study. A spectrum has been generated every ten degrees of phase angle from -90° (morning side) to 90° (afternoon side) for a set of values of the thermal inertia $\Gamma = [5, 25, 50, 100, 200, 400, 900, 2500, 5000] \text{ J m}^{-2} \text{ s}^{-0.5} \text{ K}^{-1}$. Those values of thermal inertia corresponds to $\Theta = [0.025, 0.13,$

0.25, 0.50, 1.00, 2.00, 4.60, 12.70, 25.5] for our rotational period of 6 hours. The model has been run for several degree of macroscopic roughness: $\bar{\theta} = [0, 5, 10, 20, 58]$ degrees.

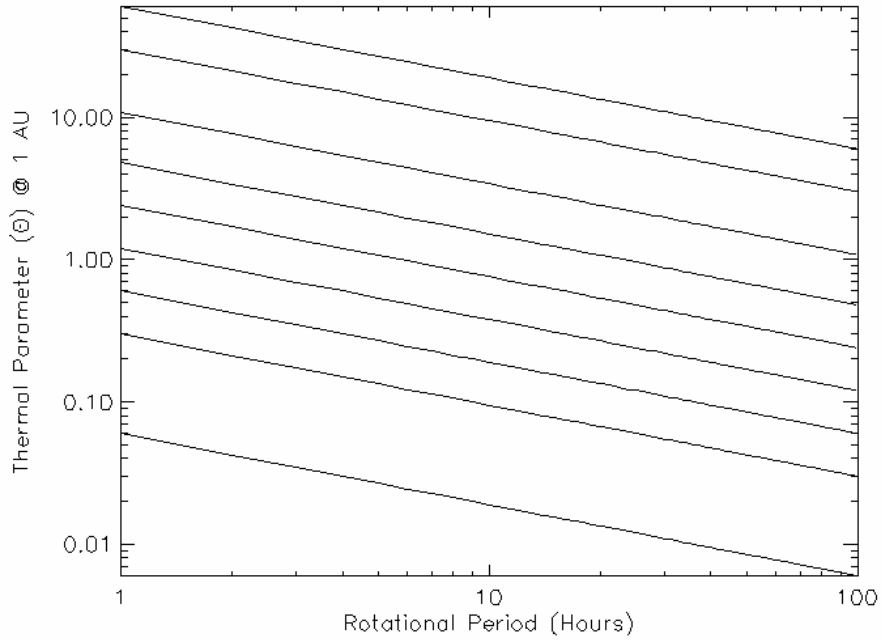


Fig. 6.5 This plot allows the thermal parameter Θ to be estimated given the thermal inertia Γ and the asteroid rotational period in hours. From the bottom of the figure to the top, the lines refers to the following values of $\Gamma = [5, 25, 50, 100, 200, 400, 900, 2500, 5000]$ $\text{J m}^{-2} \text{s}^{-1/2} \text{K}^{-1}$. The typical lunar-like value for Γ is about $40\text{-}50 \text{ m}^{-2} \text{s}^{-1/2} \text{K}^{-1}$.

For each observation of the synthetic asteroid the NEATM has been used to fit the synthetic spectrum and in the next section, results of the simulations are presented.

6.6 Results of the simulations

6.6.1 Effects of thermal inertia and rotation rate on the theoretical dependence of the NEATM η -value with the phase angle

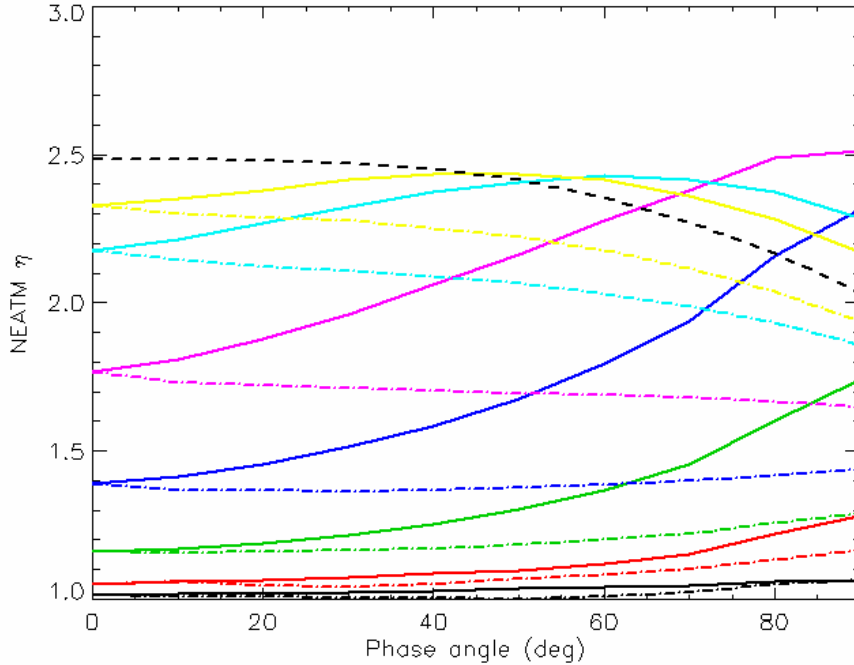


Fig. 6.6 NEATM derived beaming parameter η as a function of the phase angle and thermal parameter Θ . The sun and the observer are in the equatorial plane of the synthetic asteroid. Different colors are used for different values of Θ : η -values derived for $\Theta=0.25$ are coded with black color; those obtained for $\Theta=0.50$ are coded with red; green is used for $\Theta=1.00$ with; blue for $\Theta=2.00$; pink for $\Theta=4.60$; light-blue for $\Theta=12.70$ and yellow for $\Theta=25.5$. Note that there are two curves for each value of the thermal parameter Θ : continuous curves refer to those η -values derived by observing the morning side of the asteroid, whereas dashed-dotted curves indicate those η -values obtained observing the afternoon side. Curves obtained for $\Theta=0.025$ and 0.13 are not plotted since the derived η -values are constant with phase angle and their values between 1 and 1.05. The dotted black curve represents the expected η values for an FRM-like ($\Theta \rightarrow \infty$) asteroid.

Fig. 6.6 shows the theoretical dependence of the NEATM best fit η parameter for a smooth asteroid as a function of the phase angle for different values of the thermal parameter Θ . For each value of Θ , two curves are plotted. Continuous curves refer to those η derived by observing the cooler morning side of the asteroid, whereas dashed-dotted curves indicate those η -values obtained observing the warmer afternoon side.

We note that for values of Θ smaller than 0.5 (red curves), the value of η is small (<1.3) and rather constant up to phase angles as large as 90° . We remind here that the black colored curves correspond to

a lunar-like thermal inertia for a rotational period of six hours. No large variations of the η -value are visible when the morning rather than the afternoon hemisphere of the asteroid are observed. However, for larger Θ values, (i.e. $\Theta > 1.0$ – the green curves) such variation of the color temperature with the observing and illumination geometry appear. Moreover, large values of the thermal parameter correspond to η -values as large as 1.5 at phase angles approaching zero indicating a surface temperature distribution much cooler than the one expected by the EM. As Θ increases, the η -value at $\alpha = 0^\circ$ increases up to a maximum value about 2.5 for $\Theta \rightarrow \infty$ which correspond to a FRM-like surface temperature distribution. It is worth to point out, how for very large values of the thermal parameter, the temperature of a surface element is constant through day and night and the “morning” η curve collapses on top of the “afternoon” one.

Note that beyond 50° of phase angle asteroids with Θ roughly larger than four can have η -values higher than an object with an FRM-like temperature distribution.

Fig. 6.6 indicates that thermal inertias and direction of rotation of NEAs can be estimated on the basis of the dependence of η with the phase angle if observations at large phase angle before and after oppositions are carried out. Since we expect to be able to derive η -values with an accuracy of about 30% (this is the mean relative error affecting the determination of η in the database of our observations), the thermal inertia of a NEA might be derived if its Θ -value is as large as one.

In this simulation the asteroid sub-solar latitude was always zero. If this is not the case, the surface temperature distribution deviate less from the EM one, as the sub-solar latitude approaches 90° . Our thermophysical model allows the surface temperature distribution to be calculated for whatever observing and illumination geometry. We have thus simulated the case of an asteroid which sub-solar latitude was varied from zero to ninety degrees, with an obliquity of 0° and observed at phase angles between -90° and 90° . Our simulations indicate that the larger is the sub-solar latitude, the smaller is the amplitude of the difference between the “afternoon” and the “morning” curves and the smaller is the η -value derived by NEATM. Finally, if the Sun shines above one of the asteroid poles, the temperature distribution is analogue to the EM one for whatever value of the thermal parameter Θ . Resulting η -values will be equal to 1 for every observing direction. So, given the value of Θ , for arbitrary illumination and observing geometries, expected η -values will range between 1 and the corresponding “morning” curve of Fig. 6.6.

6.6.2 Effects of surface roughness on the theoretical dependence of the NEATM η -value with the phase angle

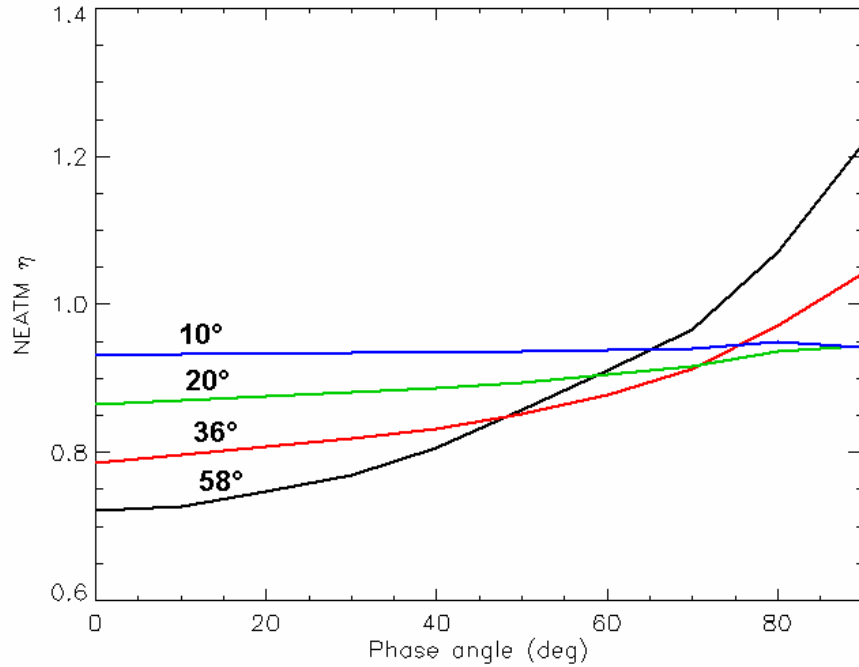


Fig. 6.7 NEATM derived η parameter as a function of the phase angle and macroscopic surface roughness $\bar{\theta}$. The sun and the observer are in the equatorial plane of the synthetic asteroid. The thermal parameter Θ is equal to 0. Different colors are used for different values of $\bar{\theta}$: η -values derived for $\bar{\theta} = 58^\circ$ are coded with black color; those obtained for $\bar{\theta} = 36^\circ$ are coded with red; for $\bar{\theta} = 20^\circ$ with green and for $\bar{\theta} = 10^\circ$ with blue.

Fig. 6.7 shows the theoretical dependence of the NEATM best fit η parameter as a function of the phase angle for different values of the macroscopic surface roughness $\bar{\theta}$. As it was expected, roughness increases the color temperature, T_C , of the surface when the asteroid is observed at small phase angles: i.e. $\eta < 1$. However, while for small values of $\bar{\theta}$, T_C is constant with the phase angle, for very rough surfaces the color temperature decreases as the phase angle increases. Since the thermal parameter Θ for this asteroid is equal to zero, no variation of the Fig. 6.7 curves are expected with sub-solar latitude. The temperature distribution is symmetrical with respect to the sub-solar point.

6.6.3 Combined effects of thermal inertia, rotation rate and surface roughness on the theoretical dependence of the NEATM η -value with the phase angle

In this section we study the combined effects of thermal inertia, rotation rate and surface roughness of the thermal emission of NEAs and we derive the dependence of the NEATM best-fit parameter η on these physical parameters.

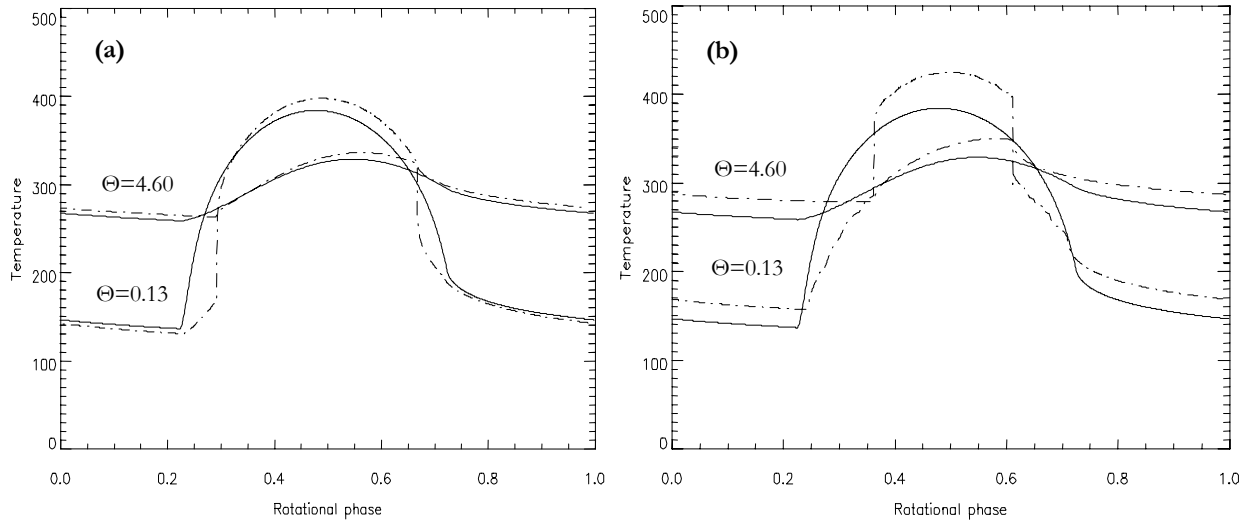


Fig. 6.8 Continuous line: diurnal temperature profiles for an equatorial tile of an object with sub-solar latitude equal to zero. Dashed-dotted line: diurnal temperature profiles for one of the four tiles on the floor of an equatorial crater with opening angle equals to 45° (a) and with opening angle equals to 90° (hemispherical crater).

Spencer (1990) has shown how the midday temperature across an equatorial crater varies with Θ . He has highlighted that for $\Theta=0$ there is a large temperature enhancement on the floor of the crater compared to the nearby horizontal surface. Fig. 6.8 shows the diurnal temperature profile of one of the four tiles on the floor of an equatorial crater with respect to the temperature of the surrounding smooth surface for two different values of the thermal parameter Θ i.e. $\Theta=4.60$ and $\Theta=0.13$, as shown by the labels of Fig. 6.8. It is interesting to note that for large values of Θ , the temperature of the bottom of the crater is almost always higher than the temperature of the surrounding surface. This effect, already visible in the case of a 45° crater, becomes significantly stronger for a 90° (hemispherical) crater. In this latter case our thermophysical model calculates a difference of more than 20° compared to the surrounding horizontal surface. This effect is due to the strong self-heating by reabsorption of thermal radiation from other parts of the crater. Furthermore, for large thermal inertias and or rotation rate, our thermophysical model indicates that a surface heavily cratered by deep depressions appear hotter than a smooth one even if observed from the night side.

The observed color temperature, derived by fitting NEATM on disk integrated thermal infrared spectra generated by means of our thermophysical model, is a function of the thermal parameter Θ , the macroscopic surface roughness $\bar{\theta}$, the illumination and the observing geometry. So, in general we can write that

$$\eta \equiv \eta(B_{SS}, r, B_{SE}, \Delta, \alpha, \Theta, \bar{\theta}) \quad (6-10)$$

where B_{SS} is the latitude of the sub-solar point and B_{SE} the latitude of the sub-Earth point on the asteroid reference frame. r is the heliocentric distance, Δ the geocentric distance and α the phase angle. However, if the asteroid has sub-solar latitude equal to zero and viewed equator-on, at 1 AU from the Sun and the Earth, the dependence of the η -value on the illumination and the observing geometry is a function of the phase angle α only i.e.

$$\eta \equiv \eta(\alpha, \Theta, \bar{\theta}) \quad (6-11)$$

To study the function of Eq 6-10, we have run our thermophysical model for the set of values of Θ and $\bar{\theta}$ as described in section 6.5 and derived the η -value by fitting the NEATM on thermal infrared spectra generated at phase angles between -90 (morning side) and 90 (afternoon side) degrees of phase angle every 10°. Fig. 6.9 shows the functional dependence of η with α for different values of Θ and $\bar{\theta}$. The numerical values of η , calculated on a fixed grid of points in the α - Θ - $\bar{\theta}$ space, have been stored in a three-dimensional array. Fig. 6.10 shows η -values on sections of this three-dimensional data volume at constant values of the macroscopic surface roughness parameter $\bar{\theta}$.

At small phase angle ($\alpha < 20^\circ$), for a given degree of roughness, η is determined by the magnitude of the thermal parameter Θ : the higher Θ is, the larger the η value, until the limiting value of 2.5 for $\Theta \rightarrow \infty$ is reached. Moreover, it appears that the values of the NETAM best fit parameter η are not very sensitive to variation of the surface macroscopic roughness. According to Spencer (1990), our model calculations show that the small values of η seen in the case of the Moon and most large main belt asteroids ($\eta \sim 0.7-0.8$) can be matched only by very rough surface models.

For $\alpha > 20^\circ$ and $\Theta > 2.0$ the morning η curves separate out from the afternoon ones and very different color temperature are observed by looking at the two opposite hemisphere of the object. The morning-afternoon effect has a maximum for Θ roughly equals to 5. For smaller values of the thermal parameter, the surface temperature distribution resembles that of the EM, whereas for large values of Θ (i.e. $\Theta > 10$) the temperature becomes smoothed out in longitude and constant throughout day and night.

At intermediate phase angles, i.e. $30^\circ < \alpha < 60^\circ$, the morning curves, calculated for a given value of the thermal parameter, can cross the afternoon curves calculated for a different Θ value. This fact does not allow the Θ parameter to be estimated when the color temperature is derived at a certain phase angle, if the direction of rotation is not known.

At large phase angle (e.g. $\alpha > 70^\circ$) surface roughness contributes to a large extent to the final observed color temperature of the asteroid: note that large η -values (~ 3) at large phase angles ($\alpha \sim 80^\circ$) are compatible with a highly cratered surface ($\bar{\theta} = 58^\circ$) and moderate Θ parameter ($\Theta \sim 1 - 2$). Very rough and irregular surfaces lead to a high degree of “beaming” of thermal radiation in the sunward direction and correspondingly less and cooler radiation is emitted at high phase angles. However, for large thermal inertia and/or rotation rates, deep craters behave like a trap for the thermal energy and consequently the contribution of the roughness in decreasing the observed color temperature of the surface at large phase angles become less significant. Under such observing conditions, i.e. for $\alpha > 70^\circ$, the η -values cannot be used to determine unambiguously the values of the thermal and roughness parameters, even if the direction of rotation of the asteroid is known.

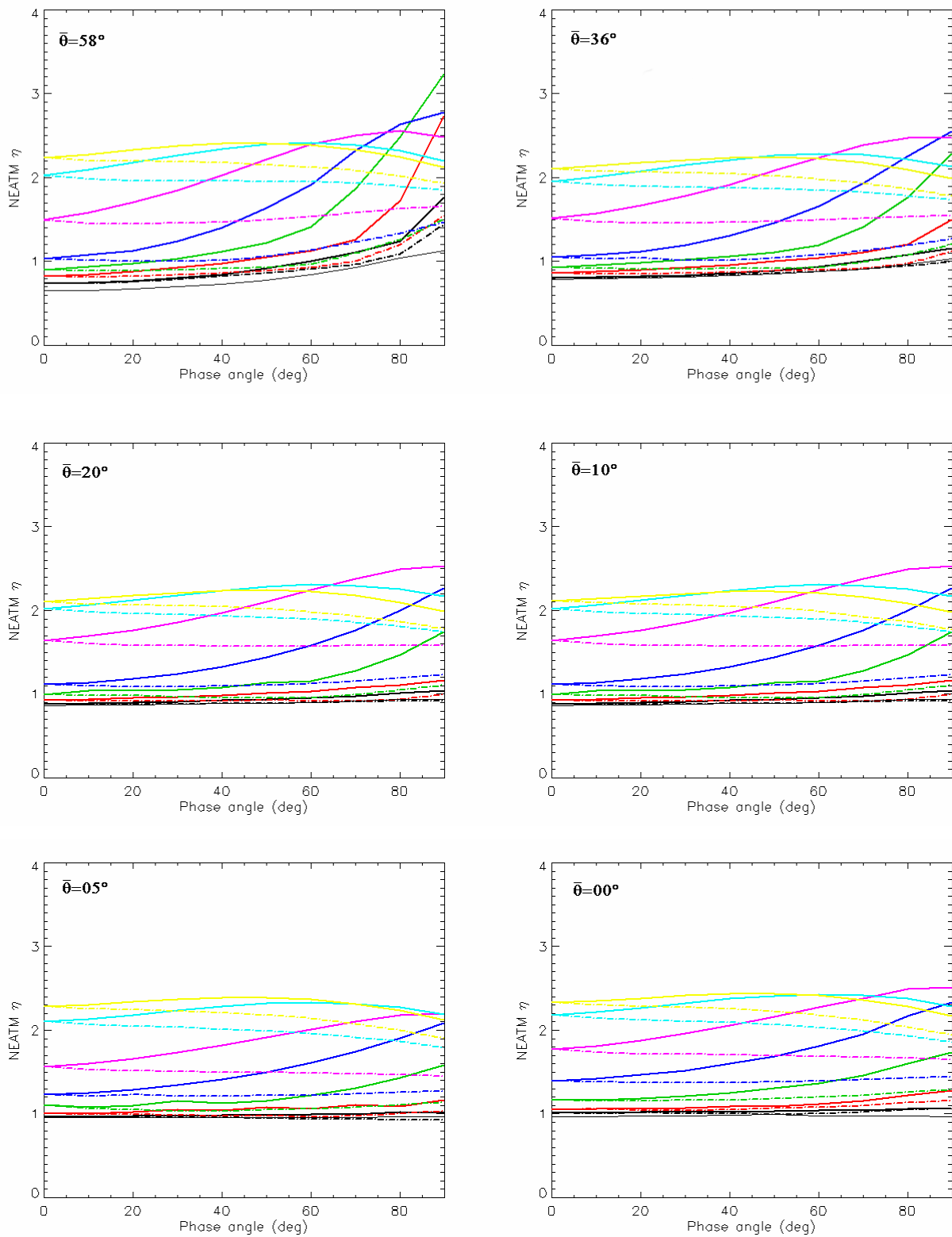


Fig. 6.9 Combined effects of thermal inertia, rotation rate and surface roughness on the theoretical dependence of the NEATM η -value with the phase angle.

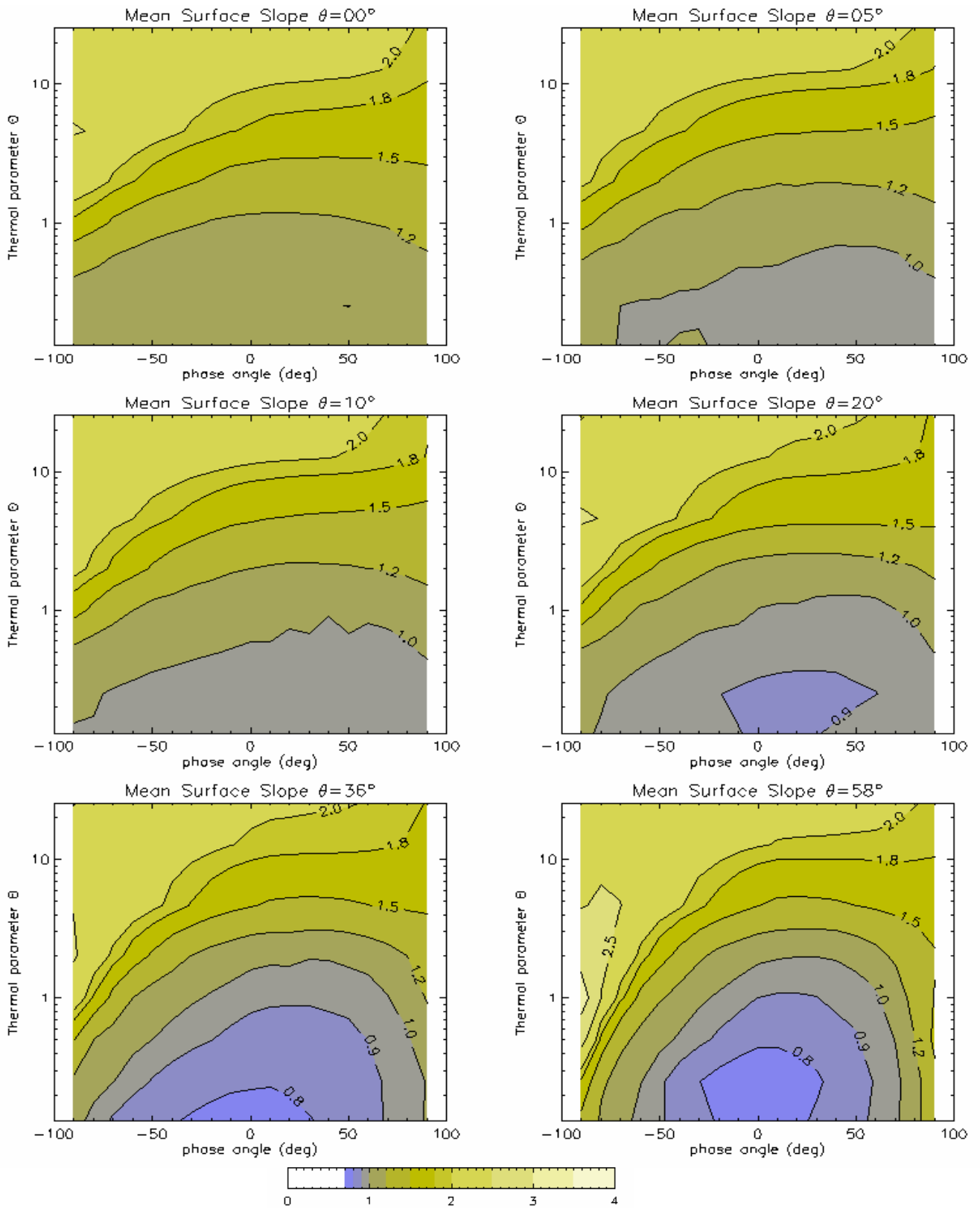


Fig. 6.10 Combined effects of thermal inertia, rotation rate and surface roughness on the theoretical dependence of the NEATM η -value with the phase angle.

6.7 The thermal inertia of NEAs

Not only surface roughness, thermal inertia, and rotation rate contribute to the phase angle dependence of the model parameter η , but the spin vector orientation and the global shape of asteroids are also important. Results that we have discussed here are based on thermophysical model calculations carried out with the asteroid spin vector perpendicular to the plane containing the Sun and the Earth. However, since for most of the observed asteroids in our database with derived η -values, pole direction and shape parameters are not known, we cannot perform detailed thermophysical model calculations for every asteroid to study the thermal inertia and the surface roughness in each case. However, we show that it is possible to constrain the mean thermal properties of our NEAs on the basis of the scatter of their η -values with the phase angle, α .

First of all, we observe that for a given value of Θ and $\bar{\theta}$, when an asteroid is illuminated and observed from a random orientation, the derived η -values are delimited by two curves in the η - α plane. The lower limit is represented by that curve calculated for $\Theta=0$ and macroscopic roughness equal to $\bar{\theta}$, i.e. $\eta(|\alpha|, \Theta=0, \bar{\theta})$, where $|\alpha|$ is the absolute value of α (the curve labeled with “N” of Fig. 6.11). In fact, the hottest temperatures (and thus the lowest η -values) on the surface are reached when its thermal inertia is zero. Furthermore, for $\Theta=0$, the surface temperature distribution is symmetrical with respect to the sub-solar point and consequently the observed color temperature and the derived η -values are a function of $|\alpha|$ only. We show that a negligible error is made by taking the curve than an observer would derive by looking at the morning hemisphere of an asteroid with a rotational axis perpendicular to the plane containing the Sun and the Earth as the upper limit for η . For such geometrical configuration, the phase angle α is always negative: the upper limit curve is thus $\eta(-|\alpha|, \Theta, \bar{\theta})$, the one labeled with “M” in Fig. 6.11. We also call this curve the “morning curve”.

To validate this hypothesis, we observe that the surface temperature distributions with the lowest temperatures are obtained when the sub-solar latitude is zero. The smaller the sub-solar latitude is, the wider the surface of the asteroid over which the incoming solar energy is spread out. However, it is not straightforward that the lowest η -values are observed when the Earth is in the equatorial plane of the asteroid. For instance: is the disk integrated color temperature lower when the morning hemisphere is pointing toward the Earth or when the observer looks straight ahead one of the poles of the object?

To answer this question, we have run our thermophysical model for a number of random orientations of the sub-Earth point and for sub-solar latitude $B_{ss}=0, 30, 60$ degrees. Results are shown in Fig. 6.11, where an asteroid with $\Theta=2.0$ and $\bar{\theta}=36^\circ$ is simulated. Clearly very few points only beyond

80° of phase angle have been found with η -values exceeding that of the morning curve. The assumption that η -values derived for random directions of the asteroid spin vector are constrained by the morning curve (M) and the one of zero thermal inertia have been verified for different degrees of surface roughness and thermal parameter values.

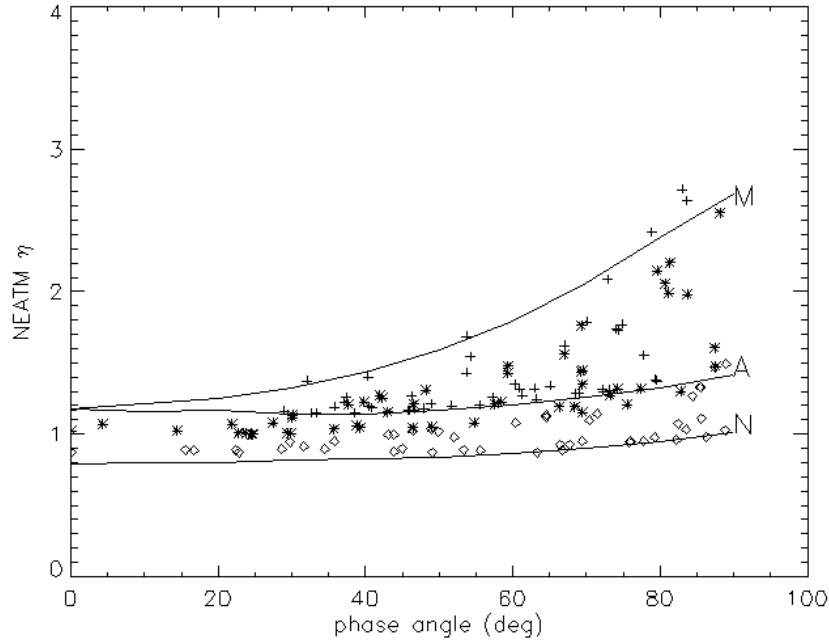


Fig. 6.11 Verification of the hypothesis that η -values derived for asteroids observed from randomly oriented directions are limited by the “morning” curve M and the curve of zero thermal inertia N. The thermophysical model was run for three values of the sub-solar latitude B_{SS} . Crosses represent those η -values derived for asteroids with $B_{SS}=0^\circ$, asterisks for asteroids with $B_{SS}=30^\circ$ and diamonds for $B_{SS}=60^\circ$. Note how η -values collapse to the curve of zero thermal inertia as B_{SS} approaches 90° . Following our notation M is the curve with $\eta=\eta(-|\alpha|, \Theta, \bar{\theta})$, A that with $\eta=\eta(|\alpha|, \Theta, \bar{\theta})$ and N that with $\eta=\eta(|\alpha|, \Theta=0, \bar{\theta})$.

So, if we assume that all NEAs had the same value of thermal parameter Θ_{NEA} and the same degree of surface roughness $\bar{\theta}_{NEA}$, their η -values would be delimited by the morning-curve $\eta(-|\alpha|, \Theta_{NEA}, \bar{\theta}_{NEA})$ and the curve of zero thermal inertia.

However, since the thermal parameter is a function of the asteroid rotation rate, T_{SID} , there is no physical reason to believe that NEAs with very different value of T_{SID} might have the same value of Θ . But, if we are interested to derive a mean value of the thermal inertia Γ_{AVE} , we can calculate the variations of the thermal parameter Θ with respect the rotational period and the asteroid surface temperature.

$$d\Theta = \frac{\partial\Theta}{\partial T_{SID}} dT_{SID} + \frac{\partial\Theta}{\partial T} dT = -\frac{\sqrt{2\pi}\Gamma_{AVE}}{\varepsilon\sigma T^3} T_{SID}^{\frac{3}{2}} dT_{SID} - 3\frac{\Gamma\sqrt{2\pi}}{\sqrt{T_{SID}}\varepsilon\sigma T^4} dT \quad (6-12)$$

where we have assumed that $d\Gamma$ is equal to the difference between the observed color temperature and that implied by the EM (from Eq 5-1):

$$dT = T_{eq}(1 - \eta^{-1/4}). \quad (6-13)$$

dT_{SID} was set as equal to the difference between the actual rotational period of the asteroid and a reference period of six hours. As $d\Theta$ was calculated for each asteroid, final corrections to the measured η -values $d\eta$ were estimated by interpolation of the numerically evaluated function $\eta(\alpha, \Theta, \bar{\theta})$. This function was previously (see Eq 6-10 and section 6.6.3) evaluated on a fixed grid of points in the α - Θ - $\bar{\theta}$ space. For those asteroids with unknown rotational period, $d\eta$ was assumed equal to 0. Correction factors to the measured η -values were found in most of the cases smaller than the formal errors affecting η -value determinations. Since this correction procedure is another source of errors, we decided to apply correction factors to measured η -values if they were found larger than the η error bars. η -corrected data points are shown with red symbols in Fig. 6.12 and Fig. 6.13 plots.

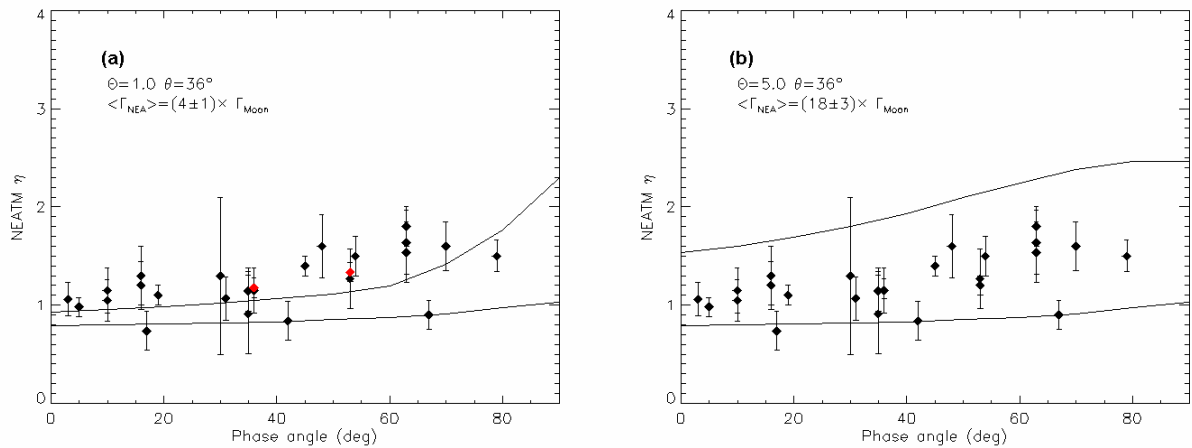


Fig. 6.12 Limiting curves which do not fit properly the observed η -values. See Fig. 6.13 caption for a description of the symbols.

We have finally looked for that set of curves giving the best fit to the observed η -values. Fig. 6.12-a shows how a Θ value too small generates curves which do not fit properly the data. Fig. 6.12-b, on the other hand, demonstrates the opposite effect of using a Θ value too large: data points are not well constrained by the upper limit morning curve.

An appropriate value for the thermal parameter which produces curves delimiting the observed distribution of η values is $\Theta \sim 3.0$. Values ranging from 2.8 up to 3.5 are also compatible with the observations. Unfortunately, constraining the degree of the surface roughness is more difficult and values for $\bar{\theta}$ ranging from 10° up to 36° are in agreement with the observed η -values (see Fig. 6.13).

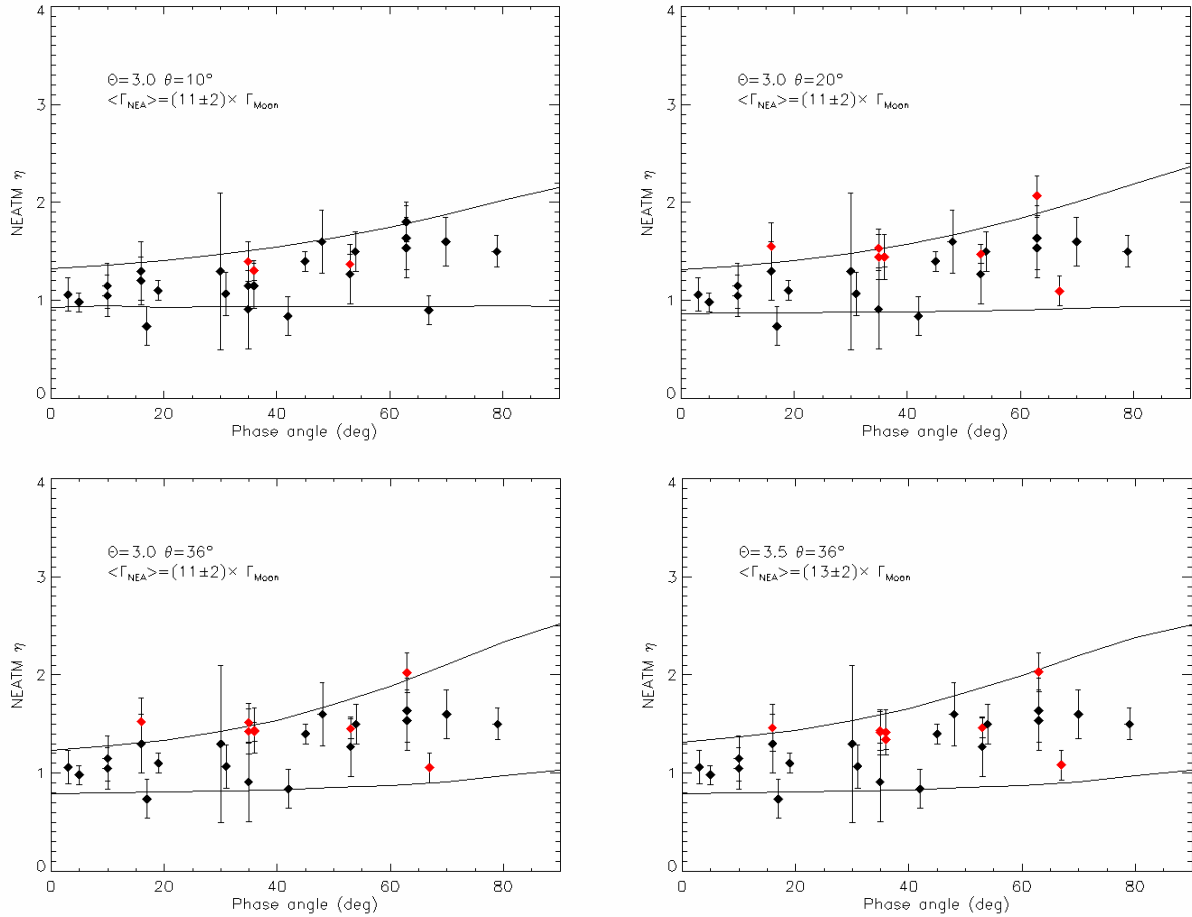


Fig. 6.13 Limiting curves which DO fit the observed η -values. The values of the Θ and the $\bar{\theta}$ parameter used to draw the curves are shown on the upper left side of each plot. For each value

Assuming that all NEAs with observed η -values enclosed by the curves of Fig. 6.13 have the same thermal parameter, taking into account the different rotational rates, we derive a best-fit thermal inertia $\Gamma = (550 \pm 100) \text{ J m}^{-2} \text{ s}^{-0.5} \text{ K}^{-1}$, or about eleven times that of the Moon which is roughly estimated between 40 and $50 \text{ J m}^{-2} \text{ s}^{-0.5} \text{ K}^{-1}$ (Harris and Lagerros, 2002 and references therein).

Only those NEAs with “common” thermal properties (see section 5.3.2) have been included in this analysis, separating out those asteroids with anomalously high η -values (see section 5.3.1) and the NEA

5381 Sekmeth. For this latter case, there are six η -values derived from observations made during a single apparition. It is clear that in such a case the hypothesis of random orientation of the spin vector with respect the Sun and the observer is no longer valid and the resulting value of the mean thermal inertia of NEAs would have been biased by including Sekmeth's results. However, Fig. 6.14 shows that if the spin axis of the NEA 5381 was perpendicular to the plane containing the Sun and the Earth at the time of the observations, it is very likely that the morning hemisphere of the asteroid was pointing towards the observer and its thermal inertia of the order of some 13 times that of the Moon. It is clear that with more accurate thermophysical model calculations, taking into account the spin vector orientation and the global shape of this object, which at the time of writing are not known, the above results may be refined much further.

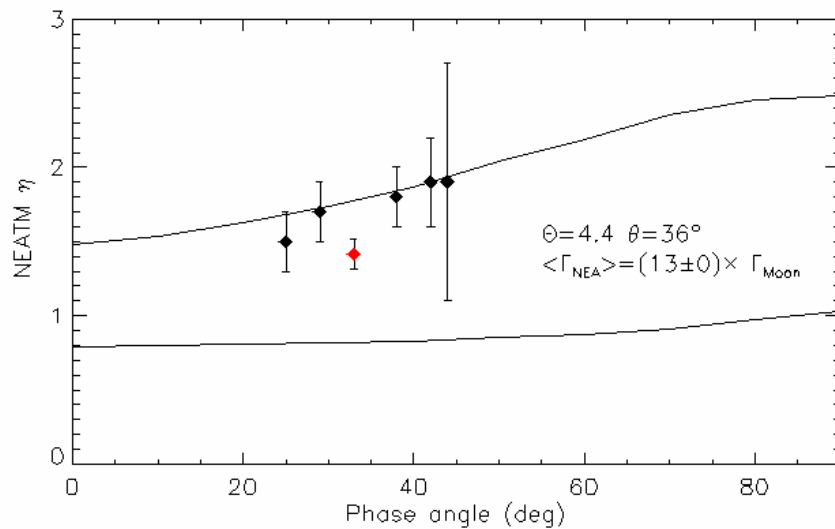


Fig. 6.14 Limiting η - α curves to fit observed η -values of 5381 Sekmeth. Those curves were calculated for $\Theta=4.4$ and $\bar{\theta}=36^\circ$

There are few estimations of the thermal inertia for asteroids and in particular for NEAs. The fact that the STM has proven to be successful in the determination of diameters and albedos of large main belt asteroids is an indication of their low thermal inertia. Müller et al. (1999) derived a thermal inertia of $15 \text{ J m}^{-2}\text{s}^{-0.5} \text{ K}^{-1}$ for the asteroid 1 Ceres. Müller and Lagerros (2002) proved this value to give thermophysical model results in agreement with observations of other main belt asteroids. Müller and Blommaert (2003) used successfully this value to analyze multi instrument multi epoch thermal infrared observations of the asteroid 65 Cybele. In general, values between 5 and $25 \text{ J m}^{-2}\text{s}^{-0.5} \text{ K}^{-1}$ are expected to apply for a few of the largest main-belt asteroids (Müller and Lagerros, 1998). These values are in good agreement with previous determinations of the thermal inertia of main belt asteroids: Spencer et al.

(1989) derived thermal inertia smaller than 30% that of the Moon for 1 Ceres and 2 Pallas and suggested that this value can be applied to other large main belt asteroids.

However, Veeder et al. (1989) have analyzed radiometric observations of 22 NEAs and found that for five of these objects the STM to give albedos well above the range expected for their spectral classes. Veeder et al. assumed that this discrepancy is due to some small asteroids having relatively high-thermal-inertia surfaces, resulting from the lack of an insulating layer of regolith, and the failure of the STM to describe their thermal characteristics adequately. Harris and Davies (1999) by combining NEATM results from thermal infrared observations obtained at the UKIRT and previously published data by Lebofsky and Rieke (1979) of the NEA 433 Eros derived a thermal inertia of $170 \text{ J m}^{-2} \text{ s}^{-0.5} \text{ K}^{-1}$, or about three times that of the Moon. Given all possible sources of uncertainties, this value is not too far from previous estimations of Morrison (1976), who derived a thermal inertia not larger than $105 \text{ J m}^{-2} \text{ s}^{-0.5} \text{ K}^{-1}$ for this asteroid. It is worth to note that our method applied to 433 Eros only (see gives a value of Γ not smaller than 4 times the thermal inertia of the Moon. The discrepancy with Morrison's result may be due to the fact that he did not take into account roughness effects leading to a lower limit on its value of the asteroid thermal inertia.

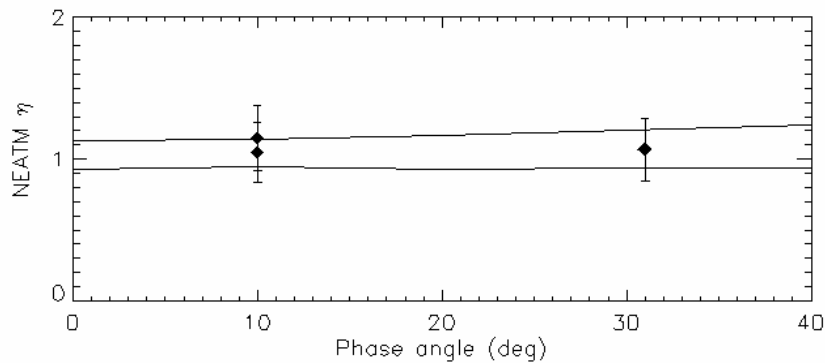


Fig. 6.15 Limiting η - α curves to fit observed η -values of 433 Eros. Those curves were calculated for $\Theta=1.0$ and $\bar{\theta}=20^\circ$

The case of asteroids with η -values larger than 2 still remains puzzling. The η value of 2100 Ra-Shalom of about 2 at $\alpha=40^\circ$ corresponds to a thermal parameter between 4 and 7, assuming a macroscopic surface $\bar{\theta}=36^\circ$ and that the cooler morning hemisphere of the asteroid was facing the observer in both observing circumstances. Given the very slow rotational period of about 20h, Fig. 6.5 leads us to estimate a very high thermal inertia value between 1500 and $2500 \text{ J m}^{-2} \text{ s}^{-0.5} \text{ K}^{-1}$. Assuming that the afternoon side was pointed towards the observer, an even higher thermal inertia is required to account for the observed low color temperature of the object.

It is very difficult to explain the very high η found for 3671, 2002 BM₂₆ and 1999 NC₄₃ in terms of the model here developed. Our model can not predict η values that high for $\alpha \approx 60^\circ$. The effect of the global shape of the objects on the thermal inferred emission and on the observed color temperature at high phase angles might explain the observed large η -values. Delbò and Harris (2002) discussed the case of 6489 Golevka for which the radiometric diameter of 350 m derived by Mottola et al. (1997) is in disagreement with the radar diameter obtained by Hudson et al. (2000), who had derived a size of $0.35 \times 0.25 \times 0.25$ kilometers. The explanation for the inconsistency probably lies in the effect of shadowing and the extreme geometry at the time of the observation. Give the availability of the three-dimensional radar shape for this asteroid, the thermophysical model described in this chapter may be used to further investigate this problem. However, if the degree of surface roughness and/or the value of the thermal inertia required are unrealistic, then perhaps more sophisticated thermal models including the effect of positive and negative relief and the effect of lateral heat conduction may be necessary.

6.8 Implications for the Yarkovsky effect on kilometer and sub-kilometer size asteroids

The best-fit value we have derived for the thermal inertia of NEAs has important implications to constrain the strength of the Yarkovsky effect of kilometer and sub-kilometer size asteroids. The Yarkovsky effect is a thermal radiation force that causes objects to undergo semimajor axis drift and spinup/spindown as a function of their spin, orbit, and material properties (see Bottke et al. 2002 and references therein). Surface thermal characteristics, in particular the thermal conductivity, affect the strength of the Yarkovsky effect. Farinella et al. (1998) have shown that the semimajor axis drift rates are function of the thermal parameter Θ . In particular, they have considered three possible values of the surface thermal inertia for meteoritic material and small asteroidal objects in the range $0.2\text{m} \leq D \leq 200\text{m}$. They have used $\Gamma=12500 \text{ J m}^{-2}\text{s}^{-0.5} \text{ K}^{-1}$ for iron rich fragments, $\Gamma=2500 \text{ J m}^{-2}\text{s}^{-0.5} \text{ K}^{-1}$ for bare basalt fragments and $\Gamma=39 \text{ J m}^{-2}\text{s}^{-0.5} \text{ K}^{-1}$ for regolith-covered fragments. This latter value roughly corresponds to the value of thermal inertia derived for the lunar soil. They have derived maximum semimajor axis drift rates of 2×10^{-5} , 2×10^{-4} and 1.5×10^{-3} AU/Myr respectively, for objects with a diameter of 200 m and a rotational period of 5 hours at 2 AU from the Sun. For such objects, Fig. 2.3 shows that the sub-solar temperature is about 300K. We derive that their thermal parameters Θ are respectively 152, 30.5 and 0.5.

However, if such objects have thermal characteristics similar to that of NEAs, their thermal inertia should have a value Γ_{NEA} of about $500 \text{ J m}^{-2} \text{ s}^{-0.5} \text{ K}^{-1}$. Consequently, the thermal parameter for a rotational period of 5 hours and a surface temperature of 300K is $\Theta \approx 6.0$.

Following Farinella et al., the drift in semimajor axis for a near circular orbit is:

$$\dot{a} = 2f_Y / n \quad (6-14)$$

where f_Y is the along track component of the Yarkovsky force per unit mass and n is the orbital mean motion. By combining Eq (5) and Eq (6) of Farinella et al, it is possible to write f_Y in terms of the thermal parameter Θ :

$$f_Y = \frac{2}{\rho_b R} \frac{\varepsilon \sigma T^4}{c} 0.667 \frac{\Theta}{(1 + 2.03\Theta + 2.04\Theta^2)} f(\zeta) \quad (6-15)$$

where ρ_b is the material bulk density, c the speed of light, ε the infrared emissivity, σ the Stefan-Boltzman constant, T the temperature and ζ the obliquity of the spin axis. For the diurnal Yarkovsky effect we have $f(\zeta)=\cos(\zeta)$. We can easily calculate the maximum drift rate of an object with NEA-like thermal inertia by taking the ratio of its f_Y with one of the f_Y -values evaluated by Farinella et al. for a different value of the thermal parameter. For instance if we take the ratio of $f_Y(\Theta=6)/f_Y(\Theta=30.5)$ we have that:

$$\dot{a}_{\Theta=6} = \left[\frac{\Theta}{(1 + 2.03\Theta + 2.04\Theta^2)} \right]_{\Theta=6} / \left[\frac{\Theta}{(1 + 2.03\Theta + 2.04\Theta^2)} \right]_{\Theta=30.5} \times \dot{a}_{\Theta=30.5} \quad (6-16)$$

Substituting numerical values into Eq (6-15), we obtain a semimajor axis drift of about 9×10^{-4} AU/Myr for an object with NEA-like thermal inertia with a diameter of 200 m, a rotational period of 5 hours at 2 AU from the Sun.

6.9 Effects of surface roughness, thermal inertia and rotation rate on the accuracy of NEA radiometric diameters and albedos.

Spencer et al. (1989) and Spencer (1990) have shown that thermal inertia and rotation rate has important effects on the thermal emission of asteroids. Systematic errors in radiometric diameters and albedos are likely to occur if simple thermal models, which do not take into account properly those effects, are used.

On the basis of thermophysical model calculations, they have estimated biases in radiometric diameters and albedos derived by the “refined” STM (with the assumption of constant $\eta=0.756$) as a function of the thermal parameter Θ , heliocentric distance and sub-solar latitude (see Fig. 8 and Fig. 9 in Spencer et al. 1989). These errors can be as large as 40 - 50% in diameter if Θ is very large ($\Theta>1$) and the object very dark. Moreover, by assuming a constant value of η , diameters and albedos derived by

mean of the STM are likely to include systematic biases especially as a function of the heliocentric distance. Spencer et al. (1998) Fig. 8 shows that for $\Theta \sim 3$, i.e. the mean value we have derived for the large majority of NEAs, radiometric diameters derived by the STM are likely to be between 40 and 20% smaller than the true value. However, Spencer et al. studies were devoted to estimate systematic errors in asteroid diameters derived by the use of the STM only. Moreover, they did not consider what the likely effects of thermal inertia, rotation rate and surface roughness are on the thermal emission of asteroids observed in near Earth space at phase angles as large as 80° .

We have used our thermophysical model to study systematic errors in diameters and albedos derived by the STM as a function of the phase angle for different values of the thermal parameter Θ and degrees of the macroscopic surface roughness. To this end, we have fitted the STM to the N-band data only (i.e. at 8.0, 10.3 and 12.5 μm) of the synthetic generated spectra calculated every 10° of phase angle, from -90° to 90° varying Θ and $\bar{\theta}$ parameters as described in section 6.5 and section 6.6. Fig. 6.16 shows the percentage of the albedo relative error: i.e. the difference between the radiometrically derived and the true albedo divided by the latter.

Our simulation show that accuracy of the STM used with fixed a η value equal to 0.756 is strongly depended on the phase angle and on the thermal parameter and this dependence varies, eventually, with the roughness of the surface. For low degrees of roughness ($\bar{\theta} < 20^\circ$) STM albedo is always larger than the true value. This systematic effect, which can be clearly identified by comparing STM with radar diameters (see section 5.5) can be as large as 50 – 100% in the albedo for typical values of the thermal parameter in the case of NEAs ($1 \leq \Theta \leq 5$). For larger values of $\bar{\theta}$, the error function becomes very variable within the studied range of phase angles and thermal parameters. In such cases, STM albedos can become smaller the true ones, provided observations of objects with low thermal parameter are carried out at low phase angle. Fig. 6.16 suggests that if we restrict the use of the STM within $\pm 45^\circ$ of phase angle and if the thermal parameter is not larger than ~ 2 , radiometric albedos are accurate to within $\pm 30\%$.

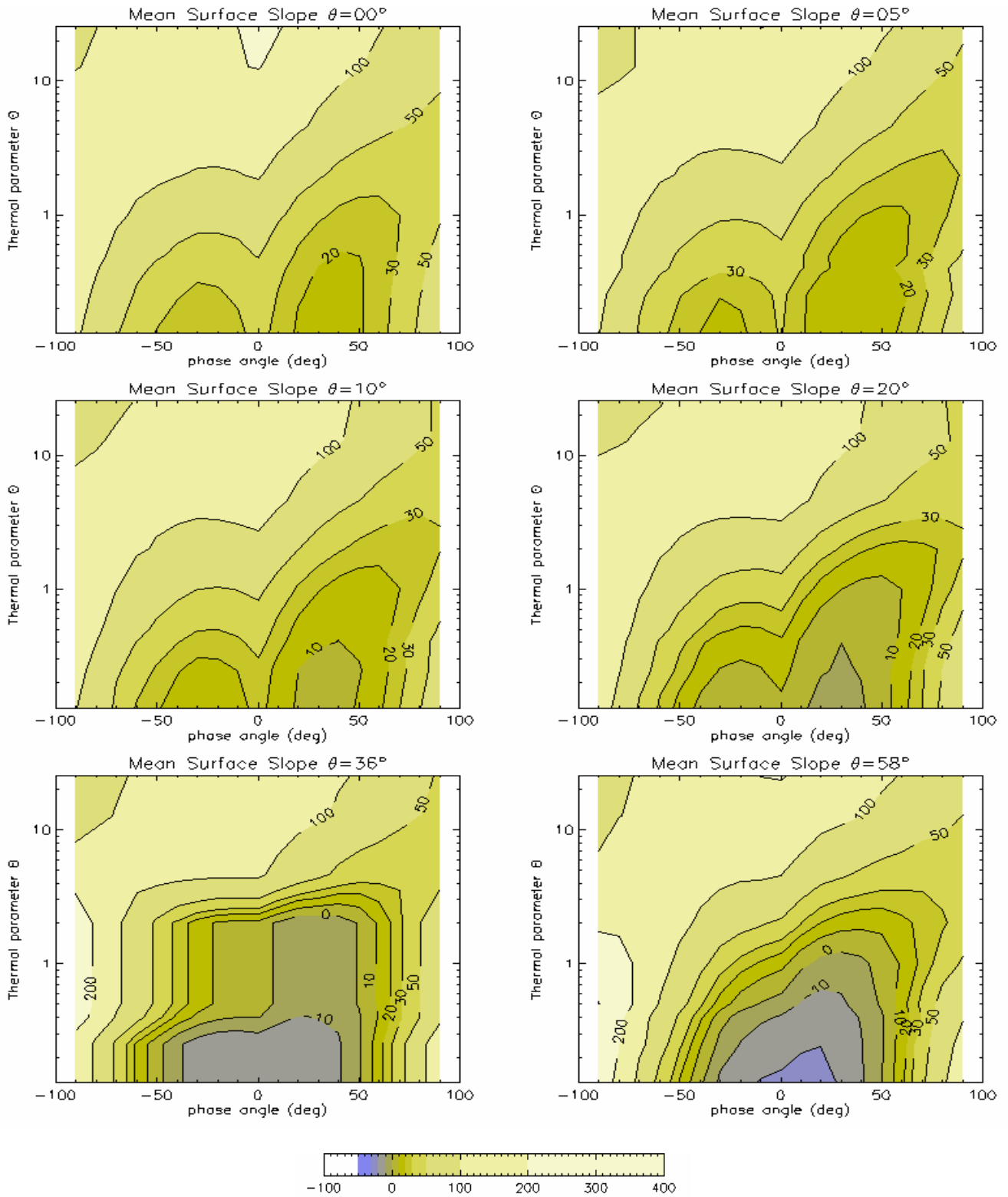


Fig. 6.16 Section of the STM relative albedo error function i.e. $(p_{V_STM}(\alpha, \Theta, \bar{\rho}) - p_{V_TM}) / p_{V_TM} \times 100$ at constant value of $\bar{\rho}$. The refined STM of Lebosfky and Spencer (1989) was used with constant $\eta=0.756$ and $\beta_E=0.01$ magnitude per degree. The function was numerically evaluated on a grid of ten degree of step size in α and at $\Theta=[0.13, 0.25, 0.40, 0.50, 1.00, 2.00, 4.60, 12.70, 25.5]$.

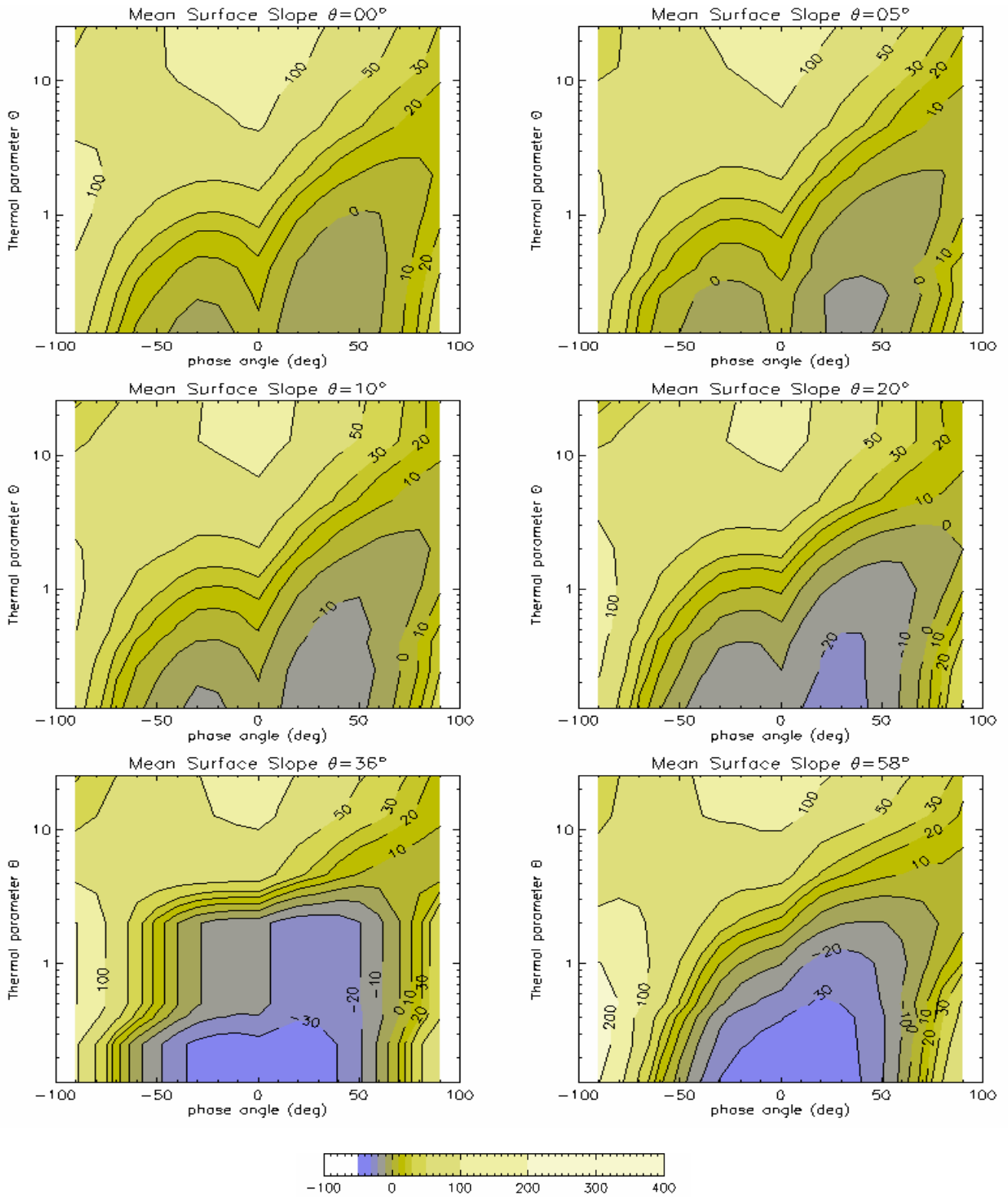


Fig. 6.17 Section of the STM relative albedo error function i.e. $(p_{V_STM}(\alpha, \Theta, \bar{\rho}) - p_{V_TM}) / p_{V_TM} \times 100$ at constant value of $\bar{\rho}$. In contrast to Fig. 6.16, here η is constant but equal to 0.95 and $\beta_E = 0.015$ magnitude per degree, as described in section 5.6. The function was numerically evaluated on a grid of ten degree of step size in α and at $\Theta = [0.13, 0.25, 0.40, 0.50, 1.00, 2.00, 4.60, 12.70, 25.5]$.

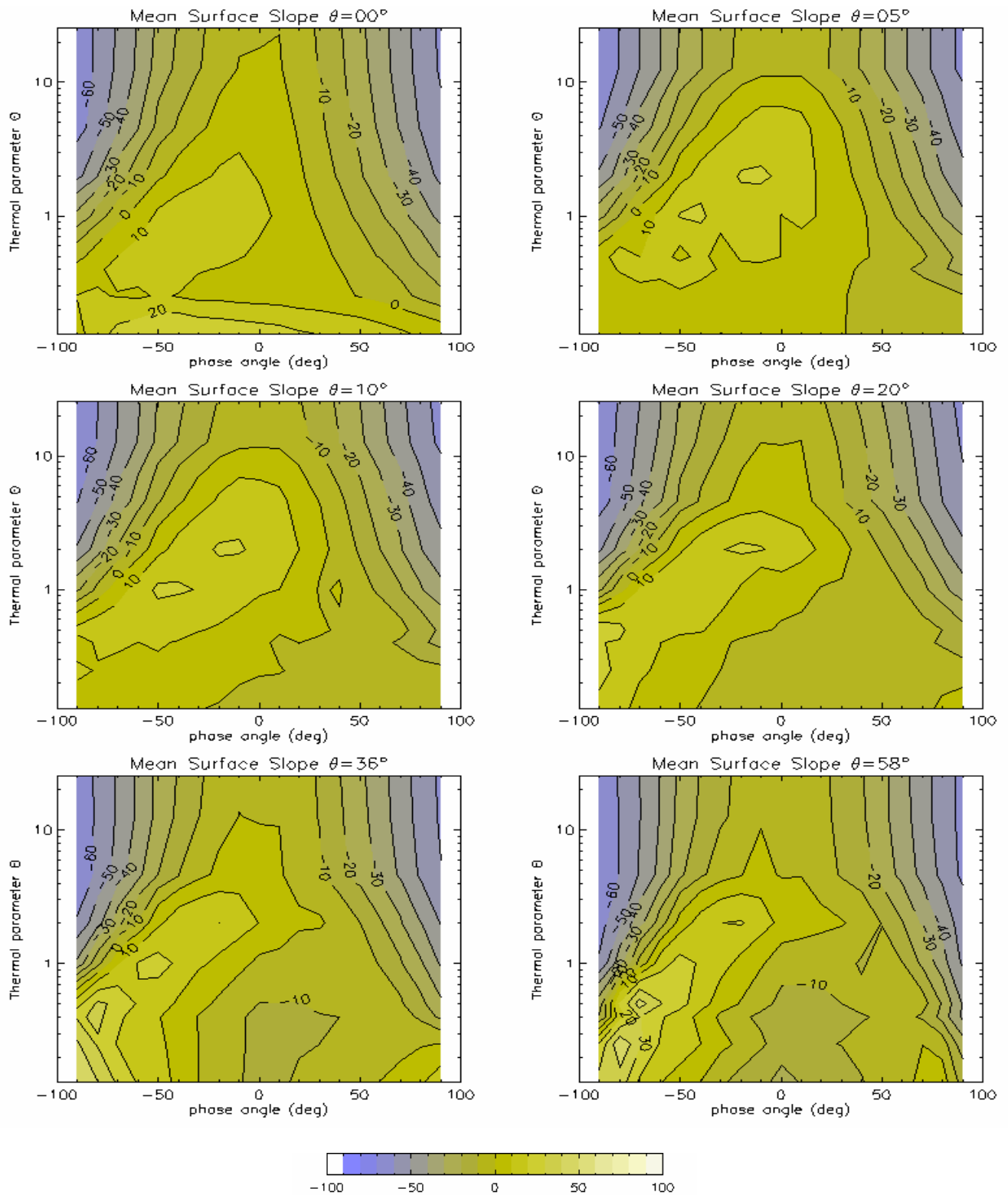


Fig. 6.18 Section of the NEATM relative albedo error function i.e. $(p_{V_NEATM}(\alpha, \Theta, \bar{\rho}) - p_{V_TM}) / p_{V_TM} \times 100$ at six different constant values of $\bar{\rho}$. The function was numerically evaluated on a grid of ten degree of step size in α and at $\Theta = [0.13, 0.25, 0.40, 0.50, 1.00, 2.00, 4.60, 12.70, 25.5]$

Fig. 6.17 shows that a slight improvement of the STM when used with NEAs can be obtained by increasing the η -value to about 0.95 and the infrared phase coefficient β_E to 0.015 magnitudes/degree as we have derived in section 5.6 by comparing STM diameter to radar ones.

Finally we may note that Fig. 6.16 suggests that STM errors are at minimum in the case of the thermal infrared observations of 433 Eros discussed by Harris & Lagerros (2002), and reported in table 2 of their paper. The STM effective diameter of 20.5 and 21.0 km are in very good agreement with the size derived by the NEAR Shoemaker spacecraft ($D_{\text{eff}}(\text{max})=20.6$ km). Those observations were obtained at phase angles of 10 and 31 degrees, respectively. Our thermophysical model calculations indicate a thermal parameter Θ of about one and a macroscopic surface roughness $\bar{\theta}$ of about 20° . This latter value is in very good agreement with the estimates obtained from measurements carried out with the near-infrared spectrometer on board the NEAR Shoemaker spacecraft which yielded $\bar{\theta} = 24 \pm 2^\circ$. For that range of phase angle and for $\Theta \sim 1$ and $\bar{\theta} = 20^\circ$, Fig. 6.16 indicate an albedo error of +10%.

In section 6.5 and section 6.6, we have used the NEATM to fit synthetic thermal infrared spectra generated by means of our thermophysical model. NEATM solves simultaneously for the η -value, the diameter and the geometric visible albedo. Not only the η -value is thus a function of the phase angle α , of the thermal parameter Θ and of the macroscopic surface roughness $\bar{\theta}$, but also the derived diameter and albedo, in general, depends on those parameter. Along with the best fit parameter η , the diameter and the albedo were derived for each point of the α - Θ - $\bar{\theta}$ space as described in chapter 6.5 and chapter 6.6.

Fig. 6.18 is the analogue of Fig. 6.16 and Fig. 6.17 for the NEATM and shows the albedo relative error, i.e. the difference between the radiometrically derived and the true albedo divided by the latter, in percent. Some irregularities in the curve are artifacts of the finite resolution of the model - we have used a mesh made of only 184 tiles in order to speed up calculations - and are also due to the fairly coarse grid spacing in the α - Θ space.

The non symmetrical shapes of the curves in Fig. 6.18 with respect $\alpha=0^\circ$ is due to the so-called morning-afternoon effect. According to our notation, for negative values of phase angle, the observer looks at the cooler morning side of the asteroid, whereas at phase angle larger than zero the warmer afternoon hemisphere is directed toward the observer. This shows that not only the NEATM derived color temperature, but also the accuracy of radiometric diameter and albedos depends on whether the morning or the afternoon hemisphere of the asteroid is observed. We remind here that diameter and

albedos are related by Eq (2-16) via the absolute magnitude H of the object: given the error on the albedo, it is straightforward to estimate the error on the diameter.

The model error is a rather complicated function of the phase angle, the thermal parameter and the degree of roughness of the surface. However, some general behavior of this function can be found even if thermal inertia, rotation rate and surface roughness are not known. In Fig. 6.19, we have plotted the relative albedo error as a function of the η -value for observations carried out at low-moderate ($-40^\circ \leq \alpha \leq 40^\circ$, Fig. 6.19, a) and at high ($|\alpha| \geq 40^\circ$, Fig. 6.19, b) phase angle.

In the first case we can easily see that the error on albedo is very rarely larger than $\pm 20\%$. Moreover, for η -values smaller than 1.1 a correlation η vs. model error appears such that NEATM underestimate the albedo of objects with higher color temperatures (i.e. smaller η -values). For η -values larger than 1.1 the correlation goes the other way and objects which appear hotter are likely to have albedos overestimated by the NEATM.

In the case of observations at large phase angle the scatter in Fig. 6.19, b) is much larger and for $\eta < \sim 1.2$ it appears that no correlation of the model error with the color temperature can be found. However, for larger η -values ($\eta > 1.5$) NEATM is likely to underestimate the albedo and consequently to overestimate the diameter. This error is incurred by ignoring thermal emission from the night side. This error increases with increasing η and increasing solar phase angle.

The general shape of the model error function plotted in Fig. 6.18 indicates that NEATM gives reliable results in the case on NEAs if their thermal parameters are neither not too high, nor too low ($0.1 \leq \Theta \leq 5$) and the phase angle not too extreme ($|\alpha| < 60^\circ$).

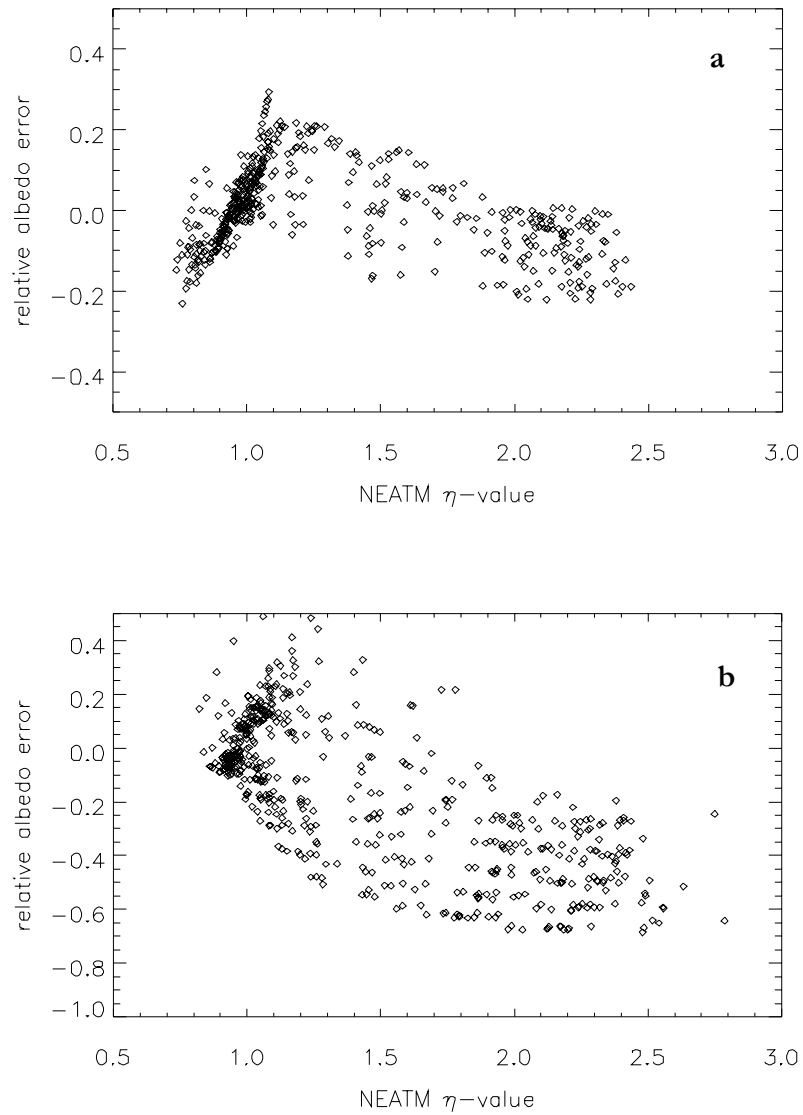


Fig. 6.19 Distribution of the albedo relative error as a function of the η -value for asteroid observed at phase angle between -40 and 40 degrees (a) and at phase angle larger than 40° or smaller than -40° .

6.10 Conclusions

In this chapter we have described a thermophysical model which can generate thermal infrared spectra taking into account the combined effect of rotation rate, pole orientation, thermal inertia and surface roughness. We have used this model on synthetic spherical asteroids; however, the implementation here described allows the use of general convex shapes.

Thermal inertia has been modeled by numerically solving the equation of vertical heat transport, whereas surface roughness has been modeled by means of spherical section craters which density and opening angle can be adjusted. The effect of surface characteristics on the thermal radiation of asteroids can be described in terms of the thermal parameter Θ and the mean surface slope $\bar{\theta}$ which gives the degree of macroscopic roughness on the surface.

We have used the thermophysical model to study the dependence of the NEATM best fit η parameter for different illumination and observing geometries as a function of the thermal parameter Θ and the mean surface slope $\bar{\theta}$. In particular we devoted great interest to model the effect of the phase angle. Indeed, information on the thermal inertia and some hints on the degree of surface roughness of NEAs may be obtained from the variation of the η -value, with solar phase angle.

Although the NEATM derived η -value is a complicated function of all those parameters, we have demonstrated that for a given value of Θ and $\bar{\theta}$, for random orientations of the asteroid spin vector with respect to the Sun and the observer, η -values are constrained by two curves: the curve of zero thermal inertia and the “morning curve” obtained by looking at the morning hemisphere of an asteroid with a rotational axis perpendicular to the plane containing the Sun and the Earth.

We have looked for that set of curves giving the best fit to the observed distribution of η -values. We found that a thermal $\Gamma=550\pm 100\text{J m}^{-2}\text{ s}^{-0.5}\text{ K}^{-1}$ gives the best fit to the large majority of the observations in our data set. This value is about eleven times the thermal inertia derived for the lunar soil. Surface roughness is not very well constrained and values of the mean surface slope between 20 and 35° are in good agreement with the observations.

Our thermophysical model cannot explain the very low color temperature observed for NEAs 3671, 2002 BM₂₆ and 1999 NC₄₃. Perhaps more sophisticated thermal models including the effect of positive and negative relief and the effect of lateral heat conduction may be necessary in those cases.

However, our thermophysical model derives values in good agreement with the findings of other researchers for the thermal inertia the mean surface slope of 433 Eros.

The relatively high η -values derived for the NEA 5381 Sekmeth are explained with a thermal parameter $\Theta\sim 4$ which implies a thermal inertia thirteen times that of the moon and a high degree of surface roughness ($\bar{\theta}\sim 36^\circ$). The variation of the η -value 5381 Sekmeth with phase angle is compatible our thermophysical model calculations if the cool mooring side of the object has been observed.

The derived average value of the NEA thermal inertia put constraints on the strength of the Yarkovsky effect on kilometer and sub-kilometer size bodies. We obtain a semimajor axis drift rate of about 9×10^{-4} AU/Myr for an object with NEA-like thermal inertia with a diameter of 200 m, a rotational period of 5 hours at 2 AU from the Sun.

With our thermophysical model we have studied the effects of surface roughness, thermal inertia and rotation rate on the accuracy of NEA radiometric diameters and albedos.

Our simulation show that the accuracy of the STM used with fixed a η value equal to 0.756 is strongly depended on the phase angle. However, if we restrict its use to within $\pm 45^\circ$ of phase angle and if the thermal parameter is not larger than ~ 2 , radiometric albedos are accurate to within $\pm 30\%$. We argue that the refinement to the STM proposed in section 5.6 reduces model errors for its use with NEAs.

In the case of the NEATM the error on albedo is very rarely larger than $\pm 20\%$ for observations obtained to within $\pm 40^\circ$ of phase angle. A correlation of the model error with η -value can be seen for both the case of observations obtained at small phase angles and for those carried out at large phase angle. In this latter case η -values larger than 1.5 correspond always to an underestimation of the real albedo with this effect increasing for increasing η .

Conclusion and future works

7.1 Conclusions

7.1.1 *This work increases the number of NEAs with measured sizes and albedos by 54%*

Overall, we have obtained radiometric diameters and albedos for thirty-two NEAs. Seven of them were observed under different observing geometries and with different instruments.

This work increments the number of NEAs with measured sizes and albedos by 54%. If we include objects for which the diameter and the albedo have been refined, this increment increases to almost 70%.

We have mainly contributed to the physical characterization of objects smaller than 1 kilometer. There were very few thermal infrared observations of asteroids in this size range, and we have more than doubled the number of subkilometer-NEAs with measured size and albedos.

We have derived the surface color temperature of 16 NEAs. This is twice the number of objects for which this information was available before. The variation of the color temperature with phase angle gives insight into the surface thermal properties of asteroids and the phase angle spanned by our observations is very broad: from 3 to 93°.

In all these respects, we have contributed to build the largest database of radiometric observations of NEAs. Following results are obtained from these measurements.

7.1.2 *The observed NEAs are on average brighter than main belt asteroids*

The mean albedo of NEAs with reliable radiometric measurements is 0.27, which is much higher than the mean albedo of observed main-belt asteroids (~ 0.11).

S-type NEAs are on average 20% brighter than S-type MBAs, while C-types NEAs have on average albedos 57% higher than C-type MBAs.

We confirm, therefore, the evidence that NEAs and small asteroids in general have a different albedo distribution than larger main-belt asteroids.

Studies of the albedos derived by IRAS had shown how the albedo distribution of main-belt asteroids smaller than 50 km has different properties than the one of larger bodies (i.e. the mean albedo increases with decreasing diameter and the clear separation between C-type and S-type asteroids vanishes at the smaller sizes. Such dichotomy between the albedo statistics of large and small asteroids is confirmed by our findings.

This implies a fundamental difference in surface properties of small asteroids with respect to the larger ones.

With our statistics we can improve the estimation of the albedo (and size, given the H value) for those NEAs for which taxonomic type is known.

7.1.3 There is a trend of increasing albedo with decreasing size for observed S-type NEAs

If real, the trend of increasing albedo with decreasing size may be indicative, for instance, of recently exposed, relatively unweathered surfaces.

This result is also consistent with the trend to ordinary-chondrite-type reflection spectra with decreasing size observed in the NEA population, which is also attributed to a lack of space weathering of relatively young surfaces.

However, a selection effect in favor of the discovery of brighter NEAs in a magnitude limited survey may explain such trend. A simulation of the NEA discovery process and the possible selection effect involved in the choice of the objects to be observed in the thermal infrared is an important future work that can clarify this issue.

7.1.4 The ambiguous taxonomic classifications of six asteroids have been clarified in the light of the new albedo values.

The taxonomic classification of the NEAs 1997 XF₁₁, 4666 Nereus, 5751 Zao, 15817 Lucianotesi, 2000 BG₁₀, 2002 BM₂₆ have been revised in the light of newly derived albedos.

7.1.5 The apparent color temperature of the observed NEAs is phase angle dependent

The NEATM best fit parameter η is inversely related to the apparent surface color temperature of asteroids (via Eq. 5-1).

The NEATM η -value is phase-angle dependent and, on average, significantly higher than the value 0.756 adopted by Lebofsky et al. (1986) in their version of the STM, which was used to derive IRAS albedos of main-belt asteroids. We have shown that this effect is due to the fact that NEAs have larger thermal inertias than big main belt asteroids.

The best linear fit to the observed distribution of NEAs η -values is: $\eta=(0.011\pm 0.002)\alpha+(0.90\pm 0.07)$, where α is the phase angle.

7.1.6 The variation of the color temperature with phase angle depends on the albedo

Darker objects have a steeper increment of η with the phase angle and smaller η -values at low phase angles. The higher color temperature displayed by these object at phase angle approaching zero is indicative of a thermal inertia lower than the mean value. Moreover, darker objects might have more pristine and rougher surfaces leading to a stronger beaming effect (and consequently to a lower η) than objects with higher albedos.

7.1.7 The observed distribution of the color temperature with the phase angle can be explained in terms of thermal inertia and surface roughness

We have developed a thermophysical model which takes into account the combined effects of surface roughness, thermal inertia and rotation rate on the thermal infrared emission of asteroids.

We show that the thermal properties of the large majority of the NEAs in our database can be described by means of that model.

7.1.8 The best-fit thermal inertia of the observed NEAs is $550\pm 100\text{J m}^{-2}\text{s}^{-0.5}\text{K}^{\pm 1}$ or about 11 times that of the Moon

For random orientations of the asteroid spin vector with respect to the Sun and the observer, η -values are constrained by two curves in the η - α plane. Those curves are function of the thermal parameter Θ and the mean surface slope $\bar{\theta}$. We have corrected the observed η -values of NEAs to take account of their different rotation rates and we have looked for the set of curves giving the best fit to the observed η -values. Surface roughness is not well constrained, but we found that $20^\circ \leq \bar{\theta} \leq 35^\circ$ is in good agreement with the observations.

Our result put constraints on the strength of the Yarkovsky effect on kilometer and sub-kilometer size bodies. As an example, we have calculated the semimajor axis drift rate for an object with NEA-like thermal inertia, with a diameter of 200 m, a rotational period of 5 hours at 2 AU from the Sun. We derive a value of 9×10^{-4} AU/Myr.

Our best estimate of the thermal inertia of the observed NEAs indicates that these bodies have surfaces with a regolith courser than the lunar one and, very likely, their surfaces differ in fractional rock coverage from those of large main belt asteroids.

However, note that our thermophysical model used is still idealized. (spherical shape, roughness described by simple hemispherical craters, lack of realistic surface topography)

7.1.9 There are asteroids with anomalously low color temperature

However, our thermophysical model cannot explain the very low color temperature observed for NEAs 3671, 2002 BM₂₆ and 1999 NC₄₃. Perhaps more sophisticated thermal models including the effect of positive and negative relief and the effect of lateral heat conduction may be necessary in those cases.

Moreover, our idealized thermophysical model assumes the emissivity equal to one at every wavelength. However, if this is not the case variations of the apparent color temperatures of asteroids may result.

7.1.10 The observed distribution of color temperature allows a calibration of thermal models for applications to NEAs

A refinement of the default η -value for the NEATM is proposed by using the linear relation in Eq. (5-2), when it is not possible to derive η via a fit of the thermal infrared continuum.

The STM with a fixed η -value equal to 0.9 and an infrared phase coefficient $\beta_E = 0.015$ mag/deg (instead of $\eta = 0.756$ and $\beta_E = 0.01$ mag/deg) derives diameters in better agreement with radar results. Such modified STM is also in better agreement with thermophysical model simulation carried out with the average value of the thermal inertia and the mean surface slope that we have derived for NEAs.

The use of the modified STM or the NEATM with default η -value given by Eq. (5-2) provides the same results for phase angles up to 30-40°.

7.1.11 We have derived a quantitative assessment of the accuracy of thermal models and a correction function for the nominal results of the NEATM and the STM

We have numerically estimated a correction function for NEAs radiometric diameters and albedos derived by means of the STM and of the NEATM, provided that spin status and thermal parameter of the asteroid are known.

When such information is not available, the accuracy of NEATM results can be still estimated on the basis of the derived η -value.

In the case of NEATM, errors on the derived albedos are very rarely larger than $\pm 20\%$ for observations obtained to within $\pm 40^\circ$ of phase angle.

At large phase angle ($|\alpha| > 40^\circ$), the accuracy of the NEATM is worse and derived albedos are likely to be underestimated if η is larger than 1.5. This is consistent with the fact that this model ignores the emission from the night side of the asteroid.

7.2 Future works

7.2.1 Application of thermophysical models to NEAs

We have shown how the use of simple thermal models can provide valuable information on the sizes and albedos of NEAs. However, the use of more sophisticated thermophysical models has to be considered if one wants to get insights into thermal and surface properties of single asteroids.

We have used our thermophysical model to get constraints on the average thermal inertia of NEAs. We have done that by fitting the distribution of the surface color temperature of a number of objects studied together. However, as in the case of 433 Eros and 5381 Sekmeth, we have shown that thermophysical modeling is very promising to study the characteristics of single objects. And indeed, NEAs appear the most intriguing and suitable bodies of the solar system where performing such study. They often appear under a large range of illumination and observing geometries and have a large variety of surface characteristics. A very interesting project would be to include radar and/or photometrically derived asteroid shapes along with their spin vector status into the thermophysical model.

7.2.2 Study of the contribution of a selection bias in the observed trend of increasing albedo with decreasing size

Small objects appear, in general, to have albedos higher than the value implied by their taxonomic classification (according to taxonomic schemes based on the study of large main belt asteroids).

However, a selection effect in favor of the discovery of brighter NEAs in a magnitude limited survey may explain such trend. A simulation of the NEA discovery process and the possible selection effect involved in the choice of the objects to be observed in the thermal infrared is an important future work that can clarify this issue.

However, the present statistics is still poor and strongly affected by possible observational and selection biases. A simulation of the NEA discovery process and the possible selection effect involved in the choice of the objects to be observed in the thermal infrared is an important future work that can clarify this issue.

7.2.3 Study the range of thermal and surface properties of NEAs by means of thermal infrared

Studying the range of thermal properties and surface structure present in the NEA population is possible by investigating the variation of the apparent color temperature, T_c , with the phase angle for selected near-Earth asteroids of different sizes and classes. Different effects such as thermal inertia and the infrared “beaming” due to surface roughness lead to different dependencies of T_c on phase angle. Measurements of T_c over a range of phase angle can therefore provide information on the physical properties of NEAs not obtainable by other means.

REFERENCES

- Abe, M., Ohba, Y., Ishiguro, et al., (2002), Physical Model of Asteroid (25143) 1998 SF36, a Target of the MUSES-C Mission. *Asteroids, Comets and Meteors, abstract*, 18-24
- Belskaya, I. N. and Shevchenko, V. G., (2000), Opposition effect of asteroids. *Icarus*, **147**, 94–105.
- Bendjoya, Ph. and Zappalà, V., (2002) Asteroid Family Identification. In *Asteroids III* (W.F. Bottke, A. Cellino, P. Paolicchi, R.P. Binzel, eds.). pp. 613-618. The University of Arizona Press, Tucson.
- Benedix, G. K., McFadden, L. A., and Morrow, E. M., (1992), Bias correction factors for near-Earth asteroids. In *Asteroids, Comets, Meteors 1991*, pp. 65–68. Lunar and Planetary Institute, Houston.
- Binzel, R.P., (1989), An overview of the asteroids. In *Asteroids II* (R. P. Binzel et al., eds.), pp. 3-18. Univ. of Arizona, Tucson.
- Binzel, R.P., Lupishko, D.F., Di Martino, M., Whiteley, R.J., and Hahn, G.J., (2002), Physical Properties of Near-Earth Objects. In *Asteroids III* (W.F. Bottke, A. Cellino, P. Paolicchi, R.P. Binzel, eds.). pp. 255-271. The University of Arizona Press, Tucson.
- Binzel, R. P., Birlan, M., Bus, S. J., Harris, A. W., Rivkin, A. S., Fornasier, S., (2004), Spectral observations for near-Earth objects including potential target 4660 Nereus: Results from Meudon remote observations at the NASA Infrared Telescope Facility (IRTF). *Planetary and Space Science*, **52**, 291-296.
- Bottke, W.F., Jedicke, R., Morbidelli, A., Petit, J.M., Gladman, B. (2000). Understanding the Distribution of Near-Earth Asteroids. *Science*, **288**, 2190-2194.
- Bottke, W. F. Jr., Cellino, A., Paolicchi, P., and Binzel, R. P., (2002a) An Overview of the Asteroids: The Asteroids III Perspective. In *Asteroids III* (W.F. Bottke, A. Cellino, P. Paolicchi, R.P. Binzel, eds.). pp. 3-15. The University of Arizona Press, Tucson.
- Bottke, W. F. Jr., Vokrouhlický, D., Rubincam, D. P., and Broz, M. (2002b) The Effect of Yarkovsky Thermal Forces on the Dynamical Evolution of Asteroids and Meteoroids. In *Asteroids III* (W.F. Bottke, A. Cellino, P. Paolicchi, R.P. Binzel, eds.). pp. 395-408. The University of Arizona Press, Tucson.

- Bowell, E., Hapke, B., Domingue, D., Lumme, K., Peltoniemi, J., and Harris A. W., (1989), Application of photometric models to asteroids. In *Asteroids II* (R. P. Binzel et al., eds.), pp. 524–556. Univ. of Arizona, Tucson.
- Brown, R. H., (1985), Ellipsoidal geometry in asteroid thermal models: the standard radiometric model, *Icarus*, **64**, 53-63
- Bus, S. J., (1999) Compositional Structure in the Asteroid Belt: Results of a Spectroscopic Survey, *Ph.D. thesis*, Massachusetts Institute of Technology.
- Bus, S.J., Binzel, R.P., (2002). Phase II of the small main-belt asteroid spectroscopic survey: a feature-based taxonomy. *Icarus*, **158**, 146–177.
- Cellino, A., Gil Hutton R., Tedesco, E. F., Di Martino, M. And Brunini, A., (1999), Polarimetric observations of small asteroids: Preliminary results. *Icarus*, **138**, 129–140.
- Cellino, A., Bus, S. J., Doressoundiram, A., and Lazzaro, D. (2002a) Spectroscopic Properties of Asteroid Families. In *Asteroids III* (W.F. Bottke, A. Cellino, P. Paolicchi, R.P. Binzel, eds.). pp. 633-643. The University of Arizona Press, Tucson.
- Cellino, A., Zappalà, V., and Tedesco, E. F., (2002b), Near-Earth objects: Origins and need of physical characterization. *Meteoritics and Planetary Science*, **37**, 1965–1974
- Cellino, A., Di Martino, M., Gil Hutton, R., Tedesco, E.F., Bendjoya, Ph, (2003), Asteroid Polarimetry at CASLEO. Talk presented at the workshop: *Photometry and polarimetry of asteroids: Impact to collaboration*. June 15–18, 2003, Kharkiv, Ukraine.
- Chapman, C., (1996), S-type asteroids, ordinary chondrites and space weathering: The evidence from Galileo's fly-bys of Gaspra and Ida. *Meteoritics and Planetary Science*, **31**, 699–725.
- Clark, B. E., Hapke, B., Pieters, C., and Britt, D., (2002), Asteroid space weathering and regolith evolution. In *Asteroids III* (W.F. Bottke, A. Cellino, P. Paolicchi, R.P. Binzel, eds.). pp. 585-599. The University of Arizona Press, Tucson.
- Cohen, M., Walker, R.G., Carter, B., Hammersley, P., Kidger, M., Noguchi, K., (1999), Spectral irradiance calibration in the infrared. X. A selfconsistent radiometric all-sky network of absolutely calibrated stellar spectra. *Astronomical Journal*, **117**, 1864–1889.

Cruikshank, D. P., and Jones, T. J., (1977), The diameter and albedo of asteroid 1976 AA. *Icarus*, **31**, 427–429.

Dandy, C.L., Fitzsimmons, A., and Collander-Brown, S.J., (2003), Optical colors of 56 near-Earth objects: trends with size and orbit. *Icarus*, **163**, 363-373

Davis, D. R., Durda, D. D., Marzari, F., Campo Bagatin, A., and Gil-Hutton, R., (2002) Collisional Evolution of Small-Body Populations. In *Asteroids III* (W.F. Bottke, A. Cellino, P. Paolicchi, R.P. Binzel, eds.). pp. 545-558. The University of Arizona Press, Tucson.

Delbó, M. and Harris, A. W. (2002), Physical properties of near-Earth asteroids from thermal infrared observations and thermal modeling. *Meteoritics and Planetary Science*, **37**, 1929–1936

Delbó, M., Harris, A. W., Binzel, R. P., Pravec, P., and Davies, J., K, (2003), Keck observations of near-Earth asteroids in the thermal infrared. *Icarus*, **166**, 116-130.

Deutsch, L., Hora, J., Adams, J., and Kassis, M., (2002), MIRSI: a mid-infrared spectrometer and imager, in *Astronomical telescopes and instrumentations*, SPIE **4841**, 106.

Di Martino, M., Montebugnoli, S., Cevolani, G., Ostro, S., Zaitsev, A., Righini, S., Saba, L., Poppi, S., Delbò, M., Orlati, A., Maccaferri, G., Bortolotti, C., Gavrik, A., Gavrik, Y., (2004), Results of the first Italian planetary radar experiment. *Planetary and Space Science*, **52**, 325-330.

Dohnanyi, J. S. (1969) Collisional model of asteroids and their debris. *Journal of Geophysical Research*, **74**, 2431-2554.

Dollfus, A., M. Wolff, J. E. Geake, D. F. Lupishko, and L. Dougherty (1989), Photopolarimetry of asteroids. In *Asteroids II* (R. P. Binzel, T. Gehrels, M. S. Matthews, Eds.), pp. 594–616. Univ. of Arizona Press, Tucson.

Emery, J. P., Sprague, A. L., Witteborn, F. C., Colwell, J. E., Kozłowski, R.W. H., and Wooden, D. H., (1998), Mercury: Thermal modeling and mid-infrared (5–12 μm) observations. *Icarus* **136**, 104–123.

Erikson, A., Mottola, S., Lagerros, J. S. V., Lindgren, M., Piironen, J., Oja, T., Hahn, G., Lagerkvist, C.-I., Harris, A. W., Nathues, A., and Neukum, G. (2000), The near-Earth objects follow-up program. *Icarus*, **147**, 487–497.

- Farinella, P., Vokrouhlicky, D., Hartmann, W.K., (1998), Meteorite delivery via Yarkovsky orbital drift. *Icarus*, **132**, 378-387.
- Fowler, J. W. and Chillemi, J. R., (1992), IRAS asteroid data processing. In *The IRAS Minor Planet Survey* (ed. E. F. Tedesco), pp. 17–43. Tech. Rep. PL-TR-92-2049, Phillips Laboratory, Hanscom Air Force Base, Massachusetts, USA.
- Harris, A.W., Harris, A.W., (1997), On the revision of radiometric albedos and diameters of asteroids. *Icarus*, **126**, 450–454.
- Harris, A.W., (1998). A thermal model for near-Earth asteroids. *Icarus*, **131**, 291–301.
- Harris, A.W., Davies, J.K., (1999), Physical characteristics of near-Earth asteroids from thermal infrared spectrophotometry. *Icarus*, **142**, 464–475.
- Harris, A.W., Davies, J.K., Green, S.F., (1998). Thermal infrared spectrophotometry of the near-Earth Asteroids 2100 Ra-Shalom and 1991 EE. *Icarus*, **135**, 441–450.
- Harris, A. W. (2001) The Albedos and Taxonomy of Small Asteroids. Talk presented at the conference: *Asteroid 2001 from Piazzzi to the 3rd millennium*, Palermo, Italy
- Harris, A. W. and Lagerros, J. S. V. (2002). Asteroids in the thermal infrared., In *Asteroids III* (W.F. Bottke, A. Cellino, P. Paolicchi, R.P. Binzel, eds.). The University of Arizona Press, Tucson.
- Hirayama K. (1918) Groups of asteroids probably of common origin, *Astronomical Journal*, **31**, 185-188.
- Housen, K. R., Wilkening, L. L., Chapman, C. R., and Greenberg, R. J., (1979), in *Asteroids* T. Gehrels (ed.), pp 601–627, The University of Arizona Press
- Howell, S. B., (1989) Two-dimensional aperture photometry: Signal-to-noise ratio of point-source observations and optimal data-extraction techniques. *Publication of the Astronomical Society of the Pacific*, **101**, 616-622
- Hudson, R. S., and 26 colleagues, (2000), Radar observations and physical model of asteroid 6489 Golevka, *Icarus*, **148**, 37–51.

Hudson, R. S., and S. J. Ostro, (1999). Physical model of asteroid 1620 Geographos from radar and optical data. *Icarus* **140**, 369-378.

Ivanov B. A., Neukum G., Bottke W. F. Jr., and Hartmann W. K., (2002) The Comparison of Size-Frequency Distributions of Impact Craters and Asteroids and the Planetary Cratering Rate. In *Asteroids III* (W.F. Bottke, A. Cellino, P. Paolicchi, R.P. Binzel, eds.). pp. 89-101. The University of Arizona Press, Tucson.

Jakosky, B.M., (1986). On the thermal properties of martian fines, *Icarus* **66**, 117–124.

Jones, B., Puetter, R.C., (1993). Keck long-wavelength spectrometer. In: Fowler, A.M. (Ed.), *Infrared Detectors and Instrumentation. Proc. SPIE*, **1946**, 610–621.

Kaasalainen, M., Mottola, S., and Fulchignoni, M., (2002), Asteroid Models from Disk-integrated Data., In *Asteroids III* (W.F. Bottke, A. Cellino, P. Paolicchi, R.P. Binzel, eds.). pp. 139-150. The University of Arizona Press, Tucson.

Kaasalainen, M., Pravec, P., Krugly, Y. N., Šarounová, L., Torppa, J., Virtanen, J., Kaasalainen, S., Erikson, A., Nathues, A., Durech, J., Wolf, M., Lagerros, J. S. V., Lindgren, M., Lagerkvist, C. I., Koff, R., Davies, J. K., Mann, R., Kušnirák, P., Gaftonyuk, N. M. V., Shevchenko, G., Chiorny, V. G., Belskaya, I. N., (2004) Photometry and models of eight near-Earth asteroids, *Icarus*, **167**, 178–196

Kiselev, N. N., Rosenbush, V. K., Jockers, K., Velichko, F. P., Shakhovskoj, N. M., Efimov, Yu. S., Lupishko, D. F., Rumyantsev, V. V., (2002), Polarimetry of near-Earth asteroid 33342 (1998 WT24). Synthetic phase angle dependence of polarization for the E-type asteroids In: *Proceedings of Asteroids, Comets, Meteors - ACM 2002. International Conference, 29 July - 2 August 2002, Berlin, Germany*. Ed. Barbara Warmbein. ESA SP-500. Noordwijk, Netherlands: ESA Publications Division, ISBN 92-9092-810-7, 2002, p. 887 – 890.

Lagerros J. S. V. (1996) Thermal physics of asteroids I: Effects of shape, heat conduction and beaming. *Astronomy and Astrophysics*, **310**, 1011–1020.

Lagerros J. S. V. (1997) Thermal physics of asteroids III. Irregular shapes and albedo variegations. *Astronomy and Astrophysics*, **325**, 1226– 1236.

- Lagerros J. S. V. (1998) Thermal physics of asteroids IV. Thermal infrared beaming. *Astronomy and Astrophysics*, **332**, 1123–1132.
- Lebofsky L. A., Veeder G. J., Lebofsky M. J., and Matson D. L. (1978) Visual and radiometric photometry of 1580 Betulia., *Icarus*, **35**, 336–343.
- Lebofsky, L. A., and Spencer, J. R., (1989), Radiometry and thermal modeling of asteroids. In *Asteroids II* (R. P. Binzel, T. Gehrels, and M. S. Matthews, Eds.), pp. 128–147. Univ. of Arizona Press, Tucson.
- Lebofsky, L. A., Sykes, M. V., Tedesco, E. F., Veeder, G. J., Matson, D. L., Brown, R. H., Gradie, J. C., Feierberg, M. A., and Rudy, R. J., (1986), A refined “standard” thermal model for asteroids based on observations of 1 Ceres and 2 Pallas. *Icarus*, **68**, 239–251.
- Luu, J. X. and Jewitt, D. C., (1989) On the relative number of C types and S types among near-Earth asteroids. *Astronomical Journal*, **98**, 1905–1911.
- Lupishko, D. F., and Di Martino, M., (1998) Physical properties of near-Earth asteroids. *Planetary and Space Science*, **46**, 47–74.
- Matson, D. L., (1971) Astronomical Photometry at Wavelengths of 8.5, 10.5 and 11.6 μm . II. Infrared Emission from Asteroids at Wavelengths of 8.5, 10.5 and 11.6 μm . *Ph.D. Thesis*, California Institute of Technology.
- Matson, D. L., (1972) Infrared observations of asteroids, In *Physical Studies of Minor Planets* (T. Gehrels, Eds.) NASA SP-267 p 45-50 U.S. Government Printing Office, Washington DC.
- McKay, D. S., Swindle, T. D., and Greenberg, R. (1989), in R. P. Binzel, T. Gehrels, and M. S. Matthews (eds.), *Asteroids II*, pp 617–642, The University of Arizona Press
- Michel, P., Zappalà, V., Cellino, A., and Tanga, P. (2000), Estimated abundance of Atens and asteroids evolving on orbits between Earth and Sun. *Icarus*, **143**, 421–424.
- Milani, A., Carpino, M., Hahn, G., and Nobili, A.M., (1989), Dynamics of planet-crossing asteroids: classes of orbital behavior. Project Spaceguard. *Icarus*, **78**, 212-269.

Morbidelli, A., Bottke, W. F. Jr., Froeschlé, Ch., and Michel, P. (2002a) Origin and Evolution of Near-Earth Objects. In *Asteroids III* (W.F. Bottke, A. Cellino, P. Paolicchi, R.P. Binzel, eds.). pp.409-422. The University of Arizona Press, Tucson.

Morbidelli, A., Bottke, W. F., Jedicke, R., Michel, P., Tedesco, E. F., (2002b). From Magnitudes to Diameters: The Albedo Distribution of Near Earth Objects and the Earth Collision Hazard, *Icarus*, **158**, 329–342

Morrison, D.; Chapman, C. R. (1976) Radiometric diameters for an additional 22 asteroids. *Astrophysical Journal*, **204**, 934-939

Morrison, D. (1973) Determination of radii of satellites and asteroids from radiometry and photometry. *Icarus* **19**, 1-14

Morrison, D. (1976) The Diameter and thermal inertia of 433 Eros. *Icarus*, **28**, 125-132

Mottola, S. and 27 colleagues, (1997), Physical model of near-Earth asteroid 6489 Golevka (1991 JX) from optical and infrared observations. *Astronomical Journal*, **114**, 1234–1245.

Müller, T. G., Lagerros, J. S. V., Burgdorf, M., et al. (1999), ESA SP-427 in *The universe as seen by ISO*, Cox & Kessler (Eds.), 141

Müller, T. G., and Lagerros, J. S. V., (2002) Asteroids as calibration standards in the thermal infrared for space observatories, *Astronomy and Astrophysics*, **381**, 324-339

Müller, T. G., and Blommaert, J. A. D. L., (2003) Cybele in the thermal infrared: Multiple observations and thermophysical analysis. *Meteoritics and Planetary Sciences*,

Müller, M., Harris, A. W., Delbo, M., Bus, S. J., (2003), The sizes and albedos of near-Earth asteroids including 6489 Golevka from recent IRTF observations. talk presented at the DPS meeting 35, 05/2003

Murdok, T. L., (1974) Mercury's infrared phase effect, *Astronomical Journal*, **79**, 1457-1464

Nolan, M., Howell, E. S., Rivkin, A. S., Neish, C. D., (2003), (5381) SEKHMET *I.A.U. Circular*, No. 8163

Nolan, M.C., Howell, E.S., Magri, C., Beene, B., Campbell, D.B., Benner, L.A.M., Ostro, S.J., Giorgini, J.D., Margot, J.-L., (2002). 2002 BM26. *IAU Circular*, No. 7824.

Ostro, S. J., D. B. Campbell, and I. I. Shapiro 1983. Radar observations of asteroid 1685 Toro. *Astronomical Journal*, **88**, 565-576.

Ostro, S. J., Hudson, R. S., Benner, L. A. M., Giorgini, J. D., Magri, C, Margot, J. L., and Nolan, M. C., (2002), Asteroid Radar Astronomy. In *Asteroids III* (W.F. Bottke, A. Cellino, P. Paolicchi, R.P. Binzel, eds.). pp. 151-168. The University of Arizona Press, Tucson.

Pettengill, G. H., Ostro, S. J., Shapiro, I. I., Marsden, B. G., Campbell, D. B., (1979), Radar observations of asteroid 1580 Betulia. *Icarus*, **40**, 350)

Pospieszalska-Surdej, A., and Surdej, J., (1985), Determination of the pole orientation of an asteroid. The amplitude-aspect relation revisited. *Astronomy and Astrophysics*, **149**, 186-194

Pravec, P., Wolf, M., Sarounova, L., Mottola, S., Erikson, A., Hahn, G., Harris, A.W., Harris, A.W., Young, J.W., (1997). The near-Earth objects follow-up program II. Results for 8 asteroids from 1982 to 1995. *Icarus* **130**, 275–286.

Pravec P., (2003), 5381 Sekhmet, *Minor Planet Mailing List*, Thu May 15, 2003 4:31 pm <http://groups.yahoo.com/group/mpml/message/10217>

Press, W. H., Teukolsky, S. A., Vetterling, W. T., Flannery, B. P. (2002), *Numerical Recipes in C The Art of Scientific Computing Second Edition*, Cambridge University Press

Reimann, H. G., Dietzsch, E., Hron, J., et al., (2000), TIMMI 2: a new Multimode Mid-Infrared Instrument for the ESO 3.6 m telescope, *Proceedings of SPIE* Vol. 4008-131.

Ressler, M. E., Werner, M. W., Van Cleve, J., Helen, C. A., (1994) The JPL deep-well mid-infrared array camera, *Experimental Astronomy*, **3**, 277-280

Sinton, W. M., (1962) The Temperature of the Lunar Surface., *Physics and Astronomy of the Moon*, edited by Z. Kopal, Chap. 11, Academic, New York, p 407-428

- Sekiguchi, T., Abe, M., Boehnhardt, H., Dermawan, B., Hainaut, O. R., and Hasegawa, S., (2003), Thermal observations of MUSES-C mission target (25143) 1998 SF36. *Astronomy and Astrophysics*, **397**, 325-328
- Shorthill, R.W., (1972), The infrared Moon: A Review, in *Thermal Characteristics of the Moon* John W. Lucas eds. MIT press, Chambridge Massachussetts.
- Spencer, J. R., Lebofsky, L. A., and Sykes, M. V. (1989) Systematic biases in radiometric diameter determinations. *Icarus*, **78**, 337–354.
- Spencer, J. R. (1990). A rough-surface thermophysical model for airless planets. *Icarus* **83**, 27–38.
- Stuart, J.S., (2001). A near-Earth asteroid population estimate from the LINEAR survey. *Science* **294**, 1691–1693.
- Tedesco E. F. (1992) The IRAS Minor Planet Survey, pp. 243–286. *Tech. Rep. PL-TR-92-2049*, Phillips Laboratory, Hanscom Air Force Base, Massachusetts, USA.
- Tedesco, E.F., (1993). Asteroid albedos and diameters. In: Milani, A., Di Martino, M., Cellino, A. (Eds.), *Asteroids, Comets, Meteors. In: Proc. LAU Symp., Vol. 160*. Kluwer, Dordrecht, pp. 55–74.
- Tedesco, E. F., Noah, P. V., Noah, M., and Price, S. D. (2002). The Supplemental IRAS Minor Planet Survey. *Astronomical ournal.* **123**, 1056-1085.
- Tholen, D.J., (1984). Asteroid taxonomy from cluster analysis of photometry. *Doctoral thesis*. University of Arizona.
- Thomas, P. C., J. Joseph, B. Carcich, J. Veverka, B. E. Clark, J. F. Bell III, A. J. Byrd, R. Chomko, M. Robinson, S. Murchie, L. Prockter, A. Cheng, N. Izenberg, M. Malin, C. Chapman, L. A. McFadden, R. Kirk, M. Gaffey, and P. G. Lucey (2002). Eros: Shape, topography, and slope processes. *Icarus* **155**, 18–37.
- Veverka J. and 32 colleagues (2000) NEAR at Eros: imaging and spectral results. *Science*, **289**, 2088–2097.
- Werner, S.C., Harris, A.W., Neukum, G., Ivanov, B.A., (2002). NOTE: The near-Earth asteroid size-frequency distribution: a snapshot of the lunar impactor size-frequency distribution. *Icarus* **156**, 287–290.

Whiteley, R. J. (2001) A compositional and dynamical survey of the near-Earth asteroids. *PhD. thesis*, University of Hawai'i. 202 pp.

Wisniewski, W. Z., Michalowski, T. M., Harris, A. W. and Mc Millan, R. S. (1997), Photometric Observations of 125 Asteroids, *Icarus*, **126**, 395).

Zaitsev, A., Di Martino, M., Konovalenko, A. A., Montebugnoli S., Ignatov, S.P., Kolyuka, Y.F., Nabatov, A. S., Falkovich, I.S., Gavrik, A.L., Gavrik, Y.A., Bortolotti C., Cattani A., Maccaferri A., Maccaferri G., Roma M., Delbò M., Saba L., (2002) Radar Detection of NEA 33342 (1998 WT24) with Eypatoria => Medicina System at 6 cm In: *Proceedings of Asteroids, Comets, Meteors - ACM 2002. International Conference, 29 July - 2 August 2002, Berlin, Germany*. Ed. Barbara Warmbein. ESA SP-500. Noordwijk, Netherlands: ESA Publications Division, ISBN 92-9092-810-7, 2002, p. 883 – 886

Zappalà V., Cellino A., Dell'Oro A., and Paolicchi P. (2002) Physical and Dynamical Properties of Asteroid Families. In *Asteroids III* (W.F. Bottke, A. Cellino, P. Paolicchi, R.P. Binzel, eds.). pp. 619-631. The University of Arizona Press, Tucson.

Zellner B., Tholen D. J., and Tedesco E. F. (1985) The eight-color asteroid survey: Results for 589 minor planets. *Icarus*, **61**, 355–416.

Zellner B. (1979) Asteroid taxonomy and the distribution of the compositional types. In *Asteroids* (T. Gehrels, ed.), pp. 783– 806. Univ. of Arizona, Tucson.

Appendix A

Observed thermal Infrared Fluxes of near-Earth asteroids

Object	Date (UTC)	Time (UTC) At start	Wavelength (μm)	Flux (mJy)	Error (mJy)
25143(1998 SF ₃₆)	01-04-08	10:11:52	8.9	83	21
		09:36:22	10.4	144	18
		09:21:15	11.9	158	20
		10:28:41	11.9	143	18
		09:54:05	12.9	158	19
25143(1998 SF ₃₆)	01-04-09	09:38:08	9.8	105	16
		09:57:25	10.4	168	27
		10:12:32	11.9	233	29
		10:26:10	11.9	186	27
		09:21:16	12.9	240	30
5587 (1990 SB)	01-04-08	05:24:15	7.9	394	66
		04:53:34	8.9	843	29
		04:21:42	10.4	953	21
		04:32:55	11.9	907	19
		04:42:47	12.9	1273	31
5587 (1990 SB)	01-04-09	05:46:41	8.19	684	77
		05:46:41	8.42	855	49
		05:46:41	8.65	950	46
		05:46:41	8.87	863	41
		05:46:41	9.10	932	42
		05:46:41	9.33	984	47
		05:46:41	10.47	1211	46
		05:46:41	10.70	1294	48
		05:46:41	10.93	1376	56
		05:46:41	11.21	1361	40
5587 (1990 SB)	01-04-09	06:18:39	8.19	451	80
		06:18:39	8.42	642	53
		06:18:39	8.65	609	43
		06:18:39	8.87	698	41
		06:18:39	9.10	777	43
		06:18:39	9.33	797	51
		06:18:39	10.47	986	47
		06:18:39	10.70	1045	44
		06:18:39	10.93	926	54

		06:18:39	11.21	1132	46
19356(1997 GH ₃)	01-04-09	07:20:06	12.9	160	30
		08:17:37	11.9	256	51
		08:00:55	9.8	170	53
		08:37:00	10.4	258	26
5604 (1992FE)	01-04-08	02:01:56	11.9	90	30
37314 (2001QP)	01-12-04	08:31:07	8.9	279	31
		07:37:46	10.4	369	13
		07:22:25	11.9	354	19
33342 (98WT ₂₄)	01-12-02	09:10:01	8.9	144	31
		08:52:38	10.4	239	15
		08:50:30	11.9	262	37
35396 (97XF ₁₁)	02-11-28	02:53:00	11.9	103	15
		03:20:00	8.6	82	15
		03:58:00	12.9	105	20
2001 LF	03-06-02	07:29:00	11.9	614	20
		08:09:00	8.6	490	15
		08:21:00	12.9	824	29
		09:33:00	11.9	620	28
		09:44:00	8.6	322	22
2001 LF	03-06-03	06:49:00	11.9	774	45
		07:01:00	8.6	465	33
		07:13:00	12.9	780	56
		08:11:00	11.9	894	28
		08:23:00	12.9	759	40
		08:40:00	8.6	452	11
		09:53:00	17.8	515	130
5381 Sekhmet	03-06-02	02:14:00	11.9	284	28
		02:26:00	11.9	268	28
		02:40:00	8.6	140	26
		02:52:00	12.9	331	33
1999 KV4	03-06-02	04:16:00	11.9	302	22
		04:38:00	8.6	150	18
		05:01:00	12.9	230	80
2002 AV4	03-06-02	23:01:00	11.9	252	15
		23:24:00	8.6	128	6
		23:55:00	12.9	212	22
		00:21:00	11.9	223	18

		01:43:00	11.9	244	19
1627 Ivar	00-03-16	10:32:43	8	107	7
		10:39:38	8	150	8
		11:01:54	8.9	199	6
		10:47:17	8.9	172	6
		21:39:49	10.7	294	10
		09:44:50	10.7	287	9
		09:54:08	11.7	421	7
		10:01:23	12.5	380	7
		10:25:03	20	705	22
1866 Sisyphus	00-03-17	15:51:30	8.9	4	2
		16:05:35	10.7	27	3
		16:12:39	11.7	36	4
		15:25:32	11.7	46	4
		15:33:30	12.5	26	4
		15:41:41	20	77	24
2100 Ra-Shalom	00-08-21	10:27:44	4.8	66	6
		10:22:43	8.9	567	10
		10:17:05	11.7	1172	20
		10:36:13	20	1421	57
4034 1986 PA	01-05-11	08:13:15	10.7	23	3
		08:00:19	11.7	25	3
		08:25:42	12.5	22	3
4055 Magellan	00-03-16	14:50:21	10.7	15	4
		14:39:48	11.7	30	4
4660 Nereus	02-02-21	16:02:11	8	80	8
		15:27:49	8.9	65	4
		14:58:54	10.7	107	4
		14:25:52	11.7	80	4
		14:35:31	11.7	109	6
		15:11:20	11.7	98	5
		14:43:20	12.5	98	5
		15:45:10	17.65	104	16
5587 1990 SB	01-05-10	09:11:59	4.8	164	4
		09:48:49	4.8	175	5
		09:00:00	8	993	22
		08:53:40	8.9	1053	22
		08:48:54	10.7	1275	27
		09:43:01	11.7	2698	46
		08:41:32	11.7	1432	24
		09:05:50	12.5	2083	44

		10:02:17	17.9	2472	80
		09:28:38	17.9	2571	81
		09:35:53	20	2972	95
5604 1992 FE	01-05-11	07:02:48	8.9	8	1
		06:49:49	10.7	14	2
		06:24:34	11.7	22	3
		06:36:50	12.5	27	3
5751 Zao	01-05-12	06:28:49	10.70	18	1
		06:04:22	11.70	34	1
		06:16:39	12.50	23	2
14402 1991 DB	00-03-16	13:26:01	4.8	46	3
		13:17:43	8	368	16
		13:13:03	8.9	445	14
		13:08:33	10.7	622	11
		13:03:30	11.7	682	12
		13:21:45	12.5	640	12
		13:58:10	20	513	21
		13:49:07	20	507	24
16834 1997 WU ₂₂	00-08-21	07:12:10	8.0	133	11
		07:05:13	8.9	156	5
		07:58:41	10.7	252	9
		07:20:58	11.7	351	8
		06:42:47	11.7	264	8
		06:47:00	12.5	283	7
19356 1997 GH ₅	01-05-11	09:17:55	8.0	21	4
		09:05:36	8.9	41	4
		08:53:11	10.7	50	2
		09:57:02	11.7	59	2
		08:41:05	11.7	63	2
		09:30:59	12.5	63	2
		09:43:55	17.9	74	12
25330 1999 KV ₄	01-05-10	07:11:05	4.8	35	5
		07:04:25	8.0	250	12
		06:55:43	8.9	292	9
		06:51:05	10.7	394	12
		06:19:41	11.7	520	16
		06:43:14	11.7	506	15
		07:21:34	17.9	629	35
		07:35:43	20.0	643	33
		07:28:11	20.0	563	32
1994 QC	00-03-17	13:49:50	8.90	8	3

		12:16:45	11.70	19	3
		13:05:10	11.70	17	3
		13:35:28	11.70	16	3
		13:16:16	12.50	12	3
1999 FK ₂₁	02-02-21	11:14:08	8.9	115	5
		11:47:22	11.7	164	6
		10:50:23	11.7	167	7
		11:01:48	12.5	142	6
		11:26:59	17.65	198	13
1999 NC ₄₃	00-03-17	07:18:18	8.9	93	5
		07:29:37	10.7	113	3
		06:35:46	11.7	173	4
		07:37:02	11.7	154	4
		07:57:03	11.7	151	3
		06:40:35	12.5	171	4
		06:58:08	20	207	16
		06:48:27	20	256	19
2000 BG ₁₉	00-03-17	10:54:00	4.8	29	4
		11:07:05	8.9	214	7
		11:18:41	10.7	279	8
		11:26:22	11.7	340	10
		10:18:15	11.7	344	10
		10:26:34	12.5	303	9
		10:46:50	20	321	25
		10:35:13	20	304	28
2000 EV ₇₀	00-03-17	14:20:10	11.70	22	4
		14:32:54	12.50	28	6
2000 PG ₃	00-08-21	09:55:45	8	47	6
		09:41:40	8.9	55	2
		09:13:28	10.7	69	2
		09:04:42	11.7	120	3
		09:20:53	12.5	108	3
2001 FY	01-05-12	09:02:13	10.70	14	1
		08:34:36	11.70	21	2
		08:47:15	12.50	15	2
2001 HW ₁₅	01-05-12	10:00:17	10.70	15	8
		08:05:53	11.70	35	8
2002 BM ₂₆	02-02-21	08:41:25	8.00	260	12
		08:36:45	8.90	335	8
		09:02:08	11.70	708	15

		08:27:36	11.70	710	15
		08:05:46	11.70	680	14
		08:31:58	12.50	687	14
		08:51:43	17.65	894	21
2002 CT ₄₆	02-02-21	13:25:55	10.70	15	3
		14:12:53	11.70	43	3
		12:39:18	11.70	30	2
		13:13:17	11.75	27	2
33342 (1998WT ₂₄)	01-12-18	05:32:00	7.91	2859	246
		05:33:00	7.91	3109	265
		06:56:00	7.91	6689	281
		07:04:00	8.81	1753	101
		07:02:00	8.81	1676	67
		05:57:00	10.27	5017	189
		05:58:00	10.27	4226	161
		05:55:00	11.70	4880	91
		05:37:59	11.70	4592	121
		05:38:59	11.70	5177	92
		06:53:00	11.70	4109	78
		06:54:00	11.70	4354	83
		05:29:59	11.70	4887	83
		05:34:00	17.92	5849	1219
		05:45:00	17.92	7005	887
		06:00:59	17.92	5159	7389
33342 (1998WT ₂₄)	01-12-19	05:48:00	7.91	1758	62
		06:47:59	7.91	1467	52
		06:15:59	7.91	1416	54
		05:04:59	11.70	3196	52
		05:49:59	11.70	3220	48
		06:51:00	11.70	2638	40
		06:20:00	11.70	3295	51
		06:23:59	17.92	2927	198
		05:10:00	17.92	4020	161
		05:55:00	17.92	3497	194
		06:58:59	17.92	3576	209
		05:21:00	20.81	4959	736
33342 (1998WT ₂₄)	01-12-21	04:51:00	7.91	487	40
		05:48:00	7.91	552	33
		06:42:00	7.91	440	31
		05:00:00	10.27	900	25
		05:54:00	10.27	1093	26
		06:00:00	11.70	1366	28
		05:06:00	11.70	1154	27
		06:12:00	17.92	1895	105
		05:18:00	17.92	1915	104
1580 Betulia	02-06-02		7.91	1522	51

			7.91	1935	62
			7.91	1989	59
			10.27	2285	53
			10.27	3258	71
			10.27	3294	75
			11.70	4131	91
			11.70	3221	73
			11.70	2456	57
			17.92	3835	215
			17.92	4282	207
			17.92	4497	190
35356 (1997 XF ₁₁)	02-11-03	07:53:42	4.90	444	29
		08:03:23	4.90	4229	28
		06:39:02	4.90	484	40
		05:22:59	7.80	1158	79
		08:26:07	7.80	769	70
		05:37:44	9.80	1945	79
		08:46:46	9.80	1533	64
		06:46:05	11.70	1948	27
		07:44:41	11.70	2044	25
		05:51:12	11.70	2501	29
		06:16:09	11.70	1947	24
		05:29:49	11.70	2368	28
		08:09:48	11.70	1451	22
		05:07:12	11.70	1882	24
		08:33:42	11.70	2173	26
		09:10:16	11.70	2438	28
		09:03:30	18.40	3092	75
		06:02:28	18.40	3140	86
35356 (1997 XF ₁₁)	02-11-05	05:31:46	4.9	347	35
		06:04:55	4.9	399	36
		07:46:02	4.9	422	53
		07:55:55	4.9	443	44
		06:45:52	7.8	733	81
		08:18:24	7.8	1117	86
		07:05:10	9.8	1770	393
		08:36:01	9.8	1513	84
		05:27:09	11.7	1623	54
		05:53:47	11.7	1277	49
		06:29:49	11.7	2177	49
		06:52:38	11.7	2140	53
		07:13:21	11.7	1621	37
		07:36:10	11.7	1402	52
		08:02:21	11.7	1962	49
		08:36:01	11.7	2156	48
		08:41:52	11.7	1640	55
		09:04:47	11.7	1196	60

08:57:42	18.4	1658	111
07:29:10	18.4	1880	85

Colour correction factors for LWS, TIMMI2, MIRSI and MIRLIN filters

B.1 LWS at Keck 1 filters and color correction factors

Using measured transmission profiles for the filters installed at the LWS (see Fig B.1) provided to us by the instrument specialists (Campbell & Wirth, personal communication, 2000), we have calculated the color correction factors – listed in Table B-1 – as a function of the black body temperature between 100 and 550 K. For the range of temperature displayed by NEAs (~300-500 K) color correction factors turn out to be no larger than a few percent.

λ_c (μm)	Black Body temperature (K)									
	100	150	200	250	300	350	400	450	500	550
4.80	0.79	0.92	0.97	0.99	1.00	1.01	1.01	1.01	1.01	1.01
8.00	1.10	1.08	1.06	1.04	1.03	1.02	1.01	1.01	1.00	1.00
8.90	1.04	1.06	1.06	1.06	1.06	1.05	1.05	1.05	1.04	1.04
9.80	1.10	1.07	1.04	1.03	1.01	1.00	1.00	0.99	0.99	0.98
10.70	0.98	1.02	1.03	1.02	1.02	1.02	1.01	1.01	1.01	1.01
11.70	1.11	1.06	1.02	1.00	0.98	0.97	0.96	0.96	0.95	0.95
12.50	1.05	1.03	1.02	1.01	1.00	1.00	0.99	0.99	0.99	0.99
17.90	1.01	1.01	1.00	1.00	1.00	1.00	1.00	0.99	0.99	0.99
17.60	1.01	1.01	1.01	1.01	1.01	1.01	1.01	1.01	1.01	1.01
20.00	1.05	1.03	1.02	1.02	1.01	1.01	1.01	1.01	1.00	1.00

Table B-1 Color correction factors for the LWS filters based on the measured filter transmission curves. The first line indicates the black-body temperature. The left-most column is the filter effective wavelength λ_c .

The LWS web page (<http://www2.keck.hawaii.edu/inst/lws/filters.html>) gives parameters for each filter available to the observing community. For convenience, filter effective wavelengths and bandwidths are reported here in Table B-2.

It is instructive to compare the color correction factors calculated with the measured transmission of the filters and those obtained assuming the filter transmission to be a window function centered on λ_c and of width $\Delta\lambda=(\lambda_{\max}-\lambda_{\min})$ i.e.

$$\begin{cases} T(\lambda) = 1.0 & \text{for } \lambda \in [\lambda_{\min}, \lambda_{\max}] \\ T(\lambda) = 0.0 & \text{otherwise} \end{cases} \quad (\text{B-7-1})$$

Table B-3 lists color correction factors for the LWS filters using the window transmission function. The difference with respect to the color corrections of Table B-1 is of a few percent.

λ_c (μm)	λ_{\min} (μm)	λ_{\max} (μm)
4.80	4.40	5.00
8.00	7.50	8.20
8.90	8.40	9.20
9.80	9.40	10.20
10.70	10.00	11.40
11.70	11.20	12.20
12.50	12.00	13.00
17.90	16.90	18.90
17.60	17.30	18.20
20.00	19.20	20.80

Table B-2 LWS filters parameters. λ_c is the effective wavelength. The filter bandwidth is given in term of λ_{\min} and λ_{\max} .

λ_c (μm)	Black body temperature (K)									
	100	150	200	250	300	350	400	450	500	550
4.80	0.79	0.95	1.00	1.02	1.03	1.03	1.02	1.02	1.02	1.01
8.00	1.01	1.02	1.02	1.02	1.01	1.01	1.00	1.00	1.00	1.00
8.90	1.01	1.02	1.02	1.01	1.01	1.01	1.00	1.00	1.00	1.00
9.80	1.02	1.02	1.01	1.01	1.01	1.00	1.00	1.00	1.00	1.00
10.70	1.01	1.03	1.02	1.01	1.01	1.00	1.00	1.00	0.99	0.99
11.70	1.02	1.02	1.01	1.01	1.00	1.00	1.00	1.00	0.99	0.99
12.50	1.02	1.02	1.01	1.00	1.00	1.00	1.00	1.00	0.99	0.99
17.90	1.02	1.01	1.00	1.00	0.99	0.99	0.99	0.99	0.99	0.99
17.60	1.01	1.01	1.00	1.00	1.00	1.00	1.00	1.00	0.99	0.99
20.00	1.01	1.01	1.00	1.00	0.99	0.99	0.99	0.99	0.99	0.99

Table B-3 Color correction factors for the LWS filters based on simplified filters parameters. The first line indicates the black-body temperature. The left-most column is the filter effective wavelength.

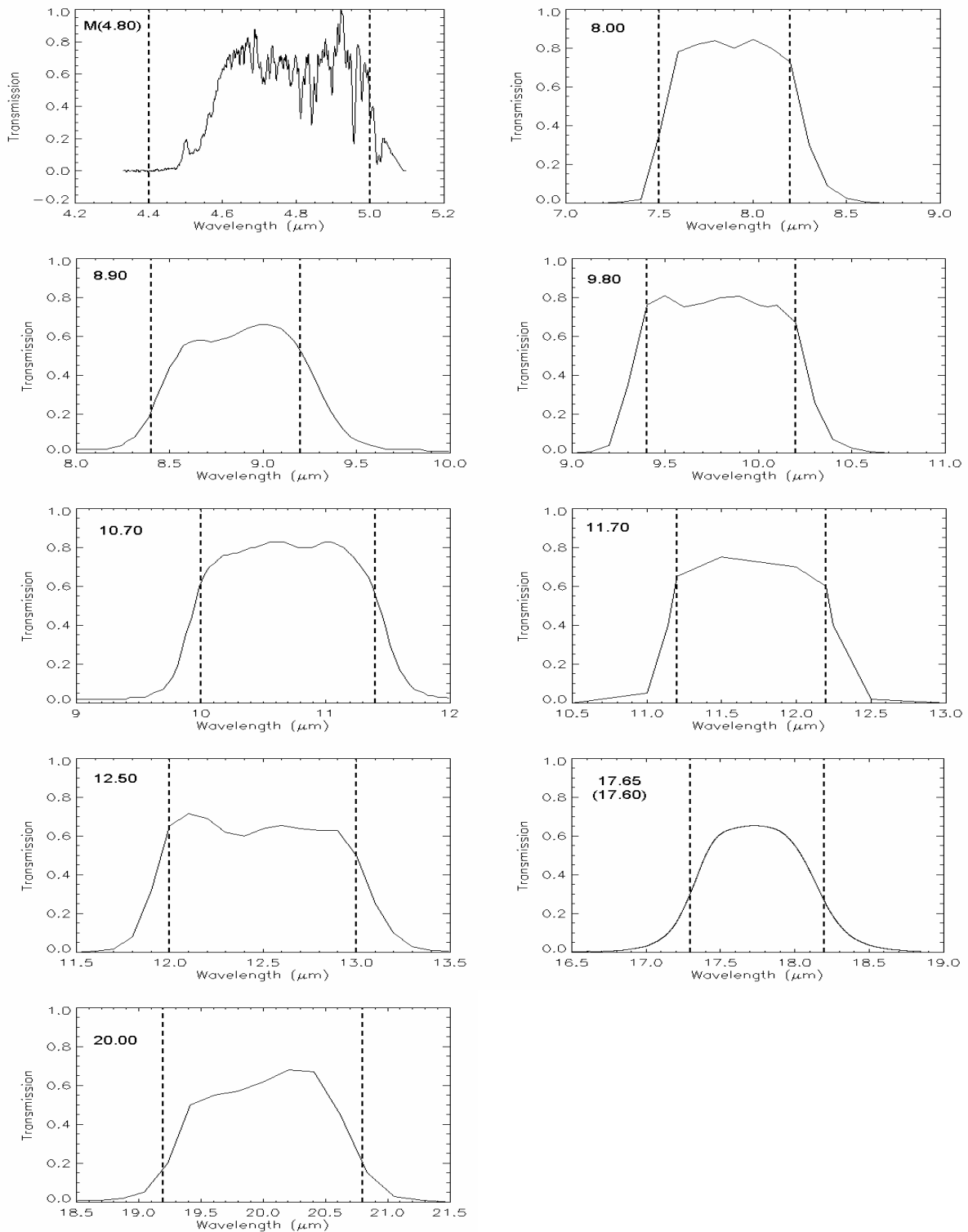


Fig B.1 Transmission curves for the filters installed at the LWS (Wirth & Campbell, personal communication, 2000). In the case of the M filter, the curve is the product of the transmission of the filter with that of the atmosphere and the optics of the instrument.

B.2 TIMMI2 filters and color correction factors

Filter Name	Blue cut (μm)	Blue (50%)	Red (50%)	Red cut (μm)
L	3.6	3.73	4.11	4.13
M	4.3	4.36	4.91	4.99
N1	7.79	7.99	9.2	9.46
N2	9.43	9.74	11.33	11.78
N7.9	7.18	7.42	8.11	8.62
N8.9	7.9	8.29	9.07	9.46
N9.8	8.76	9.1	10.02	10.49
N10.4	9.46	9.8	10.82	11.21
N11.9	10.61	10.99	12.19	12.5
SiC	10.13	10.67	12.93	13.34
N12.9	11.54	11.62	12.79	12.98
[NeII]	12.57	12.68	12.9	13.02
Q1	17.04	17.35	18.15	18.48

Table B-4 TIMMI2's filters available in imaging mode. Note that not all filters have been used in this study.

Table B-5 and Table B-6 report color correction factors for the filters installed at the TIMMI2. Filter parameters were obtained from the TIMMI2 web page (<http://www.lis.eso.org/lasilla/Telescopes/360cat/timmi/html/modes.html>) and for convenience reproduced here in Table B-4. A window function was assumed to represent the filter transmission curve $T(\lambda)$. However, while in Table B-5 the filter bandwidth was defined by using the blue and the red cut-off values, in Table B-6 the 50% value of the filters transmission limits were used. Note the slight difference in the final results by a few percent.

Filter name	Black body temperature (K)									
	100	150	200	250	300	350	400	450	500	550
L	0.60	0.85	0.96	1.00	1.02	1.03	1.03	1.03	1.02	1.02
M	0.68	0.90	0.99	1.02	1.03	1.03	1.03	1.02	1.02	1.02
N1	0.92	1.02	1.03	1.03	1.03	1.02	1.01	1.00	1.00	0.99
N2	0.96	1.03	1.04	1.03	1.02	1.01	1.00	0.99	0.99	0.98
N7.9	0.90	1.01	1.03	1.03	1.03	1.02	1.01	1.01	1.00	1.00
N8.9	0.94	1.02	1.03	1.03	1.02	1.02	1.01	1.00	1.00	0.99
N9.8	0.97	1.03	1.03	1.03	1.02	1.01	1.00	1.00	0.99	0.99
N10.4	0.99	1.03	1.03	1.02	1.01	1.01	1.00	1.00	0.99	0.99
N11.9	1.01	1.03	1.02	1.02	1.01	1.00	1.00	0.99	0.99	0.99
SiC	0.96	1.04	1.04	1.03	1.02	1.01	0.99	0.99	0.98	0.97
N12.9	1.02	1.02	1.01	1.01	1.00	1.00	1.00	0.99	0.99	0.99
[NeII]	1.01	1.01	1.00	1.00	1.00	1.00	1.00	1.00	1.00	1.00
Q1	1.02	1.01	1.00	1.00	1.00	0.99	0.99	0.99	0.99	0.99

Table B-5 Color correction factors calculated for TIMMI2's filters. A window function as of Eq. 3-19 was used. The width of the window was defined by the red and the blue cut-off values of the filters (see Table B-4)

Filter name	Black body temperature (K)									
	100	150	200	250	300	350	400	450	500	550
L	0.79	0.95	1.00	1.02	1.02	1.02	1.02	1.02	1.02	1.02
M	0.80	0.95	1.00	1.02	1.02	1.02	1.02	1.02	1.02	1.01
N1	0.98	1.02	1.03	1.02	1.02	1.01	1.01	1.00	1.00	1.00
N2	1.00	1.03	1.02	1.02	1.01	1.00	1.00	1.00	0.99	0.99
N7.9	1.00	1.02	1.02	1.02	1.01	1.01	1.01	1.00	1.00	1.00
N8.9	1.01	1.02	1.02	1.01	1.01	1.01	1.00	1.00	1.00	1.00
N9.8	1.02	1.02	1.02	1.01	1.01	1.00	1.00	1.00	1.00	1.00
N10.4	1.02	1.02	1.02	1.01	1.01	1.00	1.00	1.00	1.00	0.99
N11.9	1.02	1.02	1.01	1.01	1.00	1.00	1.00	0.99	0.99	0.99
SiC	1.00	1.03	1.03	1.02	1.01	1.00	1.00	0.99	0.99	0.98
N12.9	1.02	1.02	1.01	1.01	1.00	1.00	1.00	0.99	0.99	0.99
[NeII]	1.01	1.00	1.00	1.00	1.00	1.00	1.00	1.00	1.00	1.00
Q1	1.01	1.00	1.00	1.00	1.00	1.00	1.00	1.00	1.00	1.00

Table B-6 Color correction factors calculated for TIMMI2 filters assuming a window transmission function which limits were defined at the 50% level of the actual filters transmission (see Table B-4).

B.3 MIRLIN filters and color correction factors

Filter name	λ_c (μm)	$\Delta\lambda$ (μm)	Flux for 0 Mag (Jy)
N	10.79	5.66	33.4
Q-s	17.90	2.00	12.4
N0	7.91	0.76	60.9
N1	8.81	0.87	49.4
N2	9.69	0.93	41.1
N3	10.27	1.01	36.7
N4	11.70	1.11	28.5
N5	12.49	1.16	25.1
Q0	17.20	0.60	13.4
Q1	17.93	0.45	12.3
Q2	18.64	0.52	11.4
Q3	20.81	1.65	9.2
Q5	24.48	0.76	6.7

Table B-7 Filters available at MIRLIN and calculated in-band flux for a zero magnitude-star. Note that not all filters have been used in this study.

Table B-7 lists relevant information for the filters available for MIRLIN. Table B-8 shows color correction factors evaluated by means of Eq 3-18 for black bodies temperatures between 100 and 550 K assuming a window function centered on λ_c and of width $\Delta\lambda$ for $T(\lambda)$.

λ_c (μm)	Black body temperature (K)									
	100	150	200	250	300	350	400	450	500	550
10.79	0.67	1.00	1.10	1.10	1.08	1.05	1.02	1.00	0.98	0.96
17.90	1.02	1.01	1.00	1.00	0.99	0.99	0.99	0.99	0.99	0.99
7.91	1.00	1.02	1.02	1.02	1.01	1.01	1.01	1.00	1.00	1.00
8.81	1.01	1.02	1.02	1.02	1.01	1.01	1.00	1.00	1.00	1.00
9.69	1.02	1.02	1.02	1.01	1.01	1.00	1.00	1.00	1.00	0.99
10.27	1.02	1.02	1.02	1.01	1.01	1.00	1.00	1.00	1.00	0.99
11.70	1.02	1.02	1.01	1.01	1.00	1.00	1.00	1.00	0.99	0.99
12.49	1.02	1.02	1.01	1.01	1.00	1.00	1.00	0.99	0.99	0.99
17.20	1.01	1.00	1.00	1.00	1.00	1.00	1.00	1.00	1.00	1.00
17.93	1.01	1.00	1.00	1.00	1.00	1.00	1.00	1.00	1.00	1.00
18.64	1.01	1.00	1.00	1.00	1.00	1.00	1.00	1.00	1.00	1.00
20.81	1.01	1.00	1.00	1.00	0.99	0.99	0.99	0.99	0.99	0.99
24.48	1.00	1.00	1.00	1.00	1.00	1.00	1.00	1.00	1.00	1.00

Table B-8 Color correction factors obtained for the selection of filters listed in Table B-7. A window function centered at λ_c and of width $\Delta\lambda$ was assumed for the filter transmission.

B.4 MIRSI filters and color correction factors

Table B-9 shows relevant filter parameters of MIRSI filters and relative color correction factors evaluated for black body temperatures between 100 and 550 K assuming a window function centered on λ_c and of width $\Delta\lambda$ for the filter transmission function.

λ_c (μm)	$\Delta\lambda$ (μm)	Black body temperature (K)									
		100	150	200	250	300	350	400	450	500	550
4.90	0.98	0.54	0.83	0.95	1.01	1.03	1.03	1.04	1.03	1.03	1.02
7.80	0.78	1.00	1.02	1.02	1.02	1.01	1.01	1.01	1.00	1.00	1.00
8.70	0.87	1.01	1.02	1.02	1.02	1.01	1.01	1.00	1.00	1.00	1.00
9.80	0.98	1.02	1.02	1.02	1.01	1.01	1.00	1.00	1.00	1.00	0.99
10.30	1.03	1.02	1.02	1.02	1.01	1.01	1.00	1.00	1.00	1.00	0.99
10.60	4.85	0.72	1.01	1.08	1.08	1.07	1.04	1.02	1.00	0.98	0.97
11.70	1.17	1.02	1.02	1.01	1.01	1.00	1.00	1.00	0.99	0.99	0.99
12.50	1.25	1.02	1.02	1.01	1.01	1.00	1.00	1.00	0.99	0.99	0.99
18.40	1.85	1.02	1.01	1.00	1.00	0.99	0.99	0.99	0.99	0.99	0.99
19.00	4.94	1.04	1.03	1.01	0.99	0.98	0.97	0.97	0.96	0.96	0.95
20.90	8.78	1.07	1.06	1.02	0.98	0.96	0.94	0.93	0.92	0.91	0.90

Table B-9 Color correction factors obtained for the filters available for MIRSI. A window function centered at λ_c and of width $\Delta\lambda$ was assumed for the filter transmission.

Since color corrections were found to be only a few percent for all the instruments that have been used in this study, they were not applied to correct the final monochromatic flux densities of the asteroids.

Thermal Infrared photometry: NOTES

The flux incident on the detector follows a Poisson distribution, and the probability of receiving n photons within the time interval t is given by

$$p(n,t) = \left(\frac{\bar{n}^n}{n!} \right) e^{-\bar{n}} \quad (C-2)$$

where \bar{n} is the mean number of photons in the time t . The variance of the arrival number of photons is equal to its mean value. The uncertainty associated to \bar{n} is therefore equal to $\sqrt{\bar{n}}$. However, it is not only the number of incident photons which fluctuates, but the measuring process of the charge carriers (electrons) is statistical and Poissonian. The mean number of photo-generated electrons is $\bar{n}' = Q_E \bar{n}$ and its error $\sigma_{n'} = \sqrt{\bar{n}'} = \sqrt{Q_E \bar{n}}$. (see for example Robberto 1988, PhD thesis). The final S/N equation for a thermal IR observation must be written in terms of electrons.

A final medium infrared image results from the coadding of the 4 chop-nod channels: A-B – (A'-B') For each channel A, B, A' and B' several elementary frames are summed up together. For example, at Keck/LWS a 120s-observation consists of 12000 elementary 0.01s frames. In the S'/N' equation (I used the primed letters since the quantities are in unit of numbers of electrons) the noise term results from the quadratic sum of the various (independent) noise contributions in each elementary exposure:

$$N'^2 = \sum_{i=1}^{6000} \left[S'_i + A_{aperture} \times (B'_i + D'_i + R'^2) \right] + \sum_{i=1}^{6000} \left[A_{aperture} \times (B'_i + D'_i + R'^2) \right] \quad (C-3)$$

where S' is the total number of electrons from the source (within the aperture), $A_{aperture}$ is the area in pixel of the photometric aperture, B' is the number of electrons per pixel from the background, D' is the dark current of the detector per pixel and R' is the readout noise in electrons per pixel. There are two terms since for half of the time the source is off and it does not contribute. It is clear we can write:

$$N'^2 = N_{frames} \times \left(\frac{1}{2} S'_i + A_{aperture} \times (B'_i + D'_i + R'^2) \right) \quad (C-4)$$

where $N_{frames} = 12000$ in this example. The final S/N ratio is therefore given by:

$$\frac{S'}{N'} = \frac{\frac{1}{2} N_{frames} S'_i}{\sqrt{N_{frames} \times \left(\frac{1}{2} S'_i + A_{aperture} \times (B'_i + D'_i + R'^2) \right)}} = \frac{S'}{\sqrt{S' + A_{aperture} (B' + N_{frames} D'_i + N_{frames} R'^2)}} \quad (C-5)$$

which closely resemble the well-known ‘‘CCD equation’’ (see Howell 1989). However, in the background-limited case, detector read noise, dark current noise, etc., are negligible compared to fluctuations in the incident background photon flux rate. In fact the environmental 10 μm thermal background flux in the Cassegrain focal plane of a large, ambient-temperature telescope is of the order of 10^9 photons $\text{s}^{-1} \text{m}^{-2} \mu\text{m}^{-1} \text{arcsec}^{-2}$. (Gezari et al. 1992). For 0.01s integration time, 0.7 quantum efficiency, 0.08 arcsec/pixel scale there are about 4.5×10^6 electrons/pixel; about half of the pixel full well capacity (1.1×10^7 electrons). The dark current is about 4×10^5 electrons/pixel for such integration time while the readout noise is about 1000 electrons. We have thus $(B'_i + D'_i + R'^2) = (4.5 \times 10^6 + 4 \times 10^5 + 10^6)$ in the denominator term of the S/N equation. The dark current contribution is completely negligible, and the background dominates the readout noise contribution. Actually, the measured background value in several LWS exposures taken on the night of February 21, 2002 is about to 3500 counts per pixel in a 0.01 second frame-time. This means 7.8×10^6 electrons (given the inverse gain of 2200 electrons/counts) making the detector readout noise even more negligible in the S/N equation.

The flux from the star α Lyr at 10 μm is about 5.8×10^7 photons $\text{s}^{-1} \text{m}^{-2} \mu\text{m}^{-1}$ above the atmosphere, which gives about 4.0×10^7 electrons integrated within the photometric aperture for an integration time of 0.01s, 0.7 of detector quantum efficiency and 1 μm filter bandwidth. Using a photometric aperture of 13 pixels of radius (corresponding to about 1 arcsec) $A_{aperture}$ is equal to 530 pixels.

$$\frac{S'}{N'} = \frac{S'}{\sqrt{S' + A_{aperture} (B' + N_{frames} D'_i + N_{frames} R'^2)}} = \frac{2 \times 10^7}{\sqrt{2 \times 10^7 + 530 \times (4.5 \times 10^6)}} \approx \frac{2 \times 10^7}{\sqrt{530 \times (4.5 \times 10^6)}} \quad (C-6)$$

The source ‘‘shot noise’’ contribution to the denominator term in the signal-to-noise ratio equation is clearly negligible compared with the background one ($2 \times 10^7 \ll 2.3 \times 10^9$)

LEBENS LAUF

Persönliche Angaben

Name Marco Delbo
Geburtsdatum 25 Februar 1972
Geburtsort Novi Ligure (AL), Italien
Familienstand Ledig

Ausbildung

01.07.1991 "Diploma di Maturita' Scientifica" (zu vergleichen Abitur), Novi Ligure
15.10.1997 Italienische "Laurea" (zu vergleichen Diplom) Physik, Univeristà di Genova, Italien
25.10.2000 School of astronomical technology (Napoli, Italien)
1999-2001 Anfertigung der Dissertation am Deutschen Zentrum für Luft- und Raumfahrt e.V., Berlin
2002-2004 Anfertigung der Dissertation im Istituto Nazionale di Astrofisica, Osservatorio Astronomico di Torino, Italien
Doktorand an der Freien Universität Berlin

Ich versichere, daß ich die vorliegende Arbeit selbstständig verfaßt und keine anderen als die angegebenen Hilfsmittel und Hilfen verwendet habe.

Berlin, 21.06.2004

Marco Delbo

